I. Phase Transformations and the Spectral Reflectance of Solid Sulfur: Possible Metastable Sulfur Allotropes on Io's Surface II. Photochemistry and Aerosol Formation in Neptune's Atmosphere

Thesis by

Julianne Ives Moses

In partial fulfillment of the requirements

for the Degree of

Doctor of Philosophy

California Institute of Technology

Pasadena, California

1991

(submitted 20 May 1991)

To my parents, Barbara and Harry Moses.

Acknowledgments

I am forever indebted to those who have instilled in me the joy of learning. I have been lucky enough to have had enthusiastic and dedicated teachers throughout my life from grade school to graduate school. This thesis is the product of innumerable minds, texts, and teaching styles, and I cannot even begin to list all those who have contributed to its development.

Yuk Yung has supported me for many years at Caltech and has inspired me with his enthusiasm, generosity, wisdom, humor, eternal optimism, limitless ideas, and genuine love of science. He was always available and willing to discuss even my most trivial projects and problems. I thank him for introducing me to the delights of planetary atmospheres, and will always remember, "Science is like capitalism..." and many other philosophical discussions. In the years to come, I hope that I can be as productive and as good natured as he.

Doug Nash has graciously allowed me the opportunity to work in his laboratories at JPL and San Juan Institute and has taught me the excitement (as well as the occasional frustration) of experimental work. His excellent organizational skills and careful laboratory techniques have served as a wonderful example for me; I now have a better understanding of the advantages and limitations of laboratory data. I thank Doug most of all for his support and encouragement throughout my graduate career.

Mark Allen has been a great help in this past year and his encouragement has been much appreciated. I thank him for being my guide through the labyrinth called the KINETICS program, for giving great feedback on various papers, and for occasionally playing pessimist to Yuk's optimist.

Much of the groundwork for the Neptune project was laid by others. Yuk and

Mark developed the chemical kinetics program, and Yuk, Mark, Randy Gladstone, Joe Pinto, and many others compiled the hydrocarbon reactions, reaction rates, molecular cross sections, and solar flux files used in the Neptune model.

I have benefited from numerous scientific discussions with Andy Ingersoll, Dave Stevenson, Dewey Muhleman, and Dave Crisp. Their insight and experience have been a valuable resource. I would like to thank all the planetary science faculty for being excellent role models in science and for honestly caring about the well being of the graduate students.

Steve Ostro and Jonathan Gradie introduced me to planetary science and are directly responsible for my interest in the field. I especially appreciate Jonathan's generosity in sending a timid undergraduate to professional meetings and for his role as mentor.

Several former graduate students helped me considerably during my early years at Caltech. Jim Friedson helped me to focus my second proposition and was always willing to "talk science"; Don Rudy and Tim Dowling taught me VMS and patiently helped me with programming problems my first year (as well as created interesting e-mail limericks); Arie Grossman provided computer help and imparted his knowledge of the ins and outs of Caltech bureaucracy (and the ways around it); Ken Herkenhoff and Diane Michelangeli were great officemates and role models; and Randy Kirk (unbeknownst to him) provided the basic macros for this thesis.

To the current generation of graduate students, I owe an enormous debt of gratitude. If I hadn't had fun, I wouldn't have stayed. Great thanks go to Chris "Comet" Wilson for putting up with me as a (messy) roommate for five years, for cooking for me when I looked pitifully hungry, for the many serious and funny personal discussions, and for the French and German translation assistance. My fellow first year graduate students Mark, Mike, Rich, and Tomas helped me deal with the pressure

of orals and patiently listened to expositions of my projects. Mark Hofstadter was a primo lunch partner and enthusiastic beach volleyball organizer. Thanks for all the great discussions, scientific and otherwise. Rich Achterberg has given me computer advice and has helped solve all sorts of system problems. Thanks to all my friends, especially Chris T. (the wonder horse), Neill (Go Cubs!), Kathy, Kim, Michelle, all the planetoids, Rich R., Paolo, the Astronomers, the Physicists, Lorraine, Linda, Julia (my cats thank you too), the v-ball players, Mel's Ant Farm, Krusty members (just wait 'til this year), and all the others who have kept me entertained and sane (?) during graduate school. Sack break? Thanks, also, David for being a patient and courteous officemate these past few months.

The administrative staff of the planetary department is extremely competent and professional. Thank you, Kay, for keeping things running smoothly, Donna for TEX assistance and for typing the first draft of the sulfur paper, and Lorna for the privilege of house sitting. Michael Black has been a perfect system manager and has always been willing to help above and beyond the call of duty.

I am eternally grateful to my parents and brother for their confidence in me. With great love and affection, I dedicate this thesis to my parents to whom I owe more than I can ever express. They always encouraged me to pursue my education even when I chose a field that must have appeared very odd. Thank you for never telling me to do my homework; if you had, I probably would have rebelled and dropped out of school in third grade. I hope you know I love you.

Abstract

This thesis consists of two independent papers:

PAPER I:

The spectral reflectance of elemental sulfur is examined in a set of laboratory experiments to determine the factors that affect the transformation rate of monoclinic (β) sulfur and various other sulfur allotropes into orthorhombic (α) sulfur. The laboratory data have implications for the spectral variation and physical behavior of freshly solidified sulfur, if any exists, on Jupiter's satellite Io. Depending on its thermal history, molten sulfur on Io would initially solidify into a glassy solid or a monoclinic crystalline lattice; these forms might contain polymeric sulfur molecules as well as the more abundant S_8 molecules. If freshly frozen sulfur on Io could lose heat rapidly and approach ambient dayside Io temperatures within several hours, then some of the metastable sulfur allotropes could be maintained on Io virtually indefinitely. Small droplets of sulfur ejected during plume eruptions might cool quickly enough to preserve these allotropes, but sulfur in large volcanic flows or lakes would probably remain warm long enough for phase transformations to proceed at a visible rate.

PAPER II:

Photodissociation of methane at high levels in Neptune's atmosphere leads to the production of more complex hydrocarbon species such as ethane, acetylene, methylacetylene, propane, diacetylene, ethylacetylene, and butane. These gases diffuse to the lower stratosphere where temperatures are low enough to allow all seven of the aforementioned species to condense. Particle formation may not occur readily, however, as the vapor species become supersaturated. We present a theoretical analysis

of particle formation mechanisms at conditions relevant to Neptune's troposphere and stratosphere and show that hydrocarbon nucleation is very inefficient under Neptunian conditions: saturation ratios much greater than unity are required for aerosol formation by either heterogeneous, ion–induced, or homogeneous nucleation. Thus, stratospheric hazes may form far below their saturation levels. We compare nucleation models with detailed atmospheric photochemical models in order to place realistic constraints on the altitude levels at which we expect hydrocarbon hazes or clouds to form on Neptune.

Table of Contents

List of Figures

PAPER I:

PAPER II:

List of Tables

PAPER I

Phase Transformations and the Spectral Reflectance of Solid Sulfur: Possible Metastable Sulfur Allotropes on Io's Surface

PHASE TRANSFORMATIONS AND THE SPECTRAL REFLECTANCE OF SOLID SULFUR: POSSIBLE METASTABLE SULFUR ALLOTROPES ON IO'S SURFACE

Julianne I. Moses

Division of Geological and Planetary Sciences

California Institute of Technology

Pasadena, California 91125

and

Douglas B. Nash

San Juan Capistrano Research Institute

31872 Camino Capistrano

San Juan Capistrano, California 92675

Published in modified form in *Icarus*

February 1991

Contribution number 4808 from the Division of Geological and Planetary Sciences,

California Institute of Technology, Pasadena, California 91125.

Abstract

The spectral reflectance of elemental sulfur that has solidified from a melt changes with time after the sulfur has solidified. This temporal variation arises as a result of phase transformations occurring within the solid. In a set of laboratory investigations, we find that variations in the thermal history of the sulfur samples profoundly affect the solid–state transformation rate and the corresponding spectral variation of freshly frozen sulfur. In particular, samples that were heated to 393 K and 453 K for various lengths of time (up to 50 hrs) and then solidified and aged at various temperatures (from 260 to 318 K) brighten at visible wavelengths on very different time scales. This temporal variation is thought to be due to differences in the amount and type of metastable allotropes present in the sulfur after solidification as well as to the physics of the phase transformation process itself.

Our laboratory data have implications for the spectral variation and physical behavior of freshly solidified sulfur, if any exists, on Jupiter's satellite Io. Depending on its thermal history, molten sulfur on Io will initially solidify into a glassy solid or a monoclinic crystalline lattice; these forms may contain polymeric molecules as well as the more abundant S_8 molecules. If freshly frozen sulfur on Io can lose heat rapidly and approach ambient dayside Io temperatures within a few hours, then our laboratory results imply that the metastable monoclinic or polymeric allotropes can be maintained on Io and will take years to convert to the stable orthorhombic crystalline form. We present cooling rate calculations that indicate that metastable allotropes can be preserved in small droplets of sulfur ejected during volcanic plume eruptions on Io. However, sulfur in large volcanic lakes or flows on Io might remain warm long enough for the conversion of monoclinic sulfur into orthorhombic sulfur to proceed, and we would expect rapid brightening (on the order of hours or days) in these areas after the liquid sulfur has solidified.

1. Introduction

Considerable controversy exists regarding the presence or absence of elemental sulfur on Jupiter's satellite Io. The evidence for sulfur and sulfur compounds on and about Io has been reviewed by Nash *et al.* (1986). The indirect evidence is based on two sets of Earth–based observations: the observation that the reflectance spectrum of Io at ultraviolet, visible, and near infrared wavelengths is similar to laboratory spectra of powdered elemental sulfur (Sill 1973, Wamsteker *et al.* 1974, Fanale *et al.* 1974), and the discovery that neutral and ionized sulfur atoms exist in the Io torus (Kupo *et al.* 1976, Durrance *et al.* 1982, Brown *et al.* 1983). Direct evidence for elemental sulfur on Io was presented after the *Voyager* encounters when Pearl (1984, 1988) reported that the IRIS instrument detected S_8 in emission in the thermal infrared spectra of Io. In fact, J. C. Pearl (personal communication) finds that S_8 is more abundant than SO_2 over much of Io's surface; note that SO_2 is the only other chemical species positively identified on Io's surface (see Smythe *et al.* 1979, Fanale *et al.* 1979, Hapke 1979) although the presence of H_2S is inferred (Nash and Howell 1989, Howell *et al.* 1989).

In spite of the overwhelming evidence for sulfur compounds on Io, the suggestion that elemental sulfur (S_8) covers an extensive fraction of the surface has been seriously questioned (e.g., Young 1984, Hapke 1989). The S_8 molecule has an ultraviolet absorption band that extends to blue wavelengths. This absorption in the blue and violet is the reason that sulfur appears yellow at room temperature. At the lower temperatures typical at Io's surface (daytime temperatures of 90 – 130 K), however, the absorption band becomes substantially narrower, and S_8 appears white or very pale yellow [e.g., see spectra presented by Nash and Fanale (1977) and Gradie and Veverka (1984)]. Because of this temperature dependence of the absorption band of the S_8 molecule, one would expect a sulfur–covered Io to be brighter at short wave-

lengths as it emerges from eclipse behind the Jovian shadow and to darken gradually back to normal as the surface heats up. Veverka *et al.* (1981) have examined *Voyager* images with this "post–eclipse brightening" in mind and see no evidence for brightening at the 10% level expected for a surface covered with S_8. Similarly, Hammel *et al.* (1985) have examined Io's full–disk albedo during narrowband photometric ground–based observations of Io emerging from eclipse and conclude that no more than 50% of the surface can be covered with S_8.

Another problem with elemental sulfur as an omnipresent crustal component is its low tensile strength and low melting point. Smith *et al.* (1979a) proposed a lithospheric model in which Io's upper crust is composed primarily of elemental sulfur and SO_2 overlying a vast sulfur ocean. Pure sulfur in such a model would melt at a depth of about 1.5 km (Smith *et al.* 1979a). However, Clow and Carr (1980) note that the 1– to 3–km relief on escarpments and calderas on Io (see Arthur 1981, Schaber 1982) is inconsistent with such a thick sulfur crust, and silicates must play a prominent role in the crustal evolution. The wavelength dependence of the albedo of much of Io's surface, on the other hand, is inconsistent with silicates but is consistent with sulfur and other relatively volatile or processed materials (McEwen 1988, Simonelli and Veverka 1986). In addition, the extensive layered terrains discussed by Schaber (1982) seem more consistent with volatile materials than with silicates. It seems likely that silicate materials play a dominant role in the bulk of the crust but that a veneer of volcanic material and condensed volatiles may cover the surface, perhaps becoming thick in local areas.

One final possible problem with elemental sulfur as a widespread surface constituent has been suggested by Hapke (1989) and concerns the decrease in reflectance with decreasing wavelength in the violet region of the spectra of both Io and elemental sulfur. Hapke (1989) claims that the violet reflectance spectra of laboratory

sulfur drop off very sharply with decreasing wavelength below 0.4 μm whereas the Io spectrum decreases more gradually in this wavelength region. Hapke uses this general observation to suggest that elemental sulfur cannot be present in large amounts on Io's surface.

The evidence for and against elemental sulfur on Io's surface is therefore baffling. We know from infrared observations that S_8 exists on Io (Pearl 1984, 1988); however, the expected temperature and spectral behavior of elemental sulfur is not manifested. We also know that volatile materials dominate at least the upper optical layers of the surface since the satellite is very bright at visible wavelengths and since silicate absorption features are absent from the infrared spectra.

Many investigators have attempted to alleviate the objections to elemental sulfur on Io by suggesting (1) that unstable non–S_8 allotropes could be preserved on Io and alter the color of ordinary elemental sulfur (e.g., Nelson and Hapke 1978, Sagan 1979); (2) that impurities could modify the spectral properties of the sulfur (e.g., Nash and Fanale 1977, Moses and Gradie 1983); or (3) that exposing sulfur to UV radiation, X rays, and a vacuum environment (Steudel *et al.* 1986, Nelson *et al.* 1990, Nash 1987, Nash and Moses 1988) could alter the composition and/or texture of the solid and so change the spectral properties of any sulfur present on Io's surface. None of these attempts have been entirely successful. Young (1984) correctly points out that the highly unstable "colored" allotropes, S_3 and S_4, proposed by Sagan (1979) would be difficult or impossible to preserve on Io. The presence of UV–irradiated sulfur (Steudel *et al.* 1986) or vacuum–weathered sulfur (Nash 1987) can solve the post–eclipse brightening problem but cannot fully address the problem of the gradually decreasing violet/ultraviolet spectrum of Io (Hapke 1989). The addition of a small amount of moderately dark material such as basalt to the surface (e.g., Moses and Gradie 1983) can help the UV reflectance dilemma but cannot completely resolve the

post–eclipse brightening problem.

In this paper, we present experimental results concerning solid–state phase transformations and the related spectral changes in solid sulfur. Sulfur phase transformations (or lack thereof) have never been discussed in the context of Io's surface, yet recent publications in the planetary science literature (Nelson *et al.* 1990, Greeley *et al.* 1990) contain descriptions of processes in elemental sulfur that we believe are due to phase transformations. Our laboratory results and cooling calculations indicate that phase transformations may be suppressed under certain geological and environmental conditions on Io; thus, metastable sulfur allotropes formed during the "normal" cooling of a sulfur melt (as opposed to cooling by a rapid quenching) can persist at Io's surface. These metastable allotropes may be important surface constituents on Io, and because these forms of sulfur have physical properties different from those of orthorhombic α–S_8, some of the aforementioned difficulties with elemental sulfur being widespread on Io are no longer valid.

We have examined the temporal variation in the visible reflectance (0.35 – 0.70 μm) of sulfur samples that have solidified from a melt (hereafter referred to as sulfur "melt freezes"). The two most important metastable allotropes in which we are interested are monoclinic β–sulfur and polymeric μ–sulfur. These allotropes are present immediately after solidification of the melt, and although they are metastable at Io temperatures and will convert eventually to orthorhombic α–sulfur, the rates of the phase transformations depend strongly on the thermal history and present temperature of the solid sulfur. In fact, we will argue that these allotropes can persist for years at typical dayside temperatures on Io (90 – 130 K). The linear rate of transformation of thin films of various allotropes into α–sulfur at various temperatures has been extensively studied (see review by Thackray 1965), but detailed reflectance spectra of the process have never been presented. Our purpose in presenting such

spectra is to bridge the gap in knowledge between the linear transformation rate of thin films and the more complicated but realistic transformation rate of bulk samples, and to relate these solid–state phase transformations to the surface optical properties of bulk samples. Our ultimate goal is to predict the transformation rate of any sulfur that may exist in different geologic regimes on Io. We can then provide realistic spectra of the forms of sulfur that one would expect to see in the different geologic regimes and can estimate the magnitude and time scales of any brightness or spectral changes in localized areas on Io that one would expect to observe due to sulfur phase transformations.

2. Review of Sulfur Allotropy

Sulfur is an exceedingly complex substance whose atoms can easily bond with each other to form hundreds of intermolecular and intramolecular allotropes (see reviews by Meyer 1976, Steudel 1982). The term *intermolecular allotropy* refers to the ability of a material made of a single molecular unit such as S_8 to exist in different physical forms (e.g., different crystalline structures). *Intramolecular allotropy* refers to the ability of an element to form two or more molecular units (e.g., S_7 and S_8). Several intramolecular allotropes such as homocyclic sulfur molecules, molecules that form closed rings of 6 to 26 sulfur atoms per molecule, have been identified (Steudel 1982), and evidence for rings with greater than 26 atoms per molecule also exists (Mäusle and Steudel 1981). Small molecules S_2, S_3, and S_4 have been identified in the vapor phase and inferred in the liquid phase, and sulfur atoms can form long helical chains, commonly called catena, polycatena, or polymeric sulfur, in the liquid phase. Solid intermolecular allotropes of sulfur are also numerous. The three main solid allotropes of sulfur that are of interest in studies of Io are orthorhombic S_α, monoclinic S_β, and polymeric S_μ.

The stable form of solid sulfur at standard temperature and pressure is orthorhombic α–sulfur (S_α), which consists of puckered rings of eight sulfur atoms arranged in an orthorhombic crystal lattice (e.g., Warren and Burwell 1935, Donohue 1974). S_α is commonly a microcrystalline opaque yellow solid at room temperature but, as previously mentioned, whitens with decreasing temperature as an electronic S_8 absorption band narrows. When heated slowly to 368.5 K at 1 atm pressure, S_α converts by a solid–state phase transformation to monoclinic β–sulfur (S_β), which is the thermodynamically stable form from 368.5 K to its melting point at about 392 K. S_β is also an S_8 modification, but the S_8 molecules are arranged in a less–ordered monoclinic crystal lattice (e.g., Burwell 1937, Donohue 1974). Upon cooling, S_β crystallizes

easily from a melt and forms identifiable deep–butterscotch–colored translucent crystals, but is metastable at temperatures below 368.5 K and will convert slowly to the brighter yellow S_α.

Long chains of sulfur atoms form when liquid sulfur is heated above 432 K. These chains are stable only in the liquid but can easily be preserved in the solid if the melt is not cooled extremely slowly. The metastable polymeric sulfur (S_μ) formed in this manner is rarely observed in a pure form; that is, the polymers do not form independently from S_8 and other ring molecules. The best–known methods for concentrating S_μ in the solid are by rapidly quenching thin strands of hot (> 550 K) liquid sulfur in liquid nitrogen (see Meyer 1976) or by exposing sulfur "melt freezes" to an actively pumping vacuum environment and allowing differential sublimation of the ring and chain species to concentrate S_μ at the sample surface (Nash 1987). The chain species can be separated from the ring species in the solid by dissolving the material in carbon disulfide. The ring species dissolve readily, leaving an insoluble residue that consists primarily of polymeric sulfur. Studies of the structure of the sulfur chains indicate a helical structure with ten atoms per three turns of the helix (Tuinstra 1967, Donohue 1974). The crystal structure of S_μ depends on its method of formation; the large–scale physical structures of polymeric sulfur created by different methods are reviewed by Donohue (1974).

Because of the difficulty in obtaining pure S_μ, its color is uncertain. The carbon disulfide–insoluble part of sublimated sulfur is white (Meyer 1964). Nash (1987) showed that S_μ produced by vacuum sublimation is white or pale yellow and its color is not temperature sensitive. Steudel *et al.* (1986) find that polymeric sulfur is yellow at room temperature and white at 77 K. Crystex, the common form of commercial polymeric sulfur, is yellow, perhaps influenced by the 4% or more stabilizer used to preserve the polymers. When 99.9999% pure sulfur is heated to 520 K and allowed to

solidify to room temperature, the resulting solid appears "maize" in color; *i.e.*, yellow with a noticeable brownish tint when compared to pure orthorhombic α–sulfur. In his review of elemental sulfur, Meyer (1976) claims that polymeric sulfur is light yellow with little or no temperature dependence and that the brownish color observed in the solidified melt is due to small amounts of impurities (perhaps as little as 1 ppm) that react with the ends of the sulfur chains while the sulfur is in the liquid phase.

2.1 Some Impurities and Their Effect on Sulfur

Gaseous and other impurities have long been known to affect the properties of elemental sulfur; in particular, the viscosity of liquid sulfur and the yield of polymeric sulfur in the solid are especially altered by the presence of certain impurities. Smith and Holmes (1905) find that carbon dioxide, nitrogen, sulfur gas, and alkalies (powdered potassium hydroxide and sodium carbonate) introduced for 1.5 hrs while the sulfur is boiling reduce the amount of insoluble (polymeric) sulfur that can be preserved after solidification. They find that hydrogen sulfide and ammonia are especially effective in preventing chain formation and in reducing the polymer yield, whereas sulfur dioxide, air, phosphoric acid, and halogens (iodine, chlorine and bromine gas, hydrogen chloride, and hydrogen bromide) seem to favor polymer formation. The viscosity of liquid sulfur is affected by these impurities as well (see Schenk 1957a, Bacon and Fanelli 1943, Rubero 1964). Sulfur dioxide, organic sulfides, and sodium sulfide have no effect on the viscosity; selenium, arsenic, phosphorus, hydrogen, and halogens can reduce and change the temperature of the viscosity maximum; whereas hydrogen sulfide markedly reduces the viscosity of liquid sulfur at almost all temperatures.

Since sulfur chains have free radical ends, they react readily with impurities; thus, impurities can prevent full growth of the sulfur chains by reacting with their terminal valencies — smaller chain lengths have been interpreted as leading to lower

viscosity maxima (Schenk 1957a). However, since the sulfur chains S_x and modified sulfur chains (e.g., I–S_x–I where I represents some impurity) are still present, the yield of polymeric sulfur is still nonzero. Hydrogen sulfide and its reaction products, sulfanes (or persulfides of hydrogen, H_2S_x), are extremely effective in preventing polymer formation and in reducing the viscosity of liquid sulfur; however, the larger the value of x, the fewer differences that exist between S_x and H_2S_x, and the less influence the sulfanes have on the physical properties of sulfur (Schmidt 1965). Sulfur dioxide, on the other hand, aids polymer formation, perhaps by attacking the sulfur–sulfur bonds, allowing the rings to break and chain formation to be initiated.

Because different impurities react with sulfur in different ways, it is nearly impossible to predict the effect of impurities on the properties of any sulfur on Io. We know that SO_2 and sodium and potassium compounds exist on Io. If these compounds exist as the only impurities in any liquid elemental sulfur on Io, then we would expect sulfur polymers to exist and the viscosity of the sulfur to be similar to pure elemental sulfur observed in terrestrial laboratories. However, the addition of H_2S and other impurities may reduce polymer formation and affect the viscosity of the liquid.

In addition, minor amounts of impurities can affect the color of elemental sulfur. Greeley *et al.* (1990) describe 99.6% pure industrial sulfur mined by the Frasch process as "dusky red" when molten from 363 to 403 K and "dark reddish brown" just after solidification. They interpret these colors as being due to small amounts of impurities such as ash or carbon–containing material. The presence of extremely small amounts of hydrocarbons (as little as 1 ppm) seems to add an irreversible brownish tint to the yellow orthorhombic sulfur that has been heated above 473 K (Meyer 1976). Although the material that causes the brown coloration in $\lesssim$ 99.9999% pure sulfur when heated above the polymerization temperature can be removed by

various purification methods in the laboratory (e.g., Bacon and Fanelli 1942), it is doubtful that such extremely pure sulfur exists in volcanic areas on either the Earth or Io. Since the impurities on Io may be different from those occurring in terrestrial elemental sulfur, we are not certain that the colors that we observe in the laboratory will be relevant to Io. In our experiments, we have attempted to circumvent the whole problem of impurities and color by using highly pure sulfur, by heating the sulfur in an inert atmosphere (*i.e.*, N_2 or Ar), and especially by considering only low melting temperatures. Smith and Holmes (1905) demonstrate that impurities become especially important if the sulfur is heated above $\sim$ 520 K so we have examined only sulfur heated to 393 and 453 K. In spite of our precautions, however, the sulfur samples heated above the polymerization temperature (432 K) solidify into a light brown crystalline material that resembles S_β and noticeably converts to yellow S_α after a time but does not completely lose a brownish tint. We conclude that solid sulfur formed from the solidification of a superpolymerization–temperature melt under most natural conditions on Earth will appear brownish yellow or maize yellow. It is uncertain whether the impurities that cause the brown coloration (most likely hydrogen polysulfides or hydrocarbon species) will affect the color of frozen sulfur in the same way on Io as they do on the Earth so we will proceed with caution when we compare our high–temperature sulfur laboratory spectra to the spectra of sulfur that may have encountered similar thermal conditions on Io.

2.2 Composition of Liquid and "Amorphous" Sulfur

Some fraction of S_μ is present in all sulfur samples that have solidified from a 432 K or warmer melt. Factors such as melting temperature, duration of melting, and rate of solidification affect the percentage of S_μ preserved in the solid. Higher melt times (up to equilibrium values of 12 hrs or so) and faster cooling rates enable more polymeric S_μ to be preserved in the solid sulfur (e.g., Koh and Klement 1970,

Mäusle and Steudel 1981). Sulfur that has been heated above the polymerization temperature in the liquid, 432 K, and then chilled quickly below 323 K will solidify into a seemingly amorphous, plastic mass. In fact, if the hot liquid is chilled quickly below $\sim$ 243 K, the sulfur will be in the vitreous state . A fraction of the solid formed after solidification from a melt above the polymerization temperature will be insoluble in carbon disulfide, indicating that some of the polymers have been retained (sulfur ring species are soluble in CS_2). The presence of the metastable S_μ in the solid can be understood from the fact that the kinetics of sulfur chain disruption in the liquid is slow (so that short melt times and fast quenching rates do not allow equilibrium to be reached) and the fact that thermal energy is responsible for the breakup of sulfur rings and subsequent formation of chain molecules (so that higher temperatures imply more molecular chains). Therefore, knowledge of the thermal history of any sample of solid sulfur is important for the interpretation of its optical properties and likely composition. A knowledge of the melting history of the sample is especially important because many of the non–S_8 allotropes are formed in the liquid state.

The molecular composition of liquid sulfur is complex and only gradually becoming well determined (e.g., Aten 1914, Harris 1970, Mäusle and Steudel 1981). In particular, the molecular composition of the liquid depends strongly on temperature. Table I, which includes the results from several different investigations, illustrates this effect.

The results from Table I were actually obtained for rapidly quenched solid sulfur and were assumed to reflect the liquid composition. Below 432 K, the melt consists mostly of S_8 rings (90 – 95% by weight) with a few percent other ring species, and very little polymeric sulfur. Some of the non–S_8 ring species (especially S_7) are preserved after the quenching of the liquid and can transform, in part, into S_μ. This transformation may explain the somewhat high percentages of S_μ observed in older

Table I
Equilibrium Molecular Composition of Liquid Sulfur (wt %)

T (K)	non-S_8[a]	non-S_8[b]	S_6[a]	S_7[a]	S_x[a]	S_μ[c]	S_μ[d]	S_μ[a]
388	5.0		0.6	2.8	1.5			0.05
393		5.9						
398		6.5						
403	6.1	6.8	0.9	3.6	1.4	4.2		0.2
413		8.3				5.6		
418	6.6	9.0	0.9	4.0	1.3		2	0.4
423						6.7	2.5	
432	9.6		1.4	4.7	1.1		4	2.4
433		12.0				11.0	8	
443		20.9				18.7	17	
453		26.6				22.5	25	
469		36.6						
473						27.0	38	38.5
493		39.4				29.4	47	
513						33.0	54	
523	56.2		0.9	3.3	0.7		55	51.3
623	57.2		1.0	3.5	0.7			52.0

[a] from Mäusle and Steudel (1981). Note that S_x means sulfur rings with $x > 8$. S_μ is insoluble in CS_2 and is presumed to be polymeric sulfur.
[b] from Aten (1914).
[c] from Smith and Holmes (1905). These values may not represent equilibrium percentages.
[d] from Koh and Klement (1970).

low-temperature experimental data (see Table I); some of the older data were taken several hours or days after solidification (Smith and Holmes 1905, Koh and Klement 1970) after some of the S_7 had converted to S_μ. Mäusle and Steudel (1981) were careful to keep the quenched melt at 77 K to inhibit this transformation and find only small percentages of S_μ from low-temperature melts (*i.e.*, melt temperatures

< 432 K). However, the percentage of S_μ in the liquid increases dramatically at temperatures greater than 432 K. For instance, at 453 K about 25% of the melt is polymeric sulfur, and at 623 K just over 50% is found to be S_μ. Mäusle and Steudel (1981) note that small amounts of [solid] impurities have little influence on the molecular composition of liquid sulfur since the same results were obtained with both ultrapure (> 99.999% pure) and standard commercial–grade sulfur. As already mentioned, however, the amount of polymeric sulfur in the quenched solid is quite sensitive to gaseous impurities.

Even when the liquid is not rapidly quenched but is cooled at a finite rate faster than a degree or so per hour, slow kinetics of sulfur species in the liquid prevents equilibrium from being reached, and nonequilibrium species can easily be "frozen in" upon solidification. These nonequilibrium species are unstable and will transform to S_8 at finite rates that range from hours or days (for S_7 and S_6 at room temperature) to months or years (for S_μ at room temperature) (see Meyer 1964, Thackray 1965, Mäusle and Steudel 1981). In addition, S_8 generally crystallizes in a monoclinic (β) structure upon solidification and undergoes a phase transformation to S_α at temperatures below 369 K. The rate of this transformation is highly dependent on temperature and ranges from an hour or so in a bulk sample at 320 K to several days at 260 K (Thackray 1965, and this work, see Section 6). Therefore, the optical properties of a bulk sulfur sample that was once molten will vary on time scales that depend on its thermal history and the rate of the appropriate solid–state phase transformations. Since an understanding of the physics of phase transformations is key to the understanding of the temporal variation in the spectral reflectance of fresh solid sulfur, we briefly review the theory of phase transformations in the next section.

3. Review of Solid–State Phase Transformations

A solid–state phase transformation is a process whereby a substance transforms from one initial solid phase into another more stable modification. Substances like sulfur that can exist in more than one crystalline form are called polymorphic materials. Phase transformations in polymorphic substances are often observed upon a change in temperature or pressure, and there is usually a delay in the appearance of the new phase so that a "metastable" condition develops. The rate of the transformation into the new phase is a complicated and poorly defined quantity that depends on thermodynamic and structural properties of the material. Often, as the temperature of a polymorphic substance is lowered below the equilibrium temperature of one phase with respect to another phase, the new phase appears at a rate that is slow at first, then speeds up, and then slows again (Avrami 1939). Avrami explains that this typical "S shape" of the transformation–versus–time curve (e.g., Figure 1) is due to the separate processes of nucleation and crystal growth. "Germ nuclei" or embryos of the new phase must form spontaneously before the phase transformation can be initiated. This nucleation process is often slow unless foreign particles, minute fragments of the new phase, or favorable sites on the walls of the sample container exist (e.g., Rawson 1967). Even then, the kinetic rate of molecules diffusing to the new phase must exceed the rate of molecules diffusing away from the germ nuclei for crystal growth to begin. Therefore, the initial slow transformation rate described by Avrami is due to the slow formation of germ nuclei and the slow formation of growth nuclei from the germ nuclei. Once growth is initiated, the transformation proceeds at the rate of crystal growth. Finally, the transformation slows as no new germ nuclei are formed and as the growing crystals begin to impinge on each other (Avrami 1939). Occasionally, as in nucleation of atmospheric gases, the first step is very rapid and the last step is unimportant so that the transformation can be described by the "linear"

transformation rate defined by the crystal growth (*i.e.*, the linear part of the curve in Figure 1). Most experimental studies of transformations in solid sulfur examine this linear rate to gain some quantitative knowledge of the thermodynamic properties and characteristics of the transformation. However, the nucleation rate itself may be nonnegligible, so these studies of the linear transformation rate of thin films can only represent maximum transformation rates when compared to the behavior of larger quantities of sulfur (e.g., sulfur in a geologic setting).

Over the past several decades, attempts have been made to quantify the theory of transformation rates. With simple crystal systems and, especially, with the growth of crystals from a liquid, thermodynamic treatments have met with some success (see review by Verma and Krishna 1966). Crystals can grow by utilizing lattice imperfections such as screw dislocations found in all real crystals (Frank 1949). With more complicated solid–to–solid transformations, however, the thermodynamic theory is often too simplistic or impossible to quantify because the rate depends on several variables that depend on temperature in an unknown manner. Buerger (1951) emphasizes the importance of the structural aspects of phase transformations. He notes that the crystal structure of the old and new phases and a knowledge of the connection between the two phases during the transformation are necessary for a complete understanding of the transformation rate. The additional complication due to structural aspects makes theoretical determinations of transformation rates virtually impossible. However, simple kinetic and thermodynamic theories combined with experimental data are often sufficient for reliable predictions of transformation rates. We will use such approaches in this paper.

The following discussion of the kinetic theory of phase transformations and our application of the theory to sulfur transformations relies heavily on work by Rawson (1967) and Turnbull (1956). The treatment starts with the assumption that germ

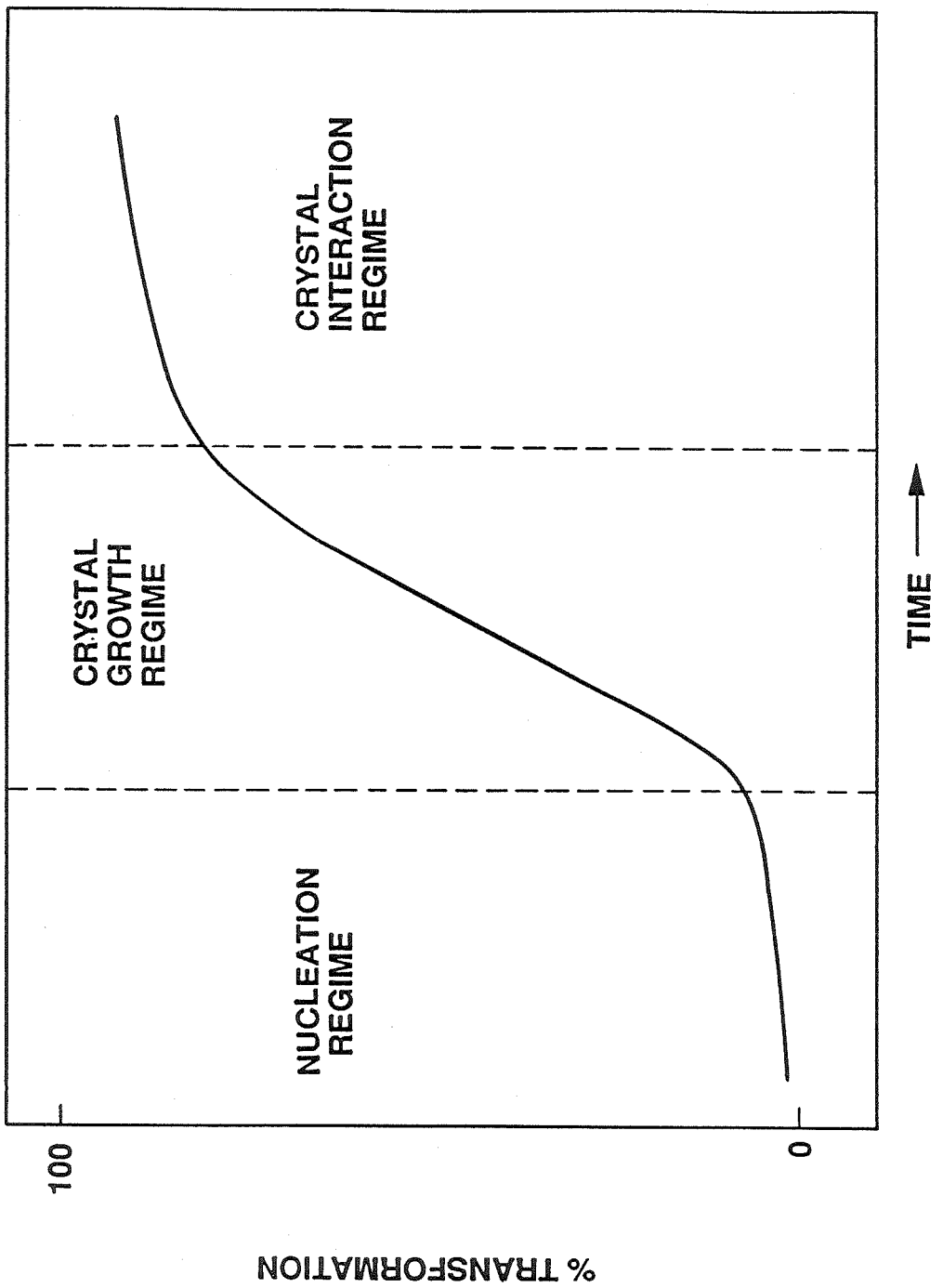

Figure 1. The transformation rate of a stable phase growing from a metastable phase as a function of the age of the metastable species.

nuclei of the new phase already exist, so that a nucleation step is irrelevant. Thus, the theory describes the growth of the new phase and provides a maximum possible transformation rate; this rate is realistic only if solid impurities or other imperfections exist within the initial solid phase.

At the equilibrium transition point between two possible phases, the Gibbs free energy of the two phases is equal. Both phases are stable. For molecules of one phase to free themselves from their neighbors in the first phase and to attach themselves to molecules of the second phase, the molecules must first diffuse through the solid and then overcome an energy barrier represented by the surface or interface of the crystals. Molecules from either phase are equally likely to proceed in this manner. However, if the temperature is raised or lowered, one phase will become stable relative to the other. Figure 2 illustrates this behavior by schematically showing the free energy versus position for molecules at an interface between phases α and β. Molecules in structure β, as illustrated, have a free energy per molecule that is higher by an amount ΔG than those of structure α, so the β phase is unstable relative to the α phase. A molecule in the β phase must acquire a free energy of activation equal to the energy of the interface, ΔG_{int}, to migrate from β to α. Molecules in the α phase have an even higher barrier to overcome; they must reach energies of $\Delta G + \Delta G_{\text{int}}$. Therefore, the net transformation rate $\beta \rightarrow \alpha$ can be described by the frequency of molecules diffusing from the β phase to the α phase relative to the frequency of molecules diffusing from α to β. That is,

$$\nu_{\beta\rightarrow\alpha} = \nu_o \exp[-\Delta G_{\text{int}}/kT]$$

while

$$\nu_{\alpha\rightarrow\beta} = \nu_o \exp[-(\Delta G + \Delta G_{\text{int}})/kT]$$

where ν_o, the fundamental jump frequency, is taken to be proportional to T. The rate of growth of the α phase from the β phase is proportional to $\nu_{\beta\rightarrow\alpha}$ minus $\nu_{\alpha\rightarrow\beta}$

so the rate of α crystal growth can be written

$$R(\beta \rightarrow \alpha) = AT \exp\left[\frac{-\Delta G_{\text{int}}}{kT}\right]\left[1 - \exp\left(\frac{-\Delta G}{kT}\right)\right] \qquad [1]$$

where A is constant. At the transition temperature T_o, $\Delta G(T_o) = \Delta H_o - T_o \Delta S_o = 0$, implying that $\Delta G = \Delta S_o(T_o - T)$ if the entropy of transition is independent of temperature. Meanwhile, ΔG_{int} is only weakly dependent on temperature so that the transformation rate versus temperature curve will have the general shape illustrated in Figure 3. For the β to α transformation of sulfur, $T_o = 368.5$ K. As T approaches T_o, ΔG is very small and the $[1 - \exp(-\Delta G/kT)]$ term approaches $\Delta G/kT$ and dominates the rate behavior. For very cold temperatures, however, the first exponential factor takes over. Since ΔG_{int} and A are generally unknown, this equation alone cannot be used to theoretically calculate the transformation rate. However, this equation combined with laboratory data can be used to estimate the transformation rate at temperatures that would otherwise be too low to observe a measurable transformation rate in the laboratory.

The rate theory described above is valid only for the case in which all possible sites on the growing crystal surface are available for molecular attachment (Turnbull 1956). In real applications, this rate equation breaks down as $(T_o - T) \rightarrow 0$. Hillig and Turnbull (1956) have attempted to resolve the differences between experiment and theory by considering that growth by screw dislocation steps allows only a fraction f of the total sites on the crystal surface to be available for molecular attachment. Then, as $\Delta T \rightarrow 0$, the rate proceeds as

$$R(\beta \rightarrow \alpha) \propto T \exp\left[\frac{-\Delta G_{\text{int}}}{kT}\right]\left(\frac{\Delta S_o \Delta T}{kT}\right) f$$

where f is proportional to ΔT. Thus, the rate as $\Delta T \rightarrow 0$ can be described by

$$R(\beta \rightarrow \alpha) = a \exp\left[\frac{-\Delta G_{\text{int}}}{kT}\right](T_o - T)^2 \qquad [2]$$

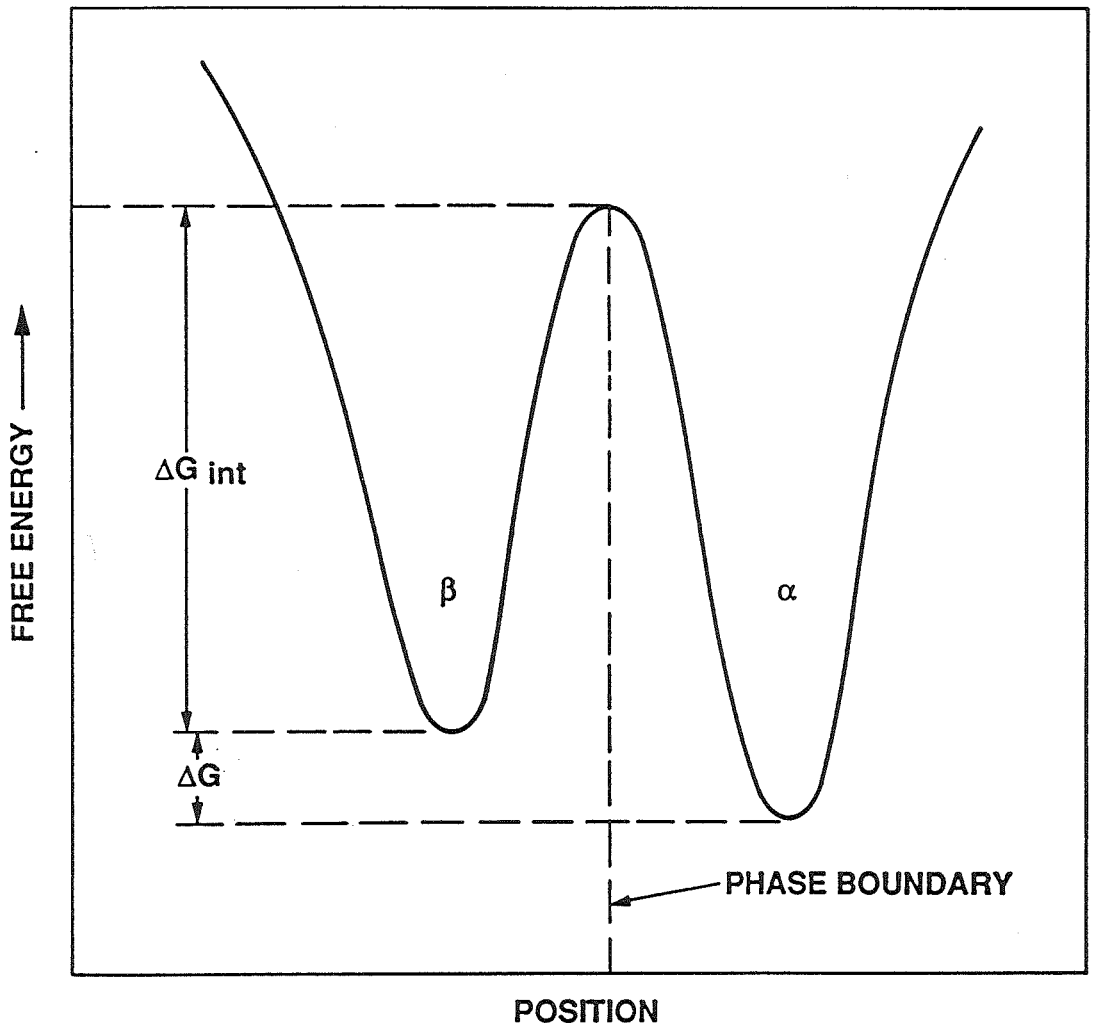

Figure 2. The free energy diagram for molecules crossing an interface between a metastable phase (β) and a stable phase (α).

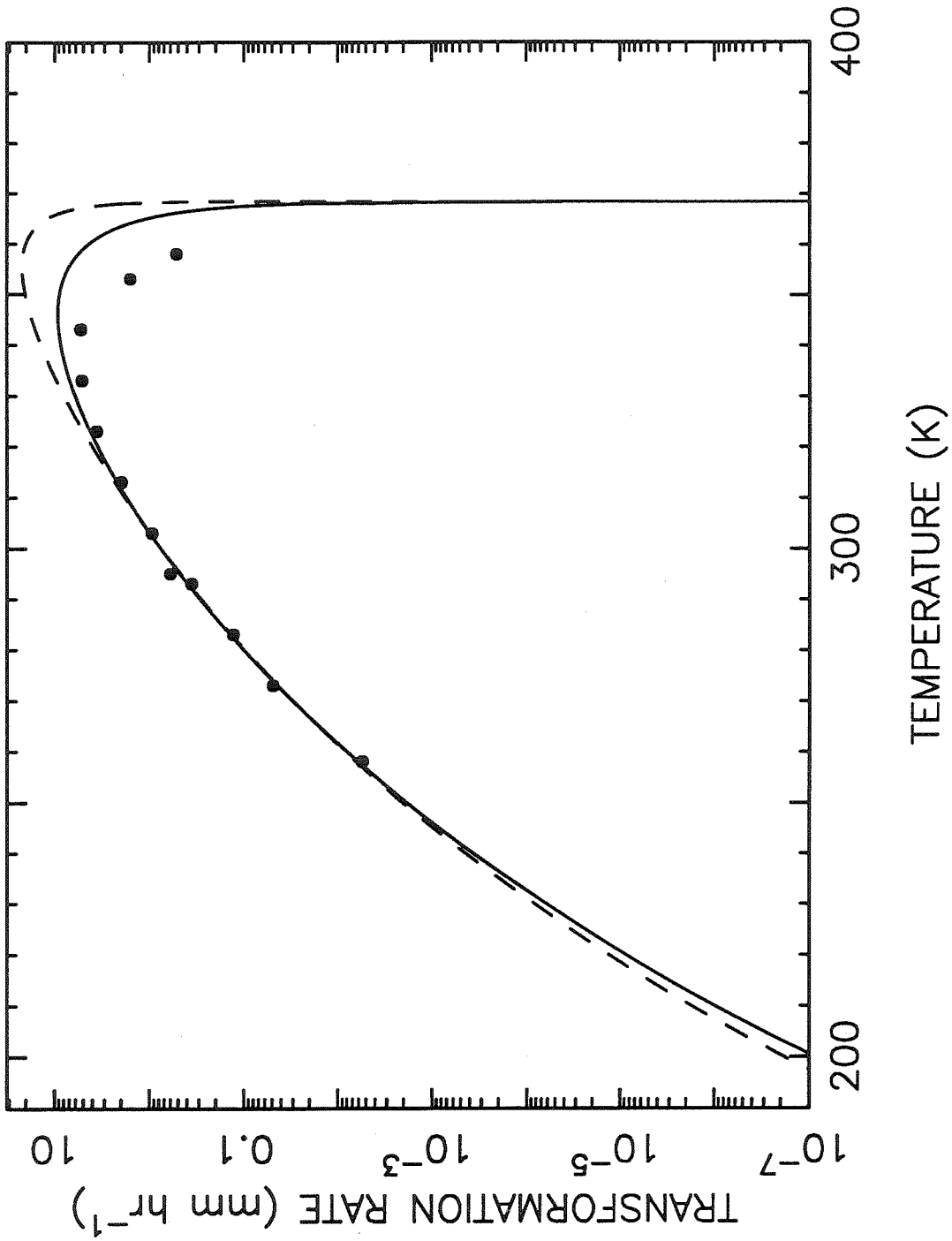

Figure 3. The effect of temperature on the solid–state linear transformation rate of meta–stable β–sulfur into stable α–sulfur. The black dots represent data presented by Thackray *et al.* concerning the linear transformation rate of S_β into S_α, and the solid line represents the best fit of equation [2] and the dashed line the best fit of equation [1] to Thackray's data.

where a is constant. For the case of sulfur, $\Delta S_o \Delta T < kT$ from 120 to 368.5 K, so equation [2] can be used to describe the behavior of the transition from β–sulfur to α–sulfur in this temperature range. At the low temperatures typical at Io's surface — 90 to 130 K — the $S_\beta \rightarrow S_\alpha$ transformation is immeasurably slow in the laboratory, but we use the above equations combined with laboratory data to provide rate estimates that are good to within an order of magnitude or so.

4. Phase Transformations in Sulfur

Because the transformation from monoclinic (β) to orthorhombic (α) sulfur is observable at temperatures easily reached in the laboratory, the process has been studied for over a century. Gernez (1885a,b) studied the linear rate of transformation of S_β into S_α. The sulfur examined by Gernez was melted and solidified in thin glass capillary tubes, and the rate was determined by direct observation. Gernez (1885b) was the first to show that melt temperature, melt time, and aging temperature affect the transformation rate of solid sulfur. He finds that the transformation from S_β into S_α proceeds the most rapidly when the sulfur is held at 328 K [slightly lower but similar to the temperature of maximum rate observed by Thackray (1965); see Figure 3] after solidification but slows as the aging temperature is decreased to 250 K or increased to 368 K. Gernez also finds that the length of the melting period affects the transformation rate: sulfur that remains melted at 402 K for 60 min before solidification transforms to α–sulfur eight times more rapidly than sulfur melted for just 5 min at the same temperature. In addition, high–temperature melts (up to 538 K) take longer to transform to S_α after solidification than low–temperature melts. These findings are consistent with current views concerning the complexity of the liquid state (see Section 2); some of the non–S_8 species that are present in the liquid sulfur and preserved after the sulfur has solidified can somehow kinetically inhibit the $\beta \rightarrow \alpha$ phase transformation.

Fraenkel and Goez (1925), who studied the linear transformation rate of thin films of S_β into S_α on microscope slides, were among the first investigators to note that the slow transformation of S_β that was once heated to high temperatures is caused by the preservation of polymeric S_μ in the monoclinic (β) sample. They claim that melt temperatures must be kept below 403 K to prevent brown polymeric sulfur from contaminating the S_β crystals and to get an accurate measurement of the $S_\beta \rightarrow S_\alpha$

transition. Elias *et al.* (1940) note that the rate of the $S_\beta \rightarrow S_\alpha$ transformation depends on the thickness of the sulfur films: thick films of β crystals transform more rapidly than thin films. The explanation for this phenomenon is uncertain.

Numerous investigators in the 1950's and 1960's attempted to carefully control the various parameters that affect the transformation rate (e.g., Hartshorne and Roberts 1951, Hartshorne and Thackray 1957, Briske and Hartshorne 1967). These later workers carefully controlled the thermal history and purity of the sulfur crystals and used thin films of pure phases to make measurements of the "linear" rate of transformation of one phase into another (*i.e.*, the linear part of Figure 1). A review of the work up until the mid–1960's is presented by Thackray (1965). Thackray has compiled various transition–rate observations and presented curves of the linear transformation rate versus temperature from 263 to 373 K. Consistent with the work of Gernez (1885b), the maximum rate of the $\beta \rightarrow \alpha$ transition occurs near 335 K (see Figure 3.1 of Thackray 1965 and Figure 3, above).

Thackray (1965) and others have tried to use the experimental data on linear transformation rates to determine the thermodynamic and kinetic properties of the transformations, but overall consensus between the studies is sometimes lacking. The results are tabulated in Meyer (1976, Table VIII). Several investigators have used thermal and/or thermomechanical analyses to investigate the relevant thermodynamic properties and to gain a better understanding of the transformation process. Currell and Williams (1974) apply differential scanning calorimetry to sulfur melt freezes and Davis and Hyne (1976) use thermomechanical analysis to measure the expansion of sulfur melt freezes as a function of temperature. Davis and Hyne (1976) show that the thermal history of the sulfur affects the thermomechanical properties as well as the optical properties of the solid. Reimschüssel *et al.* (1978) have also used calorimetry to examine the transformation kinetics of both monoclinic (β) sulfur and amorphous

sulfur melt freezes. They define amorphous sulfur as sulfur that has been heated above the polymerization temperature of 432 K and then is frozen rapidly; it is not truly amorphous but has a large S_μ component. Reimschüssel and his co–workers find that the curves of exothermicity versus time found from the calorimeter data exhibit characteristic maxima as a phase transformation takes place; two maxima exist for amorphous sulfur whereas only one maximum exists for monoclinic S_β. Reimschüssel *et al.* conclude that the second maximum found with amorphous sulfur is due to the conversion of chains of S_μ into S_8 rings, which can then transform into orthorhombic (α) crystals. The single maximum observed in the data for S_β reflects the simple transformation of S_8 rings from a monoclinic (β) structure to an orthorhombic (α) structure. No intermediate step (as is found with amorphous sulfur) is needed.

In spite of the seeming wealth of information regarding sulfur phase transformations, it is still difficult to predict the rate of any such transformations on Io. Since more accurate information on the transformation from S_β to S_α exists than for all other sulfur transformations combined, we will now use the data presented by Thackray (1965) to predict the rate at the much lower temperatures typical on Io (90 – 130 K). In Figure 3, we compare Thackray's data with the transformation theory described by equations [1] and [2]. ΔG was estimated from the entropy of transition listed by Meyer (1976). To find $\Delta G_{\rm int}$ from Thackray's data, we minimize the square of the difference between the observed and calculated (log) rates of the coldest seven points of Thackray's data. We find it necessary to use only the coldest data because the theories diverge from the data at higher temperatures (low ΔT's). Although Hillig and Turnbull's (1956) treatment of phase growth fits the data better than equation [1], neither theory is satisfactory. Since the lower temperature data depend almost entirely on $\Delta G_{\rm int}$, however, and since we are mainly interested in the behavior at cold temperatures, the successful fit to the data in the temperature range

260 to 320 K encourages us to examine the extrapolation to lower temperatures. At 200 K, the fit of equation [1] to Thackray's data predicts an $S_\beta \rightarrow S_\alpha$ linear transformation rate of 1.84×10^{-7} mm/hr or 1 mm of α–sulfur growth in 620 years, whereas the fit of equation [2] to Thackray's data predicts a rate of 8.77×10^{-8} mm/hr or 1 mm growth in 1300 years; the difference between the two extrapolations is a factor of ~ 2. This difference is illustrative of the error that is introduced by the extrapolation of Hillig and Turnbull's theory (equation [2]) to 200 K. The predictions of equations [1] and [2] diverge even more at lower temperatures. At 120 K, equation [1] predicts 1 mm growth in 4.2×10^{16} years, whereas equation [2] predicts 1 mm growth in 1.6×10^{18} years. Although the two extrapolations differ by a factor of 40 at 120 K, the qualitative conclusion that the S_β to S_α transformation is essentially nonexistent at 120 K is still valid.

If monoclinic sulfur on Io can be cooled rapidly to ambient surface temperatures (e.g., if small liquid or monoclinic sulfur particles from volcanic conduits get entrained with other volcanic material during plume eruptions and can cool below ~ 250 K in a few minutes, see Section 7), then the data presented by Thackray (1965) indicate that the linear rate of transformation of S_β into S_α will be exceedingly slow. In contrast, any S_β formed after solidification of large volcanic sulfur flows would probably remain warm for periods of months to years (Fink *et al.* 1983) so that any S_β would convert relatively rapidly to S_α, perhaps as fast as 4 mm/hr (see Thackray 1965).

Sulfur containing S_μ is expected to take longer to convert to S_α. The cohesive energy holding the polymeric molecules together is quite large and can explain why the S_μ phase is relatively stable (Meyer 1964). In addition, the polymeric chains can intertwine in a structurally complex manner that will impede the reversion of chains into molecular rings as well as inhibit ordering into a crystal lattice (Haisty and Krebs

1969). Since the transformation of S_μ into S_α involves some complicated intermediate steps and structural and physical aspects become important, simple kinetic views of the transformation are inadequate. Mondain-Monval (1934), Koh and Klement (1970), Prins *et al.* (1956), and others have measured the transformation rate of S_μ into S_α in the laboratory near room temperature, but more data are needed before accurate predictions of this rate at Io temperatures can be made. The only statement that can be made for certain is that the conversion of S_μ to S_α will take longer than the conversion of S_β to S_α.

How can we determine whether any metastable allotropes such as S_β or S_μ exist on Io? The easiest method is to examine the normal spectral reflectance of laboratory samples of the various sulfur allotropes and compare these reflectances to the properly calibrated colors and albedos of various areas on Io's surface available from *Voyager* spacecraft data. Similarly, we could look for localized areas that have albedos that vary with time on time scales that are consistent with the transformation of the metastable allotropes into stable S_α. Neither of these methods is useful without knowledge of the geologic areas and physical environments on which we are focusing our observations; in particular, we need to know the expected thermal history of any sulfur present in the areas we are examining. For instance, sulfur in volcanic plume deposits would behave differently from sulfur in large volcanic flows. In the next two sections, we examine the cooling rates of sulfur samples that have experienced various thermal histories, and later compare the estimated spectral reflectance of such sulfur samples to observations of Io's surface.

5. Experimental Methods

Solid sulfur "melt freezes" were prepared by melting laboratory–grade sublimed sulfur powder in aluminum cups of 0.32–cm depth and 1.9–cm diameter on a hot plate heated to temperatures just above the melting point of sulfur (393 K). Enough powdered sulfur was added to fill the cups to the rim once the sulfur had melted. Then the sample cups (usually five samples per heating episode) were placed in a flat covered Pyrex dish in a dry, once–flushed, nitrogen–filled vacuum oven (at 600 Torr N_2) and kept at either 393 or 453 K for various lengths of time (up to 50 hrs). These two temperatures were chosen for specific reasons. As just mentioned, 393 K is just above the melting point of sulfur, and, as shown in Table I, a melt at this temperature consists mostly of S_8 rings with virtually no S_μ and 5 to 6% other ring species. The melt appears clear yellow and is very fluid at this temperature. Samples melted at this temperature and allowed to cool slowly to room temperature will crystallize into monoclinic S_β. At 453 K, on the other hand, the melt is just above the temperature of the maximum in viscosity of liquid sulfur, 432 K (Bacon and Fanelli 1943). About 25% of the sulfur melt at this temperature consists of polymeric chains, 7% consists of non–S_8 species, and 68% is S_8 rings. Much of the S_μ is preserved in the solid upon freezing as a fine–grained exsolved phase (Nash 1987, Nash and Moses 1988), and the S_8 initially crystallizes in a monoclinic (β) lattice. Since there is evidence that N_2 slightly reduces the amount of polymeric sulfur formed in 453 K melts (Smith and Holmes 1905), we also performed some of the experiments with Ar in the oven rather than N_2.

After a specified number of hours, the sample cups were removed from the oven and the sulfur was frozen by the emplacement of room–temperature glass microscope slides over the top of the sample cups in such a way that the glass slide was in contact with the liquid sulfur surface. This glass–slide quenching technique ensures that the

sulfur melt freezes have flat, smooth surfaces and that all the samples freeze within a few seconds of the emplacement of the glass slide and within a minute of their removal from the oven. This technique also guarantees that the crystalline surface texture of each sulfur melt freeze is fine–grained and uniform on a macroscopic level so that differences in texture do not affect our optical results. For pure monoclinic S_β, no glass slide was used and the samples were allowed to crystallize freely.

Within minutes of freezing, the spectral reflectance at visible wavelengths (0.35 – 0.70 μm) of the sulfur melt freezes was measured using a Beckman DK–2A diffuse reflectance (integrating sphere) spectrometer. The spectrometer beam spot size was approximately 1 cm^2, and the same area on the sample was always examined during each measurement. Between sequential spectral measurements, the samples were aged in air either in a closed Pyrex dish on a countertop at room temperature, on a hot plate at higher temperatures, or in an ice–packed cooler at lower temperatures (using either water ice or salt–saturated water ice). Reflectance measurements were taken periodically for periods up to a year. The spectral measurements take 3 min per sample so that the samples being aged at temperatures other than room temperature were exposed to another thermal environment briefly during measurement. This brief exposure should have little effect on our transformation rate measurements.

The monoclinic S_β samples heated to 393 K and allowed to cool slowly to room temperature appear translucent and butterscotch colored. As the transformation to orthorhombic S_α occurs, the samples appear mottled, with two to five individual opaque light yellow patches of microcrystalline S_α growing within the 1.9 cm diameter samples after a few hours at room temperature. The linear transformation rate is just slow enough to be difficult to observe at room temperature, but it appears as if a light yellow fog is intruding and spreading inside the translucent, darker crystals of S_β. Eventually, the entire sample has converted to S_α. The sample is then

opaque light yellow, but the overall macroscopic monoclinic crystalline texture (usually spherulitic) remains visible. Sulfur melt freezes (quenched using the glass–slide technique) that were heated to 393 K appear almost identical in color to the monoclinic S_β samples after solidification. The only real difference between the two cases is the presence of more than one nucleation site of the monoclinic crystals (usually three to eight individual sites) and a more uniform surface texture in the case of the quenched melt freezes; however, since the unquenched samples have larger, more well–defined crystals, we found it necessary to check whether the monoclinic (β) crystals were transparent enough to cause the bottom of our aluminum cups to influence our reflectance measurements.

To test this effect, we hollowed out one of our usual sample cups, clipped the cup to a glass slide, and poured molten 393 K sulfur into this hollow ring. After the sample solidified into a monoclinic (β) structure, we removed the glass slide from the sample, taped a smoked–MgO sample to the bottom of the β–sulfur sample, and examined the reflectance in the normal manner. Immediately afterward, we removed the MgO and put a black bottle cap in its place to check the difference in the spectrum. We also examined the effect of an aluminum cup bottom and another sulfur sample (a well–aged 453 K melt freeze) on the reflectance. We find that some light (at red to green wavelengths) does penetrate to the bottom of the sample and back to the detector, but the overall effect on the reflectance is very small. For example, at 0.70 μm, the reflectance of the β sample plus MgO bottom is 0.450 while the reflectance of the sample with a black–cap bottom is 0.428, a 5% difference. The difference between the aluminum cup bottom and the extra sulfur sample is much smaller. At 0.70 μm, the reflectance is 0.445 with the aluminum and 0.443 with the sulfur — a difference of 0.4%. The reflectance of our fresh monoclinic samples presented in Figure 4 is therefore brighter than that of a sample that is twice as deep

by a factor of less than 1%. The difference is due to the fact that the monoclinic (β) crystals are transparent and that the aluminum cup bottom is brighter than β–sulfur at all visible wavelengths.

Samples heated to the higher temperature, 453 K, and quenched by a glass slide at room temperature were generally a dark butterscotch immediately after quenching and converted to light maize within a day. The maize color continued to lighten slowly with time for months after solidification. The spectral reflectance measurements were appropriately spaced in time to monitor the visible transformations. Many spectra were required during the first day after solidification, but few were required after this period.

Because the presence of minute amounts of impurities may be causing the "maize" color rather than a pure yellow color, we have examined the reflectance of high–purity melts as well as the laboratory–grade sulfur. As already mentioned, 99.9999% pure sulfur when heated to 453 K and quenched at room temperature turns yellow after a day or so, but never loses a brownish tint; in other words, the high–purity sulfur behaves just like the laboratory–grade sulfur. Thus, we found it necessary to try another purification procedure. We purified 125 ml of our powdered laboratory–grade sulfur using the method of Bacon and Fanelli (1942). The sulfur was boiled in a Pyrex flask over an open flame. A few percent powdered MgO was added to neutralize any acids that might form from organic impurities. After 48 hrs, the sulfur was filtered and the whole process repeated again. The sulfur purified in this manner was poured into aluminum cups, the cups heated to 453 K for half an hour, the samples quenched using a glass slide, and the reflectance taken in the usual manner.

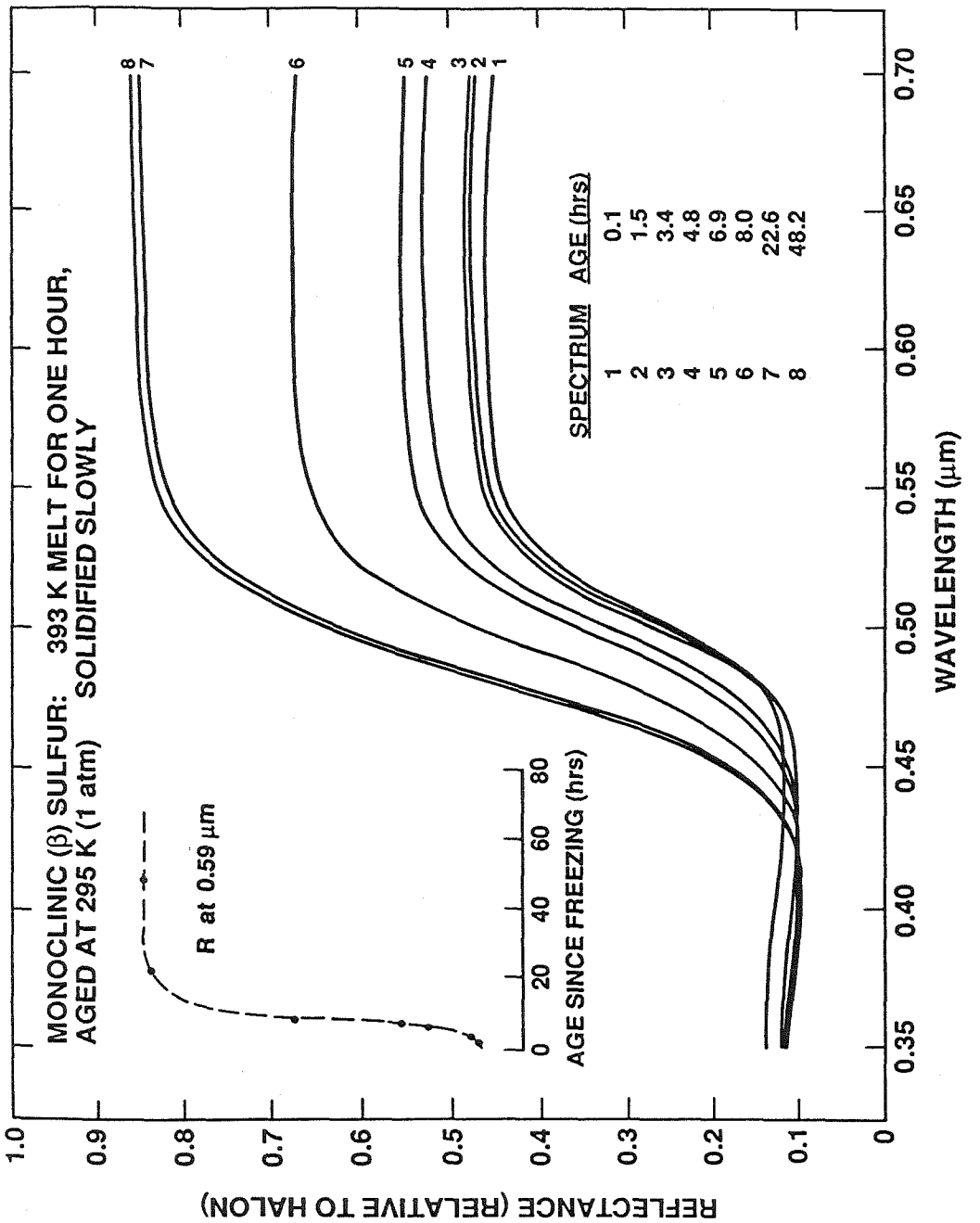

Figure 4. The temporal variation in the spectral reflectance of monoclinic (β) sulfur at room temperature. The sample was created by heating and melting powdered orthorhombic sulfur at 393 K for one hour, then by allowing the liquid to crystallize slowly as the sample cooled from 393 K to room temperature.

6. Experimental Results

All solid sulfur samples that were once molten exhibit noticeable brightening at visible wavelengths with time after solidification. For samples that were melted at 393 K, and then solidified and kept at room temperature, a rapid increase in the spectral reflectance of the solid sulfur occurs in the first day after freezing, and gradual brightening continues for months afterward. Figure 4 shows the spectral reflectance change of a typical pure monoclinic (β) sample as it ages after solidification. The sample initially exhibits the deep butterscotch coloring of S_β (see spectra 1 – 3 of Figure 4). Little variation occurs in the first few hours until orthorhombic (α) nucleation sites begin to appear in the sample (after $\sim$ 4 hrs). As the light yellow patches of S_α crystals grow, the samples begin to brighten rapidly at wavelengths greater than 0.45 μm until the separate nucleation sites encounter each other, at which time the reflectance variation begins to slow down again (recall Figure 1). After several days, the sample appears indistinguishable from pure orthorhombic (α) sulfur (see spectrum 8 of Figure 4).

The spectral variation of the 393 K melt freezes (quenched rapidly with a glass microscope slide) is similar to that of pure S_β (see Figure 5). The samples shown in Figures 4 and 5 were formed in an identical manner except that the 393 K melt freezes (Figure 5) were melted for 23 hrs prior to freezing rather than for 1 hr and, more importantly, were rapidly quenched rather than cooled slowly. The glass–slide quenching technique discourages large S_β crystals from forming. The main differences in the spectra of Figures 4 and 5 are that rapid brightening due to the growth of S_α crystals begins almost immediately after solidification of the 393 K melt freezes and that the S_α crystal growth is initiated from three to eight individual nucleation sites rather than from the one to five individual sites typical of the unquenched pure monoclinic (β) samples. The lack of a long delay in the formation of growth nuclei

of S_α indicates that favorable growth sites already exist in the quickly frozen solid melt freezes; for example, incompletely melted crystals of S_α, favorable sites at the surface due somehow to the glass–slide quenching technique, or perhaps impurities that do not get incorporated into the monoclinic structure during the rapid freezing may exist in the solid melt freeze. Therefore, the linear transformation rate of S_β into S_α sets in almost immediately after solidification and, like the pure S_β samples, the spectral reflectance of the 393 K melt freezes varies rapidly in the first 24 hrs or so and slowly for days afterward (Figures 4 and 5).

The transformation rate to S_α is significantly affected by the original temperature of the melt. Freshly frozen 453 K melt freezes are generally darker than 393 K melt freezes at visible wavelengths (Figure 6); the differences are especially obvious in the wavelength region 0.5 to 0.7 μm. The spectral variation associated with the transformation is also noticeably slower with the higher temperature melt freezes. In fact, samples heated to 453 K then cooled and aged at room temperature take about ten times longer to reach a reflectance of 60% at a wavelength of 0.59 μm (near the center of the *Voyager* narrow–angle camera orange filter) than samples heated to 393 K for the same amount of time. Steady brightening of 453 K melt freezes at wavelengths greater than 0.45 μm occurs in the first 2 days after solidification as the S_β converts to S_α, but brightening continues for years afterward. It is clear from Figure 6 that the 453 K melt freeze has not converted completely to S_α even after nearly 4 months. The sample will continue to brighten for years, presumably as some of the polymeric sulfur (S_μ) breaks down and converts to S_8. Remember that the main difference between the 453 K and the 393 K melts is the percentage of S_μ present in equilibrium concentrations in the liquid (see Table I). S_μ reacts slowly as the temperature is changed so that polymeric sulfur can be retained as the sample solidifies. The S_μ is unstable at room temperature, but slow kinetics inhibits the breakdown

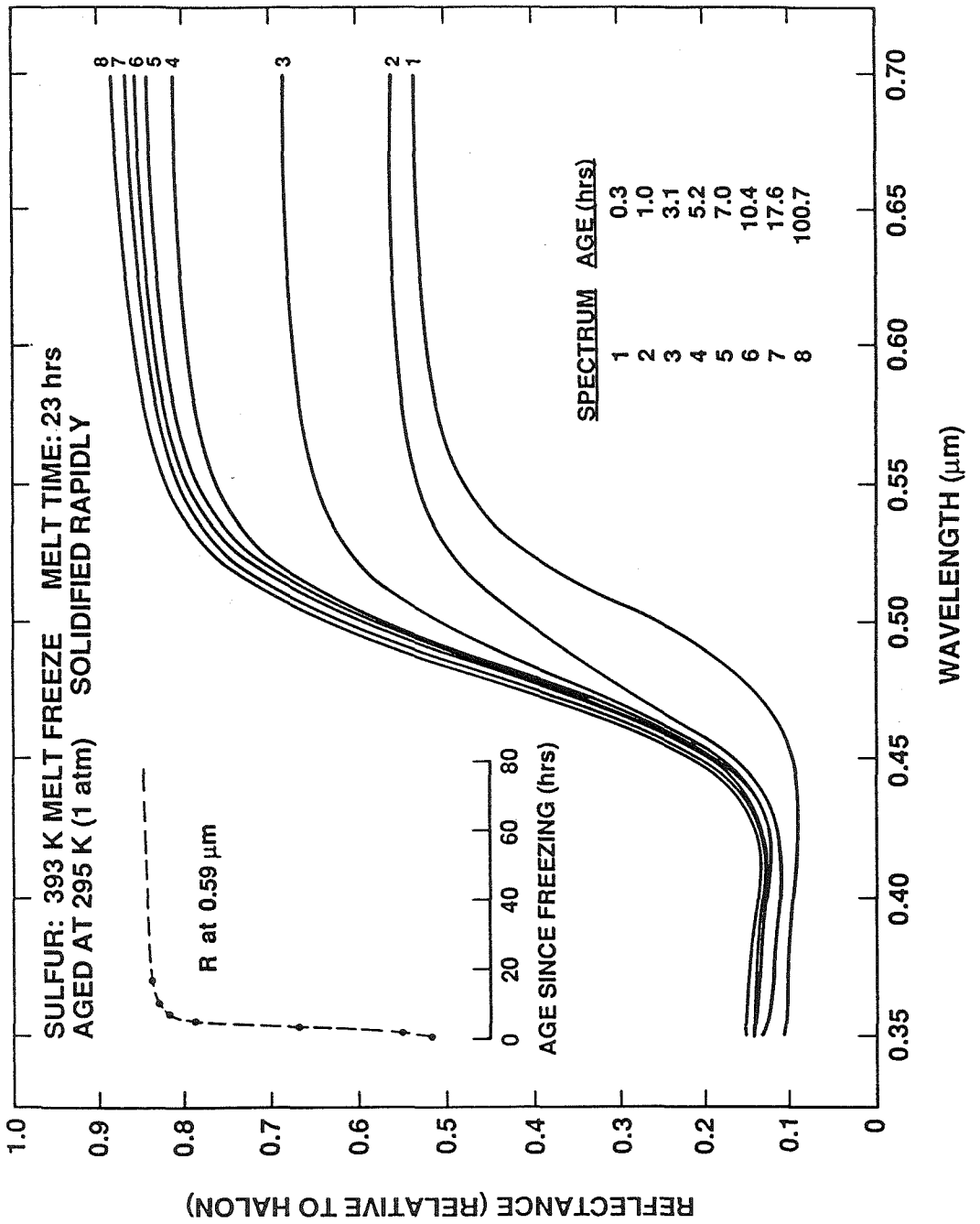

Figure 5. Temporal variation in the spectral reflectance of a 393 K sulfur melt freeze sample that was heated to 393 K for 23 hours, solidified quickly at room temperature, then aged at room temperature.

of long polymers into S_8 rings and into the eventual orthorhombic crystal structure. The polymers may also allow physical separation of the S_8 rings, and thus slow the conversion of the available S_8 into the orthorhombic lattice. The 453 K melt freezes occasionally have short delays in the onset of the steady spectral variation, implying that the nucleation step is nonnegligible; however, this delay is short compared to the time scale of the bulk of the transformation (0 – 2 hrs as compared with $\sim$ 30 hrs) so that the linear S_α growth process dominates the spectral variation. The samples heated in an argon–filled oven aged in a similar manner to the samples heated in a nitrogen–filled oven.

The results of the 453 K Bacon and Fanelli high–purity melts are much different, however (Figure 7). The samples convert to yellow orthorhombic α–sulfur much more rapidly and behave more like 393 K melt freezes. The differences between 99.9999% pure samples and those purified by the Bacon and Fanelli method indicate that impurities present at the level of a few parts per million may be responsible for the brownish tint observed in the melt freezes.

Figures 4 – 7 show the spectral reflectance changes of *individual* samples that were chosen to be representative of all samples of the same thermal history. However, a large amount of variation between samples of the same age and thermal history can exist after sample solidification as the S_β to S_α transformation proceeds. For instance, Figures 8a and b show the typical variation in the spectral reflectance of three different 393 K melt freezes heated for the same amount of time and cooled at the same rate to the same final temperature. Immediately after freezing, the samples are nearly identical in appearance, but Figure 8a shows that the three samples have very different reflectances 1 hr after solidification. The differences are due to the different number and location of nucleation sites of S_α within the overall S_β matrix of the fresh sulfur melt freeze. For instance, a sample that has three S_α nucleation sites near the

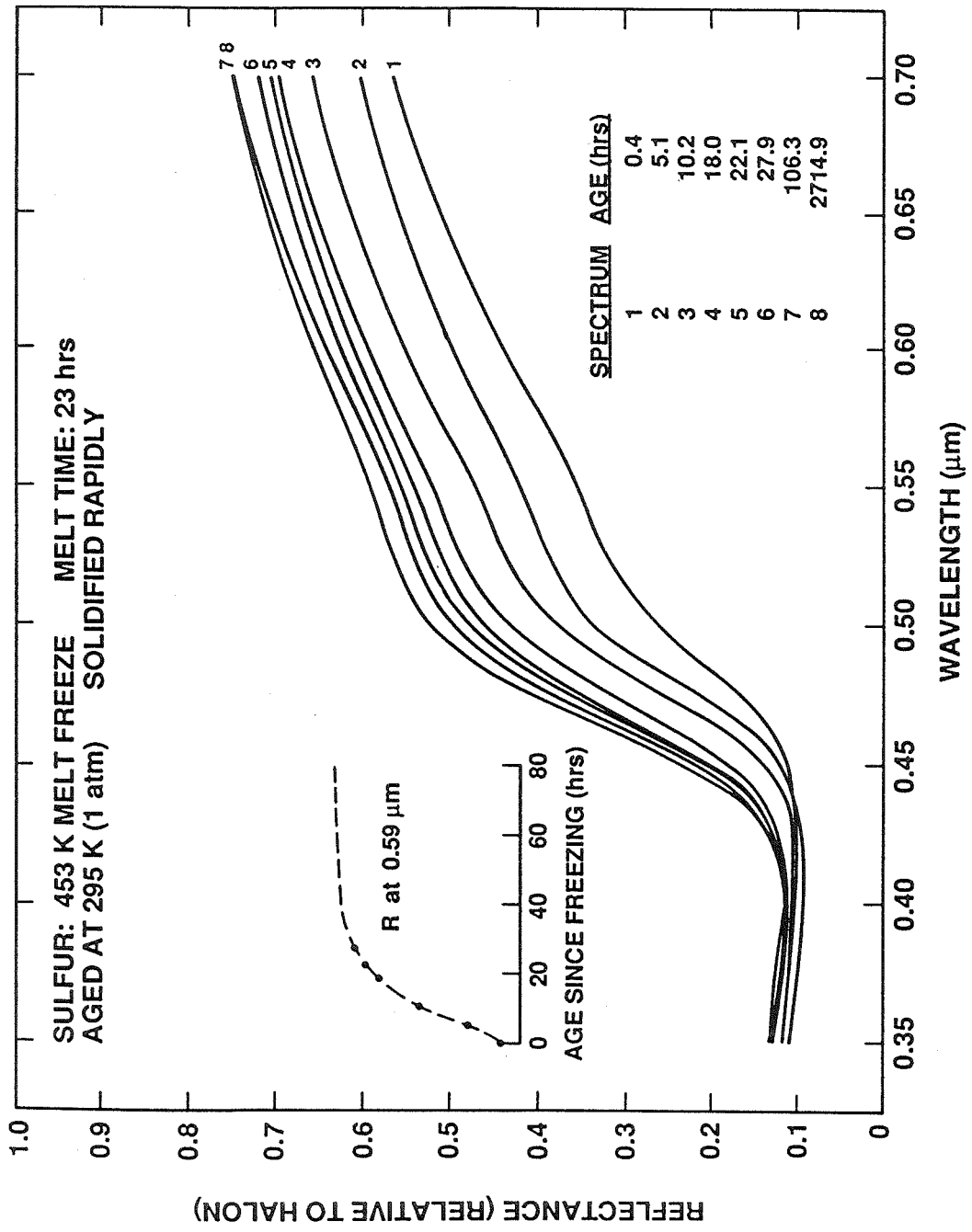

Figure 6. Temporal variation in the spectral reflectance of a 453 K sulfur melt freeze sample that was heated to 453 K for 23 hours, solidified quickly at room temperature, then aged at room temperature.

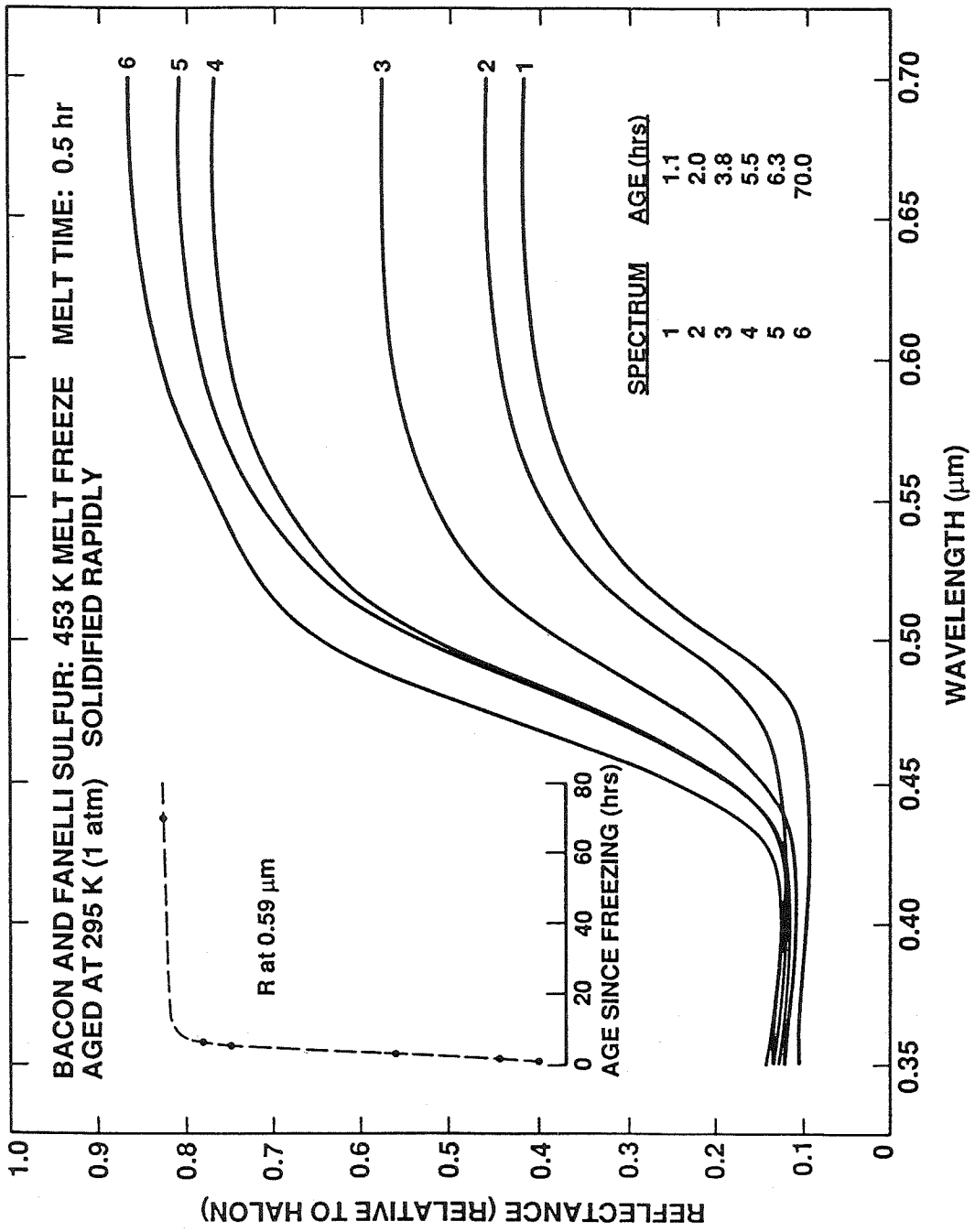

Figure 7. Temporal variation in the spectral reflectance of an ultrahigh–purity 453 K sulfur melt freeze sample (purified using the Bacon and Fanelli method) that was heated to 453 K for half an hour, solidified quickly at room temperature, then aged at room temperature.

center of the spectrometer beam spot (sample A) will appear brighter than a sample that has two nucleation sites growing at the edges of the beam (sample C). If the samples have the same composition and thermal history, differences in the number and location of nucleation sites simply reflect either the location of impurities or the effect of statistical microscopic density and temperature fluctuations that can cause stable "embryos" or germ nuclei of the S_α phase to form within the solid. S_8 molecules will then diffuse to the growing S_α crystals at a rate that is kinetically described in Section 3 (see equation [2]). The growth is approximately spherical about the initial germ nucleus and will continue until the boundary encounters a boundary from another S_α growth nucleus. Eventually, all the S_β has transformed into S_α. At this time (see Figure 8b), the samples again appear nearly identical in reflectance. Therefore, we can never say, "393 K sulfur melt freezes that have aged for 3 hrs at 298 K will have *this* particular spectral reflectance." We can only show average spectra from a large number of samples or show the spectra of a "typical" individual sample and explain that there is individual variation during the transformation process itself. We have chosen to average a parameter we call the "spectral time constant" rather than to average the spectra themselves. In this manner, we can compare samples with different thermal histories without altering the individual spectra.

The effect of melt time on the transformation rate is shown in Figure 9. The term *spectral time constant* refers to the time the samples take to finish the bulk of the initial linear transformation into S_α. For example, for 393 K melt freezes, the spectral time constant is defined as the time the samples take to reach a reflectance of 0.75 at 0.59 μm. For 453 K melt freezes, the time constant is defined as the time the samples take to reach a reflectance of 0.50 at 0.59 μm. Most of the initial transformation is complete after this time. Since the 453 K melt freezes are much darker than the 393 K melt freezes at any stage in the transformation, there is no

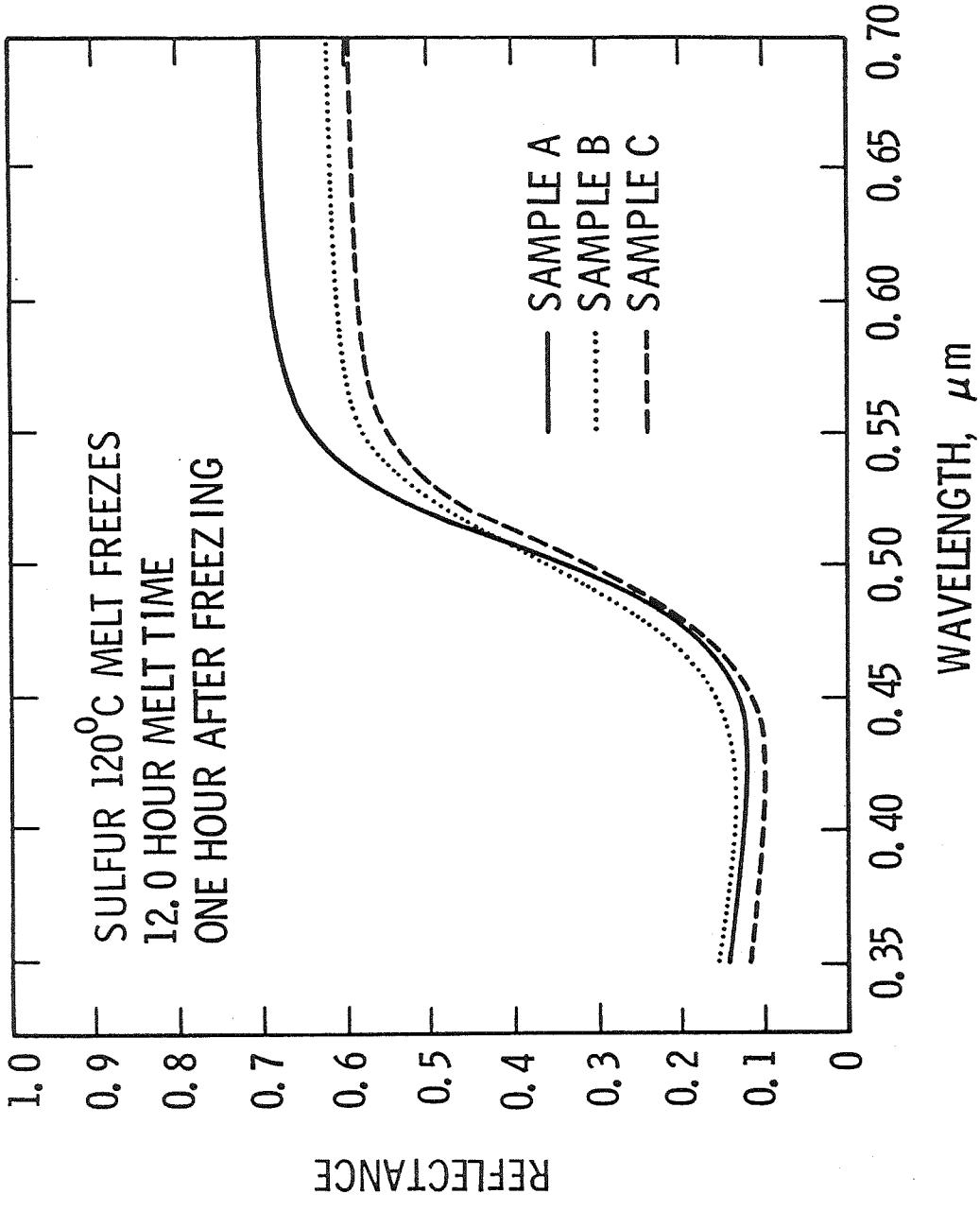

Figure 8a. The spectral reflectance of three sulfur 393 K melt freeze samples one hour after freezing: note the individual variation in the visible appearance of the samples at this time (just after the transformation from S_β to S_α has been initiated).

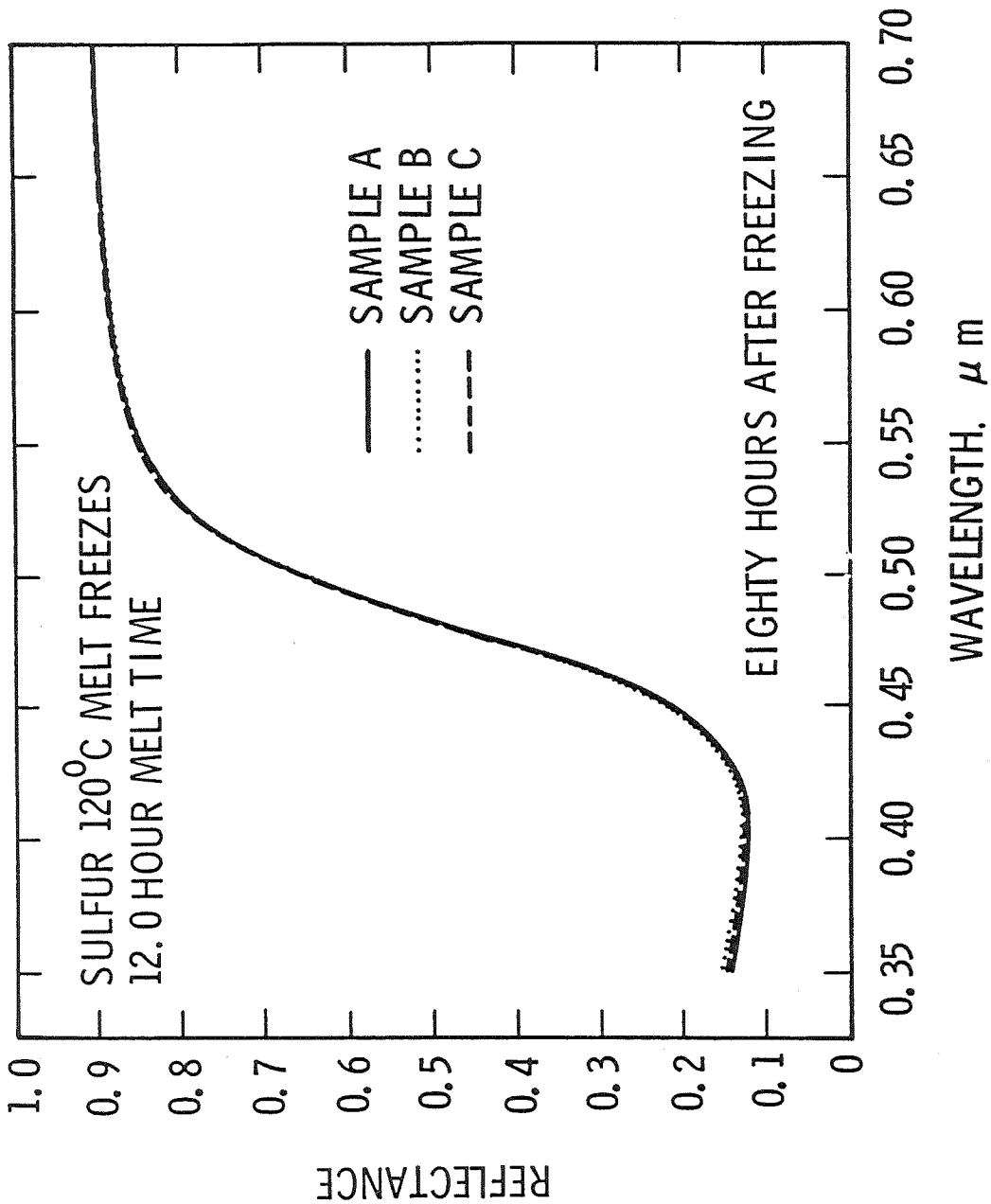

Figure 8b. The spectral reflectance of three sulfur 393 K melt freeze samples 80 hours after freezing: note the uniformity of the sample spectra at 80 hours (long after complete conversion to α–sulfur has occurred).

convenient definition to choose for both classes of sulfur samples; *i.e.*, no definition that would enable us to plot the spectral change of the two classes on the same scale. The 453 K melt freezes always brighten more slowly than the 393 K melt freezes.

Figure 9 shows that the length of time the sulfur remained melted prior to freezing affects the transformation rate of the solid; 393 K melt freezes that were originally melted for less than $\sim$ 10 hrs take less time to convert to S_α after solidification. This result is consistent with a statement by Mäusle and Steudel (1981) claiming that the equilibrium between the different molecular species in a low temperature melt takes about 12 hrs to develop. However, equilibrium at 453 K seems to take longer to develop; the sulfur must remain at 453 K for at least 24 hrs for the conversion to S_α to occur with a maximum, steady time constant. The longer the samples are heated prior to equilibrium, the more non–S_8 species that can form in the melt, and the more likely that these non–S_8 species are still present after the sample solidifies. We postulate that the presence of these non–S_8 species inhibits the transformation from S_β to S_α and so slows the spectral variation. We emphasize that laboratory investigators who are examining the properties of sulfur that was once molten should be aware of the effect of melt time on their results and should heat the samples for $\sim$ 24 to 48 hrs prior to solidification to ensure reproducible results.

The parameter that has the most potential for affecting the transformation rate is the "aging temperature" or the temperature at which the samples remain after solidification. The transformation rate varies with aging temperature as illustrated in Figure 3 and as described by the kinetic rate equation [2] in Section 3. We have examined the spectral variation of samples that have been heated to 393 K for 24 hrs and then solidified and kept at several different temperatures until the transformation process was complete. We measure the time it takes the samples to reach a reflectance of 0.75 at 0.59 μm (the spectral time constant) for samples kept at 260, 273, 295,

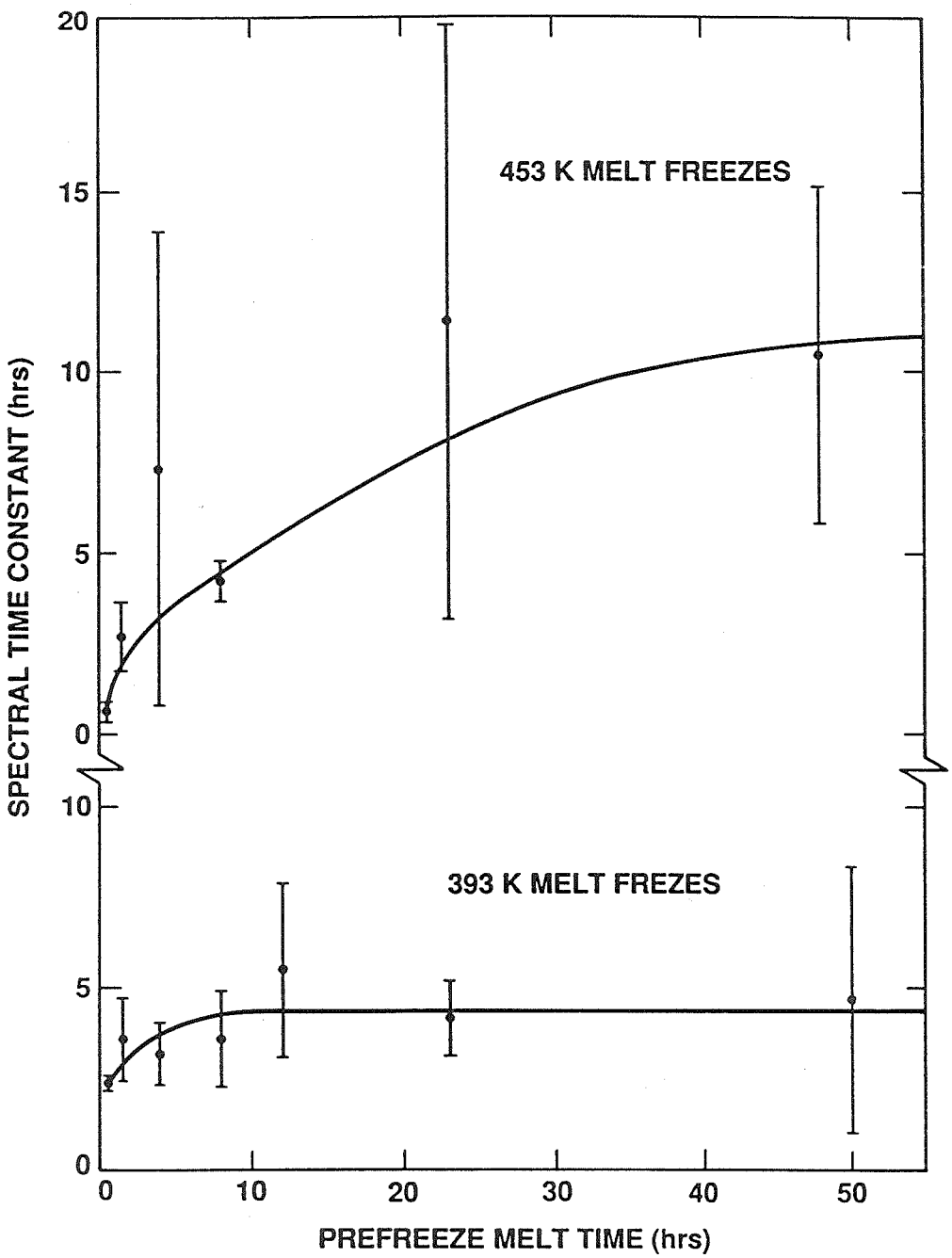

Figure 9. The effect of melt time on the transformation rate of 393 and 453 K sulfur melt freezes. The error bars represent the standard deviation, σ_{rms}, of the results for the individual samples.

308, and 318 K. The results are shown in Figure 10. In this figure, the data are represented by black dots and the solid line represents the best fit of equation [2] to the coldest four data points in a manner similar to that of Figure 3. ΔG_{int} is found from these data to be 1.41 $\times$ 10^{-12} erg (20,300 cal), very similar to that found with Thackray's data on the linear transformation rate (Figure 3). Our results imply that the time constant for significant spectral variation in β–sulfur is 1700 years at 200 K and 5 $\times$ 10^{17} years at 120 K. Because of the extrapolation to temperatures far below those examined in the laboratory, both values are uncertain; however, these time scales are virtually infinite compared with Io's rapid resurfacing rate. If sulfur melt freezes can cool rapidly to Io ambient temperatures in less than a few hours then we would expect S_β to form and persist for many years. On the other hand, if the cooling rate is slow, the conversion to S_α could take place on measurable time scales, and we would expect to see a temporal variation in the albedo of localized areas on Io if such sulfur exists in these areas. In the next section, we examine the cooling times for any sulfur that might exist in different volcanic regimes on Io and discuss the implications of these time scales for the possible sulfur phase transformations on Io.

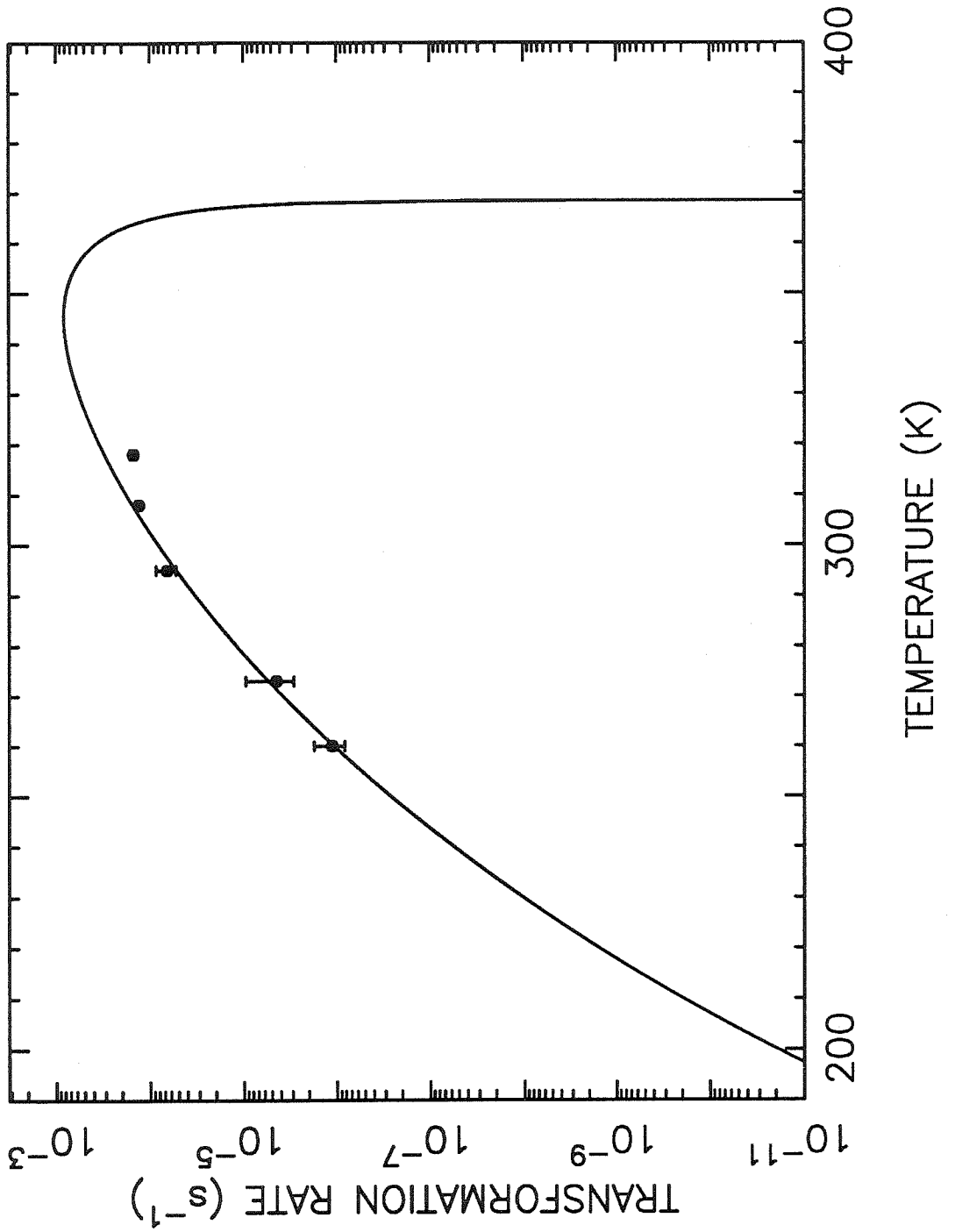

Figure 10. The effect of aging temperature on the transformation rate of 393 K melt freezes. The transformation rate (ordinate) is inversely proportional to the spectral time constant. The data points represent our laboratory results and the solid curve represents the best–fit theoretical solution as described by equation [2] in the text.

7. Cooling Times for Sulfur on Io

Since the ambient temperature controls the rate at which the phase transformations proceed in solid sulfur, we have attempted to estimate the cooling history of molten sulfur on Io. We have divided this discussion into two sections: the first section deals with the cooling rate of small liquid droplets or hot solid particles that are entrained in the gas flow and ejected during plume eruptions on Io, and the second section deals with the cooling rate of large bodies of molten sulfur that may pool into ponds or lakes or be present as volcanic flows on Io.

7.1 Volcanic Plumes

Nine volcanic plumes on Io were observed to be erupting during the *Voyager 1* encounter, and eight of these plumes were still active 4 months later as *Voyager 2* passed by the Jovian system (Smith *et al.* 1979b, Strom *et al.* 1981). In addition, two other major plume eruptions seem to have erupted and disappeared sometime between the two encounters as evidenced by surface and albedo markings (Smith *et al.* 1979b, Strom *et al.* 1981, McEwen and Soderblom 1983). The pyroclastic deposits from these and other presumed plumes dapple the surface of the satellite; in fact, such plume deposits cover a substantial fraction of the surface. For instance, in the 4–month period between the *Voyager* encounters, about 12% of Io's disk was resurfaced by the known plumes alone, and material from the known plumes covered as much as $\sim$ 30% of the longitude region from 240 to 360° (McEwen 1988, McEwen and Lunine 1989). This rapid resurfacing suggests that much of Io's surface is covered by fine–scaled volcanic debris and/or condensed volcanic gases.

Particle sizes of the plume material have been estimated based on the photometric and dynamic models of Smith *et al.* (1979b) and Collins (1981). Collins suggests that the plume at Loki can be best explained by a model with two particle–size distributions — an outer plume region that is dominated by small, Rayleigh

scattering particles of radii 0.001 to 0.01 μm and an inner portion of the plume that consists of particles with radii greater than 1 μm. Kieffer (1982) presents a discussion of the dynamics and thermodynamics of the plume eruptions and concludes that both sulfur and SO_2 can erupt on Io under certain geologic conditions. McEwen and Soderblom (1983) have organized the observed plume eruptions into two distinct categories: (1) Small plume eruptions (e.g., Prometheus) that have smaller heights during eruption (50 – 120 km), smaller areas associated with surface plume deposits (encircling 100 – 300 km about the vent), smaller eruption velocities ($\sim$ 0.5 km s^{-1}), a longer duration of eruption (months to years), and brighter surface deposits than (2), the large plume eruptions (e.g., Pele) that have surface deposits that are darker and more widespread (500 – 750 km about the vent), with higher inferred eruption velocities ($\sim$ 1 km s^{-1}) and plume heights (250 – 300 km), and shorter eruptive durations (days to months). McEwen and Soderblom suggest that the observed dichotomy between the plume types is due to the type of eruption mechanism and reservoir fluid. Specifically, they suggest that the small plumes are consistent with the "low entropy volcanism" described by Kieffer (1982) and are consistent with SO_2 as the reservoir fluid whereas the large Pele–type plumes are characterized by much higher reservoir temperatures and are consistent with hot liquid sulfur as the reservoir fluid. We might then expect small droplets of liquid sulfur or particles of hot solid sulfur (*i.e.*, S_β) present in the supply region, the reservoir, or the conduit walls to become entrained along with other pyroclasts and gases during plume eruptions on Io; sulfur might be especially likely to be present in the plumes and plume deposits of the large Pele class of volcanoes.

A typical pyroclastic particle will be "airborne" for several hundred seconds. If, to first order, we neglect heat transfer between the entrained pyroclasts, sulfur droplets in the plume will lose heat primarily by evaporative and radiative cooling.

Thermal coupling between the gas and proposed sulfur particles during the eruption can be neglected for two reasons: (1) The plumes on Io are erupting into a low–density atmosphere so that small pyroclasts quickly become spatially separated, can follow nearly ballistic trajectories, and lose thermal contact with the isentropically expanding gases (Wilson and Head 1983); and (2) sulfur particles are extremely transparent in the infrared and contain few absorption bands that would overlap with emission features of the plume gases. Therefore, our assumption that the particles cool only by radiative and evaporative processes is probably valid, at least while the particles are in flight.

The cooling rate is then described by two coupled differential equations:

$$mC_p \frac{dT}{dt} = -4\pi \left(\frac{3m}{4\pi\rho}\right)^{2/3} \epsilon\sigma \left(T^4 - T_e^4\right) + L\frac{dm}{dt} \qquad [3]$$

$$\frac{dm}{dt} = -4\pi \left(\frac{3m}{4\pi\rho}\right)^{2/3} P_v(T) \left(\frac{\mu}{2\pi kT}\right)^{1/2} \qquad [4]$$

where m is the total mass of the particle; t represents time; $C_p(T)$ is the specific heat of the particle at temperature T; ρ is the density; ϵ is the emissivity, and L is the latent heat of vaporization of the particle; σ is the Stefan–Boltzmann constant; $P_v(T)$ is the equilibrium vapor pressure of sulfur at the appropriate temperature; μ is the mass of a sulfur molecule; k is the Boltzmann constant, and T_e is the effective radiation temperature of the environment in which the particle is found. The first term on the right–hand side of equation [3] represents the radiative heat loss of the spherical particle. The term containing T_e is included to account for the heat gained from the environment surrounding the particle (e.g., from the atmosphere if it is thick enough for collisions to be important). For simplicity, we have assumed that this heat source is isotropic while the particle is cooling, and T_e is about 120 K; note that the actual choice of T_e has little effect on the final results concerning the cooling time. The final term on the right–hand side of equation [3] represents the evaporative cooling

rate of the particle (here we assume that sulfur droplets or particles in the plume will be in equilibrium with the surrounding sulfur vapor). The mass (and radius) of the particle will change with time as the particle evaporates. We have solved the two equations using a fourth–order Runge–Kutta technique. Because of the changes in C_p, L, and P_v with temperature, the liquid droplets were considered separately from solid particles; that is, the sulfur droplet was given an initial temperature and the equations were solved using liquid parameters until the droplet reached a temperature of 390 K, at which time we used the parameters relevant to solid sulfur.

The liquid sulfur parameters that we use are consistent with those used by Lunine and Stevenson (1985). The vapor pressure of liquid sulfur was derived from data presented by West (1950) and has the expression

$$\log_{10} P_v(\text{bars}) = \frac{-4295.}{T} + 7.383 - (1.908 \times 10^{-3})\,T$$

$$\text{from } 390 < T < 919 \text{ K.}$$

The specific heat of liquid sulfur has the form

$$C_p\left(\frac{\text{erg}}{\text{g K}}\right) = 2706.(T-388)^2 + 9.92 \times 10^6 \qquad \text{for } 390 < T < 432 \text{ K}$$

$$= 5.239 \times 10^6 \exp\left[\frac{466.3}{T}\right] \qquad \text{for } T > 432 \text{ K}$$

based on data by West (1959). The liquid sulfur density was derived from data by Kennedy and Wheeler (1983) and Tuller (1954) and has the form

$$\rho(g\,\text{cm}^{-3}) = 1.775[1 - \alpha(T - 432)]$$

where $\alpha = 4.6 \times 10^{-4}$ K^{-1} at T < 432 K and 2.5×10^{-4} K^{-1} for T > 432 K. The latent heat of vaporization of sulfur from the liquid phase is found to be 3.3×10^9 erg/g (Meyer 1976).

For the case of solid particles, we use the data of West and Menzies (1929) to derive the expression for the vapor pressure of the solid:

$$\log_{10} P_v(\text{atm}) = 10.273 - (5.676 \times 10^3)\frac{1}{T}$$

$$\text{for } 120 \leq T \leq 390 \text{ K} .$$

The specific heat of the solid was found from Eastman and McGavok (1937) to be

$$C_p \left(\frac{\text{erg}}{\text{g K}}\right) = 6.51 \times 10^6 (\log_{10} T) - 8.98 \times 10^6$$

$$\text{for } 120 \leq T \leq 390 \text{ K} .$$

The density of solid sulfur was assumed constant at 2.0 g/ cm^3 and the latent heat of vaporization from solid sulfur was assumed to be $L = 3.8 \times 10^9$ erg/g (Meyer 1976).

The emissivity of the sulfur particles or droplets is actually quite difficult to calculate correctly. The emissivity is

$$\epsilon = \frac{\int_0^\infty Q_a(\lambda)\, B_\lambda(T)\, d\lambda}{\sigma T^4} \qquad [5]$$

where $B_\lambda(T)$ is the Planck function for a particular temperature, Q_a is the absorption efficiency of the particle, and σ is the Stefan–Boltzmann constant. Q_a and, hence, the emissivity, ϵ, is a function of particle size. For instance, particles that are much smaller than the wavelength for maximum emission will have difficulty losing heat by radiation and will thus have low emissivities. The absorption efficiency also depends on the complex index of refraction $n_c = n - ki$. To solve equation [5], one needs to know Q_a (and n_c) at all wavelengths. Unfortunately, the index of refraction for liquid sulfur has been measured only out to 2 μm (Sasson *et al.* 1985, Sasson and Arakawa 1986). We have therefore solved for the emissivity of sulfur droplets or particles by assuming the droplets are spherical, by assuming that the imaginary refractive index is constant at all wavelengths, and by using a Mie scattering approach to calculate the absorption efficiency (e.g., Hansen and Travis 1974).

The resulting values for the emissivity for differently sized particles are shown in Figure 11a. We have done the calculation for four different possible imaginary indices of refraction and have assumed that the real index of refraction $n = 1.8$ for molten droplets at 393 K (at infrared wavelengths). For large particle sizes, we have used the Mie–scattering algorithm developed by Wiscombe (1980). Both liquid and solid sulfur are very transparent at infrared wavelengths below about 10 μm. The imaginary index of refraction of molten sulfur at 406 K is $k = 2 \times 10^{-7}$ at $\sim$2 μm (Sasson *et al.* 1985). Unfortunately, we have no way of extrapolating this value to longer wavelengths. Solid sulfur has some weak–to–moderate resonant vibrational absorption features longward of 7 μm, but is relatively transparent at near– and mid–IR wavelengths (Nash 1986). We therefore expect the imaginary index to be quite low ($k \lesssim 10^{-2}$) and pure sulfur particles or droplets to be poor emitters (although impurities in the droplet may raise these values). Figure 11a shows that the emissivity is low for small particles for the low assumed values of the imaginary refractive index but grows as the particle radius is increased.

The solution to equations [3] and [4] is illustrated in Figure 11b. This figure shows the time it takes sulfur droplets to cool from 393 K to 200 K as a function of particle size and imaginary index of refraction, k. At 200 K, the transformation from S_β to S_α proceeds at a negligible rate; *i.e.*, equation [2] indicates that the conversion to S_α will take longer than 1000 years at this temperature so that any progress made by S_α crystal nuclei growing in the S_β matrix will be essentially halted or "frozen" by the time the particle cools to 200 K. The particles initially lose heat by evaporative cooling. As the temperature drops, however, the exponential dependence of the vapor pressure with temperature causes evaporative cooling to rapidly lose importance and radiative cooling to dominate. Figure 11b shows the importance of the imaginary index of refraction for the calculation of cooling time. The cooling time will change

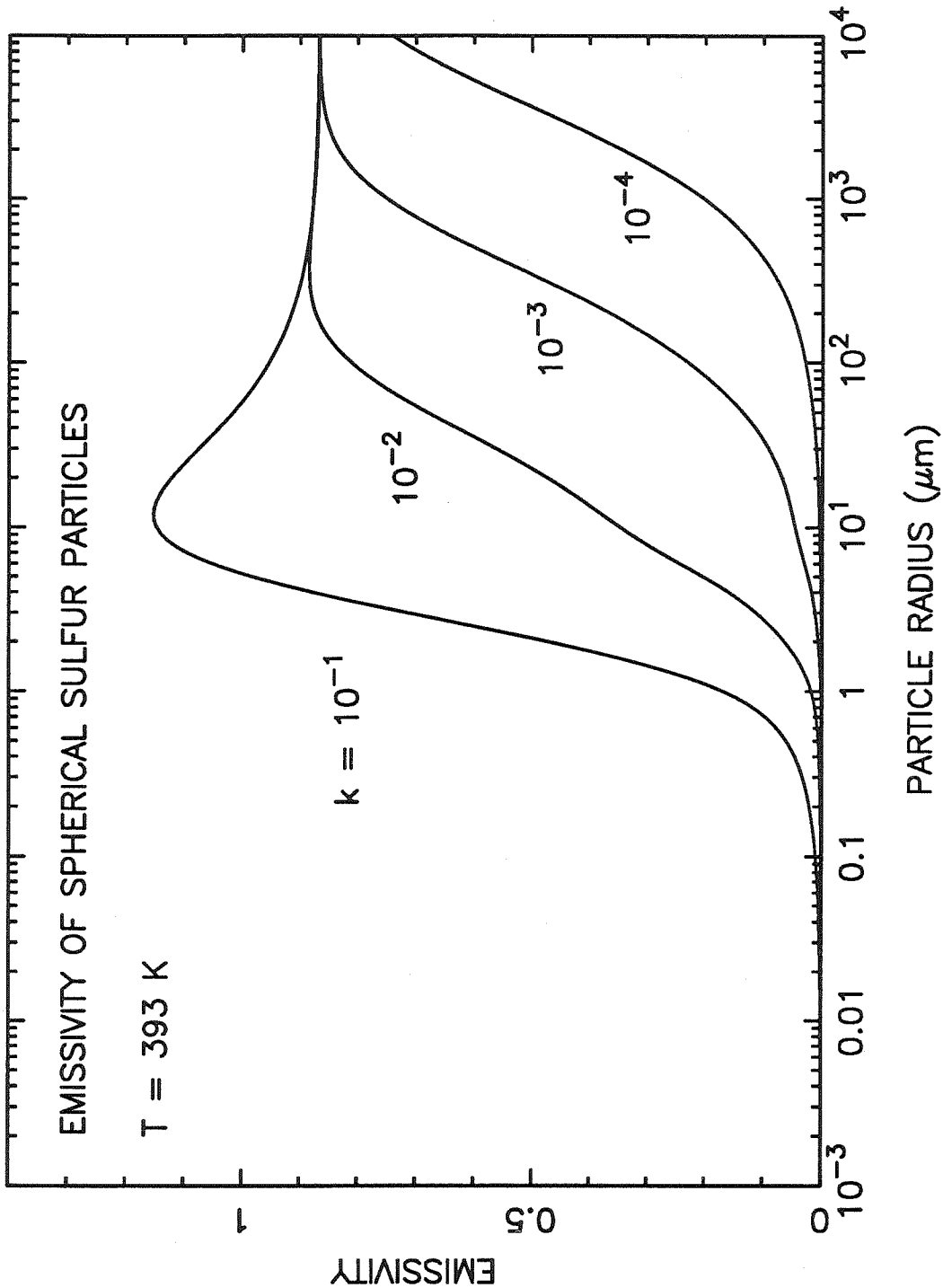

Figure 11a. The calculated emissivity of spherical sulfur droplets or particles near 390 K.

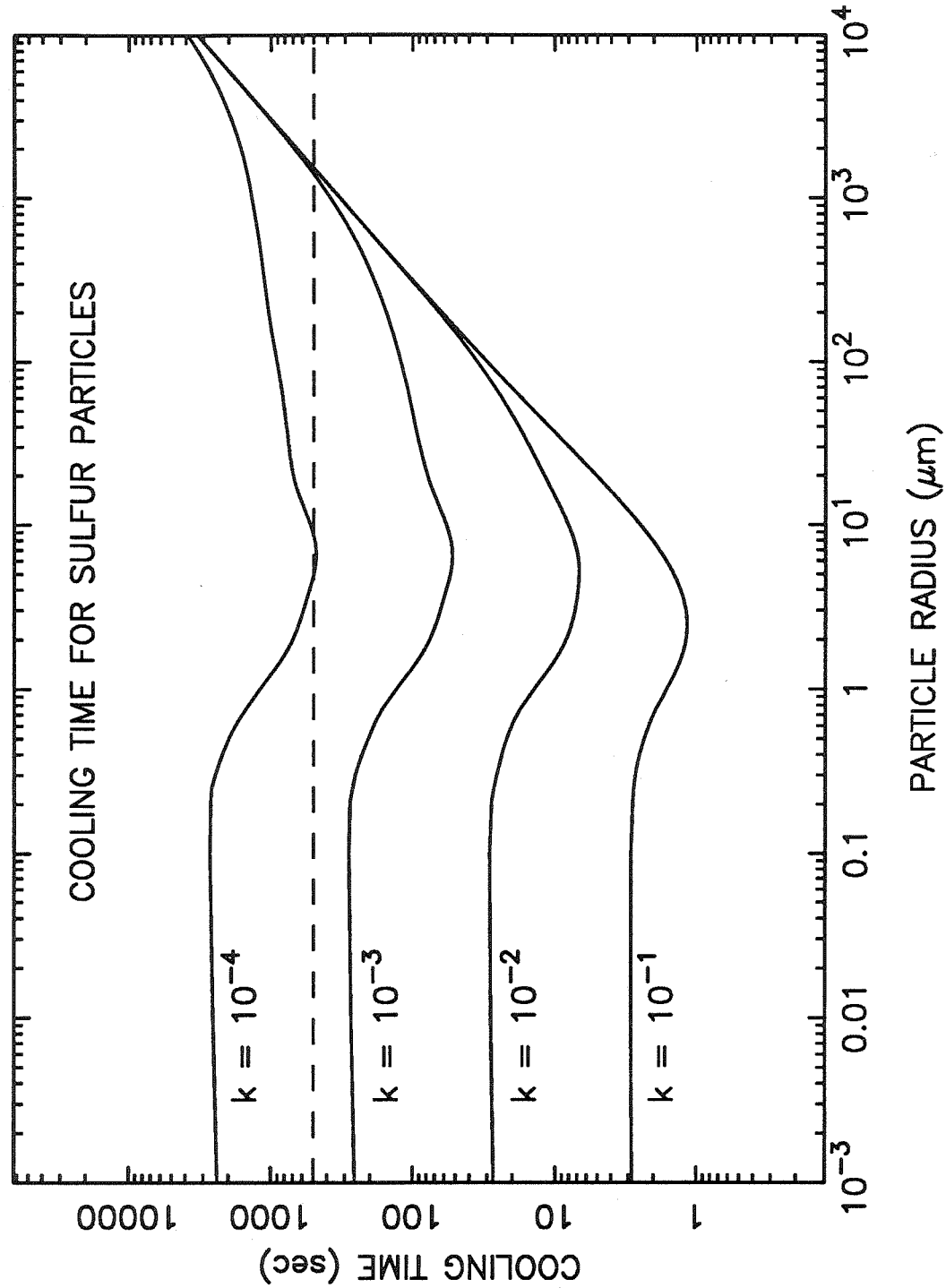

Figure 11b. The calculated cooling time for sulfur droplets cooling from 393 to 120 K as a function of particle size and imaginary index of refraction, k. The dashed line represents a typical flight time for particles in the large plumes on Io.

by as much as an order of magnitude with a change in the imaginary refractive index of an order of magnitude. If k is greater than or equal to 10^{-4} then particles of all sizes from 0.001 μm to 1 cm will cool to 200 K in less than an hour. As already mentioned, the flight times of the particles themselves are on the order of 500 sec so equations [3] and [4] become less relevant if the cooling time is long (*i.e.* if $k \lesssim 10^{-4}$). In this case, conduction to the ground or conductive blanketing by newly–fallen particles may also be important. However, the refractive index is most likely greater than 10^{-4} so that equations [3] and [4] still provide realistic cooling time estimates except when the particles are very large ($r > 1$ mm). Such large particles, which can be found only near the source region, may take longer to cool because of blanketing effects than Figure 11b indicates. For small particles ($r \lesssim 0.5$ μm), the emissivity varies directly with the particle radius. Meanwhile, the radiative cooling time

$$\tau_{rad} \approx \frac{r\rho C_p \Delta T}{3\epsilon\sigma T_e^4}$$

varies directly with the particle radius and inversely with the emissivity so that the cooling time is essentially constant with particle size. However, Figure 11a shows that the emissivity eventually levels out and little variation of ϵ with particle size occurs once the particles become large enough. At this stage, the cooling time will begin to increase as the particle size is increased and as the total heat of the particle becomes large.

The results for particles that have an initial temperature of 453 K are similar to the 393 K results. Figure 12 shows the degree of cooling that is achieved while the particles are airborne; *i.e.*, it shows the temperature according to equations [3] and [4] that the particles reach after 500 sec as a function of initial particle size and imaginary refractive index. If $k = 10^{-3}$ or larger, the particles cool quite rapidly to temperatures at which the transformation from S_β to S_α or S_μ to S_α is negligible. If $k = 10^{-4}$ or smaller, however, some visible transformation may already have been initiated. For

instance, particles 10^{-1} μm in radius with an imaginary refractive index of 10^{-4} will cool to only 278 K after 500 sec. At 278 K, equation [2] and Figure 3 predict that the α–sulfur phase will grow at a rate of 7.93 $\times$ 10^{-2} mm/hr. Although this is a small rate, it is nonnegligible, and significant S_α growth may be visible within the S_β matrix after the particle reaches the ground. A particular example of the cooling behavior of a sulfur droplet, illustrated in Figure 13, shows the solution to equations [3] and [4] for a particle with $k = 10^{-3}$, an initial radius of 0.1 μm, and an initial temperature of 453 K. The particle cools rapidly by evaporative cooling and solidifies in about a tenth of a second. Evaporative cooling becomes less important after about 10 sec as evidenced by the constant radius after this amount of time. Since the S_β to S_α transformation rate is a maximum at about 340 K, the cooling behavior near this temperature is very important. For example, S_β converts to S_α in about an hour at this temperature. If the particle remains near 340 K for this amount of time then we would expect almost complete conversion to S_α to have occurred by the time the samples cool to Io ambient temperatures. In the case illustrated in Figure 13, the particles are in the $\sim$ 340 K temperature range for only a few minutes; S_α nucleation may occur in this amount of time, but it is doubtful whether significant progress of the S_α crystal growth will have occurred before the particles fall below 273 K ($\sim$ 10 min). No significant growth will occur 10 – 20 min after such particles have erupted from the vent.

Although we have only mentioned solidification into a monoclinic crystal structure, some of the particles erupted from the plumes may solidify into an amorphous glassy solid (Gradie *et al.* 1984, Tobolsky *et al.* 1962). Sulfur that has been heated above the polymerization temperature of the liquid (432 K) can solidify in the vitreous state if the sulfur is cooled below the glass transition temperature more rapidly than crystal nuclei can form (Prins 1960, Tobolsky *et al.* 1962, Rawson 1967). The glass

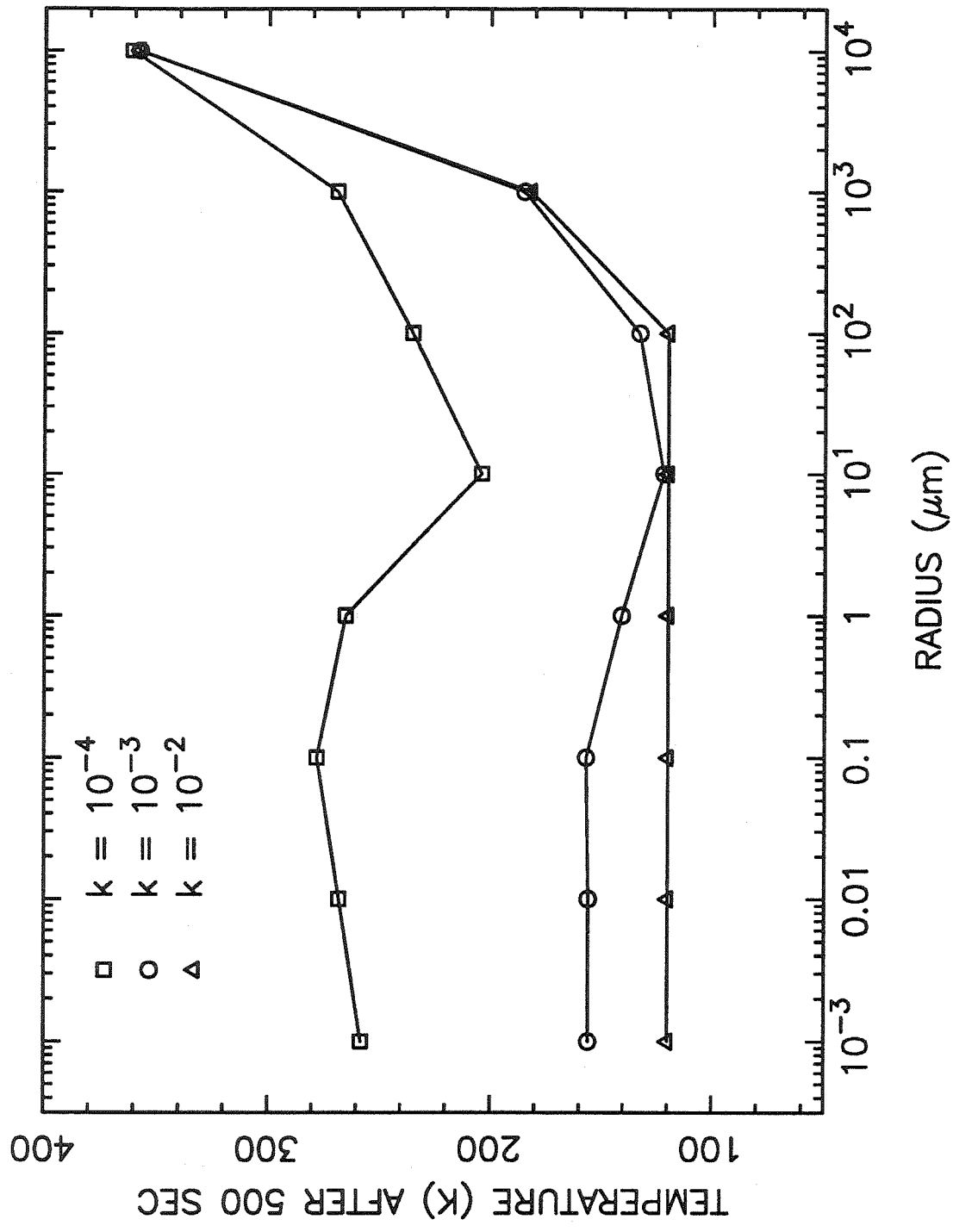

Figure 12. The calculated temperature (as a function of initial particle size and imaginary refractive index) attained by sulfur particles after being airborne for 500 seconds during plume eruptions on Io. The initial temperature of the particles was 453 K.

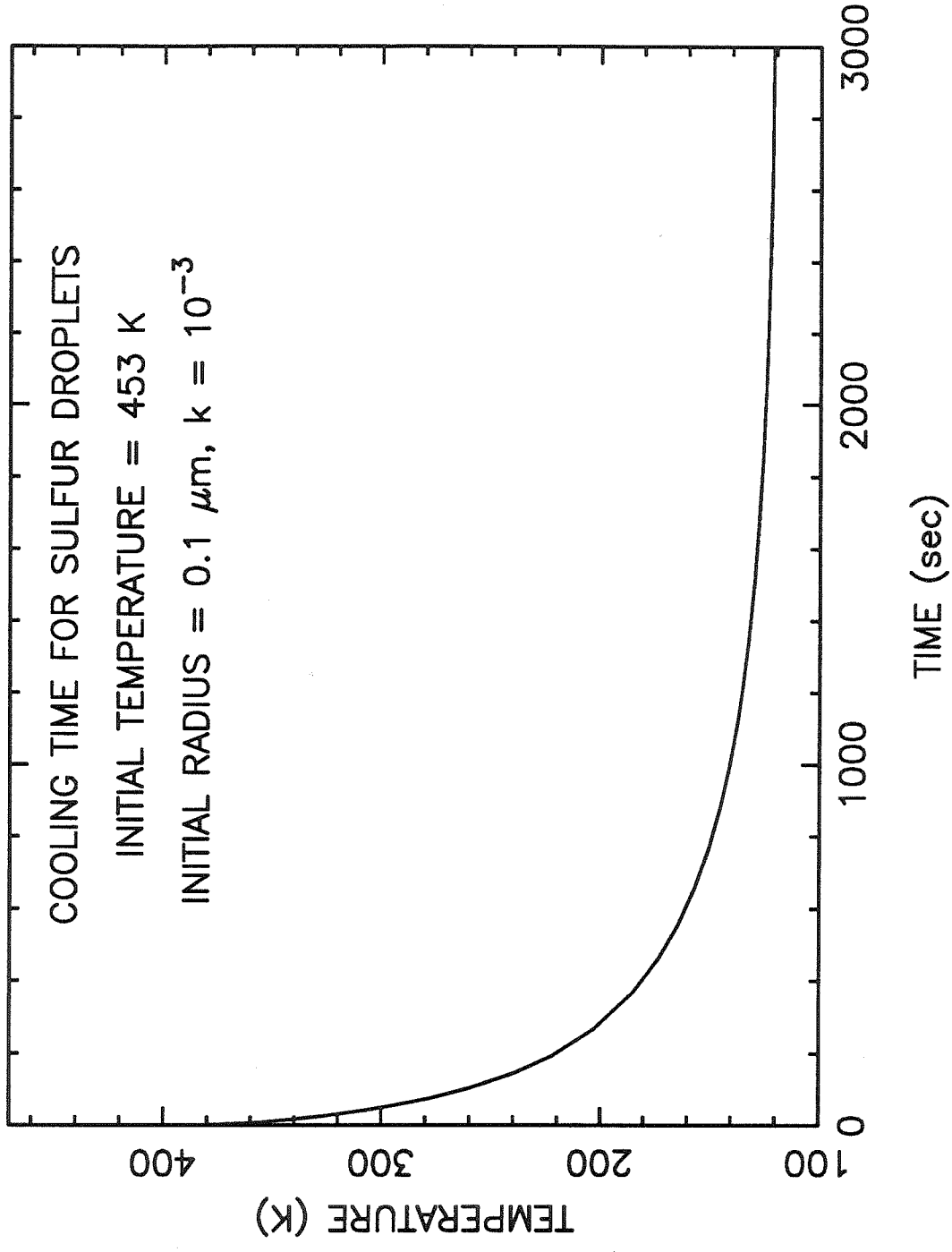

Figure 13. The time sequence for a molten sulfur droplet initially 0.1 μm in radius with imaginary refractive index $k = 10^{-3}$ as the droplet cools from 453 to 120 K. In this case, 10% of the radius is lost due to evaporation in the first second of cooling, but little evaporation occurs after 10 seconds, and the particles lose half their heat in about 3 minutes.

transition temperature of sulfur is 246 K (Tobolsky *et al.* 1962). Sulfur glass kept below this temperature will remain in the vitreous state virtually indefinitely. Some of the higher–temperature small liquid droplets that contain significant amounts of polymeric sulfur may cool below the glass transition temperature rapidly enough to prevent crystal formation, and a reddish glassy sulfur may form and be preserved on Io.

In any case, for imaginary refractive indices greater than $k \sim 10^{-4}$, our rough calculations show that the cooling time for particles less than 1 cm in radius on Io is rapid enough to inhibit the transformation of S_β or S_μ into the stable S_α. Therefore, the large Pele–type plume deposits may contain some metastable sulfur allotropes as well as orthorhombic sulfur condensed directly from the gas phase. Specifically, monoclinic S_β, polymeric S_μ, and glassy sulfur as well as the expected S_α may be present in these regions on Io.

7.2 Volcanic Flows or Lakes

Although Io's bulk density, heat flow, and topography denote a crust that is dominated by silicate materials, the migration of subsurface silicate magmas may allow more volatile species to mobilize and erupt or effuse at the surface of the satellite. Low temperature melts such as sulfur might then be able to flow across the surface and/or pool in topographic depressions such as calderas. The *Voyager* images reveal several distinct flow–like features across Io's surface. Although the resolved morphology of these flows is consistent with both elemental sulfur and basaltic lavas (Pieri *et al.* 1984, Fink *et al.* 1983, Carr 1986), the colors of the flow surfaces are inconsistent with basalt but are consistent with sulfur (Pieri *et al.* 1984, McEwen 1988). This observation does not preclude basalt from constituting the bulk of the flow but simply means that the optical surface itself is inconsistent with basalt and other silicate materials. Similarly, the colors and albedos of the caldera floors on Io

are often consistent with liquid sulfur or solid sulfur that was once molten (McEwen *et al.* 1985). Lunine and Stevenson (1986) suggest that the hot spot emission at Loki is consistent with a constantly convecting and evaporating molten sulfur lake heated from below by silicate magma. The exponential behavior of the vapor pressure with temperature forces the temperature at the surface of Lunine and Stevenson's model sulfur lake to fall within a narrow range, and crustal constraints on the depth of the lake indicate the lakes can completely evaporate in 1 to 100 years if the silicate magma heat source remains unchanged. Heat loss from such large bodies of sulfur will be slow so that if large volumes of molten sulfur are present on Io, their cooling histories and associated spectral changes will be very different from those of sulfur ejected as droplets or small particles during plume eruptions.

The physical properties of the upper few millimeters of a sulfur flow or lake will determine its color and the likelihood of phase transformations at the surface of the body; however, estimating the thermal history of the surface of a flow or lake is quite difficult because the cooling behavior of liquid sulfur is quite complicated. Liquid sulfur at 393 K is about 5% less dense than monoclinic sulfur. This fact has led Young (1984) to emphasize that nonporous solid crusts cannot form stably at the top of a flow; for example, a 7–m–wide flow cannot support a 1–cm crust. However, as McEwen *et al.* (1985) point out, a porosity of just 5% will allow solid S_β to float on the liquid. On Earth, sulfur flows and lakes are observed in association with other volcanism but are not very common. Most terrestrial flows are associated with the remelting of sulfur that has condensed around fumarolic vents. A sulfur lake was recently reported in Volcán Poás, Costa Rica, by Oppenheimer and Stevenson (1989). Two sulfur lakes $\sim$ 20 – 30 m in length formed when elemental sulfur deposits contained within the sediments of a volcanic crater lake heated up due to the evaporation and removal of water from the crater lake. The sulfur liquid was brown

and very fluid and bubbled vigorously over most of the lake surface, implying that the passage of hot gases through the melt prevented a crust from forming at the lake surface (Oppenheimer and Stevenson 1989).

Greeley *et al.* (1990) observed some of the properties of anthropogenic sulfur flows created by the sulfur mining industry in the United States. In the observed industrial sulfur flows, 99.6% pure liquid sulfur at $\sim$ 403 K was poured into large vats, allowing very thin widespread deposits of liquid sulfur to cool and solidify in open air. Greeley *et al.* report that durable crusts formed easily over much of the flow surface. Crustal blocks were found to be stable against foundering and there was some evidence of flow continuing in channels that had completely crusted over — behavior similar to that of lava tubes in basalt. Greeley *et al.* describe that sulfur in the industrial flows first solidifies into a dark reddish brown solid (which we note is probably monoclinic β–sulfur) followed by a gradual transition to pale yellow or yellow (as the transition to orthorhombic α–sulfur takes place). The transformation occurs from numerous nucleation sites at the flow surface. The α–sulfur nucleation sites were first observed at about 30 min after solidification of the top of the flow, and the transformation was complete after 1 hr. This observed behavior is very similar to the description of Watanabe (1940) of a natural volcanic sulfur flow at Siretoko–Iôsan Volcano in Japan.

Watanabe (1940) observed a terrestrial sulfur eruption and flow in progress. He found that the sulfur solidified at the sides and surface of the flow simultaneously while the inner portion of the flow remained fluid. According to Watanabe, the flow solidified into what he describes as a rigid light brown glass, not into monoclinic sulfur. Watanabe observed what is clearly orthorhombic nucleation sites forming in the crust soon after the crust solidified, and the entire surface converted to yellow orthorhombic S_α in about an hour. It is uncertain from Watanabe's description whether the glassy

sulfur was less dense than the liquid or whether the flow was small enough to support a rigid crust.

On Io, we would need to know the physical properties of such a sulfur crust, its cooling rate, its stability against foundering and cracking, and the thermal history of the sulfur from which it was formed before we could estimate the temperature history of the upper crust and the corresponding transformation rate of any metastable species into orthorhombic sulfur at the surface of the flow. It seems likely that a crust could form, but it also seems likely that the crust could be easily broken up and roughened as the flow proceeded. Thus, we might expect a solid crust to remain warm long enough for S_α conversion to take place. If the initial liquid temperature were near 393 K and if the flow or lake were several meters deep, then we might expect on the basis of our experimental results and the descriptions of Watanabe (1940) and Greeley *et al.* (1990) that conversion to S_α would occur in as little as an hour after the flow or lake surface had solidified, and that the final product would be light yellow and similar to the well–aged spectra in Figures 4 and 5. However, if the original temperature of the liquid were higher than the polymerization temperature and if similar impurities were found in sulfur on Io as on the Earth, we might expect a lighter brown/yellow (maize) solid (or a darker solid if the sulfur is heated to very high temperatures) to form after a slightly longer amount of time (see the well–aged spectrum in Figure 6). In addition, if foundering and cracking does not occur, the insulating properties of sulfur may allow the very top portion of a sulfur crust to cool rapidly and to keep the top surface thermally decoupled from the rest of the flow. In this latter case, if the upper portion of the crust cools to ambient Io temperatures in less than several hours, then the monoclinic (β) structure may persist indefinitely.

Young (1984) has argued that no sulfur allotropes except S_α can exist in large flows on Io. In particular, he correctly emphasizes that deep flows or lakes of sulfur on

Io will contain no S_3 or S_4 and little S_6 and S_7 after solidification; thus, they will not be red. In addition, Young claims that sulfur polymers will be highly unstable on Io. We believe this claim to be misleading and contrary to much of the literature concerning polymeric sulfur. We believe that deep flows or lakes on Io can contain significant fractions of polymeric sulfur S_μ that can remain metastable virtually indefinitely and that may darken the final product (depending on the presence of impurities in the sulfur). Young's statement that impurities (especially SO_2 and H_2S) generally accelerate the conversion of unstable molecules into S_8 is not really correct for the case of SO_2 in S_μ and is contrary to the observations of many observers (see Section 2). While it is true that H_2S readily destroys the polymers in liquid sulfur, dissolved SO_2 seems to aid polymer formation in the liquid and to stabilize the polymer in the final solid. Young (1984) argues that polymeric S_μ would not last long on Io where it would be exposed to X rays and sunlight. Again, this may not be correct. Young bases his conclusion on a paper by Meyer and Go (1934); the conclusions of the Meyer and Go paper have been refuted by many later workers. For instance, Prins *et al.* (1956) discuss (p. 770) the differences between their interpretation of "fibrous" sulfur (sulfur that has been quenched rapidly from above the polymeric temperature into ice water and then stretched into fibers) and the interpretation of Meyer and Go:

> In two respects we are completely at variance with [Meyer and Go 1934]. They considered the fibres as very unstable, necessitating continuous renewal during exposure. It is true that our fibres too get brittle after a few days, but their X–ray diagrams hardly changed, even after the unprotected fibres had been kept for more than a year.

It is likely that Meyer and Go (1934) were observing the hardening that is associated with the conversion of the available S_8 into an orthorhombic crystalline lattice; Meyer and Go conclude that the polymeric structure rather than the S_8 crystal structure is unstable. However, later workers find that polymeric molecules are maintained in the solid, as evidenced by the X–ray diffraction pattern and the percentage of

insoluble sulfur found with amorphous sulfur samples tested more than a year after their formation (see Prins *et al.* 1956, Schenk 1957b, Meyer 1964). Although the S–S bond is sensitive to ultraviolet light, X rays, and other forms of radiation, polymeric sulfur is not completely destroyed by irradiation. The scission of both chains and rings occurs, allowing an equilibrium condition between the ring and chain species to develop (Meyer 1965). In bulk samples, polymeric chains seem to be intermixed with S_8 molecules in such a way as to make the polymers kinetically stable against breakdown and conversion to rings (Haisty and Krebs 1969, Meyer 1976).

The presence of polymers in higher–temperature melts may help explain the visual appearance of flows such as Ra Patera. If we assume that the flow color and morphology are due to sulfur that was initially at a temperature of about 500 K (as discussed by Pieri *et al.* 1984) and if we further assume that the Ionian sulfur has impurities similar to those of terrestrial sulfur, then we can explain its color variation with distance from the source region. Initially, the hot sulfur flowing from the vent will contain a large percentage of polymeric molecules and will be highly viscous. If a crust forms on top of the flow, then the flow surface near the vent will solidify into a dark solid consisting of S_μ and S_β. The outer surface will remain light brown or brown/yellow (see Figure 6) even after the available S_8 molecules have realigned from a monoclinic to an orthorhombic crystal lattice because of the enduring presence of darker, impurity–affected sulfur polymers. As the sulfur continues to flow from the vent, the subcrustal liquid sulfur will cool, the molecular species within the flow will have time to fully or partially equilibrate (Pieri *et al.* 1984 estimate flow durations of several days), the polymer content will drop, and the sulfur will become less viscous and flow over larger areas. Since less polymeric sulfur will be found farther from the source region, the final solid will be lighter (pale yellow or white). As will be shown in the next section, sulfur with this prescribed thermal history will have visible albedo

and color ratios consistent with the *Voyager* data of the Ra Patera flows on Io (as presented by McEwen 1988).

A similar color association may be present for any elemental sulfur that ponds in topographic lows such as calderas; that is, sulfur heated above the polymeric temperature in these areas may be darker (depending on the types of impurities that are present) than sulfur that has always been kept below 432 K. The higher the temperature to which the liquid is heated, the darker the solid will be even after most of the S_8 has converted to orthorhombic S_α. However, the molten sulfur will be quite difficult to "quench" and keep in a monoclinic or glassy form — the flow surface temperature may remain warm long enough for the phase transformation of S_β to S_α to take place — but, because of the very slow kinetics of polymer decomposition in the solid, some S_μ may still be present long after the flow has solidified and cooled.

We must insert a strong note of caution now with regard to the discussion of color both above and in the next section. The brown tint observed in our high-temperature melts seems to be due to minute amounts of impurities that react with sulfur chains during the heating process. It is by no means certain that any sulfur on Io would contain the same types of impurities as are found in sulfur on the Earth. Although our 393 K melt freezes are unaffected by the impurities, the spectra of the 453 K melt freezes clearly show the signature of very small amounts of nonsulfur species. The reader must therefore regard any comparison of our high-temperature sulfur melt freeze spectra with spectra of Io as speculative.

8. Comparisons with Io Spectra

To fully apply our laboratory results to Io's surface, we must provide a comparison of our laboratory spectra with spectra of Io's surface. In this section we discuss such comparisons between our spectra and those of both whole–disk and localized areas on Io.

8.1 Whole–Disk Observations

Although little useful knowledge can be gained from comparing laboratory data taken at visible wavelengths at a single phase angle to whole–disk observations of a planet, we have included such a comparison here to illustrate three points: (1) Such comparisons are not very helpful because such model fits are nonunique (not to mention the problems encountered by the different viewing geometries), (2) models made up of several potential species usually provide better fits than models consisting of one or two species, and (3) Hapke's (1989) claim that elemental sulfur cannot match the blue–UV slope of Io is untrue when other allotropes besides S_α are considered. Figure 14a shows the reflectance spectra of some of the materials used in our models. The SO_2 frost spectrum was taken from Nash *et al.* (1980) and the spectrum of quenched red sulfur glass was taken from Soderblom *et al.* (1980). This figure is presented mainly to show how the spectra of the samples present in Figures 4 – 6 vary with temperature. Both the 393 and 453 K sulfur melt freezes presented in Figure 14a are well–aged; that is, their spectra were taken after the samples had aged for several months at room temperature so that the transformation from the β phase to the α phase had already ensued. The monoclinic β–sulfur sample is fresh; the spectrum was taken 1 hr after the sample had crystallized and aged at room temperature. The spectra of all the sulfur samples in Figure 14a have been altered to illustrate how we believe they would appear at 120 K. This adjustment to the room temperature spectra was accomplished by shifting the S_8 absorption "edge" farther toward the ultraviolet

at a rate of 1.6 Å/K and by slightly strengthening the absorption in the band. Such alterations have been shown to accurately account for the thermochromicity of sulfur (Gradie and Veverka 1984).

These alterations in the spectra may not accurately account for any difference in spectra between sulfur on Io and sulfur on the Earth. The 1.6 Å/K shift in the absorption edge is really only a maximum shift and is only relevant to S_8; some other allotropes such as S_μ and S_7 have less temperature dependence. Ultraviolet radiation (Steudel *et al.* 1986), X rays (Nelson *et al.* 1990), and vacuum weathering (Nash 1987) have been described as affecting the physical and chemical properties (including the color) of solid elemental sulfur. Steudel *et al.* (1986) report that sulfur irradiated with ultraviolet light turns bright yellow at 77 K rather than remains white. Steudel and Holz (1988) suggest that the yellow color is due to S_7 rings contaminating the α–sulfur samples. They suggest that any sulfur on Io that has solidified from a liquid will contain S_7 molecules and will remain yellow rather than white at Io temperatures. We find that our 393 K melt freezes brighten slightly ($\sim$ 1%) at visible wavelengths and our 453 K melt freezes darken by a few percent at visible wavelengths after being exposed to sunlight for 6 hrs. Irradiation of sulfur by X rays can alter the spectra of solid sulfur (Nelson *et al.* 1990) and may be relevant to Io if the accumulated X–ray dosage is large (*i.e.*, if resurfacing in certain local areas is slow). Vacuum weathering (Nash 1987) will not be important in areas of plume deposits and will be important in sulfur flows only if the surface of the flow remains warm for periods of several hours to days. In any case, the reader must keep in mind that other processes exist on Io that may affect the spectral behavior of solid sulfur; a detailed study of the simultaneous effects of the various processes has not been presented.

Figure 14b shows how a model consisting of 9% SO_2 frost and 91% sulfur 453 K melt freeze compares to ground–based whole–disk observations of Io (Wamsteker 1972,

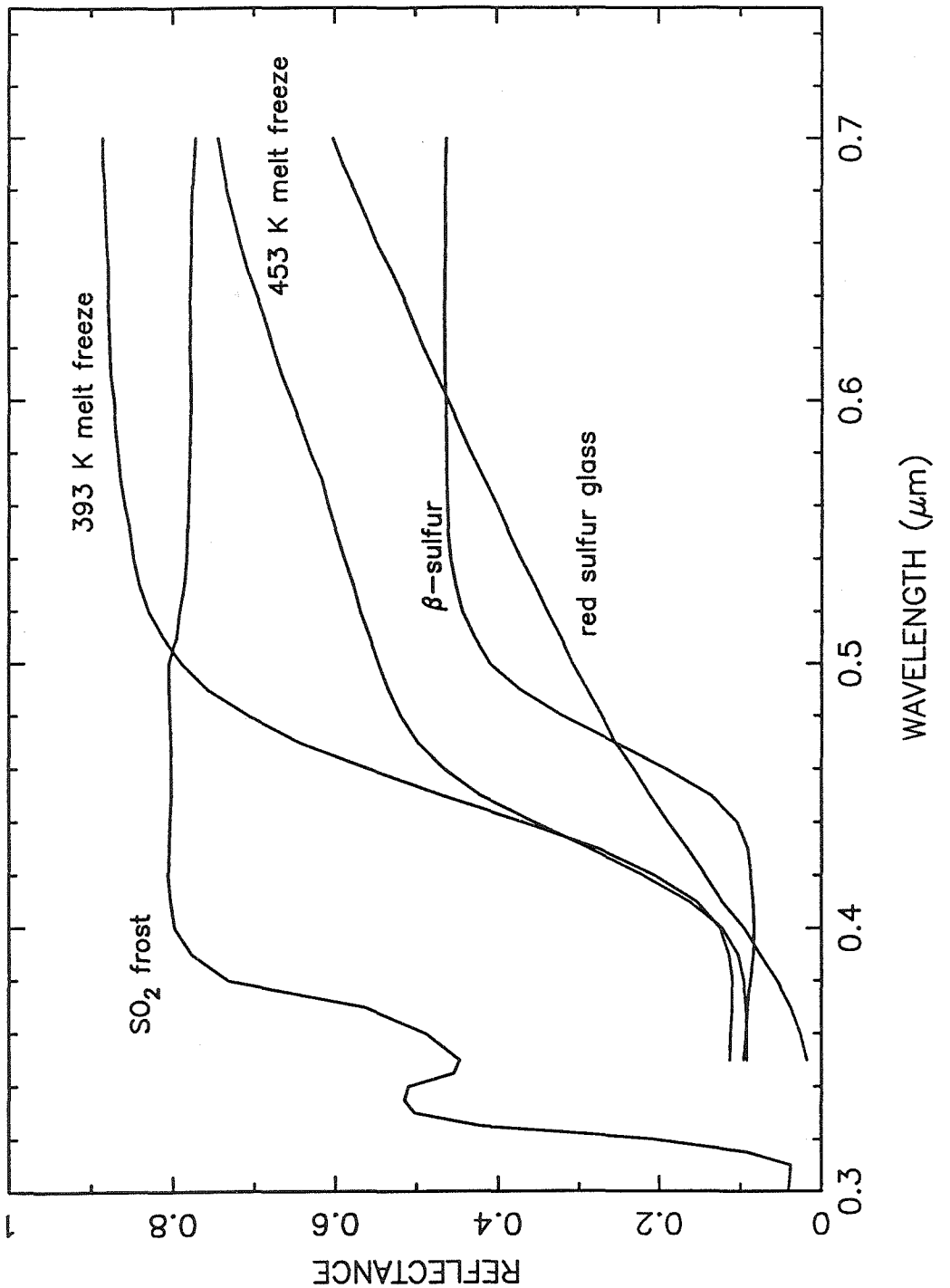

Figure 14a. The reflectance spectra of laboratory sulfur species compared with whole–disk observations of Io: The reflectance spectra of individual laboratory species used in the models.

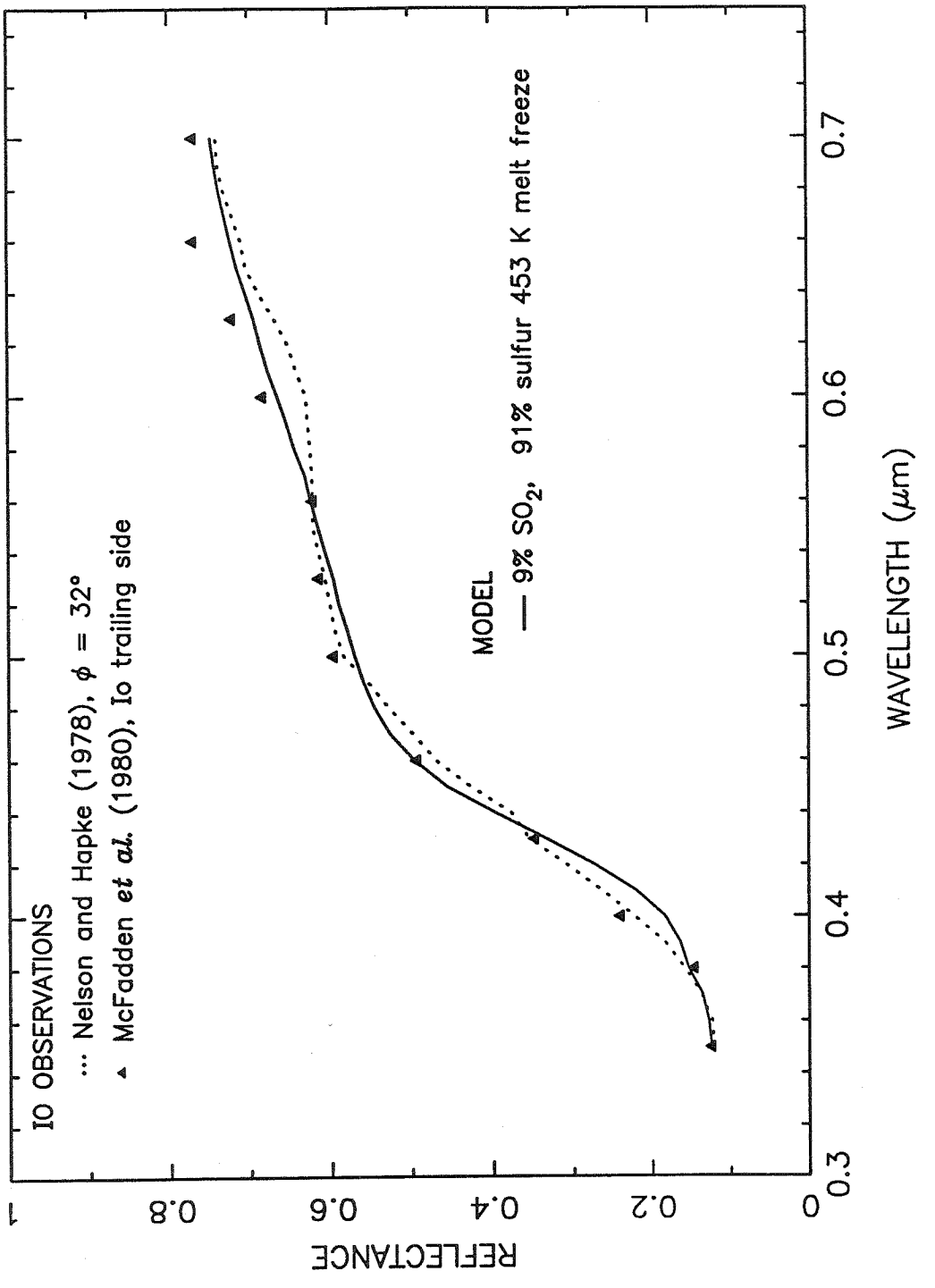

Figure 14b. The reflectance spectra of laboratory sulfur species compared with whole–disk observations of Io: a simple model mixture (solid line) compared to Io observations (triangles and dotted line).

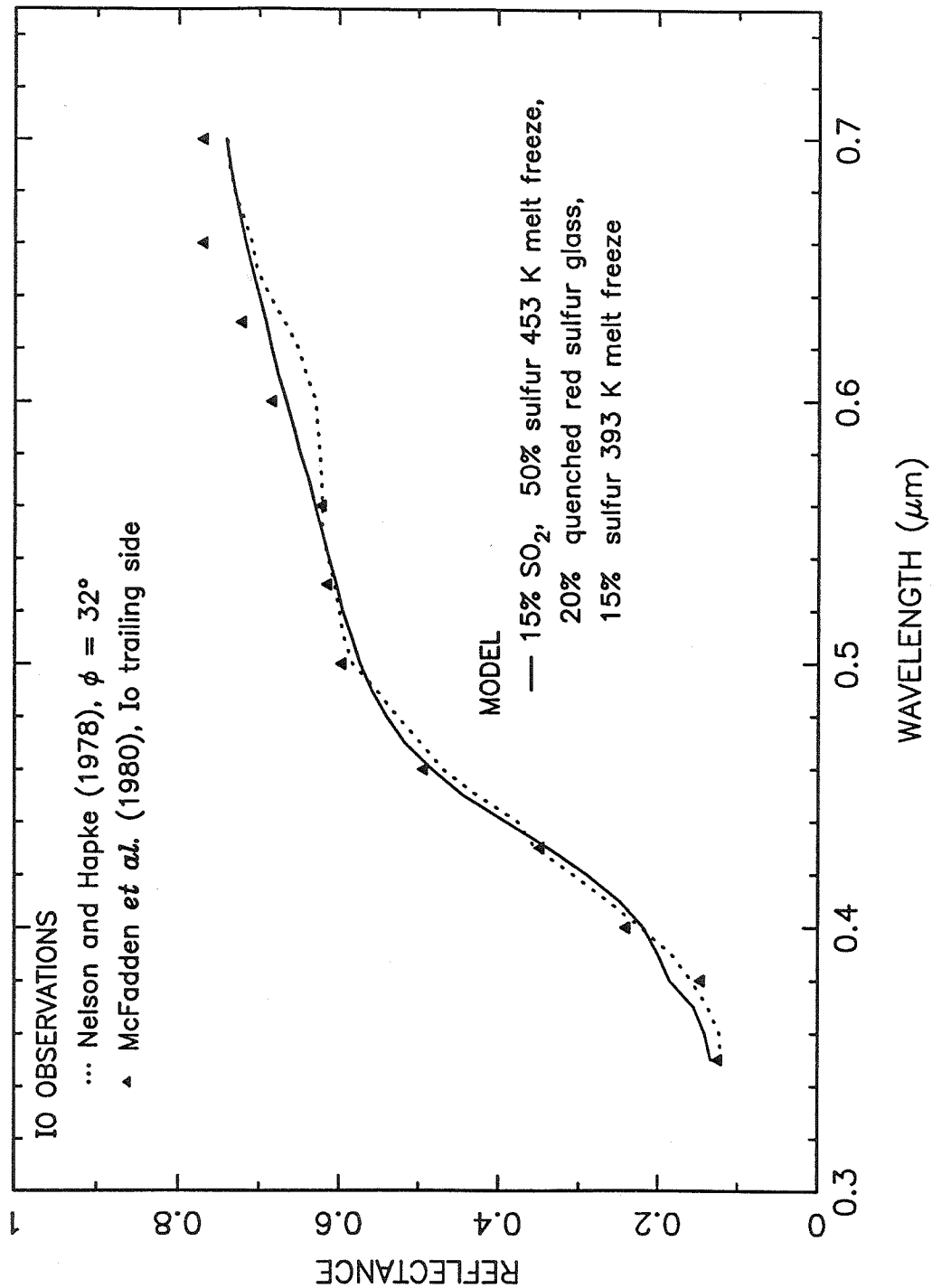

Figure 14c. The reflectance spectra of laboratory sulfur species compared with whole–disk observations of Io: A more complex model mixture (solid line) compared to Io observations (triangles and dotted line). The Io observations have been normalized to the 0.56 μm albedo of Morrison and Cruikshank (1974).

Nelson and Hapke 1978, McFadden *et al.* 1980). The overall fit is not bad for a two–species comparison. The biggest problems with the model appear to be the steepness of the slope from 0.35 to 0.5 μm and the model's lack of an absorption band at $\sim$ 0.6 μm. Although a slight "dip" appears at $\sim$ 0.55 μm in the reflectance spectra of $<$ 99.9999% pure sulfur that has been heated above the polymerization temperature of liquid sulfur (e.g., Figure 6) probably due to the presence of impurities reacting with sulfur chains, the absorption is not nearly as strong as that observed between 0.55 and 0.65 μm in whole–disk observations of Io. In addition, the visible tail of the S_8 absorption band falls very steeply with decreasing wavelength from 0.45 to 0.40 μm so that the spectra of any sulfur containing S_8 molecules will be rapidly changing from 0.45 to 0.40 μm but will then flatten out at wavelengths shorter than 0.40 μm (see Figure 14a); the slope of the UV–violet absorption of Io is less precipitous.

This behavior of sulfur in the violet region of the visible spectrum has led Hapke (1989) to claim that elemental sulfur is completely inconsistent with whole–disk visible spectra of Io. Hapke himself favors a model consisting of polysulfur oxides, S_2O condensates, SO_2 frost, and basalt, with no elemental sulfur. His match to the Io spectra at visible wavelengths using mixtures of these species is quite good (see his Figure 1), and the species used in his model are geologically feasible (although perhaps not probable given Io's rapid resurfacing rate; see McEwen and Lunine 1989). However, we claim that any model consisting of four or more geologically– and spectrally–reasonable materials will have an advantage over models of one or two species. For instance, Figure 14c shows a comparison between the Io data and a model consisting of SO_2 frost and three reasonable varieties of elemental sulfur. The match is much better than that of Figure 14b. The match in the slope from 0.35 to 0.50 μm is as good as or better than that of Hapke's model, so, clearly, there is not necessarily a problem with elemental sulfur at shorter wavelengths. The main advantage of Hapke's

model is that Hapke includes the spectrum of a bright red material (condensed S_2O) to account for the broad absorption feature at ~0.6 μm in Io's spectra. The addition of such a material would also benefit the model presented in Figure 14c.

In any case, as numerous workers have emphasized, most of the diagnostic information concerning the composition of atmospheres and surfaces comes from infrared and ultraviolet absorption and emission features rather than from visible spectra. Since S_8 emission features have been identified in the infrared in the *Voyager* IRIS spectra (Pearl 1984, 1988), we feel justified in continuing to examine elemental sulfur as a possible surface constituent. The convincing fit of Hapke's model with visible ground–based Io spectra has encouraged people to go back and search for the signature of polysulfur oxides in the infrared spectra, but it will be this IR identification (or lack thereof) that will most convince people of the likelihood of polysulfur oxides as surface constituents.

8.2 Spacecraft Observations of Local Areas

We now compare our laboratory data with *Voyager* observations of local areas on Io. As already mentioned, comparisons of planetary albedo at visible wavelengths with laboratory data are not very diagnostic. Spacecraft data, however, have one advantage over ground–based data; namely, photometric information can be removed from the spacecraft data so that normal reflectances of laboratory materials can be directly compared with derived normal reflectances of specific areas on the planet's surface. McEwen and Soderblom (1983), McEwen *et al.* (1985), Simonelli and Veverka (1986), McEwen (1988), and McEwen *et al.* (1988) have used this procedure to compare laboratory spectra of possible materials with specific regions on Io. In this section, we compare the reflectances of the elemental sulfur species produced in our experiments with the reflectances of the localized areas on Io's surface examined by the above investigators. We adjusted the reflectance spectra of our samples to a

lower temperature, 120 K, as discussed in the previous part of this section (see Figure 14a). Then we convolved the spectra with the *Voyager* filter response functions, instrument response functions, and solar spectrum to accurately compare the *Voyager* narrow–angle camera filter observations with our laboratory data (e.g., McEwen 1988). Following McEwen (1988), the effective wavelengths of the *Voyager* narrow–angle camera filters are orange, 0.591 μm; green, 0.566 μm; blue, 0.479 μm; violet, 0.416 μm; and ultraviolet, 0.346 μm.

Table II shows the normal reflectances and color ratios of typical sulfur samples used in our experiments. These data are most useful when compared with the two–dimensional histograms of equal–area *Voyager 1* albedos and color ratios shown in Figures 14 and 15 of McEwen (1988).

Table II
Reflectivities of various forms of elemental sulfur at 120 K after convolution with the *Voyager* narrow–angle camera bandpasses

Material	OR	GR	BL	VI	VI/BL	BL/OR
Well–aged 393 K melt freeze	0.870	0.859	0.653	0.224	0.343	0.750
Well–aged 453 K melt freeze	0.643	0.613	0.488	0.219	0.448	0.759
Fresh monoclinic S_β	0.463	0.459	0.292	0.095	0.325	0.631
Fresh 453 K melt freeze	0.357	0.324	0.229	0.102	0.444	0.641

We find that all the varieties of sulfur listed in Table II fall within the Io two–dimensional histograms. In fact, elemental sulfur with various thermal histories can account for an entire "edge" of the histogram data. SO_2 seems to mark one endmember of McEwen's triangular–looking color diagrams (McEwen's Figures 14 and 15) whereas elemental sulfur is consistent with the entire opposite (bottom) edge of McEwen's diagrams: well–aged 393 K melt freezes (S_α) are consistent with the lower right points of the "triangles," fresh 453 K melt freezes ($S_\mu + S_\beta$) and monoclinic sulfur (S_β) are near the lower left points of the "triangles," and well–aged 453 K melt

freezes ($S_\alpha + S_\mu$) are gradational between the two points and are often near the center of the histogram data. Also, fresh 453 K melt freezes and monoclinic S_β are quite similar to unit 2 of McEwen (1988) and unit C of McEwen *et al.* (1988). These units make up most of the polar regions but, more significantly, match the caldera floors on Io. This result provides further evidence that molten and recently solidified sulfur are consistent with the caldera material as suggested by McEwen *et al.* (1985). Well–aged 453 K melt freezes are consistent with much of Io's surface, especially units 1 and 3 of McEwen (1988).

Once–molten elemental sulfur is also consistent with the pyroclastic deposits from the large plumes. Figure 15 shows the normal reflectances of some laboratory sulfur samples compared with the normal albedos of the deposits from the Pele–type plumes (McEwen and Soderblom 1983). 453 K melt freezes at various ages and fresh monoclinic S_β fall within the boundaries of the albedo region of the large–plume deposits. S_α is brighter than these deposits. This result is consistent with our suggestion that sulfur droplets ejected from the large plumes could cool quickly enough to preserve some metastable sulfur allotropes such as S_β and S_μ.

The flows at Ra Patera are also consistent with the presence of metastable sulfur allotropes (see spectral map and histogram plots of McEwen 1988). The source region itself is relatively dark and has color and albedo ratios consistent with those of liquid sulfur, monoclinic (β) sulfur, or sulfur that contains a large portion of polymers (*i.e.*, sulfur heated to high temperatures). The distinct sinuous flows radiating from the Ra source region are more consistent with orthorhombic (α) sulfur that contains a significant portion of the metastable polymeric μ–sulfur. The regions surrounding the distinct flows may or may not be associated geologically with the Ra Patera source region (see Pieri *et al.* 1984) and tend to be lighter in color similar to orthorhombic (α) sulfur that contains smaller amounts of polymers. As previously mentioned, this

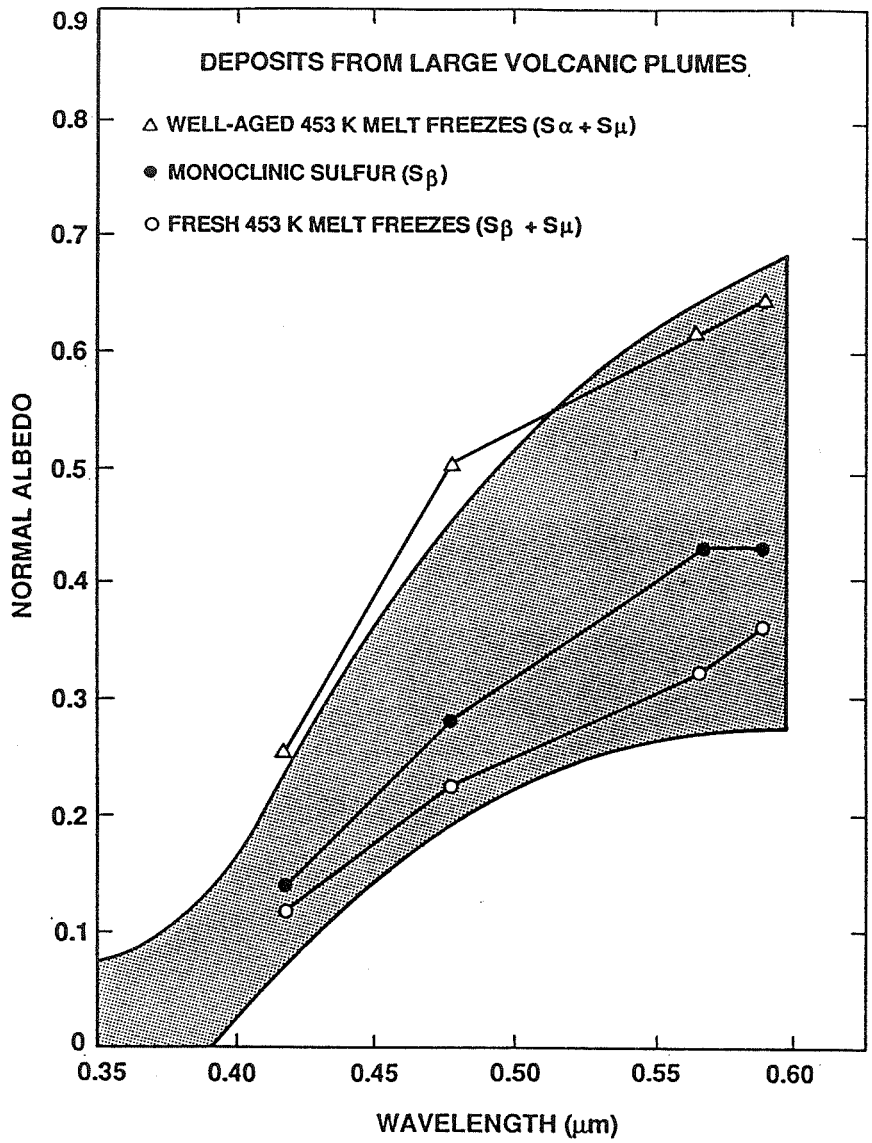

Figure 15. Normal reflectance measurements of the ejecta from the large Pele–type plumes on Io (stippled area, from McEwen and Soderblom 1983) compared with laboratory reflectance measurements of various sulfur samples (data points). All laboratory data were convolved with the *Voyager* narrow–angle camera bandpasses. Additional correction factors for the *Voyager* filters have been suggested by T.V. Johnson to calibrate the *Voyager* data with Earth–based observations [A.S. McEwen, personal communication]. Since the Pele–type plume–deposit spectra do not include these calibration factors, the boundaries of the stippled area should be multiplied by 0.935 for the orange filter (at 0.59 μm), 0.926 for the green filter (at 0.57 μm), 1.000 for the blue filter (at 0.48 μm), 1.125 for the violet filter (at 0.42 μm), and 1.186 for the ultraviolet filter (at 0.35 μm).

observed color trend may be consistent with the flows being caused by the eruption of hot liquid sulfur. Pieri *et al.* (1984) claim that the morphology of the flows is consistent with the viscosity–temperature behavior of sulfur that originally erupted at a temperature of 500 K. We claim that the flow colors are also consistent with such an origin.

8.3 Post–Eclipse Brightening

The increase in brightness at short wavelengths that appears with a decrease in temperature is evident with S_β and S_μ allotropes as well as with S_α, but the magnitude is smaller for larger amounts of non–S_8 allotropes (Steudel and Holz 1988). We now examine the extent of the brightness change expected as a hypothetical sulfur–covered Io emerges from behind Jupiter's shadow. We consider this "post–eclipse brightening" (or really "darkening" at visible wavelengths) from the standpoint of both Earth–based and *Voyager*–spacecraft observations. Hammel *et al.* (1985) have presented thermal models for Io in which the surface of the satellite heats up from 67 to 97 K in just 5 min after eclipse reappearance from behind Jupiter. Using a "worst–case–scenario" in which all our sulfur samples were taken to have a shift in absorption edge with temperature of 1.6 Å/K, we have readjusted our sulfur sample spectra to correspond to the relevant 67 and 97 K temperatures. We then examine the difference in brightness between the two spectra in the desired wavelength range. For the *Voyager* observations, we convolve the spectra with the narrow–angle camera response functions (blue and violet filters) to inspect the darkening expected in these filters. For the ground–based observations, we use a method similar to that of Simonelli and Veverka (1986) to convert our normal reflectances to geometric albedos in order to compare our model with the post–eclipse observations of Hammel *et al.*

In the *Voyager* narrow–angle camera blue filter (effective wavelength 0.479 μm), orthorhombic sulfur (or a well–aged 393 K melt freeze) would darken 3.6% with an

increase in temperature from 67 to 97 K. In contrast, well–aged 453 K melt freezes, which contain polymeric S_μ as well as S_α, would darken just 1.8% with the same increase in temperature. More "post–eclipse brightening" would be observed in the violet filter (effective wavelength 0.416 μm), however, where both S_α and well–aged 453 K melt freezes darken 10% with an increase in temperature from 67 to 97 K. Monoclinic sulfur darkens 6.1% in the violet and 5.9% in the blue with this temperature change. A surface covered with 50% well–aged 453 K melt freeze, 20% red sulfur glass, 15% SO_2 frost, and 15% S_α as shown in Figure 14c would darken 5.4% in the *Voyager* violet filter and 1.5% in the blue filter after eclipse reappearance if the thermal model of Hammel *et al.* is correct and if the SO_2 does not change (*i.e.*, sublime away) during this period.

For the ground–based data at 0.44 μm, the geometric albedos of the above combinations of materials would be about 0.380 at 120 K, 0.398 at 97 K, and 0.418 at 67 K, implying a 4.8% change in geometric albedo at 0.44 μm in the first 5 min after eclipse reappearance for the Hammel *et al.* (1985) thermal model. This predicted variation is near the observational 4% (2σ level) upper limit proposed by Hammel *et al.* (1985). Remember that this is a worst case scenario in the sense that the temperature effects were assumed to influence all the sulfur samples in the same manner as S_8; however, the non–S_8 allotropes are probably much less temperature sensitive. Even with the 1.6 Å/K shift, some of the metastable allotropes have less expected brightness variation with temperature than pure S_α at short wavelengths simply because they are darker. Thus, geologically realistic models of surface constituents that predict large amounts of elemental sulfur on Io may be consistent with ground–based and spacecraft observations if metastable allotropes are considered as well as stable S_α.

9. Summary

The spectral reflectance of solid elemental sulfur changes with time following solidification from a melt as solid–state phase transformations take place; specifically, sulfur that was heated to 393 and 453 K and then cooled slowly to room temperature ($\sim$ 297 K) will brighten at visible wavelengths as it eventually converts to pure orthorhombic sulfur, S_α. The two metastable solid phases of importance in our experiments are monoclinic β–sulfur and polymeric μ–sulfur. Sulfur heated to 393 K and then allowed to solidify and age at 297 K will crystallize first into S_β and transform eventually into pure S_α. Sulfur heated to 453 K and then allowed to solidify and age at 297 K will contain a substantial fraction of polymeric molecules (S_μ) as well as the S_8 in a monoclinic (β) lattice. The S_β converts to S_α relatively rapidly, but the S_μ can remain in the solid for years at 297 K.

Our laboratory data support the conclusion that the thermal history of sulfur melt freezes affects the transformation rate of the solid back into S_α. Heating sulfur above its polymerization temperature (432 K) before solidification at 297 K allows polymeric sulfur, S_μ, to exist in the solid. In general, the higher the temperature to which the liquid sulfur is heated, the larger the proportion of polymers that develops in the liquid and is preserved in the solid (see Table I). The rate of transformation of polymeric sulfur into orthorhombic α–sulfur is much slower than the rate of transformation of S_β into S_α. Since the presence of minute amounts of impurities that react with the sulfur polymers when molten sulfur is heated above 432 K seems to cause a brown coloration in the bulk solid, the visible reflectance of the sulfur remains darker than that of pure S_α for periods of months or years at 297 K. The prefreeze melt time (duration of melting) affects the transformation rate of the frozen sulfur back into S_α because the melt time affects the concentration of non–S_8 species in the liquid. Equilibrium between the various molecular species in the melt takes about 12 hrs to

develop at 393 K but about 2 days to develop at 453 K. The actual temperature at which the sulfur ages after solidification strongly affects the transformation rate of the metastable sulfur species into stable S_α. In particular, the transformation rate decreases exponentially with decreasing aging temperature as the temperature falls below 290 K (e.g., see Figure 10). Thus, metastable species such as monoclinic S_β or polymeric S_μ that are kept at very low temperatures will not revert to S_α or change spectrally on noticeable time scales.

Some metastable sulfur species (e.g., S_μ and S_β) may form and remain present on Jupiter's satellite Io if the phase transformations are inhibited by the low temperatures typical at the surface. Deposits from large volcanic plumes such as Pele might be expected to contain particles of once–molten elemental sulfur. These particles may contain metastable species such as S_μ or S_β. The very rapid cooling to ambient Io temperatures of small droplets in volcanic plumes will essentially prevent the phase transformations of metastable species into S_α from occurring so that particles will not change spectrally on observable time scales.

Any elemental sulfur present in large molten flows or lakes may cool slowly enough for the phase transformation from S_β to S_α to proceed. However, the transformation of S_μ into S_α may still be sluggish. This sluggish transformation may explain the morphologies and colors of some of the volcanic flows on Io. Hot liquid sulfur at the source region will be viscous and will contain a large percentage of S_μ. As the sulfur flows slowly across Io's surface, it will cool and equilibrate slowly so that smaller equilibrium percentages of S_μ will be found in the liquid farther from the source region. At 400 K, the sulfur will have a very low viscosity, can spread over large areas of flat terrain, and will be almost pure S_8 in an orthorhombic crystal structure soon after solidification. Since solid sulfur containing a large fraction of polymers formed under most conditions on Earth is light brown or maize (due to the

presence of minor amounts of impurities that react with sulfur chains in the liquid), if sulfur on Io behaves in a similar manner then this model of an elemental sulfur flow is consistent with correctly processed *Voyager* images (McEwen 1988) and with the resolved morphology (Pieri *et al.* 1985) of the flows at Ra Patera on Io.

Some arguments against the presence of elemental sulfur on Io (Young 1984, Hapke 1989) are no longer valid if one considers that metastable sulfur allotropes may be present. In particular, polymeric sulfur is probably very stable at Io surface conditions and, once formed, can exist indefinitely on Io. Hapke's claim that the UV–violet absorption edge of elemental sulfur is too steep to explain the Io data is incorrect when metastable elemental sulfur allotropes besides stable S_α are considered. Post–eclipse brightening is less significant for the case of polymeric S_μ or monoclinic S_β, but should still be present if the sulfur contains any S_8 molecules.

Elemental sulfur or polysulfur oxides (this paper or Hapke and Graham 1989) have the unfortunate property that their thermal history and method of formation profoundly affect the spectrum of the material so that altering the conditions of formation can provide a material with just about any reflectance spectrum that is desired. This property implies that it is relatively easy to fit both ground–based and spacecraft observations of Io at visible wavelengths with mixtures of elemental sulfur or polysulfur oxides. However, the visible region of the spectrum does not contain much diagnostic information about materials. Since elemental sulfur (S_8) has been detected in emission in the *Voyager* infrared spectra (Pearl 1984, 1988), it is certainly an important substance to consider on Io's surface. In that case, we have shown that metastable sulfur allotropes may also be present on Io.

Acknowledgments

We thank A. S. McEwen, J. C. Gradie, D. J. Stevenson, Y. L. Yung, and an anonymous reviewer for valuable discussions and helpful suggestions and comments, and

C. D. Wilson for German translation assistance. A portion of the laboratory work was carried out at the Jet Propulsion Laboratory. This research was funded by NASA Grant NAGW 1350 and represents Contribution 3 from the San Juan Capistrano Research Institute and Contribution 4808 from the Division of Geological and Planetary Sciences, California Institute of Technology. The first author gratefully acknowledges support from the NASA Graduate Student Researchers Program.

References

Arthur, D. W. G. 1981. *Vertical dimensions of the Galilean satellites.* NASA TM–81776.

Aten, A. H. W. 1914. Über eine dritte Schwefelmolekülart (Dritte Mitteilung). *Z. Phys. Chem.* **86**, 1 – 35.

Avrami, M. 1939. Kinetics of phase change. I. General theory. *J. Chem. Phys.* **7**, 1103 – 1112.

Bacon, R. F., and R. Fanelli 1942. Purification of sulfur. *Ind. Eng. Chem. Soc.* **34**, 1043 – 1048.

Bacon, R. F., and R. Fanelli 1943. The viscosity of sulfur. *J. Amer. Chem. Soc.* **65**, 639 – 648.

Briske, C., and N. H. Hartshorne 1967. Linear rate of the polymorphic transformations of sulphur. *Trans. Faraday Soc.* **63**, 1546 – 1552.

Brown, R. A., C. Pilcher, and D. Strobel 1983. Spectrophotometric studies of the Io torus. In *Physics of the Jovian Magnetosphere* (A. J. Dessler, Ed.), pp. 197 – 225. Cambridge Univ. Press, Cambridge.

Buerger, M. J. 1951. Crystallographic aspects of phase transformations. In *Phase Transformations in Solids* (R. Smoluchowski, J. E. Mayer, and W. A. Weyl, Eds.), pp. 183 – 211. Wiley, New York.

Burwell, J. T. 1937. The unit cell and space group of monoclinic sulfur. *Z. Krist.* **97**, 123 – 124.

Carr, M. H. 1986. Silicate volcanism on Io. *J. Geophys. Res.* **91**, 3521 – 3532.

Clow, G. D., and M. H. Carr 1980. Stability of sulfur slopes on Io. *Icarus* **44**, 268 – 279.

Collins, S. A. 1981. Spatial color variations in the volcanic plume at Loki, Io. *J. Geophys. Res.* 86, 8621 – 8626.

Currell, B. R., and A. J. Williams 1974. Thermal analysis of elemental sulphur. *Thermochim. Acta* 9, 255 – 259.

Davis, C. S., and J. B. Hyne 1976. Thermomechanical analysis of elemental sulphur: The effects of thermal history and ageing. *Thermochim. Acta* 15, 375 – 385.

Donohue, J. 1974. *The Structures of the Elements,* pp. 324 – 369. Wiley–Interscience, New York.

Durrance, S. T., P. Feldman, and H. Weaver 1982. Rocket detection of ultraviolet emission from neutral oxygen and sulfur in the Io torus. *Astrophys. J.* 267, L125 – L129.

Eastman, E. D. and W. C. McGavock 1937. The heat capacity and entropy of rhombic and monoclinic sulfur. *J. Amer. Chem. Soc.* 59, 145 – 151.

Elias, P. G., N. H. Hartshorne, and J. E. D. James 1940. Studies in polymorphism. Part V. The linear rate of transformation of monoclinic into rhombic sulphur. *J. Chem. Soc.,* 588 – 595.

Fanale, F. P., R. H. Brown, D. P. Cruikshank, and R. N. Clark 1979. Significance of absorption features in Io's IR spectrum. *Nature* 280, 760 – 763.

Fanale, F. P., T. V. Johnson, and D. L. Matson 1974. Io: A surface evaporite deposit? *Science* 186, 922 – 925.

Fink, J. H., S. O. Park, and R. Greeley 1983. Cooling and deformation of sulfur flows. *Icarus* 56, 38 – 50.

Fraenkel, V. W. and W. Goez 1925. Über die räumliche Umwandlungsgeschwindigkeit von Schwefelmodifikationen. *Z. anorg. Chem.* 144, 45 – 59.

Frank, F. C. 1949. The influence of dislocations on crystal growth. *Disc. Faraday Soc.* **5**, 48 – 54.

Gernez, D. 1885a. Sur le phénomène de la surfusion cristalline du soufre et sur la vitesse de transformation du soufre prismatique en octaédrique. *Compt. rend.* **100**, 1343 – 1345.

Gernez, D. 1885b. Sur la vitesse de transformation du soufre prismatique en octaédrique. *Compt. rend.* **100**, 1382 – 1385.

Gradie, J., S. J. Ostro, P. C. Thomas, and J. Veverka 1984. Glass on the surfaces of Io and Amalthea. *J. Non-Crystal. Solids* **67**, 421 – 432.

Gradie, J., and J. Veverka 1984. Photometric properties of powdered sulfur. *Icarus* **58**, 227 – 245.

Greeley, R., S. W. Lee, D. A. Crown, and N. Lancaster 1990. Observation of industrial sulfur flows: Implications for Io. *Icarus* **84**, 374 – 402.

Haisty, R. W., and H. Krebs 1969. Electrical conductivity of melts and their ability to form glasses I. The Ge–Sb–Se system. *J. Non-Crystal. Solids* **1**, 399 – 426.

Hammel, H. B., J. D. Goguen, W. M. Sinton, and D. P. Cruikshank 1985. Observational test for sulfur allotropes on Io. *Icarus* **64**, 125 – 132.

Hansen, J. E., and L. D. Travis 1974. Light scattering in planetary atmospheres. *Space Sci. Rev.* **16**, 527 – 610.

Hapke, B. 1979. Io's surface and environs: A magmatic–volatile model. *Geophys. Res. Lett.* **6**, 799 – 802.

Hapke, B. 1989. The surface of Io: A new model. *Icarus* **79**, 56 – 74.

Hapke, B., and F. Graham 1989. Spectral properties of condensed phases of disulfur monoxide, polysulfur oxide, and irradiated sulfur. *Icarus* **79**, 47 – 55.

Harris, R. E. 1970. The molecular composition of liquid sulfur. *J. Phys. Chem.* 74, 3102 – 3111.

Hartshorne, N. H., and M. H. Roberts 1951. Studies in polymorphism. Part VI. A further investigation of the linear rate of transformation of monoclinic into orthorhombic sulphur. *J. Chem. Soc.,* 1097 – 1114.

Hartshorne, N. H., and M. Thackray 1957. Studies in polymorphism. Part VIII. The linear rate of transformation of β– into α–sulphur at low temperatures and at temperatures just below the transition point. *J. Chem. Soc.,* 2122 – 2131.

Hillig, W. B., and D. Turnbull 1956. Theory of crystal growth in undercooled pure liquids. *J. Chem. Phys.* **24**, 914.

Howell, R. R., D. B. Nash, T. R. Geballe, and D. P. Cruikshank 1989. High–resolution infrared spectroscopy of Io and possible surface materials. *Icarus* 78, 27 – 37.

Kennedy, S. J., and J. C. Wheeler 1983. On the density anomaly in sulfur at the polymerization transition. *J. Chem. Phys.* **78**, 1523 – 1527.

Kieffer, S. W. 1982. Dynamics and thermodynamics of volcanic eruptions: Implications for the plumes on Io. In *Satellites of Jupiter* (D. Morrison, Ed.), pp. 647 – 723. Univ. of Arizona Press, Tucson.

Koh, J. C., and W. Klement, Jr. 1970. Polymer content of sulfur quenched rapidly from the melt. *J. Chem. Phys.* 74, 4280 – 4284.

Kupo, I., Yu. Mekler, and A. Eviator 1976. Detection of ionized sulfur in the Jovian magnetosphere. *Astrophys. J.* **205**, L51 – L53.

Lunine, J. I., and D. J. Stevenson 1986. Physics and chemistry of sulfur lakes on Io. *Icarus* 64, 345 – 367.

Mäusle, V-J., and R. Steudel 1981. Molecular composition of liquid sulfur. Part

3: Quantitative analysis in the temperature region 115–350°C. *Z. anorg. allg. Chem.* **478**, 177 – 190.

McEwen, A. S. 1988. Global color and albedo variations on Io. *Icarus* **73**, 385 – 426.

McEwen, A. S., and J.I. Lunine 1989. Comment on "The surface of Io: A new model" by Bruce Hapke. *Icarus* **84**, 268 – 274.

McEwen, A. S., T.V. Johnson, D.L. Matson, and L.A. Soderblom 1988. The global distribution, abundance, and stability of SO_2 on Io. *Icarus* **75**, 450 – 478.

McEwen, A. S., D. L. Matson, T. V. Johnson, and L. A. Soderblom 1985. Volcanic hot spots on Io: Correlation with low–albedo calderas. *J. Geophys. Res.* **90**, 12345 – 12379.

McEwen, A. S., and L. A. Soderblom 1983. Two classes of volcanic plumes on Io. *Icarus* **55**, 191 – 217.

McFadden, L. A., J. F. Bell, and T.B. McCord 1980. Visible spectral reflectance measurements (0.33 – 1.1 μm) of the Galilean satellites at many orbital phase angles. *Icarus* **44**, 410 – 430.

Meyer, B. 1964. Solid allotropes of sulfur. *Chem. Rev.* **64**, 429 – 451.

Meyer, B. 1976. Elemental sulfur. *Chem. Rev.* **76**, 367 – 388.

Meyer, K. H., and Y. Go 1934. Sur le soufre filiforme et sa structure. *Helv. Chim. Acta* **17**, 1081 – 1093.

Mondain–Monval, P. 1934. Sur la cristallisation des corps vitreux. *Compt. rend.* **198**, 1413 – 1415.

Morrison, D., and D. Cruikshank 1974. Physical properties of the natural satellites. *Space Sci. Rev.* **15**, 641 – 739.

Moses, J., and J. Gradie 1983. Spectral reflectance properties of sulfur/silicate mixtures. *Bull. Amer. Astron. Soc.* **15**, 850.

Nash, D. B. 1986. Mid–infrared reflectance spectra (2.3 – 22 μm) of sulfur, gold, KBr, MgO, and halon. *Appl. Opt.* **25**, 2427 – 2433.

Nash, D. B. 1987. Sulfur in vacuum: Sublimation effects on frozen melts, and applications to Io's surface and torus. *Icarus* **72**, 1 – 34.

Nash, D. B., M. H. Carr, J. Gradie, D. M. Hunten, and C. F. Yoder 1986. Io. In *Satellites* (J.A. Burns and M.S. Matthews, Eds.), pp. 629 – 688. Univ. of Arizona Press, Tucson.

Nash, D. B. and F. P. Fanale 1977. Io's surface composition based on reflectance spectra of sulfur/salt mixtures and proton–irradiation experiments. *Icarus* **31**, 40 – 80.

Nash, D., F. Fanale, and R. Nelson 1980. SO_2 frost: UV–visible reflectivity and limits on Io surface coverage. *Geophys. Res. Lett.* **7**, 665 – 668.

Nash, D. B. and R. R. Howell 1989. Hydrogen sulfide on Io: Evidence from telescopic and laboratory infrared spectra. *Science* **244**, 454 – 457.

Nash, D. B. and J. I. Moses 1988. Vacuum weathering of sulfur: Temperature effects and applications to Io. *Geophys. Res. Lett.* **15**, 697 – 700.

Nelson, R., and B. Hapke 1978. Spectral reflectivities of the Galilean satellites and Titan, 0.32 to 0.86 micrometers. *Icarus* **36**, 304 – 329.

Nelson, R. M., W. D. Smythe, B. W. Hapke, and A. J. Cohen 1990. On the effect of x–rays on the color of elemental sulfur: Implications for Jupiter's satellite Io. *Bull. Amer. Astron. Soc.* **85**, 326 – 334.

Nickless, G. (Ed.) 1968. *Inorganic Sulfur Chemistry.* Elsevier, Amsterdam.

Oppenheimer, C. and D. Stevenson 1989. Liquid sulfur lakes at Poás volcano. *Nature* **342**, 790 – 793.

Pearl, J. 1984. Spatial variations in the surface composition of Io based on Voyager infrared data. *Bull. Amer. Astron. Soc.* **16**, 653.

Pearl, J. C. 1988. A review of Voyager IRIS results on Io. *Eos* **69**, 394.

Pieri, D. C., S. M. Baloga, R. M. Nelson, and C. Sagan 1984. Sulfur flows of Ra Patera, Io. *Icarus* **60**, 685 – 700.

Powell, R. E., and H. Eyring 1943. The properties of liquid sulfur. *J. Amer. Chem. Soc.* **65**, 648 – 654.

Prins, J. A. 1960. Amorphous sulfur and selenium. In *Non–Crystalline Solids* (V. D. Fréchette., Ed.), pp. 322 – 327. John Wiley and Sons, Inc., New York.

Prins, J. A., J. Schenk, and P. A. M. Hospel 1956. The x–ray diagram of fibrous sulfur. *Physica* **22**, 770–772.

Rawson, H. 1967. *Inorganic Glass–Forming Systems,* pp. 31 – 43. Academic Press, New York.

Reimschüssel, W., W. Świątkowski, and G. Trybulska 1978. Umwandlungskinetik des amorphen und des monoklinen Schwefels. *J. Therm. Anal.* **14**, 99 – 109.

Rubero, P. 1964. Effect of hydrogen sulfide on the viscosity of sulfur. *J. Chem. Eng. Data* **9**, 481 – 484.

Sagan, C. 1979. Sulfur flows on Io. *Nature* **280**, 750–753.

Sasson, R., and E. T. Arakawa 1986. Temperature dependence of index of refraction, reflection, and extinction coefficient of liquid sulfur in the 0.4 – 2.0–μm wavelength range. *Appl. Opt.* **25**, 2675 – 2680.

Sasson, R., R. Wright, E. T. Arakawa, B. N. Khare, and C. Sagan 1985. Optical

properties of solid and liquid sulfur at visible and infrared wavelengths. *Icarus* 64, 368 – 374.

Schaber, G. G. 1982. The geology of Io. In *Satellites of Jupiter* (D. Morrison, Ed.), pp. 556 – 597. Univ. of Arizona Press, Tucson.

Schenk, J. 1957a. Some properties of liquid sulfur and the occurrence of long chain molecules. *Physica* **23**, 325 – 337.

Schenk, J. 1957b. On the molecular constitution of liquid and amorphous sulfur. *Physica* **23**, 546 – 550.

Schmidt, M. 1965. Reactions of the sulfur–sulfur bond. In *Elemental Sulfur, Chemistry and Physics* (B. Meyer, Ed.), pp. 301 – 326. Interscience, New York.

Sill, G. T. 1973. Reflection spectra of solids of planetary interest. *Commun. Lunar Planet. Lab.* **10**, 1 – 7.

Simonelli, D. P. and J. Veverka 1986. Disk– resolved photometry of Io. II. Opposition surges and normal reflectances. *Icarus* **66**, 428 – 454.

Smith, A., and W. B. Holmes 1905. On amorphous sulphur. III. The nature of amorphous sulphur and contributions to the study of the influence of foreign bodies on the behavior of supercooled melted sulphur. *J. Amer. Chem. Soc.* 27, 979 – 1013.

Smith, B. A., E. M. Shoemaker, S. W. Kieffer, and A. F. Cook II 1979a. The role of SO_2 in volcanism on Io. *Nature* **280**, 738 – 743.

Smith, B. A., L. A. Soderblom, R. Beebe, J. Boyce, G. Briggs, M. Carr, S. A. Collins, A. F. Cook II, G. E. Danielson, M. E. Davies, G. E. Hunt, A. Ingersoll, T. V. Johnson, H. Masursky, D. Morrison, T. Owen, C. Sagan, E. M. Shoemaker, R. Strom, V. E. Suomi, and J. Veverka 1979b. The Galilean satellites and Jupiter: Voyager 2 imaging science results. *Science* **206**, 927 – 950.

Smythe, W. D., R. M. Nelson, and D. B. Nash 1979. Spectral evidence for SO_2 frost or adsorbate on Io's surface. *Nature* **280**, 766.

Soderblom, L., T. Johnson, D. Morrison, E. Danielson, B. Smith, J. Veverka, A. Cook, C. Sagan, P. Kupferman, D. Pieri, J. Mosher, C. Avis, J. Gradie, and T. Clancy 1980. Spectrophotometry of Io: Preliminary Voyager I results. *Geophys. Res. Lett.* **7**, 963 – 966.

Steudel, R. 1982. Homocyclic sulfur molecules. *Top. Curr. Chem.* **102**, 149 – 176.

Steudel, R., G. Holdt, and A.T. Young 1986. On the colors of Jupiter's satellite Io: Irradiation of solid sulfur at 77 K. *J. Geophys. Res.* **91**, 4971 – 4977.

Steudel, R., and B. Holz 1988. Detection of reactive sulfur molecules (S_6, S_7, S_9, S_∞) in commercial sulfur, in sulfur minerals, and in sulfur melts slowly cooled to 20°C. *Z. Naturforsch.* **43b**, 581 – 589.

Strom, R. G., N. M. Schneider, R. J. Terrile, A. F. Cook, and C. Hansen 1981. Volcanic eruptions on Io. *J. Geophys. Res.* **86**, 8593 – 8620.

Thackray, M. 1965. Phase transition rate measurements. In *Elemental Sulfur, Chemistry and Physics* (B. Meyer, Ed.), pp. 45 – 69. Interscience Publishers, New York.

Tobolsky, A. V., and A. Eisenberg 1959. Equilibrium polymerization of sulfur. *J. Amer. Chem. Soc.* **81**, 780 – 782.

Tobolsky, A. V., G. D. T. Owen, and A. Eisenberg 1962. Viscoelastic properties of S–Se–As copolymers. *J. Colloid Sci.* **17**, 717 – 725.

Tuinstra, F. 1967. *Structural Aspects of the Allotropy of Sulfur and the Other Divalent Elements.* Uitgeverij Waltman, Delft.

Tuller, W. N. (Ed.) 1954. *The Sulfur Data Book.* McGraw–Hill, New York.

Turnbull, D. 1956. Phase transformations. In *Solid State Physics* (F. Seitz and D.

Turnbull, Eds.), pp. 226 – 306. Academic Press, New York.

Verma, A. R., and P. Krishna 1966. *Polymorphism and Polytypism in Crystals,* pp. 7 – 60. Wiley, New York.

Veverka, J., D. Simonelli, P. Thomas, D. Morrison, and T.V. Johnson 1981. Voyager search for post–eclipse brightening on Io. *Icarus* **47**, 60 – 74.

Wamsteker, W. 1972. Narrow band photometry of the Galilean satellites. *Commun. Lunar Planet. Lab.* **167**, 171 – 177.

Wamsteker, W., R. L. Kroes, and J. A. Fountain 1974. On the surface composition of Io. *Icarus* **23**, 417 – 424.

Warren, B.E. and J.T. Burwell 1935. The structure of rhombic sulphur. *J. Chem. Phys.* **3**, 6 – 8.

Watanabe, T. 1940. Eruptions of molten sulphur from the Siretoko–Iôsan volcano, Hokkaidô, Japan. *Japan. J. Geol. Geog.* **17**, 289 – 310.

West, E.D. 1959. The heat capacity of sulfur from 25 to 450°, the heats and temperatures of transition and fusion. *J. Amer. Chem. Soc.* **81**, 29 – 37.

West, J. R. 1950. Thermodynamic properties of sulfur. *Ind. Eng. Chem. Soc.* **42**, 713 – 718.

West, W. A., and A. W. C. Menzies 1929. The vapor pressure of sulfur between 100° and 550° with related thermal data. *J. Phys. Chem.* **33**, 1880 – 1892.

Wilson, L., and J. W. Head III 1983. A comparison of volcanic eruption processes on Earth, Moon, Mars, Io and Venus. *Nature* **302**, 663 – 669.

Wiscombe, W. J. 1980. Improved Mie scattering algorithms. *Appl. Opt.* **19**, 1505 – 1509.

Young, A. T. 1984. No sulfur flows on Io. *Icarus* **58**, 197 – 226.

PAPER II

Photochemistry and Aerosol Formation in Neptune's Atmosphere

PHOTOCHEMISTRY AND AEROSOL FORMATION IN NEPTUNE'S ATMOSPHERE

Julianne I. Moses, Yuk L. Yung, and Mark Allen

Division of Geological and Planetary Sciences

California Institute of Technology

Pasadena, California 91125

Contribution number 4995 from the Division of Geological and Planetary Sciences,

California Institute of Technology, Pasadena, California 91125.

Abstract

Photodissociation of methane at high levels in Neptune's atmosphere leads to the production of more complex hydrocarbon species such as ethane, acetylene, methylacetylene, propane, diacetylene, and butane. These gases diffuse to the lower stratosphere where temperatures are low enough to allow all six of the aforementioned species to condense. Particle formation may not occur readily, however, as the vapor species become supersaturated. We present a theoretical analysis of particle formation mechanisms at conditions relevant to Neptune's troposphere and stratosphere and show that hydrocarbon nucleation is very inefficient under Neptunian conditions: saturation ratios much greater than unity are required for aerosol formation by either heterogeneous, ion–induced, or homogeneous nucleation. Homogeneous nucleation will not be important for any of the hydrocarbon species considered. The relative efficiencies of heterogeneous and ion–induced nucleation depend on the physical and thermodynamic properties of the particular species, the temperature at which the vapor becomes supersaturated, and the number and type of condensation nuclei or ions available. Typical saturation ratios required for significant particle formation range from 2 to 10 for methane in the upper troposphere to greater than 1000 for diacetylene in the lower stratosphere. Thus, stratospheric hazes may form far below their saturation levels. We compare nucleation models with detailed atmospheric photochemical models in order to place realistic constraints on the altitude levels at which we expect hydrocarbon hazes or clouds to form on Neptune.

1. Introduction

Hydrocarbon hazes in the upper troposphere and lower stratosphere of Neptune constitute a major stage in the evolution of carbon–bearing molecules in the atmosphere. Methane, which is relatively abundant in Neptune's deep atmosphere, provides the main source of carbon found in the photochemical hazes. Ultraviolet photolysis of methane in Neptune's upper atmosphere initiates the production of more complex hydrocarbon molecules. These molecules diffuse to the lower stratosphere where temperatures are low enough to evoke condensation of the less volatile species; consequently, haze layers form in the lower stratosphere. Carbon is ultimately lost from the stratosphere through precipitation of these haze particles. A thorough understanding of the production mechanisms and nucleation rates of the condensates is necessary for the elucidation of vapor abundances, the details of the carbon recycling, and many other aspects of atmospheric photochemistry on Neptune.

Evidence confirming the presence of particulate scatterers in Neptune's atmosphere originates from ground–based and Earth–orbiting ultraviolet, visible, and near–infrared observations of Neptune (see reviews by Trafton 1981, Caldwell *et al.* 1984, Bergstralh and Baines 1984, and Orton and Appleby 1984). The ultraviolet observations are somewhat inconclusive with regard to hazes; Neptune's geometric albedo at 2100 to 2800 Å is very similar to that expected from a purely molecular Rayleigh and Raman scattering atmosphere but drops below this ideal curve at wavelengths longer than 2800 Å (Wagener *et al.* 1986). Wagener and colleagues conclude that absorption from low altitude hazes is responsible for the 3000 to 4000 Å spectrum whereas Rayleigh scattering in a clear (aerosol–free) overlying gas dominates the shorter wavelength data. The visible and near–infrared regions of the spectrum provide more positive evidence for haze layers in Neptune's atmosphere. The effect of aerosol scattering shows up clearly as residual intensity in the strong near–infrared

methane bands (Fink and Larson 1979), and the geometric albedo of Neptune from 3500 to 10500 Å is best modeled by absorption and scattering from aerosol particles (Neff *et al.* 1984, Pollack *et al.* 1986, and Baines and Smith 1990).

Results from the *Voyager* photopolarimeter (PPS) experiment support the conclusion that an ultraviolet–absorbing haze exists on Neptune (Lane *et al.* 1989). Spatially resolved images of Neptune at 0.26 μm obtained with the PPS instrument indicate that a thin UV–absorbing haze is widespread across the planet. Distinct polar hazes are absent from these images, but haze absorption seems prevalent at equatorial latitudes. At longer wavelengths, the *Voyager* Imaging Science results (Smith *et al.* 1989) and the PPS images at 0.75 μm (Lane *et al.* 1989) reveal many spatially distinct features suggestive of clouds. These longer wavelength features (which are presumably at lower altitudes than the UV–absorbing hazes) are optically thin and seem to overlie a much more opaque cloud deck deeper in the planet's troposphere (Lane *et al.* 1989).

Several modelers have used Earth–orbiting satellite and ground–based observations to analyze the vertical structure and optical properties of the clouds and hazes on Neptune (e.g., Pollack *et al.* 1986, Hammel *et al.* 1989, and Baines and Smith *et al.* 1990). However, the numerous unknown free parameters involved in such radiative transfer modeling make detailed quantitative modeling very difficult. By simultaneously analyzing a multiwavelength dataset, Baines and Smith (1990) are able to derive the physical and optical properties of separate cloud and haze layers in Neptune's atmosphere. In their analysis, the stratosphere is probed by ultraviolet wavelengths and by the strong methane bands in the near infrared while the troposphere is probed by visible radiation and by the weaker methane bands. Parameters such as the stratospheric methane mixing ratio, the atmospheric temperature profile, and the stratospheric haze condensation levels are fixed in the models of Baines and

Smith. Parameters such as the column density, imaginary refractive index, and average radius of the stratospheric haze particles; the single–scattering albedo, optical depth, and pressure levels of the tropospheric clouds; and the methane mixing ratio of the deep atmosphere are constrained by their analysis. Such analyses are useful and ambitious, but the models can only be as accurate as the knowledge of the fixed parameters. In particular, the derived vertical structure of the clouds and hazes depends strongly on assumptions of the stratospheric methane mixing ratio and the locations of the stratospheric hazes.

Some of the free parameters needed for aerosol modeling can be constrained by photochemical models. For instance, recent theoretical models of photochemistry in Neptune's atmosphere help to pinpoint the location and composition of the photochemical hazes (Romani and Atreya 1988, 1989). These models predict that diacetylene (C_4H_2), acetylene (C_2H_2), and ethane (C_2H_6) will condense in the lower stratosphere below altitude levels corresponding to pressures of a few mbar. Romani and Atreya (1989) estimate the total stratospheric aerosol mass production rate to be on the order of 4×10^{-15} g cm^{-2} s^{-1} — a value that could easily lead to the production of optically thick haze layers in the stratosphere. Most of this production rate (75%) is found to result from ethane condensation (with 25% due to acetylene condensation and only trace amounts due to diacetylene condensation); the bulk of the aerosol mass is predicted to be located at altitudes below ~30 mbar in their model.

Although theoretical photochemical models such as those of Romani and Atreya (1988, 1989) can be used to gain information necessary for constraining many of the parameters needed in aerosol modeling (e.g., hydrocarbon vapor abundances, diffusion rates, and saturation levels), the models may not be reliable indicators of the levels at which the hazes will actually form on Neptune. Temperatures in Neptune's

lower stratosphere and upper troposphere are sufficiently below the triple points of several of the condensable hydrocarbon species that we do not expect to encounter supercooled liquids in the haze layers; instead, aerosol formation would proceed by direct nucleation of the ice phase (note that methane, ethane, and propane have triple points only ten degrees or so warmer than their expected condensation levels and may be exceptions to this statement about supercooled liquids). Formation of ice nuclei occurs at greater supersaturations than is typical with liquids because nucleation can proceed only by heterogeneous nucleation onto ions or *insoluble* particles; that is, ice nucleation cannot occur on *soluble* particles. Furthermore, ice nucleation on insoluble particles is only effective if the insoluble nuclei have a favorable crystal structure and/or morphology. More importantly, nucleation of both solid and liquid particles will be inefficient in Neptune's atmosphere because the low temperatures and saturation vapor pressures encountered in the saturation regions greatly inhibit the kinetics of particle formation and reduce the rates of all nucleation mechanisms. A good example of the inefficiency of nucleation at cold temperatures is the situation in the Earth's polar mesosphere where noctilucent clouds form only at saturation ratios of $\sim$ 100 (Arnold 1980, Gadsen 1981, Keesee 1989).

Because nucleation at stratospheric conditions on Neptune may be inefficient, the hazes may form at altitude levels significantly below those predicted by assuming that the hydrocarbon species condense as soon as the vapor becomes saturated. The purpose of this paper is to explore this hypothesis further. First (Section 2), we develop the photochemical models needed for accurate determinations of gas abundances. We consider the effect of including the chemistry of C_3 and C_4 species as well as the traditional C_1 and C_2 species. Besides the previously mentioned condensable hydrocarbons (C_2H_6, C_2H_2, and C_2H_4), we identify other species that have the potential to condense in Neptune's stratosphere. By comparing the photochemical model

results with ground–based and spacecraft observations, we attempt to constrain several properties of the Neptune atmosphere. In Section 3, we discuss nucleation theory in detail. In Section 4, we apply nucleation theory to our photochemical models of Neptune's troposphere and stratosphere developed in Section 2. We discuss the relative efficiencies of the various nucleation mechanisms, and determine the critical saturation ratios required for significant particle formation. We then estimate the levels at which we expect the methane clouds and stratospheric hazes to form on Neptune. Finally (Section 5), we summarize our principal conclusions and suggest directions for future research.

2. Photochemical Model

Atmospheric photochemistry of the outer planets has been a topic of much study in the past few decades (see reviews by Strobel 1985 and Atreya 1986). An early investigation of hydrocarbon chemistry in the Jovian atmosphere was presented by Cadle (1962). Strobel (1969, 1973) provided the basis for subsequent modeling. Recently, Gladstone *et al.* (1991) have presented the most detailed model of Jovian hydrocarbon photochemistry to date. Most of the modern photochemical studies of the outer planets (e.g., Romani and Atreya 1989, Summers and Strobel 1989, and Gladstone *et al.* 1991) take their basic hydrocarbon chemistry from a Titan study by Yung *et al.* (1984) with minor modifications suggested by new kinetic rate coefficients and reaction pathways. For Neptune, detailed photochemical models have been presented by Romani and Atreya (1988, 1989). Since the models of Romani and Atreya are based on pre–*Voyager* views of Neptune, we have refined the models to include updated hydrocarbon photochemistry (Gladstone *et al.* 1991) and recent *Voyager* observations (e.g., Broadfoot *et al.* 1989, Lindal *et al.* 1990) that help constrain the atmospheric temperature structure and diffusion coefficients. At the time of the writing of this paper, however, we have become aware of a more recent Neptune photochemical model. Bishop *et al.* (1991) have independently developed a model of Neptune's thermosphere and stratosphere for use in the reduction and analysis of *Voyager* UVS data. The similarities and differences among all the Neptune models will be discussed in Section 2.3.

2.1 Model Assumptions

Before we discuss our photochemical model in detail, we first consider the basic assumptions that have gone into the modeling. Inputs to the model include (1) the initial hydrostatic model atmosphere containing our first guesses of the composition,

mean molecular mass, density, temperature, and diffusion profiles as a function of altitude; (2) the details of the chemistry to be considered, (e.g., the specific chemical species, reactions, and rate constants); (3) the values of the molecular absorption cross sections as a function of wavelength for all the species in the model; and (4) the photon spectrum responsible for driving the photochemistry in the model. Our standard model Neptune atmosphere was constructed by solving the hydrostatic equation with assumed volume mixing ratios of 83.3% H_2, 14.7% He, and 2% CH_4 (*i.e.*, a He/H_2 ratio of 15/85); we also test models with helium mixing ratios of 19%. The molecular cross sections were taken from Gladstone *et al.* (1991). Our choice of temperature profile, eddy diffusion profile, ultraviolet radiation field, and boundary conditions are discussed below. The basic chemistry used in the model is discussed in Section 2.2.

Temperature profile

The thermal structure employed in our Neptune model atmosphere is illustrated in Fig. 1. Below 1 mbar, the temperature profile follows that derived from the *Voyager 2* ingress radio occultation (RSS) experiment (Lindal *et al.* 1990). Above 10^{-2} mbar, we have adopted two different profiles: (1) an isothermal atmosphere with a temperature of 155 K, consistent with the model upper atmosphere of Romani and Atreya (1988, 1989), and (2) a rapidly varying profile deduced from the ingress solar occultation experiment of the *Voyager* ultraviolet spectrometer (UVS) (Broadfoot *et al.* 1989). Both profiles are reasonably consistent with the 10^{-3} to 10^{-2} mbar temperatures derived from Earth-based stellar occultations of Neptune (French *et al.* 1983, 1985, Hubbard *et al.* 1985, 1987); however, the two profiles rapidly diverge above $\sim$1 μbar. Since methane dissociation occurs above the microbar region, the photochemical model may be sensitive to the choice of temperature in this thermospheric

region. We will occasionally refer to the UVS profile as our "warm" thermospheric model and the isothermal profile as our "cold" thermospheric model.

No direct information is available at this time concerning the temperature in the 10^{-1} to 1 mbar region. We have simply connected the upper and lower profiles (discussed above) by a curve that is approximately linear with log pressure (Fig. 1). Observations of an ethane emission line at 11.89 μm on Neptune (Kostiuk *et al.* 1990) suggest that the temperature in this pressure region on Neptune could be as much as 25 K warmer than our adopted profile. Such a small increase in temperature in this region of the atmosphere should have little effect on the chemistry in this region; moreover, the hydrocarbon condensation levels are well constrained by the RSS profile. However, temporal or spatial variations in the atmospheric thermal structure may affect our model results. In particular, changes in the exospheric temperature and location of heat input into the atmosphere may affect our photochemistry at high altitudes while changes in the lower stratospheric and upper tropospheric temperatures will change the locations at which we expect methane and other hydrocarbon species to condense.

Eddy diffusion

The choice of eddy diffusion coefficient is a difficult one. Very few observations constrain this parameter in Neptune's troposphere and stratosphere. The UVS observations in the CH_4 continuum region ($1106 < \lambda < 1189$ Å) suggest an eddy diffusion coefficient near 10^7 to 10^8 cm^2 s^{-1} in the 0.01 to 0.1 μbar region (Broadfoot *et al.* 1989). This range is consistent with UVS measurements of He 584 Å intensity at Neptune (Parkinson *et al.* 1990) that imply an eddy diffusion coefficient of $\sim 5 \times 10^7$ cm^2 s^{-1} at the homopause. To test the sensitivity of our photochemical

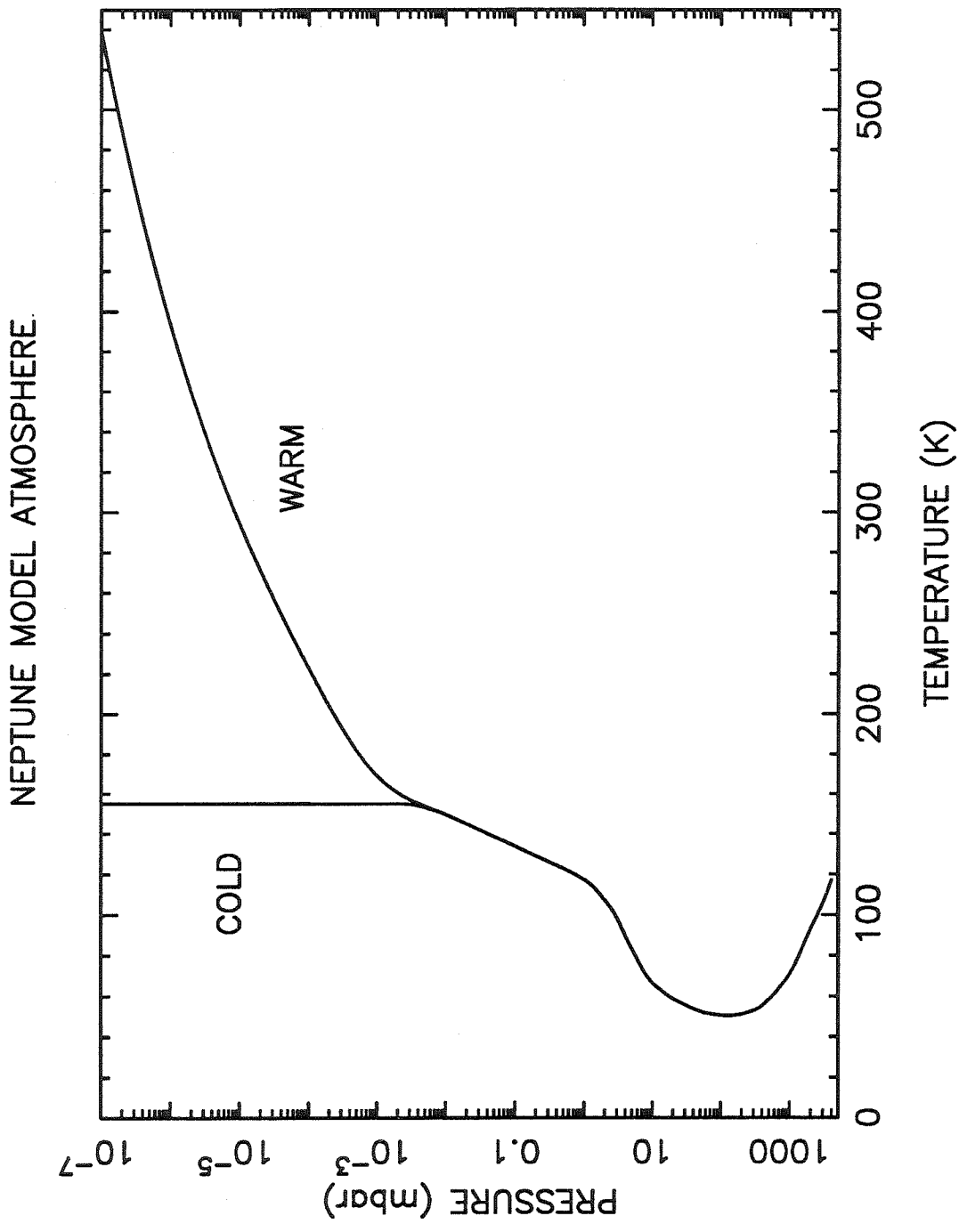

Figure 1. Temperature profiles used in our atmospheric models. The two profiles differ in the upper atmosphere: the isothermal profile will be called the "cold" model while the UVS profile will be called the "warm" model.

models to the eddy diffusion profile, we have chosen values that range from 10^6 to 10^8 in the 0.01 to 0.1 μbar region (see Fig. 2). We then let the eddy diffusion coefficient vary in the stratosphere as the inverse square root of the atmospheric number density, consistent with theoretical studies internal gravity–wave amplitudes in a stable atmosphere (e.g., Lindzen 1971). The methane homopause altitudes are also indicated in Fig. 2; note that increasing the eddy diffusion coefficients in the upper atmosphere decreases the relative importance of molecular diffusion and increases the homopause altitude.

The tropospheric diffusion values shown in Fig. 2 were derived assuming the upper troposphere is a free–convective regime. If the convection is dry, then we can use mixing–length theory to determine the diffusion coefficient, K. According to Stone (1976), the eddy diffusion coefficient can be approximated from the product of the characteristic vertical velocity of a convective cell with the characteristic vertical scale of the atmosphere ($\sim$ one scale height):

$$K = H\left(\frac{RF}{C_p n m}\right)^{1/3}$$

where H is the atmospheric scale height, R is the gas constant, F is the outgoing internal heat flux through the atmosphere, C_p is the specific heat of a parcel of gas at constant pressure, n is the atmospheric number density, and m is the mean molecular mass of the atmosphere. Consistent with Lunine and Hunten (1989), we use a value of 400 ergs cm^{-2} s^{-1} for the internal heat flux. The values of H, C_p, n, and m are determined from the solution to the hydrostatic equation for the atmospheric temperature profile shown in Fig. 1. At one bar, the atmospheric number density is $\sim 10^{20}$ cm^{-3}, $C_p/R \sim 4$, $m \sim 2.5$ amu, and $H \sim 20$ km, implying that $K \sim 10^8$.

The method described above may have caused us to incorrectly estimate the eddy diffusion coefficient in the upper troposphere. Since the temperature gradient above the few hundred mbar region is subadiabatic, the diffusion coefficient may be

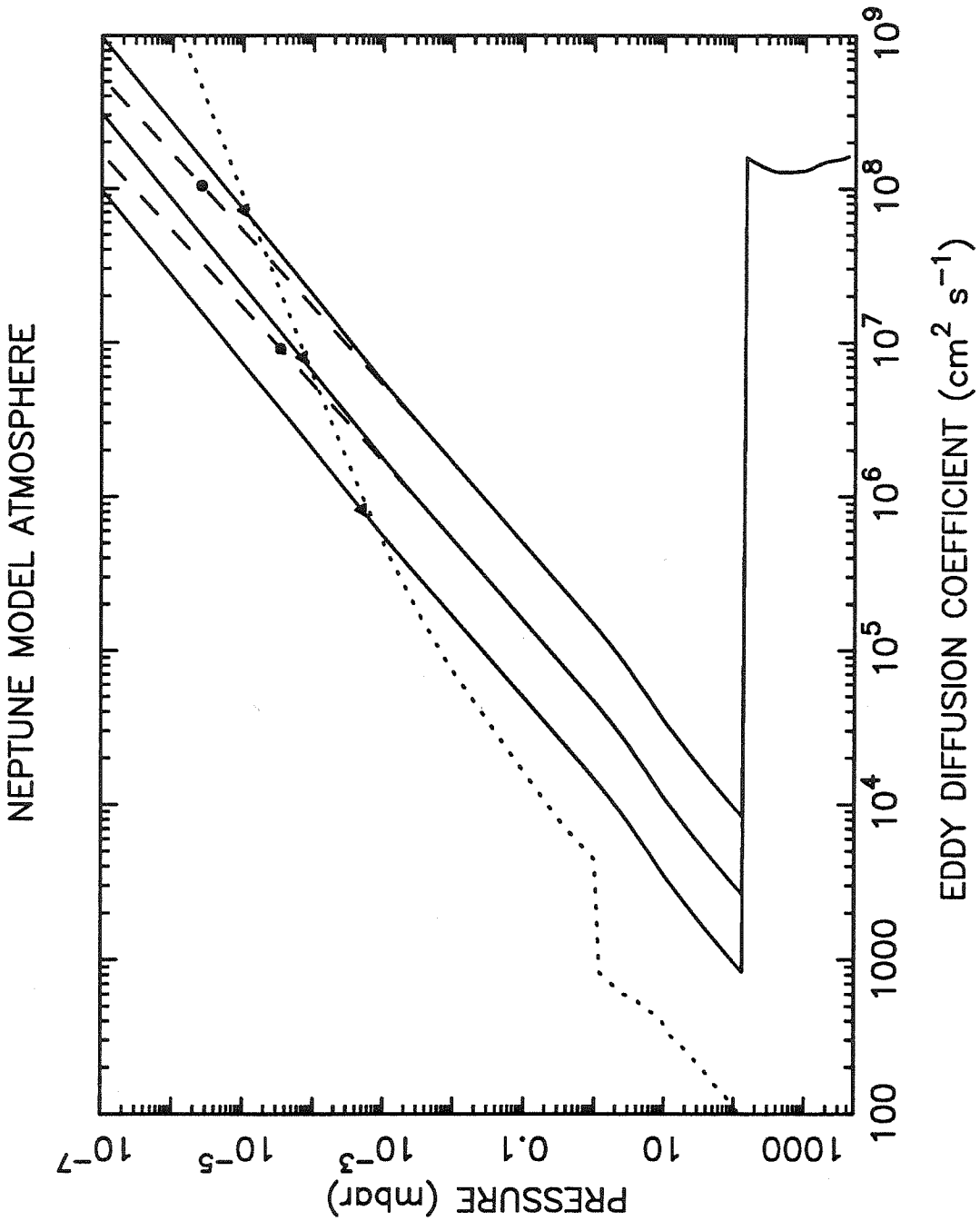

Figure 2. Some of the different eddy diffusion profiles used in our models. The solid lines refer to the "warm" temperature profile of Fig. 1 whereas the dashed lines refer to the "cold" profile. The individual points indicate the location of the methane homopause levels in our models. The dotted line is the molecular diffusion coefficient for the warm profile.

substantially less than 10^8 in this region. However, if methane is enhanced in the stratosphere over its saturation value near the tropopause as suggested by ground–based observations (e.g., Orton *et al.* 1983, 1987, 1990a) and radiative–equilibrium models (e.g., Appleby 1986), then strong vertical mixing (perhaps even greater than $K = 10^8$) must be present in this region (see the moist convection models of Lunine and Hunten 1989, Stoker and Toon 1989). Since the tropospheric diffusion coefficient can have a noticeable effect on the stratospheric profiles of minor species in the atmosphere (Hunten 1975, Landry *et al.* 1991), we have briefly examined the sensitivity of our models to the tropospheric value of K. The results are presented in Section 2.3.

Ultraviolet flux

The solar flux values used in our models were compiled from a variety of sources. Since the *Voyager 2* encounter with Neptune took place in August 1989 under active solar conditions, we use solar flux values representative of those near solar maximum in our modeling. The fluxes were binned in 20 Å intervals below 1225 Å (except for individual solar lines, which were assumed to be 1 Å wide), 50 Å intervals between 1225 and 4025 Å, and 100 Å intervals between 4025 and 8000 Å. From 50 to 290 Å, the flux was taken from the solar maximum (Feb. 1979) values of Torr and Torr (1985), and from 290 to 1085 Å, the flux was taken from a recent (November 1988) sounding rocket experiment (Woods and Rottman 1990). Between 1085 and 1175 Å, we estimate the flux in the manner of Gladstone *et al.* (1991); between 1175 and 3150 Å, we use data presented by Mount and Rottman (1983) from a May 1982 rocket experiment; between 3150 and 3300 Å, we use the rocket flight data from a September 1980 experiment (Mentall *et al.* 1981); and between 3300 and 8000 Å, we use values compiled by the World Meteorological Organization (Hudson *et al.* 1982).

The resulting solar flux spectrum at 30 AU is given in Fig. 3a. The conditions are not those of solar maximum itself but are typical of those encountered just before or just after solar maximum.

Special attention was given to the H Ly α flux at 1216 Å since this line is responsible for a large percentage of the methane dissociation and, hence, the photochemistry in Neptune's atmosphere. The solar value (at 1 AU) used in our models is 3.32×10^{11} photons cm^{-2} s^{-1} in a 1 Å interval centered at 1215.7 Å. This value is typical of those reported from rocket flight data (Woods and Rottman 1990) and from Solar Mesospheric Explorer satellite data for November, 1988; however, solar cycle 22 was still ascending towards its maximum at this time, and our value might be lower than that at the time of the *Voyager* Neptune encounter (August, 1989). To determine the sensitivity of our models to a variation in the solar ultraviolet flux, we let the solar flux vary between extreme solar maximum and solar minimum conditions. Further discussion of the solar flux and its effect on Neptune photochemistry can be found in Section 2.3.

We also examine the effect of interstellar ultraviolet radiation on our model. At Neptune's large distance from the sun, the contribution from interstellar sources becomes nontrivial (e.g., Strobel *et al.* 1990). We estimate the average interstellar radiation intensity (erg cm^{-2} s^{-1} μm^{-1}) from the method of Mathis *et al.* (1983):

$$
\begin{aligned}
4\pi J_\lambda &= 0 && \text{for } 0 < \lambda < 912 \text{ Å} \\
&= 38.57\ \lambda_{\mu m}^{3.4172} && \text{for } 912 < \lambda < 1100 \text{ Å} \\
&= 2.045 \times 10^{-2} && \text{for } 1100 < \lambda < 1340 \text{ Å} \\
&= 7.115 \times 10^{-4}\ \lambda_{\mu m}^{-1.6672} && \text{for } 1340 < \lambda < 2500 \text{ Å} \\
&= 4\pi \left[W_1 B_\lambda(T_1) + W_2 B_\lambda(T_2) + W_3 B_\lambda(T_3) \right] && \text{for } \lambda > 2500 \text{ Å}
\end{aligned}
$$

where $B_\lambda(T)$ is the Planck function, $T_1 = 7500$ K, $T_2 = 4000$ K, $T_1 = 3000$ K, $W_1 =$

1.0×10^{-14}, $W_2 = 1.0 \times 10^{-13}$, and $W_3 = 4.0 \times 10^{-13}$. Fig. 3b shows the resulting interstellar spectrum. The interstellar values are generally much lower than the solar maximum flux values, except in the wavelength region 1000 to 1200 Å. Remember that the interstellar source is isotropic; absorption of the isotropic interstellar photons will lead to absorption peaks that are at higher altitudes in the atmosphere than absorption peaks from solar photons at the same wavelength.

More important to our Neptune models is the contribution from radiation scattered from H and He atoms in the interplanetary medium (Fig. 3b). Broadfoot *et al.* (1989) measured the H Ly α emission from the local interstellar medium and find a flux of approximately 3.4×10^8 photons cm^{-2} s^{-1} from this source. This value is almost identical to the solar value at 30 AU and indicates that scattering from the interplanetary medium should be included in all photochemical models of Neptune's atmosphere. Although Broadfoot *et al.* do not give values from local interstellar H Ly β and He 584 Å, we have estimated these fluxes from the Ly β/Ly α and He 584/Ly α ratios measured by Sandel *et al.* (1978).

Numerical model and boundary conditions

Chemical kinetics, ultraviolet radiation, and vertical transport control the vertical distribution of hydrocarbon species on Neptune as long as zonal and meridional transport of species is of minor importance. Therefore, to estimate the concentrations of the condensable species in Neptune's stratosphere, we have solved the coupled one–dimensional continuity equations for all the major carbon–bearing species in Neptune's atmosphere:

$$\frac{\partial n_i}{\partial t} + \frac{\partial \Phi_i}{\partial z} = P_i - L_i \qquad [1]$$

where z is the altitude, t is time, n_i is the concentration (number density, molecules

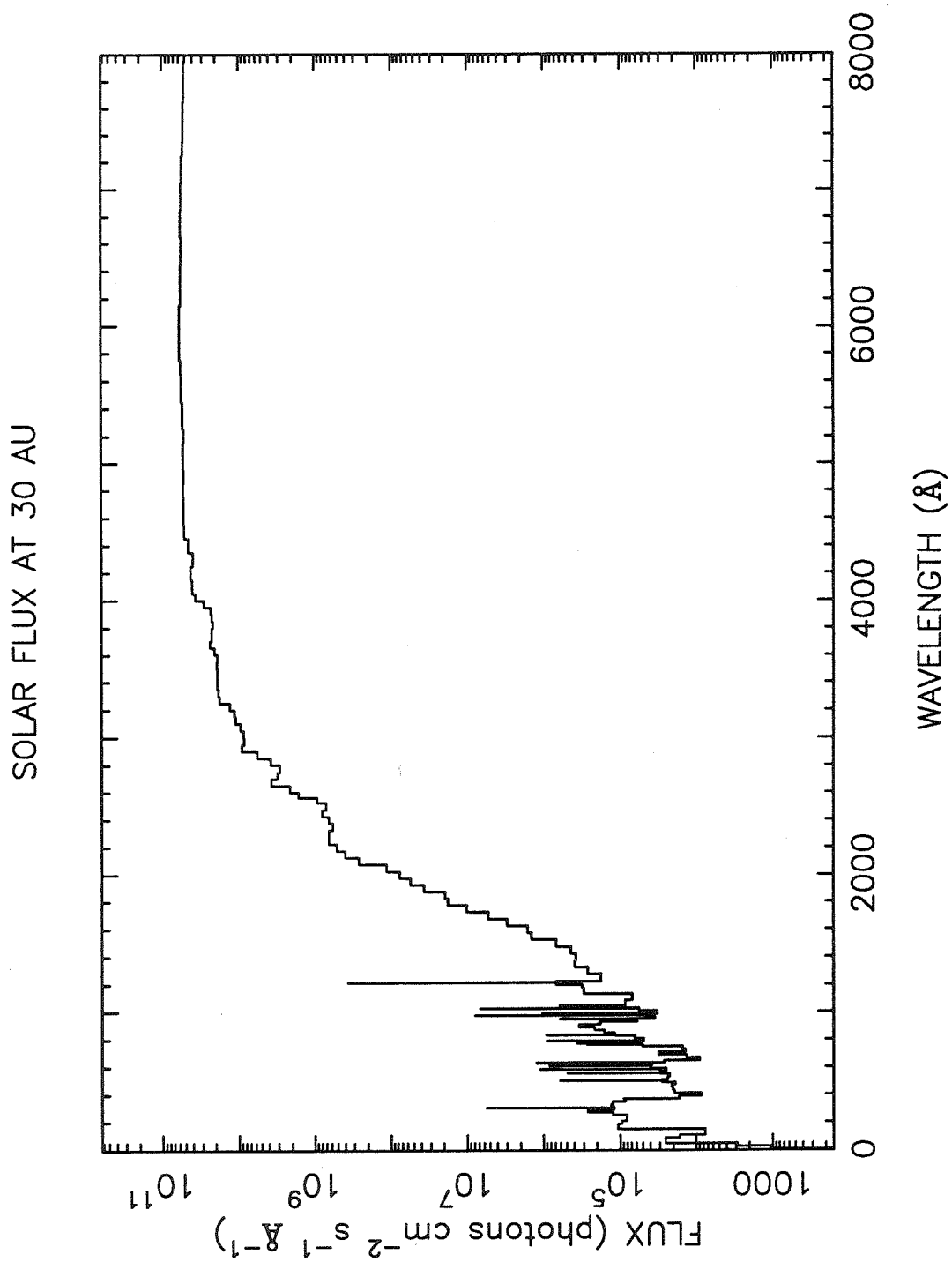

Figure 3a. The solar flux values used in our models.

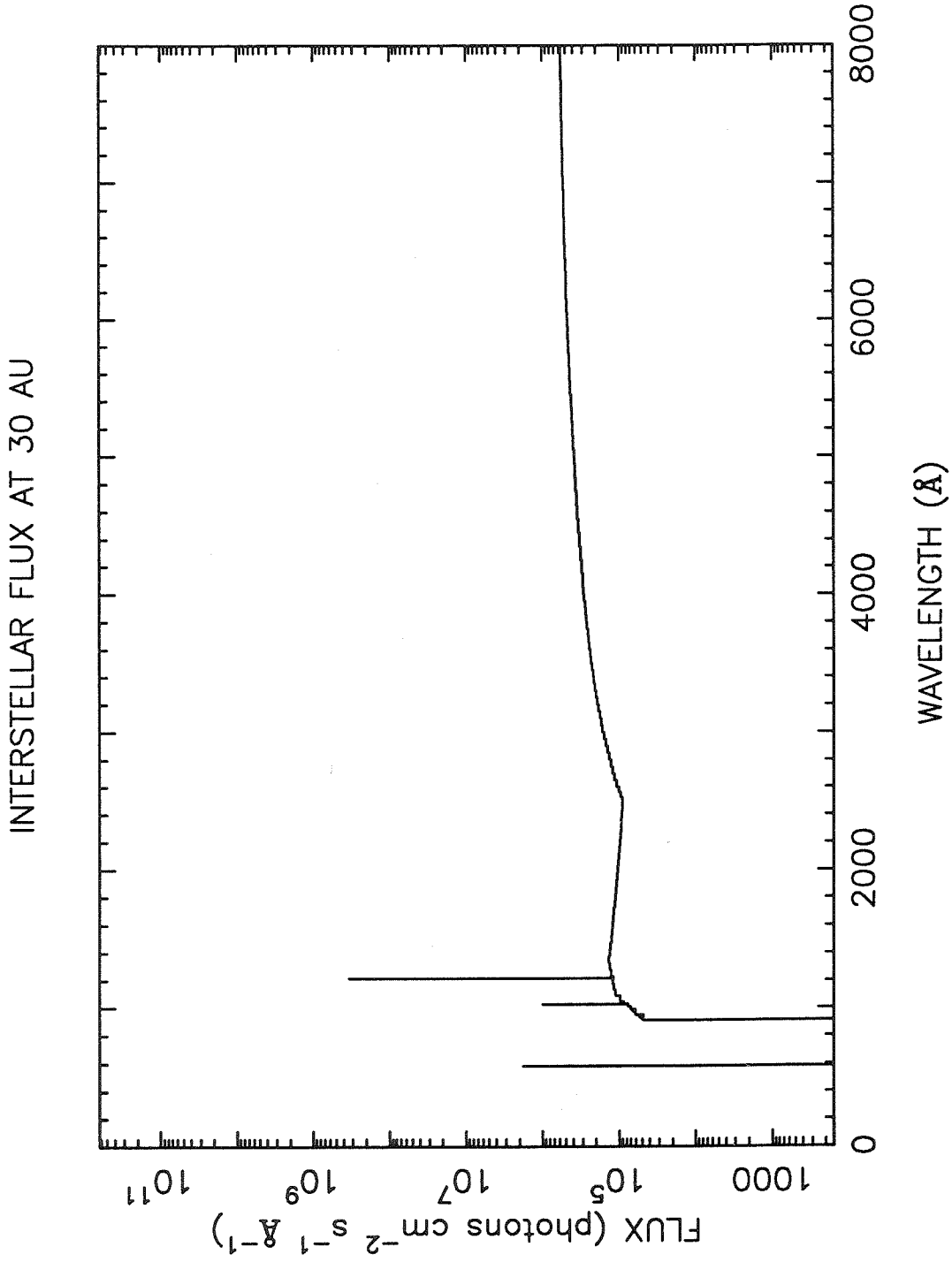

Figure 3b. The local interstellar flux values used in our models. The three individual lines are from scattering from local helium and hydrogen atoms: He 584 Å, H Ly β, and H Ly α.

cm^{-3}) of the i-th species, P_i and L_i are the local chemical production and loss rates of the i-th species (molecules cm^{-3} s^{-1}), and Φ_i is the flux of the i-th species (molecules cm^{-2} s^{-1}). We examine only steady–state solutions to equation [1]; in other words, solutions where $\partial n_i/\partial t = 0$, so that P_i, L_i, and Φ_i are diurnally–averaged quantities. Both eddy and molecular diffusion are considered in the transport terms:

$$\Phi_i = - n_i D_i \left(\frac{1}{n_i}\frac{dn_i}{dz} + \frac{1}{H_i} + \frac{(1+\alpha_i)}{T}\frac{dT}{dz} \right) - n_i K \left(\frac{1}{n_i}\frac{dn_i}{dz} + \frac{1}{H} + \frac{1}{T}\frac{dT}{dz} \right)$$

where D_i is the molecular diffusion coefficient, H_i is the density scale height of the i-th constituent, H is the average atmospheric (density) scale height, T is the temperature, α_i is the thermal diffusion factor, and K is the eddy diffusion coefficient.

The coupled equations [1] are solved using finite–difference techniques (e.g., Allen *et al.* 1981) with 139 atmospheric levels and a vertical resolution of at least three levels per scale height; the resolution in the stratosphere is even higher: $\gtrsim 5$ levels per scale height. Calculations were performed until successive iterations differed by no more than one part in 1000. A total of 38 different species are allowed to vary with vertical transport and with 194 different chemical reactions. Of these 194 reactions, 78 involve photodissociation. We assume that only the long–lived species contribute noticeably to atmospheric opacity (e.g., H_2, CH_4, C_2H_2, C_2H_4, C_2H_6, C_3H_8, C_4H_2, C_4H_{10}, and C_6H_2).

At the lower boundary (4 bar), the volume mixing ratios of He and CH_4 are fixed at 14.7% and 2%, respectively. All other species are assumed to have a zero concentration gradient at the lower boundary so that the species are transported through the lower boundary at a maximum possible velocity given by the diffusion coefficient divided by the atmospheric density scale height ($\sim$ 30 cm s^{-1}). At the upper boundary (10^{-7} mbar), most species are too heavy to escape thermally, and

other sources and sinks of the species are expected to be small above this level; thus, zero flux is assumed as an upper boundary condition for these species. However, atomic hydrogen is produced by ion chemistry higher up in the atmosphere and will diffuse down to lower levels. Consistent with Romani and Atreya (1988, 1989), we impose a downward flux of 4×10^7 atoms cm^{-2} s^{-1} for atomic hydrogen at the upper boundary.

To develop general models applicable to ground–based as well as *Voyager* observations, most of our model calculations have been performed at 30° N latitude at vernal equinox ($L_s = 0°$; subsolar point at the equator). This choice of latitude and season allows us to develop models with approximately seasonally–averaged sun angles. We have also examined the photochemistry at conditions relevant to the *Voyager* occultations; *i.e.*, 61° N and ~ 45° S latitude at $L_s = 243°$ (late spring in the southern hemisphere; the subsolar point is at 26° S latitude at this time).

2.2 Hydrocarbon Photochemistry

The hydrocarbon chemistry in our Neptune model is almost identical to that of the Jupiter model of Gladstone *et al.* (1991) and describes the sequence through which methane in the upper atmosphere is converted to 35 other possible different hydrocarbon species. Table I lists the formulas and common names of the species used in our models. We generally use the same nomenclature as in combustion studies; alternative names are provided. Aside from C_3H_4 and C_4H_6, we do not distinguish between different species with the same chemical formula (i.e., different isomers) in our reactions. For the major species, we provide the names of the more common isomers that may play a part in our reactions; however, our list of both names and isomers is not complete and is only included as an aid for the non-chemist. Table II lists the reactions used in this study; the rate coefficients and a thorough discussion of

the hydrocarbon photochemistry can be found in Gladstone *et al.* (1991). The photochemistry of C_1 and C_2 hydrocarbons in outer planetary atmospheres is discussed extensively in Gladstone (1983), Strobel (1985), and Atreya (1986); we will briefly outline the important reactions.

TABLE I

Chemical Formulas and Nomenclature

formula	name	alternative names
CH	methylidyne	methine, methenyl
$^3CH_2$	ground state methylene	
$^1CH_2$	excited methylene	
CH_3	methyl	
CH_4	methane	
C_2	diatomic carbon	
C_2H	ethynyl	
C_2H_2	acetylene	ethyne
C_2H_3	vinyl	ethenyl
C_2H_4	ethylene	ethene
C_2H_5	ethyl	
C_2H_6	ethane	
C_3H_2	propargylene	propynylidene
	allenylcarbene	propadienylidene
C_3H_3	propargyl	propynyl
	allenyl	propadienyl
CH_3C_2H	methylacetylene	propyne, allylene
CH_2CCH_2	allene	propadiene
C_3H_5	propenyl	
C_3H_6	propylene	propene
C_3H_7	propyl	
C_3H_8	propane	
C_4H	butadiynyl	
C_4H_2	diacetylene	1,3–butadiyne
C_4H_3	butenynyl	
	butatrienyl	
C_4H_4	vinyl acetylene	1–buten–3–yne
	butatriene	

TABLE I (*cont.*)

formula	name	alternative names
C_4H_5	butadienyl	
	butynyl	
$1-C_4H_6$	ethylacetylene	1–butyne
$2-C_4H_6$	dimethyl acetylene	2–butyne
$1,2-C_4H_6$	methylallene	1,2–butadiene
$1,3-C_4H_6$	bivinyl	1,3–butadiene
C_4H_7	butenyl	
C_4H_8	*cis*–2–butene	
	trans–2–butene	
	1–butene	
	isobutylene	2–methylpropene
C_4H_9	butyl	
C_4H_{10}	butane	*n*–butane
	isobutane	2–methylpropane
C_6H	hexatriynyl	
C_6H_2	hexatriyne	
C_6H_3	hexadiynyliumylidene	
C_6H_6	benzene	
C_8H_2	octatetrayne	

TABLE II

List of Reactions for Hydrocarbon Photochemistry on Neptune

	Reaction		
R1	$H_2 + h\nu$	$\rightarrow$	$2H$
R2	$^3CH_2 + h\nu$	$\rightarrow$	$CH + H$
R3	$CH_3 + h\nu$	$\rightarrow$	$CH + H_2$
R4		$\rightarrow$	$^1CH_2 + H$
R5	$CH_4 + h\nu$	$\rightarrow$	$^1CH_2 + H_2$
R6		$\rightarrow$	$^3CH_2 + 2H$
R7		$\rightarrow$	$CH + H + H_2$
R8	$C_2H_2 + h\nu$	$\rightarrow$	$C_2H + H$
R9		$\rightarrow$	$C_2 + H_2$
R10	$C_2H_3 + h\nu$	$\rightarrow$	$C_2H_2 + H$
R11	$C_2H_4 + h\nu$	$\rightarrow$	$C_2H_2 + H_2$
R12		$\rightarrow$	$C_2H_2 + 2H$
R13		$\rightarrow$	$C_2H_3 + H$
R14	$C_2H_5 + h\nu$	$\rightarrow$	$CH_3 + {}^1CH_2$
R15	$C_2H_6 + h\nu$	$\rightarrow$	$C_2H_4 + H_2$
R16		$\rightarrow$	$C_2H_4 + 2H$
R17		$\rightarrow$	$C_2H_2 + 2H_2$
R18		$\rightarrow$	$CH_4 + {}^1CH_2$
R19		$\rightarrow$	$2CH_3$
R20	$C_3H_3 + h\nu$	$\rightarrow$	$C_3H_2 + H$
R21	$CH_3C_2H + h\nu$	$\rightarrow$	$C_3H_3 + H$
R22		$\rightarrow$	$C_3H_2 + H_2$
R23	$CH_2CCH_2 + h\nu$	$\rightarrow$	$C_3H_3 + H$
R24		$\rightarrow$	$C_3H_2 + H_2$
R25	$C_3H_5 + h\nu$	$\rightarrow$	$CH_3C_2H + H$
R26		$\rightarrow$	$CH_2CCH_2 + H$
R27		$\rightarrow$	$C_2H_2 + CH_3$
R28	$C_3H_6 + h\nu$	$\rightarrow$	$C_3H_5 + H$

TABLE II (*cont.*)

	Reaction		
R29	$C_3H_6 + h\nu$	$\rightarrow$	$CH_3C_2H + H_2$
R30		$\rightarrow$	$CH_2CCH_2 + H_2$
R31		$\rightarrow$	$C_2H_4 + {}^1CH_2$
R32		$\rightarrow$	$C_2H_3 + CH_3$
R33		$\rightarrow$	$C_2H_2 + CH_4$
R34	$C_3H_8 + h\nu$	$\rightarrow$	$C_3H_6 + H_2$
R35		$\rightarrow$	$C_2H_6 + {}^1CH_2$
R36		$\rightarrow$	$C_2H_5 + CH_3$
R37		$\rightarrow$	$C_2H_4 + CH_4$
R38	$C_4H_2 + h\nu$	$\rightarrow$	$C_4H + H$
R39		$\rightarrow$	$C_2H_2 + C_2$
R40		$\rightarrow$	$2C_2H$
R41	$C_4H_4 + h\nu$	$\rightarrow$	$C_4H_2 + H_2$
R42		$\rightarrow$	$2C_2H_2$
R43	$1-C_4H_6 + h\nu$	$\rightarrow$	$C_4H_4 + 2H$
R44		$\rightarrow$	$C_3H_3 + CH_3$
R45		$\rightarrow$	$C_2H_5 + C_2H$
R46		$\rightarrow$	$C_2H_4 + C_2H + H$
R47		$\rightarrow$	$C_2H_3 + C_2H + H_2$
R48		$\rightarrow$	$2C_2H_2 + H_2$
R49	$1,2-C_4H_6 + h\nu$	$\rightarrow$	$C_4H_5 + H$
R50		$\rightarrow$	$C_4H_4 + 2H$
R51		$\rightarrow$	$C_3H_3 + CH_3$
R52		$\rightarrow$	$C_2H_4 + C_2H_2$
R53		$\rightarrow$	$C_2H_3 + C_2H_2 + H$
R54		$\rightarrow$	$C_2H_3 + C_2H + H_2$
R55		$\rightarrow$	$2C_2H_2 + H_2$
R56	$1,3-C_4H_6 + h\nu$	$\rightarrow$	$C_4H_5 + H$
R57		$\rightarrow$	$C_4H_4 + H_2$

TABLE II (*cont.*)

	Reaction		
R58	$1,3-C_4H_6 + h\nu$	$\rightarrow$	$C_3H_3 + CH_3$
R59		$\rightarrow$	$C_2H_4 + C_2H_2$
R60		$\rightarrow$	$2C_2H_3$
R61	$C_4H_8 + h\nu$	$\rightarrow$	$1,3-C_4H_6 + 2H$
R62		$\rightarrow$	$C_3H_5 + CH_3$
R63		$\rightarrow$	$CH_3C_2H + CH_4$
R64		$\rightarrow$	$CH_2CCH_2 + CH_4$
R65		$\rightarrow$	$C_2H_5 + C_2H_3$
R66		$\rightarrow$	$2C_2H_4$
R67		$\rightarrow$	$C_2H_2 + 2CH_3$
R68	$C_4H_{10} + h\nu$	$\rightarrow$	$C_4H_8 + H_2$
R69		$\rightarrow$	$C_3H_8 + {}^1CH_2$
R70		$\rightarrow$	$C_3H_6 + CH_4$
R71		$\rightarrow$	$C_3H_6 + CH_3 + H$
R72		$\rightarrow$	$C_2H_6 + C_2H_4$
R73		$\rightarrow$	$2C_2H_5$
R74		$\rightarrow$	$C_2H_4 + 2CH_3$
R75	$C_6H_2 + h\nu$	$\rightarrow$	$C_6H + H$
R76		$\rightarrow$	$C_4H + C_2H$
R77	$C_8H_2 + h\nu$	$\rightarrow$	$C_6H + C_2H$
R78		$\rightarrow$	$2C_4H$
R79	$2H + M$	$\rightarrow$	$H_2 + M$
R80	$H + {}^3CH_2$	$\rightarrow$	$CH + H_2$
R81	$H + {}^3CH_2 + M$	$\rightarrow$	$CH_3 + M$
R82	$H + CH_3 + M$	$\rightarrow$	$CH_4 + M$
R83	$H + CH_4$	$\rightarrow$	$CH_3 + H_2$
R84	$H + C_2H_2 + M$	$\rightarrow$	$C_2H_3 + M$
R85	$H + C_2H_3$	$\rightarrow$	$C_2H_2 + H_2$
R86	$H + C_2H_4 + M$	$\rightarrow$	$C_2H_5 + M$

TABLE II (*cont.*)

	Reaction		
R87	$H + C_2H_5$	$\rightarrow$	$2CH_3$
R88		$\rightarrow$	$C_2H_4 + H_2$
R89	$H + C_2H_5 + M$	$\rightarrow$	$C_2H_6 + M$
R90	$H + C_2H_6$	$\rightarrow$	$C_2H_5 + H_2$
R91	$H + C_3H_2 + M$	$\rightarrow$	$C_3H_3 + M$
R92	$H + C_3H_3 + M$	$\rightarrow$	$CH_3C_2H + M$
R93		$\rightarrow$	$CH_2CCH_2 + M$
R94	$H + CH_3C_2H + M$	$\rightarrow$	$CH_3 + C_2H_2 + M$
R95		$\rightarrow$	$C_3H_5 + M$
R96	$H + CH_2CCH_2 + M$	$\rightarrow$	$CH_3 + C_2H_2 + M$
R97		$\rightarrow$	$C_3H_5 + M$
R98	$H + CH_2CCH_2$	$\rightarrow$	$CH_3C_2H + H$
R99	$H + C_3H_5$	$\rightarrow$	$CH_3C_2H + H_2$
R100		$\rightarrow$	$CH_2CCH_2 + H_2$
R101		$\rightarrow$	$CH_4 + C_2H_2$
R102	$H + C_3H_5 + M$	$\rightarrow$	$C_3H_6 + M$
R103	$H + C_3H_6$	$\rightarrow$	$C_3H_5 + H_2$
R104	$H + C_3H_6 + M$	$\rightarrow$	$C_3H_7 + M$
R105	$H + C_3H_7$	$\rightarrow$	$C_3H_6 + H_2$
R106		$\rightarrow$	$C_2H_5 + CH_3$
R107	$H + C_3H_7 + M$	$\rightarrow$	$C_3H_8 + M$
R108	$H + C_3H_8$	$\rightarrow$	$C_3H_7 + H_2$
R109	$H + C_4H_2 + M$	$\rightarrow$	$C_4H_3 + M$
R110	$H + C_4H_3$	$\rightarrow$	$2C_2H_2$
R111		$\rightarrow$	$C_4H_2 + H_2$
R112	$H + C_4H_5$	$\rightarrow$	$C_4H_4 + H_2$
R113	$H + C_4H_5 + M$	$\rightarrow$	$1\text{-}C_4H_6 + M$
R114	$H + C_4H_9$	$\rightarrow$	$C_4H_8 + H_2$
R115	$H + C_6H_2 + M$	$\rightarrow$	$C_6H_3 + M$

TABLE II (*cont.*)

	Reaction		
R116	$H + C_6H_3$	$\rightarrow$	$C_2H_2 + C_4H_2$
R117		$\rightarrow$	$C_6H_2 + H_2$
R118	$CH + H_2$	$\rightarrow$	$^3CH_2 + H$
R119	$CH + H_2 + M$	$\rightarrow$	$CH_3 + M$
R120	$CH + CH_4$	$\rightarrow$	$C_2H_4 + H$
R121	$CH + C_2H_2$	$\rightarrow$	$C_3H_2 + H$
R122	$CH + C_2H_4$	$\rightarrow$	$CH_2CCH_2 + H$
R123	$CH + C_2H_6$	$\rightarrow$	$C_3H_6 + H$
R124	$^1CH_2 + H_2$	$\rightarrow$	$^3CH_2 + H_2$
R125		$\rightarrow$	$CH_3 + H$
R126	$^1CH_2 + CH_4$	$\rightarrow$	$^3CH_2 + CH_4$
R127		$\rightarrow$	$2CH_3$
R128	$2\ ^3CH_2$	$\rightarrow$	$C_2H_2 + 2H$
R129	$^3CH_2 + CH_3$	$\rightarrow$	$C_2H_4 + H$
R130	$^3CH_2 + CH_4$	$\rightarrow$	$2CH_3$
R131	$^3CH_2 + C_2H_2$	$\rightarrow$	$C_3H_2 + H_2$
R132		$\rightarrow$	$C_3H_3 + H$
R133	$^3CH_2 + C_2H_5$	$\rightarrow$	$CH_3 + C_2H_4$
R134	$CH_3 + H_2$	$\rightarrow$	$CH_4 + H$
R135	$2CH_3 + M$	$\rightarrow$	$C_2H_6 + M$
R136	$CH_3 + C_2H_3$	$\rightarrow$	$CH_4 + C_2H_2$
R137		$\rightarrow$	$C_3H_5 + H$
R138	$CH_3 + C_2H_3 + M$	$\rightarrow$	$C_3H_6 + M$
R139	$CH_3 + C_2H_5$	$\rightarrow$	$CH_4 + C_2H_4$
R140	$CH_3 + C_2H_5 + M$	$\rightarrow$	$C_3H_8 + M$
R141	$CH_3 + C_3H_3 + M$	$\rightarrow$	$1,2-C_4H_6 + M$
R142		$\rightarrow$	$1-C_4H_6 + M$
R143	$CH_3 + C_3H_5$	$\rightarrow$	$CH_4 + CH_3C_2H$
R144		$\rightarrow$	$CH_4 + CH_2CCH_2$

TABLE II (*cont.*)

	Reaction		
R145	$CH_3 + C_3H_5 + M$	$\rightarrow$	$C_4H_8 + M$
R146	$CH_3 + C_3H_6 + M$	$\rightarrow$	$C_4H_9 + M$
R147	$CH_3 + C_3H_7$	$\rightarrow$	$CH_4 + C_3H_6$
R148	$CH_3 + C_3H_7 + M$	$\rightarrow$	$C_4H_{10} + M$
R149	$CH_3 + C_3H_8$	$\rightarrow$	$CH_4 + C_3H_7$
R150	$CH_3 + C_4H_5$	$\rightarrow$	$CH_4 + C_4H_4$
R151	$CH_3 + C_4H_5 + M$	$\rightarrow$	products
R152	$C_2 + H_2$	$\rightarrow$	$C_2H + H$
R153	$C_2 + CH_4$	$\rightarrow$	$C_2H + CH_3$
R154	$C_2H + H_2$	$\rightarrow$	$C_2H_2 + H$
R155	$C_2H + CH_4$	$\rightarrow$	$C_2H_2 + CH_3$
R156	$C_2H + C_2H_2$	$\rightarrow$	$C_4H_2 + H$
R157	$C_2H + C_2H_4$	$\rightarrow$	$C_4H_4 + H$
R158	$C_2H + C_2H_6$	$\rightarrow$	$C_2H_2 + C_2H_5$
R159	$C_2H + C_3H_8$	$\rightarrow$	$C_2H_2 + C_3H_7$
R160	$C_2H + C_4H_2$	$\rightarrow$	$C_6H_2 + H$
R161	$C_2H + C_4H_{10}$	$\rightarrow$	$C_2H_2 + C_4H_9$
R162	$C_2H + C_6H_2$	$\rightarrow$	$C_8H_2 + H$
R163	$C_2H + C_8H_2$	$\rightarrow$	products
R164	$C_2H_3 + H_2$	$\rightarrow$	$C_2H_4 + H$
R165	$C_2H_3 + C_2H_2 + M$	$\rightarrow$	$C_4H_5 + M$
R166	$2C_2H_3$	$\rightarrow$	$C_2H_4 + C_2H_2$
R167	$2C_2H_3 + M$	$\rightarrow$	$1,3-C_4H_6 + M$
R168	$C_2H_3 + C_2H_5$	$\rightarrow$	$2C_2H_4$
R169		$\rightarrow$	$C_2H_6 + C_2H_2$
R170		$\rightarrow$	$CH_3 + C_3H_5$
R171	$C_2H_3 + C_2H_5 + M$	$\rightarrow$	$C_4H_8 + M$
R172	$C_2H_5 + H_2$	$\rightarrow$	$C_2H_6 + H$
R173	$2C_2H_5$	$\rightarrow$	$C_2H_6 + C_2H_4$

TABLE II (*cont.*)

	Reaction		
R174	$2C_2H_5 + M$	$\rightarrow$	$C_4H_{10} + M$
R175	$C_3H_2 + C_2H_2$	$\rightarrow$	$C_4H_2 + {}^3CH_2$
R176	$C_3H_3 + C_2H_2$	$\rightarrow$	$C_4H_2 + CH_3$
R177	$C_3H_5 + H_2$	$\rightarrow$	$C_3H_6 + H$
R178	$C_3H_7 + H_2$	$\rightarrow$	$C_3H_8 + H$
R179	$C_4H + H_2$	$\rightarrow$	$C_4H_2 + H$
R180	$C_4H + CH_4$	$\rightarrow$	$C_4H_2 + CH_3$
R181	$C_4H + C_2H_2$	$\rightarrow$	$C_6H_2 + H$
R182	$C_4H + C_2H_6$	$\rightarrow$	$C_4H_2 + C_2H_5$
R183	$C_4H + C_4H_2$	$\rightarrow$	$C_8H_2 + H$
R184	$C_4H + C_6H_2$	$\rightarrow$	products
R185	$C_4H + C_8H_2$	$\rightarrow$	products
R186	$C_4H_5 + H_2$	$\rightarrow$	$1{-}C_4H_6 + H$
R187	$C_4H_5 + C_2H_2$	$\rightarrow$	$C_6H_6 + H$
R188	$C_6H + H_2$	$\rightarrow$	$C_6H_2 + H$
R189	$C_6H + CH_4$	$\rightarrow$	$C_6H_2 + CH_3$
R190	$C_6H + C_2H_2$	$\rightarrow$	$C_8H_2 + H$
R191	$C_6H + C_2H_6$	$\rightarrow$	$C_6H_2 + C_2H_5$
R192	$C_6H + C_4H_2$	$\rightarrow$	products
R193	$C_6H + C_6H_2$	$\rightarrow$	products
R194	$C_6H + C_8H_2$	$\rightarrow$	products

[a]M refers to any molecule in the background atmosphere.

[b]The term "products" is used when we choose not to distinguish between the products of a reaction; e.g., this situation arises when we consider the production of C_5 and higher-order hydrocarbons.

Since methane absorbs ultraviolet radiation below about 1500 Å and since H Ly α dominates the solar spectrum below this cutoff wavelength, the methane photochemistry is driven, to a large extent, by solar and interstellar Ly α radiation. The photolysis products of methane dissociation will react with other species to either ultimately recycle methane or to form the C_2 hydrocarbons ethane and ethylene. Although methane, being more abundant than the other hydrocarbons, will absorb most of the ultraviolet photons with wavelengths less than ~1500 Å and will help to shield ethane and ethylene somewhat from photolysis, both C_2H_6 and C_2H_4 have absorption cross sections significantly larger than methane at wavelengths longer than 1400 Å. Thus, ethane and ethylene will absorb some of the longer wavelength radiation ($\lambda > 1400$ Å) and will dissociate. Ethane can absorb out to ~1600 Å and ethylene out to ~2000 Å. Ethane is very stable, but its photolysis leads to either the recycling of methane or the formation of ethylene. Ethylene dissociates rapidly to produce C_2H_2 and to recycle methane. Acetylene has an appreciable cross section out to ~2200 Å; however, C_2H_2 photolysis products efficiently react back to form acetylene and, in the process, catalytically destroy H_2 in the upper atmosphere and CH_4 in the lower atmosphere.

At high altitudes, reaction of acetylene, ethane, and ethylene with the CH radical initiates the formation of higher–order C_3 and C_4 hydrocarbon species such as methylacetylene, propane, and butane. The principal pathways for forming the stable, potentially condensable, C_3 and C_4 species are illustrated in Fig. 4; the C_3 species shown in this figure are primarily formed by reactions R121, R122, R123, R138, and R140. The dominant loss of C_3 species is reaction with atomic hydrogen to reform C_2 species (R94, R101, R106) and formation of diacetylene from reaction with acetylene (R175, R176).

In the middle and lower stratosphere, diacetylene formation is also initiated

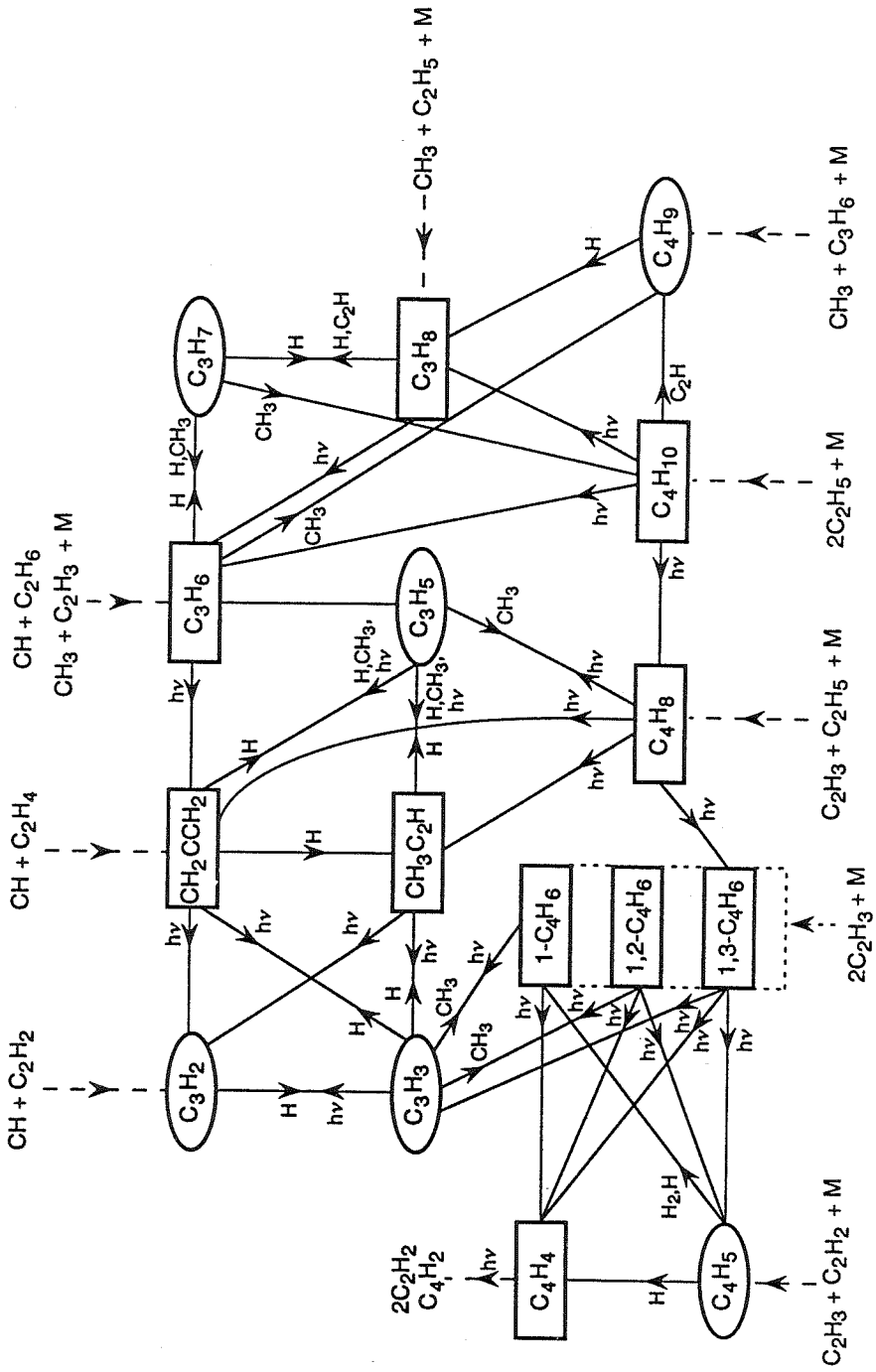

Figure 4. Schematic diagram illustrating the important reaction pathways for interconversion of C_3 and C_4 species. Diacetylene and its related products and pathways are not included in this diagram.

by the dissociation of acetylene (see R156). Reactions of C_4H_2 with C_2H and C_4H will, in turn, produce higher–order polyacetylenes (C_6H_2, C_8H_2, etc.) that are potentially important sources of condensates in the stratosphere. Thorough discussions of diacetylene photochemistry can be found in Romani and Atreya (1988), Summers and Strobel (1989), and Gladstone *et al.* (1991).

The list of C_3 and C_4 reactions in Table II is not complete, and many of the reaction rates and cross sections have not been measured at low temperatures. Thus, our photochemical results are only preliminary. Refinements to reaction pathways and rate constants await further laboratory investigations; however, the behavior of the principal C_3 and C_4 hydrocarbons should survive any minor changes. In addition, we have not considered the effect of nitrogen species in our model. If a significant source of atomic nitrogen is flowing in from the top of the atmosphere (e.g., from escape from Triton) then nitrogen chemistry needs to be included in the model. The dominant effect of including nitrogen will be to tie up some of the carbon in species such as HCN or CH_3NH_2; these species may also condense in the stratosphere.

Interactions of energetic charged particles with neutral atmospheric molecules can also lead to interesting hydrocarbon chemistry. Galactic and solar cosmic rays and particles from Neptune's magnetosphere will affect the production of higher–order hydrocarbons in the atmosphere. We have neglected the chemistry of charged–particle impact processes in this paper, but acknowledge that numerous laboratory simulations performed under conditions relevant to the stratospheres of Uranus and Neptune suggest that such processes may be important in determining the global chemistry on the outer planets (e.g., Thompson *et al.* 1987). We will briefly compare the predictions from our photochemical models with predictions from plasma discharge experiments.

2.3 Photochemical Model Results

Standard model

Our "standard model" (also called Model A) has a temperature profile illustrated by the "warm" profile in Fig. 1. The eddy diffusion coefficient is $\sim 10^7$ cm^2 s^{-1} at the homopause (0.05 μbar) and falls off with the inverse square root of the atmospheric density down to the tropopause; below the tropopause, the diffusion coefficient is calculated from free–convection theory (see section 2.1 and Fig. 2). The methane mixing ratio is taken to be 2% in the troposphere below the methane saturation level, but falls off with the saturation density profile in the upper troposphere, and then remains constant at 2×10^{-4} in the rest of the atmosphere. The temperature and diffusion profiles were chosen to be consistent with preliminary *Voyager* analyses reported by Broadfoot *et al.* (1989) and Lindal *et al.* (1990). Comparisons with observations and a discussion of the sensitivity of the results to changes in these parameters will be discussed later.

Our standard model calculations are performed for a diurnally–averaged atmosphere at 30° latitude and vernal equinox. Initially, all the carbon in the atmosphere is contained in methane. As methane becomes photolyzed in the upper atmosphere, radical species and higher–order hydrocarbons are formed. The resulting steady–state concentrations and mixing ratios of the major stable hydrocarbon species are shown in Figs. 5a – f. The mixing ratios of the radical species are shown in Figs. 6a – d. Many of the long–lived species are also dissociated by ultraviolet radiation — the photolysis rates (J–values) for these species are shown in Fig. 7.

In the following discussion, we often refer to certain atmospheric regions as the upper, middle, and lower atmosphere. Our use of these terms differs from terrestrial

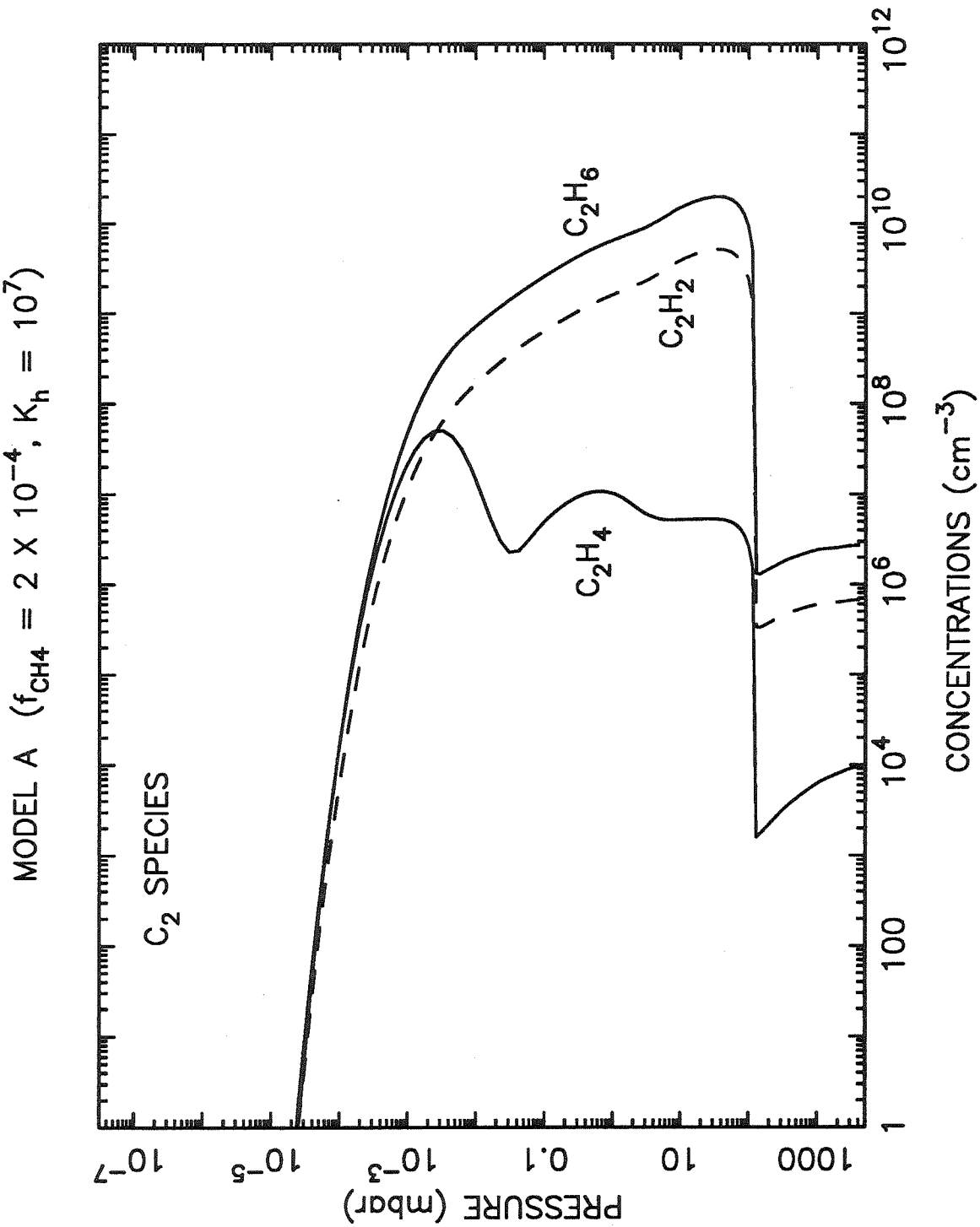

Figure 5a. Concentrations of the major C_2 species in our standard model.

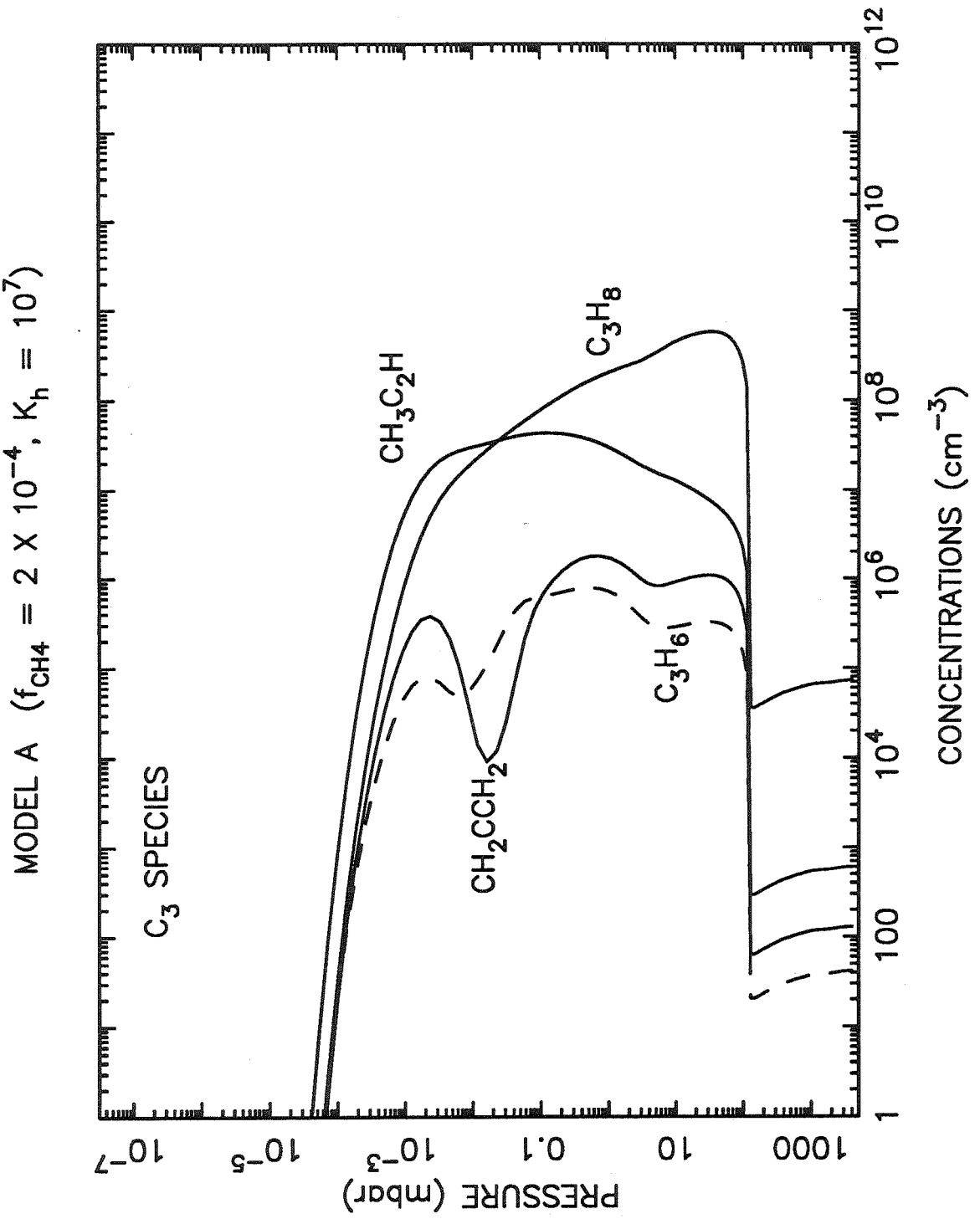

Figure 5b. Concentrations of the major C_3 species in our standard model.

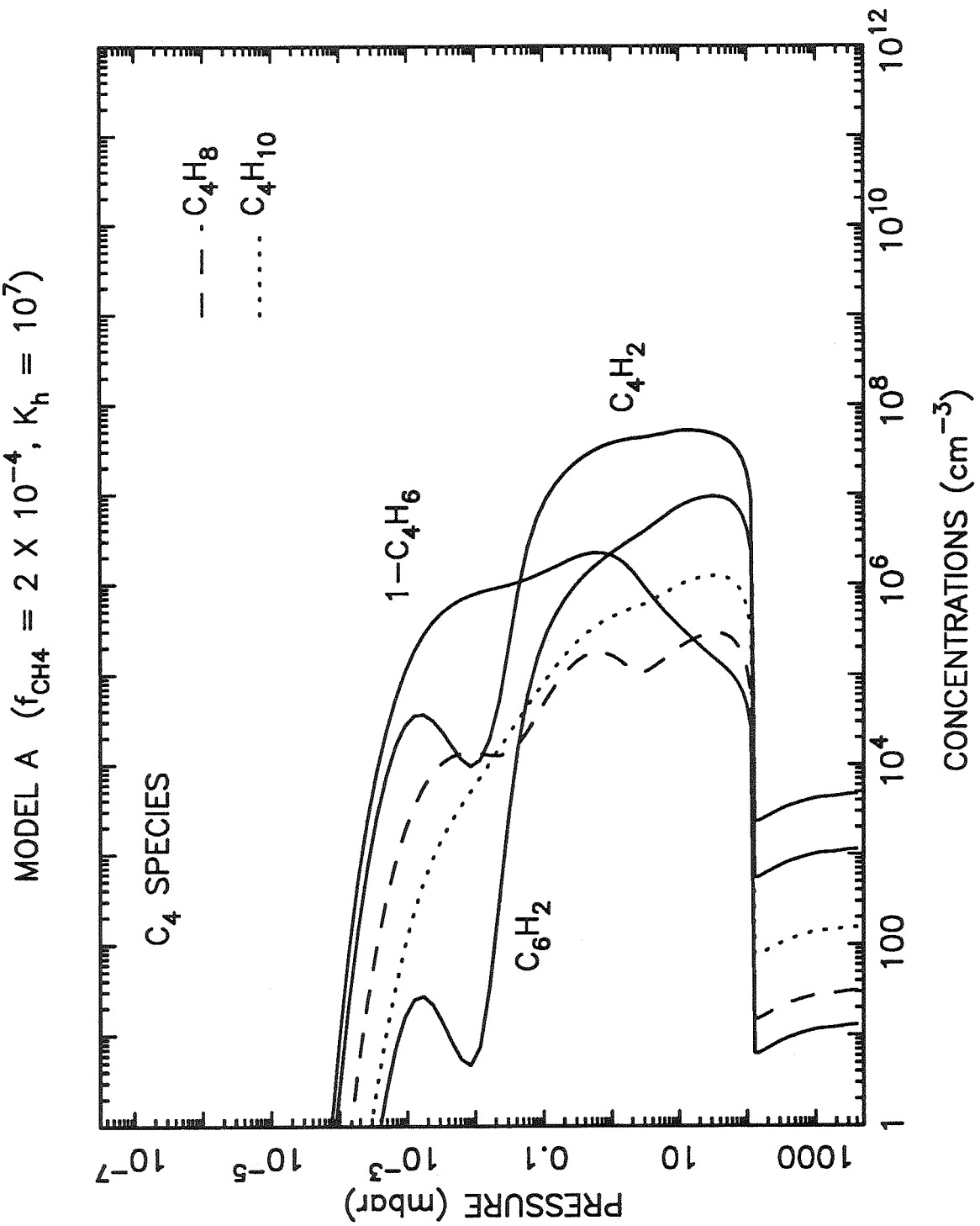

Figure 5c. Concentrations of the major C_4 species in our standard model.

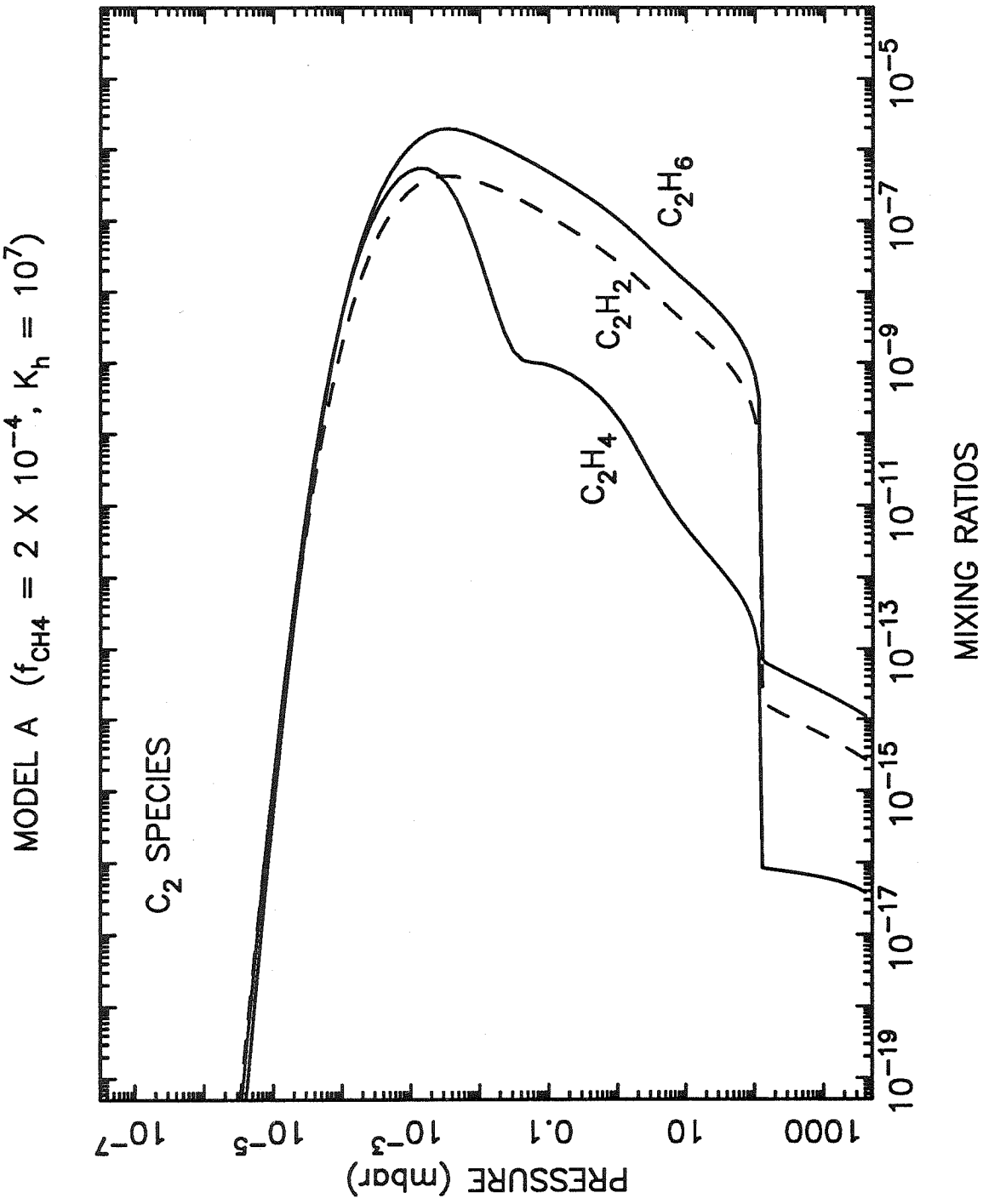

Figure 5d. Mixing ratios of the major C_2 species in our standard model.

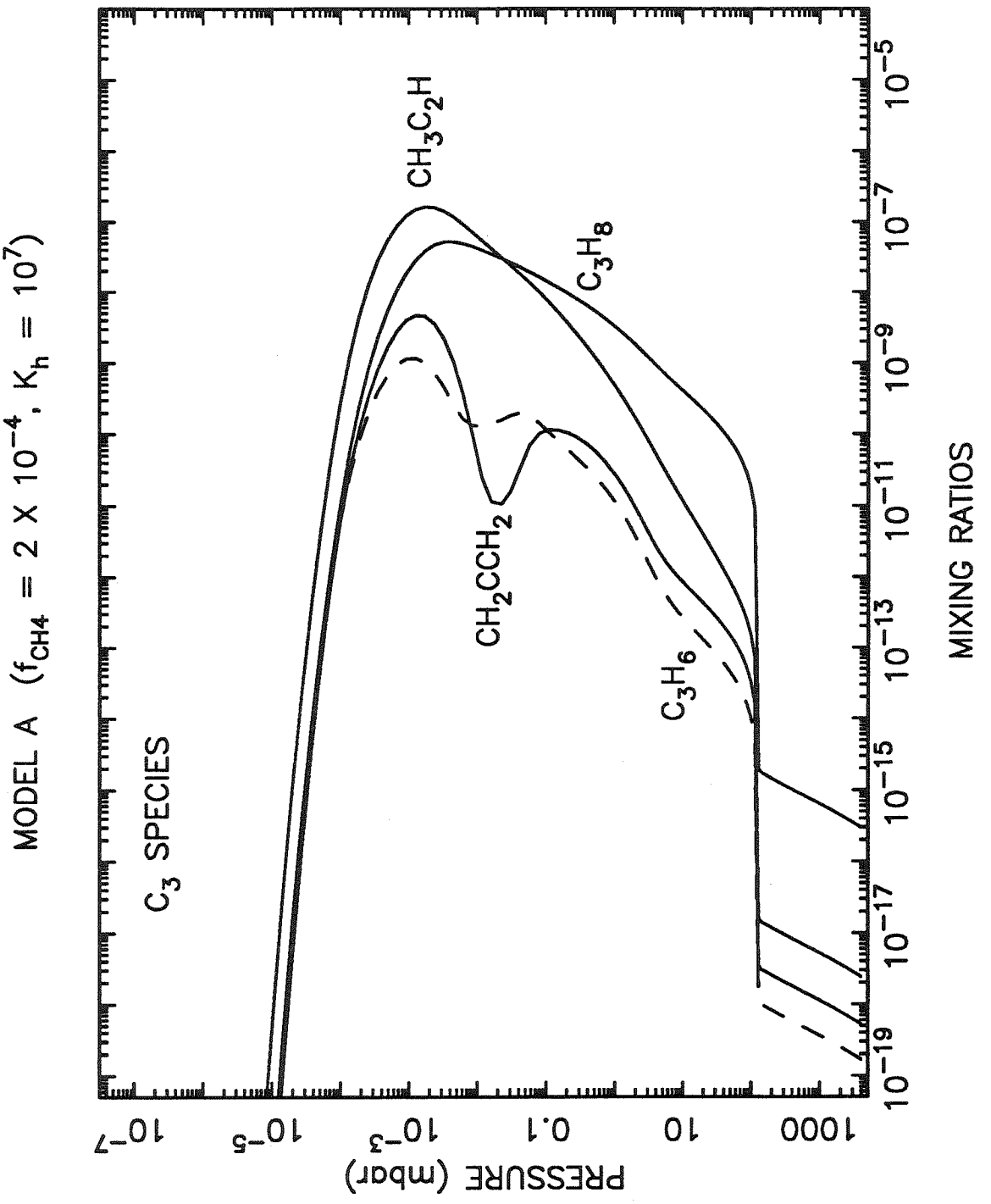

Figure 5e. Mixing ratios of the major C_3 species in our standard model.

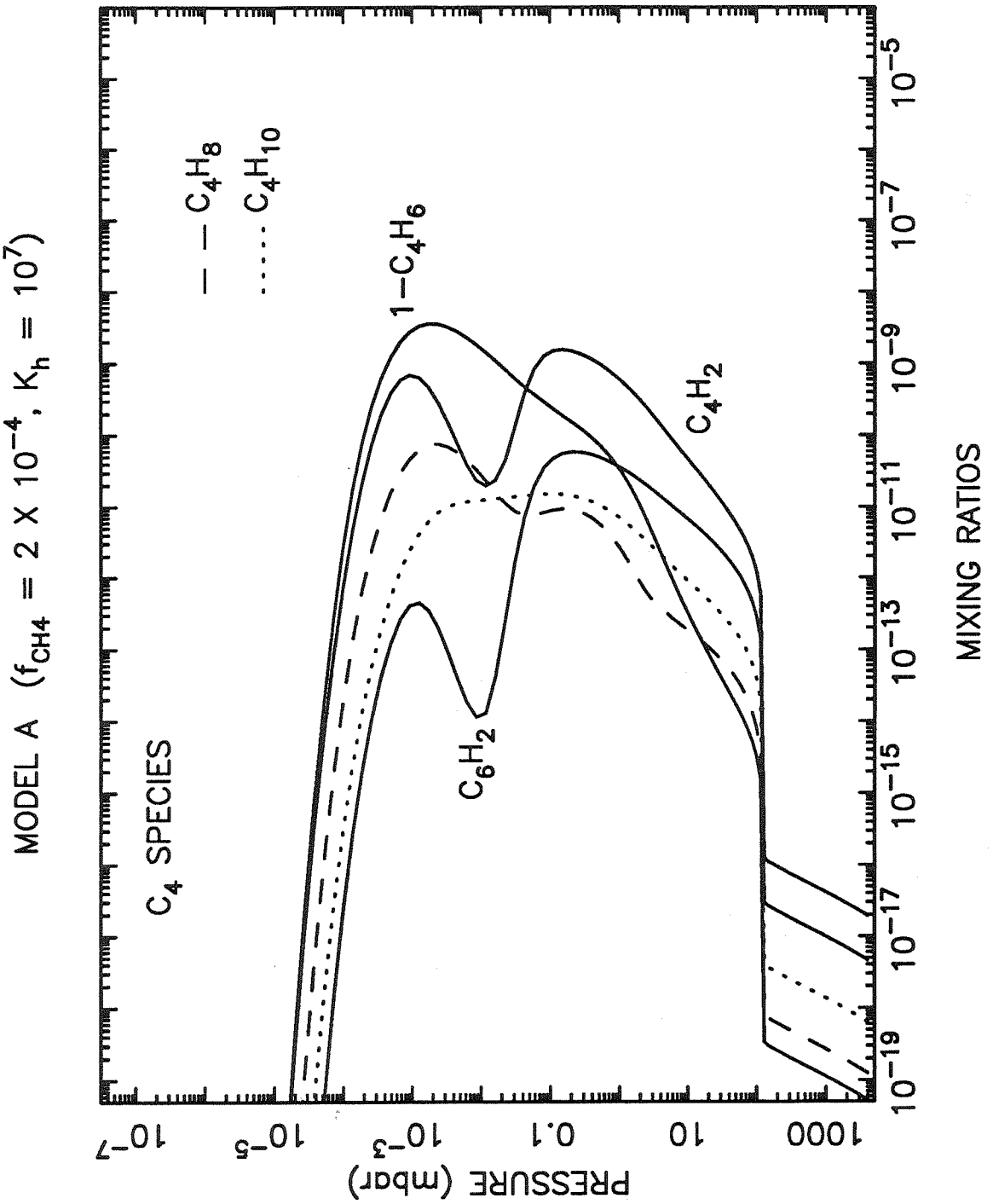

Figure 5f. Mixing ratios of the major C_4 species in our standard model.

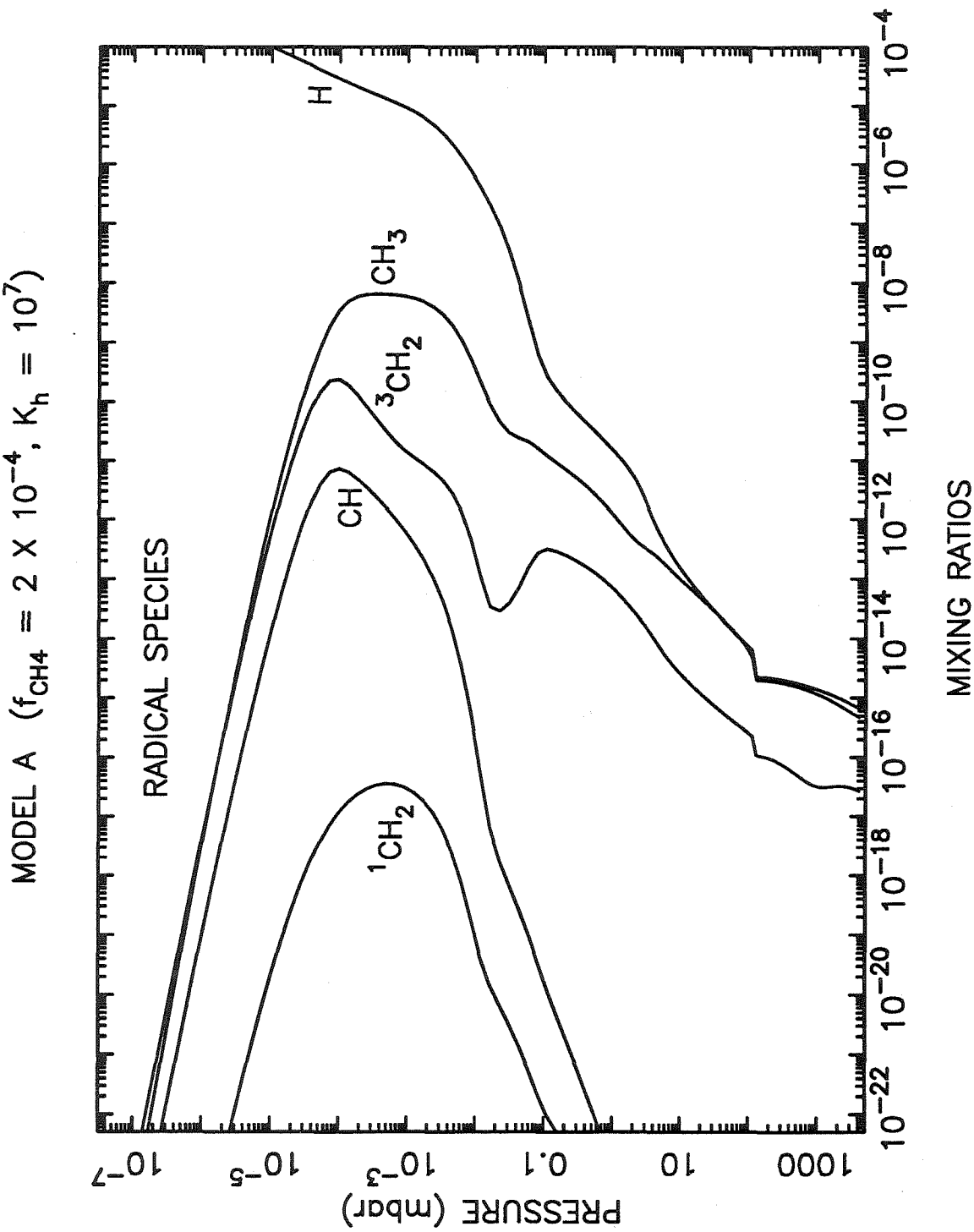

Figure 6a. Mixing ratios of atomic hydrogen and the C_1 radicals in our standard model.

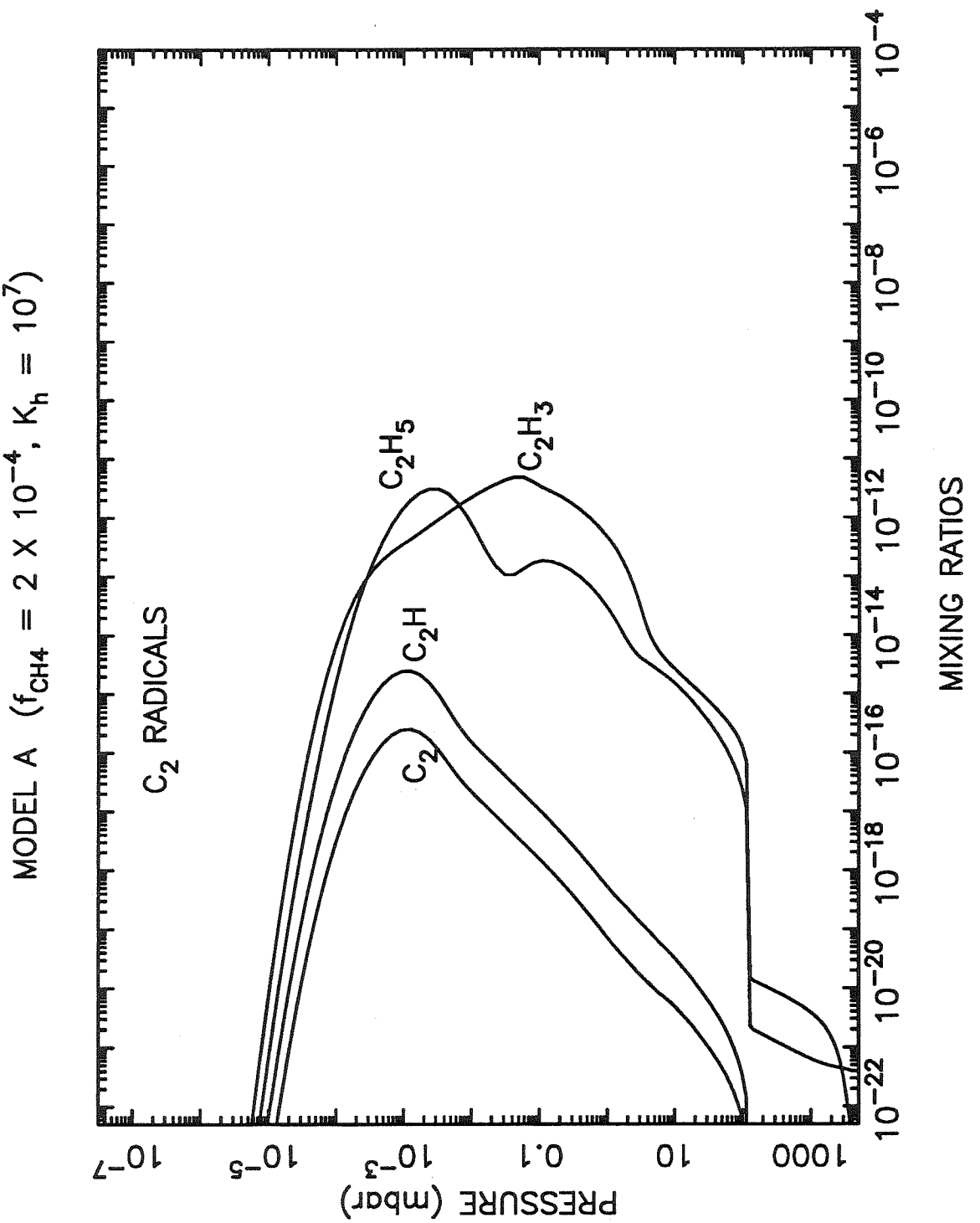

Figure 6b. Mixing ratios of the C_2 radicals in our standard model.

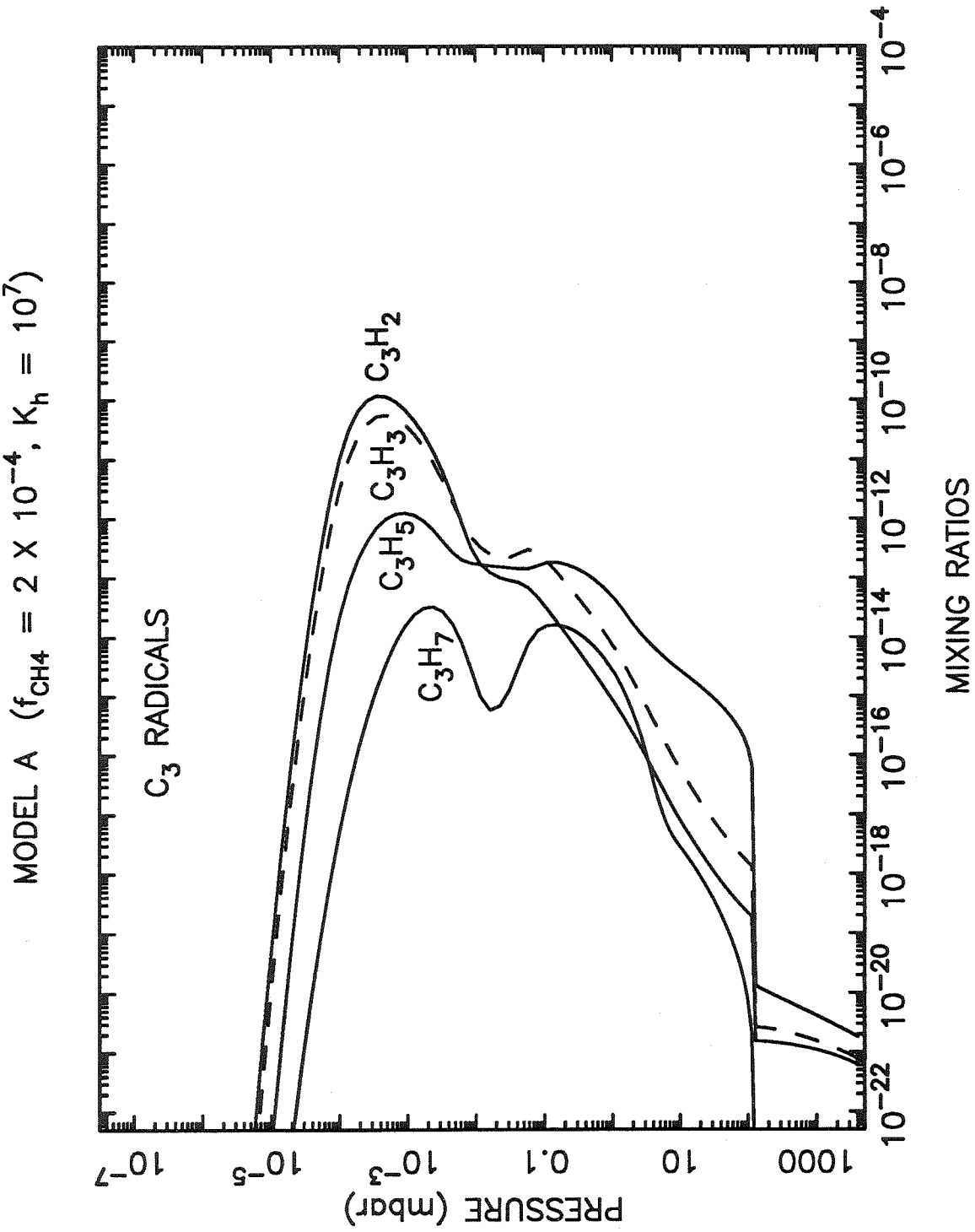

Figure 6c. Mixing ratios of the C_3 radicals in our standard model.

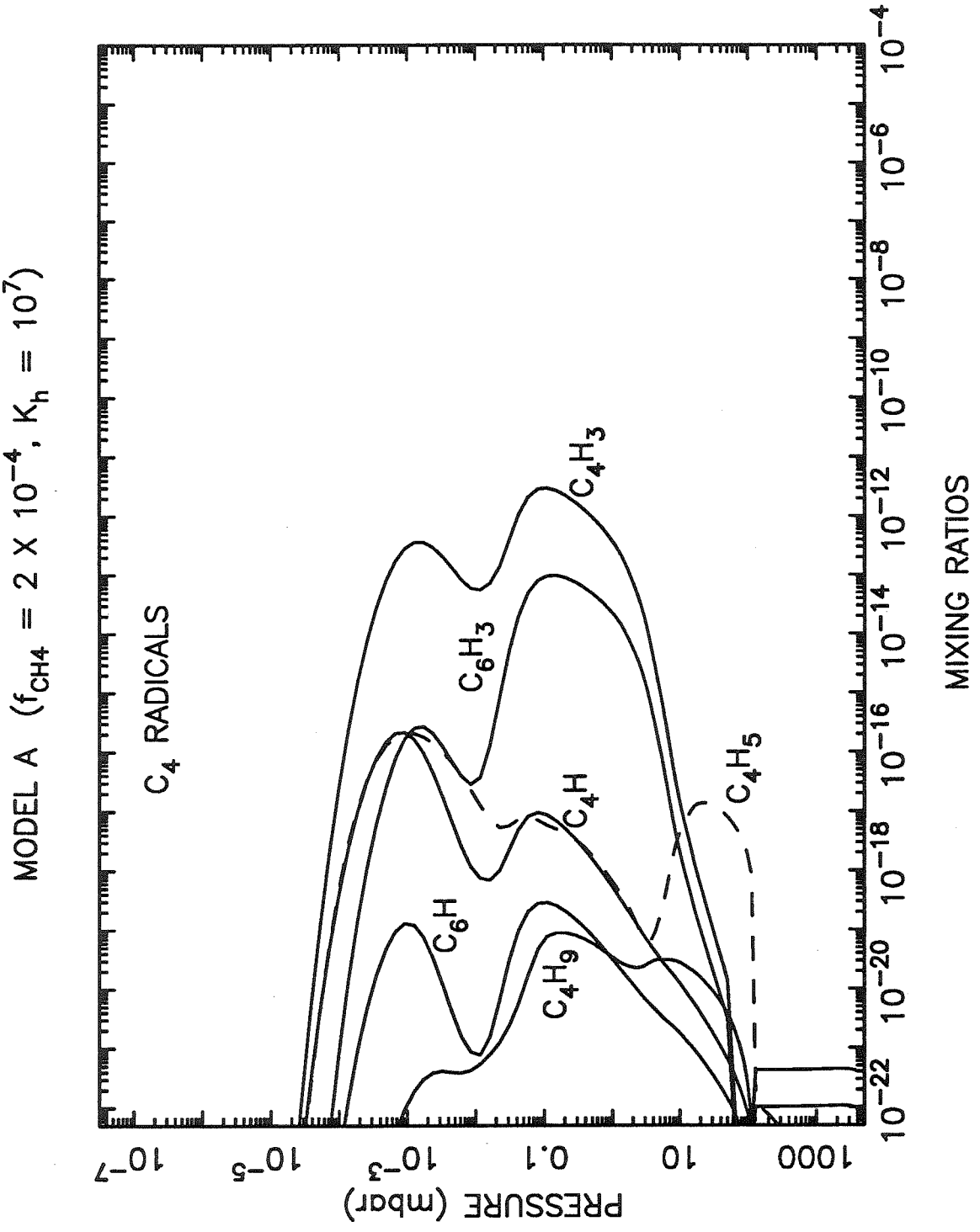

Figure 6d. Mixing ratios of the major C_4 and C_6 radicals in our standard model.

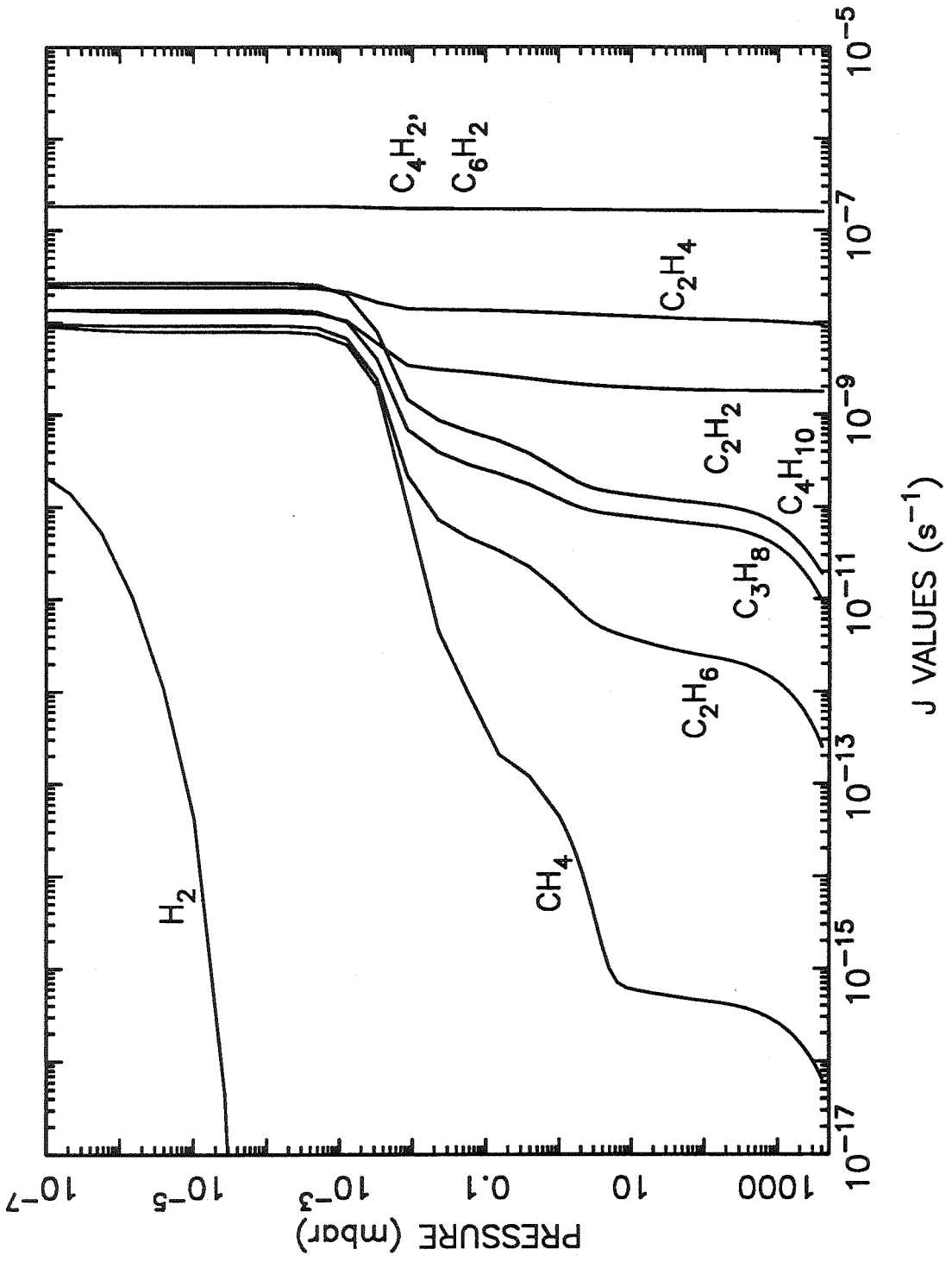

Figure 7. J–values for major atmospheric species in our standard model.

nomenclature. The "upper atmosphere" in our terminology corresponds to levels above $\sim 10^{-2}$ mbar and encompasses the thermosphere, the "middle atmosphere" corresponds to the upper stratospheric region between a few mbar and 10^{-2} mbar, and the "lower atmosphere" corresponds to lower stratospheric levels below a few mbar. Occasionally, we include the troposphere in our definition of lower atmosphere.

Methane is photolyzed for the most part by H Ly α radiation at the few μbar level. Most of the hydrocarbon photochemistry is initiated in this region, and most of the hydrocarbon species have peak mixing ratios at this location. However, the loss rate of CH_4 in our standard model has three peaks: (1) the dominant, high-altitude peak where methane is dissociated by H Ly α and other short wavelength radiation (see reactions R5, R6, and R7), (2) a smaller, broader peak in the middle and lower stratosphere where methane destruction is catalyzed by the photolysis products of acetylene and other species (see reactions R155 and R153), and (3) a secondary methane photolysis peak in the troposphere resulting from absorption of longer wavelength radiation (mainly by reaction R5). Even though the methane cross section is quite low in the 1500 Å region, the concentrations of the other hydrocarbon species are falling so rapidly in the lower atmosphere that the total column abundance of CH_4 is much larger than that of C_2H_2 or C_4H_2; therefore, ~1500 Å photons can reach the troposphere to be absorbed by methane. Methane absorbs 1450 Å photons at $\sim$ 1 mbar and 1500 Å photons at $\sim$ 1 bar.

The short-lived radical species produced by methane photolysis in the upper atmosphere will react to either form C_2 species or to recycle methane. Methane is recycled by reaction R82: $H + CH_3 + M \rightarrow CH_4 + M$. Of all the methane destroyed by photolysis and other reactions throughout the entire atmosphere, 42% is recycled by R82 and other reactions, 56% goes to making C_2 hydrocarbons, and ~1% goes to making C_3 and higher hydrocarbons. The only reactions that make C_2 hydrocarbons

from C_1 radicals are R120, R128, R129, and R135, the most important of these reactions being R120 ($CH + CH_4 \rightarrow C_2H_4 + H$) and R135 ($2CH_3 + M \rightarrow C_2H_6 + M$). The reactions that return C_2 hydrocarbons to C_1 radicals are R14, R18, R19, and R87, the most important reaction being R87 ($H + C_2H_5 \rightarrow 2CH_3$). These latter four reactions return about 40% of the C_2 species produced by reactions R120, R128, R129, and R135 to C_1 species. Most of the rest of the C_1 and C_2 reactions listed in Table II control the abundances of the C_2 species but do not form or break C–C bonds. The exceptions to this statement are those reactions that produce C_3 and higher hydrocarbon species. Of all the C_2 species produced from C_1, C_3, C_4, and higher hydrocarbons, 47% get converted to other hydrocarbon species, and 53% remain as C_2 species.

The net (column) production of C_2 species from C_1 radicals and higher hydrocarbons in our standard model is 1.02×10^8 cm^{-2} s^{-1}. This net production of C_2 species is balanced by the flux of C_2H_6 and C_2H_2 (and to a lesser extent by C_2H_4) through the lower boundary. A relatively large percent of the C_2 hydrocarbons formed in our model will react to produce C_3 and C_4 species; however, photolysis of C_3 and C_4 hydrocarbons or reactions of these species with atomic hydrogen efficiently recycle the C_2 species. The net loss of C_2 species to C_3 and higher-order hydrocarbons is only about 3% of the total net C_2 production.

Fig. 5d shows that ethylene behaves differently from the other major C_2 species. In the peak CH_4 dissociation region at high altitudes, C_2H_4 is formed primarily by the reaction $CH + CH_4 \rightarrow C_2H_4 + H$ (R120). The C_2H_4 production rapidly falls off as methane dissociation loses importance, but a second (smaller) C_2H_4 production peak occurs in a narrow altitude range centered near 0.3 mbar resulting from the reaction $C_2H_3 + H_2 \rightarrow C_2H_4 + H$ (R164). The C_2H_3 found in this region is produced from reaction of acetylene with atomic hydrogen (R84). Ethylene has a third

relatively unimportant production peak in the lower stratosphere caused mainly by the reaction $^3CH_2 + CH_3 \rightarrow C_2H_4 + H$ (R129); however, eddy diffusion dominates the profile of ethylene by this altitude, so the C_2H_4 concentration is rapidly decreasing.

Ethylene is lost in the upper atmosphere by reaction R86 ($H + C_2H_4 + M \rightarrow C_2H_5 + M$); however, this loss process becomes relatively unimportant below a few mbar as the concentration of atomic hydrogen drops off rapidly. Therefore, dissociation takes over as the major loss process for ethylene in the lower stratosphere (see reactions R11, R12, and R13).

Ethane is produced almost entirely from reaction R135 ($2CH_3 + M \rightarrow C_2H_6 + M$) at all altitudes in our Neptune models. The rate constant for this reaction is unknown at low temperatures. In our only deviation from the rate constants used in the Gladstone *et al.* (1991) Jovian photochemical model, we have used the low-temperature extrapolation of Yung *et al.* (1984) for this rate constant rather than that of Slagle *et al.* (1988) because we feel that the Slagle *et al.* extrapolation grossly underestimates the rate constant at temperatures below ~150 K. An extrapolation by Macpherson *et al.* (1985) also supports this conclusion. Note that the reaction rate was only measured at temperatures above 296 K in the experiments of Slagle *et al.* (1988) and Macpherson *et al.* (1985), and a large extrapolation is required to estimate the rate at temperatures relevant to Neptune. The difference between the Slagle *et al.* values and the Yung *et al.* expressions produces a variation in the stratospheric hydrocarbon concentrations of $\lesssim 20\%$.

Ethane is lost both by photolysis (R16, R17, R18, and R19) and by reaction R123 ($CH + C_2H_6 \rightarrow C_3H_6 + H$) in the upper atmosphere. Some of the photolysis products help to recycle both ethane and methane. Formation of C_3 hydrocarbons represents an important net loss of ethane; in fact, R123 is the dominant loss process in the upper atmosphere and represents 8% of the total column loss of ethane. In the

middle and lower stratosphere, reaction R123 rapidly loses importance and photolysis processes operate at reduced rates; therefore, ethane is not efficiently lost by chemical means. Diffusion controls the profile in the lower atmosphere.

Acetylene is produced directly from the dissociation of C_2H_4 and C_2H_6 in the upper atmosphere and indirectly from reaction R85 ($H + C_2H_3 \rightarrow C_2H_2 + H_2$) just below the methane photolysis peak. At middle and lower altitudes, acetylene is either photolyzed or lost through through reaction R84 ($H + C_2H_2 + M \rightarrow C_2H_3 + M$); however, the reaction products are efficiently recycled by reactions R85, R154, and R155. Therefore, C_2H_2 production is fairly constant with altitude, and acetylene, like ethane, is stable in the lower atmosphere. The shape of the C_2H_2 mixing ratio profile is controlled by diffusion in the lower atmosphere.

The net column production of C_3 species in our standard model is 2.19×10^6 cm^{-2} s^{-1}. This production is balanced by the flux of the C_3 species through the lower boundary; C_3H_8 is responsible for most of this flux. As much as 86% of the C_3 species produced by all reactions from C_1, C_2, and C_4 compounds gets converted back to C_1, C_2, and C_4 compounds while 14% stays as C_3 species. Reactions with atomic hydrogen (e.g., R94, R101, R106) are responsible for the bulk of the C_3's returning to C_2's, and reactions R175 and R176 that form C_4 species represent a large net loss of the C_2 and C_3 compounds.

Methylacetylene (CH_3C_2H) is produced relatively efficiently in Neptune's upper atmosphere. Most of the production at the few μbar level comes from the exchange reaction $H + CH_2CCH_2 \rightarrow CH_3C_2H + H$ (R98) with some contribution from reactions R92 and R99. The species that form allene (CH_2CCH_2) and methylacetylene in the upper atmosphere are ultimately derived from reaction R121 ($CH + C_2H_2 \rightarrow C_3H_2 + H$). Production of methylacetylene falls off fairly rapidly below 10^{-2} mbar as reactions R92 and R98 lose importance; however, loss by photolysis (R21, R22)

remains fairly constant throughout the atmosphere. The net result is that eddy diffusion and efficient loss processes in the lower atmosphere conspire to create a steep gradient in the mixing ratio profile of CH_3C_2H (see Fig. 5e).

Propane (C_3H_8) is more stable than methylacetylene in Neptune's lower atmosphere. The primary production mechanisms for propane in our standard model are R107 ($H + C_3H_7 + M \rightarrow C_3H_8 + M$) in the middle and upper atmosphere and R140 ($CH_3 + C_2H_5 + M \rightarrow C_3H_8 + M$) in the lower atmosphere. The C_3H_7 required for reaction R107 comes from C_3H_6, which in turn is derived from reactions with ethane (R123) and C_2H_3 plus methyl (R138). Photodissociation (R34, R35, R36, R37) keeps the loss rate fairly constant throughout the atmosphere. However, the photolysis products can be recycled in part back to propane in the lower atmosphere by reaction R140; therefore, the C_3H_8 concentration does not drop off as sharply in the stratosphere as that of CH_3C_2H.

The net column production of C_4 species is 1.47×10^5 cm^{-2} s^{-1}. Diffusion of C_4H_2 (and other C_4 species) through the lower boundary balances this production. Out of all the C_4 compounds made from other hydrocarbon species, 97% are returned to other compounds and only 3% remain as C_4 species. Reactions R176, R175, and R167 dominate the formation of C_4 compounds. Photolysis processes (e.g., R39, R40) and reactions with hydrogen (e.g., R110) are primarily responsible for C_4 destruction.

Diacetylene and polyacetylene chemistry is discussed in more detail in other papers (e.g., Summers and Strobel 1989, Romani and Atreya 1988). In our standard model, reactions R111, R175, and R176 are responsible for C_4H_2 production in the upper and middle atmosphere; however, the C_4H_2 production rate peaks in the lower atmosphere where reaction R180 dominates. The reaction $H + C_4H_2 + M \rightarrow C_4H_3 + M$ (R109) destroys diacetylene in the upper atmosphere, but its reaction rate falls off sharply below a few mbar, at which point photolysis takes over (R38, R39, R40).

In the upper atmosphere, 65% of the C_4H_3 produced by R109 is recycled back to diacetylene by reaction R111. In the lower atmosphere, 98% of the C_4H produced from diacetylene photolysis (R38) is recycled back to C_4H_2 by R180; hence, no efficient C_4H_2 loss processes exist in the lower atmosphere. The double peak visible in the mixing ratio profile of diacetylene (see Fig. 5f) results from the double peak in the production rate and from the lack of efficient loss processes in the lower atmosphere.

Ethylacetylene (butyne, $1\text{–}C_4H_6$) also has two production peaks in the middle and upper atmosphere, but photodissociation operates throughout the atmosphere, and no efficient recycling schemes are present in the lower atmosphere. Thus, the ethylacetylene concentration peaks near the μbar level where reaction R142 ($CH_3 + C_3H_3 + M \rightarrow 1 - C_4H_6 + M$) dominates and remains high in the middle atmosphere because of production by reaction R186 ($C_4H_5 + H_2 \rightarrow 1 - C_4H_6 + H$), but falls off rapidly below this point because of diffusion and lack of efficient recycling.

Butane (C_4H_{10}) has a maximum production rate in the middle atmosphere resulting from the reaction R148 ($CH_3 + C_3H_7 + M \rightarrow C_4H_{10} + M$). Reaction R174 ($2C_2H_5 + M \rightarrow C_4H_{10} + M$) contributes to the production at lower altitudes. Photodissociation (e.g., R68, R72, R73) is responsible for destroying C_4H_{10}. The resulting profile for the butane mixing ratio exhibits a peak in the middle atmosphere.

The loss time scales for the major species in our Neptune model atmosphere are shown in Fig. 8. One Neptune day is $\sim$16.1 hours or 5.8×10^4 seconds. All the major hydrocarbon species are long lived with respect to a Neptunian day so little diurnal variation in these species should be visible. The solar cycle has a period of 11 years or 3.5×10^8 seconds. This time scale is longer than the chemical loss time constants of the major species in Neptune's upper atmosphere but shorter than those in the middle and lower stratosphere. Some solar cycle variation should be visible, but less noticeable for the stable species such as ethane and propane. On the other

hand, one Neptune year is 5.2×10^9 seconds. Since the chemical loss time scales in the upper atmosphere are less than a Neptunian year, some seasonal variation might be expected. Throughout much of the atmosphere, CH_4, C_2H_6, C_3H_8, and C_2H_2 are photochemically stable and have profiles controlled by diffusional transport. These species therefore dominate the flux of carbon atoms to the troposphere.

In our standard model, we find total net column production rates that differ substantially from the yields of hydrocarbon species derived from plasma discharge experiments (e.g., Thompson *et al.* 1987). For instance, we find ratios in either stratospheric column abundances or net production rates that indicate that C_2H_6 should be the most abundant hydrocarbon constituent aside from CH_4, followed by C_2H_2, C_3H_8, CH_3C_2H, C_4H_2, C_2H_4, C_6H_2, 1-C_4H_6, C_3H_6, C_4H_{10}, and CH_2CCH_2 in order of decreasing abundance. Plasma discharge experiments, on the other hand, find higher yields of the higher-weight alkanes (e.g., propane, butane) relative to ethane and often find acetylene to be more abundant than ethane.

For instance, in an experiment conducted at 57 mbar with 0.12% CH_4, 11.3% He, and 88.6% H_2, Thompson *et al.* (1987) find yields of $C_3H_8/C_2H_6 = 69\%$ and $C_4H_{10}/C_2H_6 = 21\%$ compared with our results of $C_3H_8/C_2H_6 = 3\%$ and $C_4H_{10}/C_2H_6 = 6 \times 10^{-5}$. In an experiment conducted at lower pressures (0.63 mbar) and a higher methane abundance (2.2%), Thompson *et al.* find that propylene (C_3H_6) is the most abundant species, followed by C_4H_8, C_5H_{10}, and C_3H_8. In this experiment, $C_3H_8/C_2H_6 = 600\%$ and $C_4H_{10}/C_2H_6 = 157\%$. These results are markedly different from our photochemical results. Advances in ground-based telescopes and detectors (especially at infrared wavelengths) may allow determinations of the abundances of some of the heavy hydrocarbon species (e.g., propane and methylacetylene) and might help to distinguish between the relative importance of charged particles and photons in controlling atmospheric chemistry on Neptune.

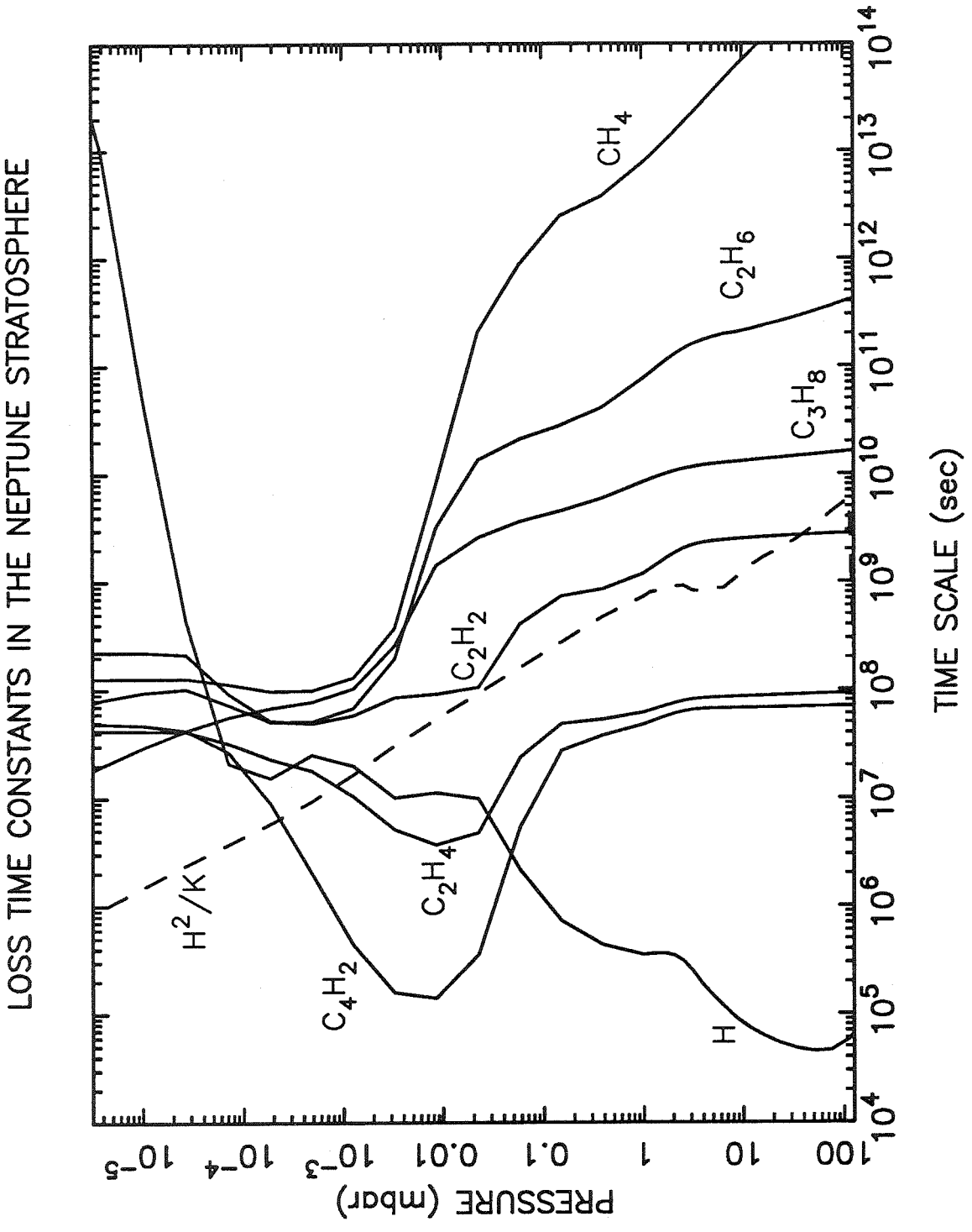

Figure 8. Time constants for chemical loss and eddy transport in our standard model. Because of efficient recycling schemes, some of the species are more stable than these results indicate; thus, the chemical loss time constants should be regarded as minimum time scales.

We now examine the sensitivity of our photochemical model to variations in some of the input parameters. In particular, we consider how the abundances of hydrocarbon species in our model are affected by changes in the upper atmospheric temperature profile, the stratospheric methane mixing ratio, the eddy diffusion profile, the solar flux, and the planetary latitude (season). The stratospheric methane mixing ratio and the eddy diffusion profile of Neptune are very uncertain; we vary these parameters within reasonable theoretical and observational limits. The influence of solar flux and season is investigated to help provide a basis for comparison between different observational datasets, and two different thermospheric temperature profiles are investigated to determine whether the adoption of cold thermospheric temperatures in previous photochemical models (e.g., Romani and Atreya 1988, 1989) affects the photochemical results.

Table III lists the different combinations of input parameters used in our model calculations. The column under T refers to upper atmospheric temperature: "cold" corresponds to the isothermal profile and "warm" corresponds to the UVS profile of Fig. 1. The assumed stratospheric mixing ratio is listed in the column labeled f_{CH_4}, the eddy diffusion coefficient at the homopause is listed under K_h, and the slope of the diffusion coefficient in the stratosphere and thermosphere is listed under β. Some of the models are discussed in more detail below.

Sensitivity to upper atmospheric temperature

Most previous photochemical models of Neptune's atmosphere consider the atmospheric temperature to be isothermal above ~10 μbar (e.g., Romani and Atreya 1988, 1989); however, the *Voyager* UVS experiment demonstrated that Neptune has

TABLE III

Summary of Model Input Parameters

model	T	f_{CH_4}	K_h	β	Shown in Figure
1	cold	2.5×10^{-5}	$\sim 10^7$	0.5	9
2	cold	2.5×10^{-5}	$\sim 10^8$	0.5	no
3	cold	2×10^{-2}	$\sim 10^7$	0.5	no
4	cold	2×10^{-2}	$\sim 10^8$	0.5	no
5	warm	2.5×10^{-5}	$\sim 10^6$	0.5	12
6	warm	2.5×10^{-5}	$\sim 10^7$	0.5	9, 10, 12
7	warm	2.5×10^{-5}	$\sim 10^8$	0.5	12
8	warm	2×10^{-2}	$\sim 10^6$	0.5	no
9	warm	2×10^{-2}	$\sim 10^7$	0.5	10
10	warm	2×10^{-2}	$\sim 10^8$	0.5	no
11	warm	2×10^{-4}	$\sim 10^7$	0.6	13
12	warm	2×10^{-4}	$\sim 10^7$	0.65	13
A	warm	2×10^{-4}	$\sim 10^7$	0.5	5-8, 10, 13, 14, 16
B	warm	2×10^{-4}	$\sim 5 \times 10^8$	0.65	15, 16
C	warm	2×10^{-4}	$\sim 10^8$	0.65	15, 16

Note: We also examined the sensitivity of Model A to the solar flux and the sensitivity of Models B and C to season (see Figs. 14 and 15 and Table IV).

a hot thermosphere and a substantial temperature gradient in the region in which methane is photolyzed by short wavelength radiation (Broadfoot *et al.* 1989; see also Fig. 1 and photochemistry discussion in Section 2.2). The consequences of varying the upper atmospheric temperature profile are not immediately obvious.

The most drastic consequence of changing the temperature profile is to change the background hydrostatic atmosphere; specifically, the altitude dependence of den-

sity and pressure will change significantly. However, the density itself will not change much with pressure. Since $dp/p = dn/n + dT/T$ where p is the pressure, n is the density, and T is the temperature of the background atmosphere, the positive temperature gradient of the UVS profile (our "warm" atmospheric model) causes the atmospheric density at any fixed pressure in the upper atmosphere to be slightly less than the corresponding case for the isothermal atmosphere. Thus, more methane is photolyzed at low pressures in the isothermal model than in the warm thermosphere model, and, consequently, more higher–order hydrocarbons are produced.

However, Fig. 9 demonstrates that this effect does not propagate into the middle and lower stratosphere. This figure shows the ethane and acetylene mixing ratios calculated with different assumed temperature profiles: the solid lines refer to the "warm" profile of Fig. 1 whereas the dotted lines refer to the "cold" profile. Although the net production of higher hydrocarbon species above $\sim$1 μbar varies greatly between the two models, the production rates at the methane photolysis peak of the two models are almost identical, and the C_2, C_3, and C_4 abundances in the lower stratosphere are unaffected by the upper atmospheric temperature change. Thus, the photochemical model is relatively unaffected by drastic changes in the upper atmospheric ($<$ 1 μbar) temperature profile.

Sensitivity to stratospheric methane abundance

Although numerous multispectral ground–based and spacecraft observations of Neptune's atmosphere have been conducted over the past two decades (e.g., see review by Trafton 1981), interpretations of methane abundances from these observations have often been inconsistent; that is, different observers have derived different hydrocarbon abundances. For example, Orton *et al.* (1987) and Baines and Smith

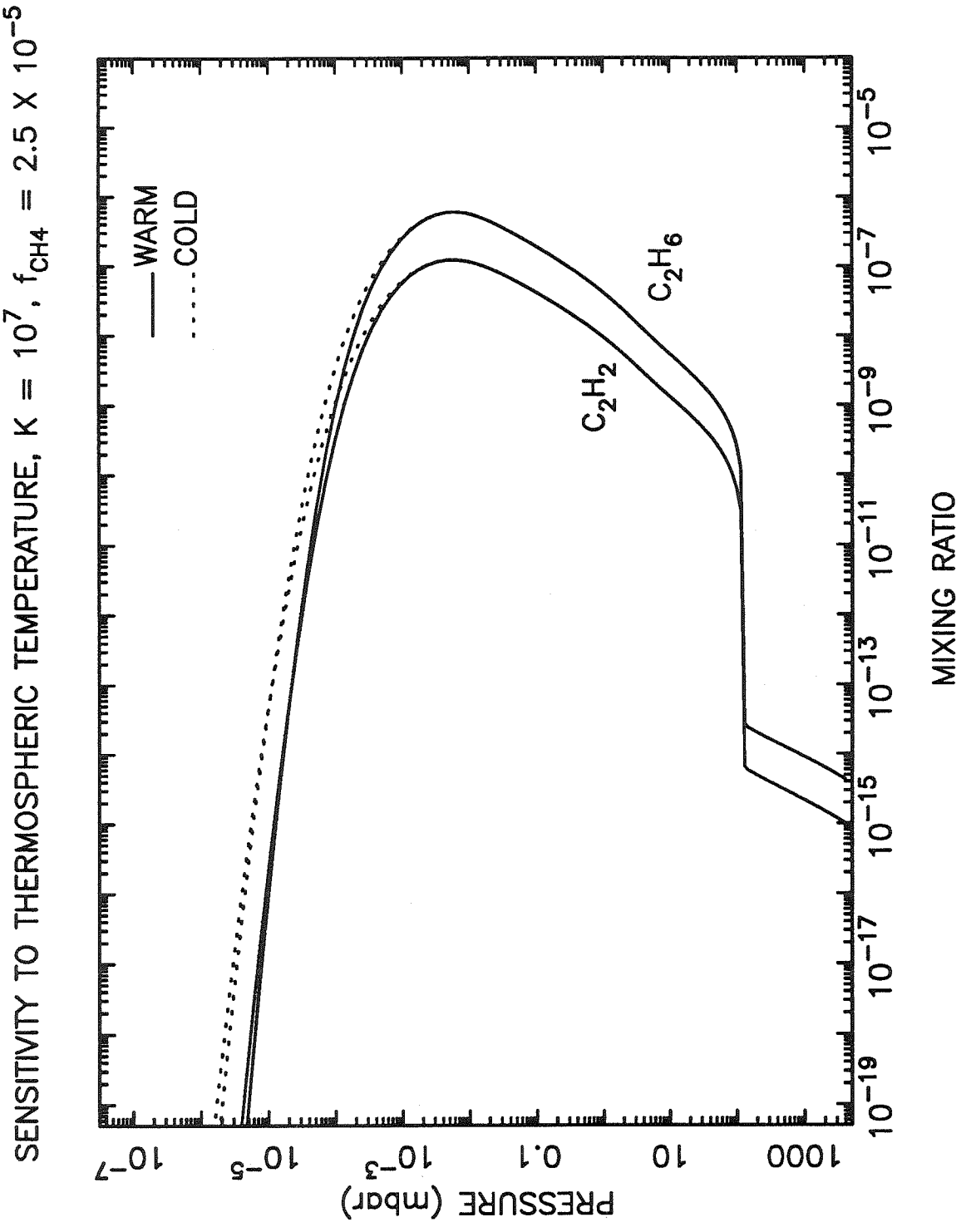

Figure 9. Photochemical model sensitivity to thermospheric temperature. In this model, the stratospheric methane mixing ratio is assumed to be 2.49 $\times$ 10^{-5}, and the eddy diffusion coefficient at the methane homopause is 10^7 cm^2 s^{-1}.

(1990) have used multiwavelength observations to derive methane volume mixing ratios of 2 to 4% in Neptune's troposphere below a proposed methane cloud deck, a methane abundance constrained by local saturation equilibrium in the methane condensation region, and a 2 to 3% methane mixing ratio in Neptune's stratosphere. These large stratospheric abundances imply that Neptune's tropopause does not act as an efficient cold trap for methane. These results as well as similar earlier observations have led investigators to examine the role of strong updrafts and/or moist convection and convective penetration in the transport of large amounts of methane to the stratosphere (Hunten 1974, Macy and Trafton 1975, Lunine and Hunten 1989, Stoker and Toon 1989). Meanwhile, *Voyager* observations and more recent interpretations of ground–based data are consistent with a lower tropospheric methane abundance (e.g., 1 to 2% according to interpretations of the *Voyager* RSS results, Lindal *et al.* 1990) and a much lower stratospheric methane abundance (3×10^{-5} in Neptune's thermosphere according to preliminary *Voyager* UVS results, Broadfoot *et al.* 1989; 2×10^{-4} according to recent interpretations of ground–based infrared data, Orton *et al.*. 1990b, and to a more recent analysis of UVS data, Bishop *et al.* 1991).

Inconsistencies in the derived methane abundances among the various observations are probably due to the fact that the interpretations are model dependent, and the models contain many free parameters. In particular, the stratospheric hydrocarbon abundances derived from infrared observations are sensitive to the assumed stratospheric temperature. Since the temperature in the middle stratospheric region of interest is not well constrained by observations, the methane mixing ratio remains uncertain.

If we assume that the tropospheric temperature profile derived from the *Voyager* RSS experiment (Lindal *et al.* 1990) is correct and that no convective penetration

of methane into the stratosphere occurs, then the stratospheric methane mixing ratio will be 2.49×10^{-5} — a value determined by the minimum saturation mixing ratio below the tropopause. However, if convective penetration does occur, a mixing ratio as high as 2% might develop.

We have examined the sensitivity of our hydrocarbon photochemical model to the assumed stratospheric methane mixing ratio. The acetylene, ethylene, and ethane abundances resulting from different assumed methane abundances are shown in Figs. 10a–c. As Romani and Atreya (1988, 1989) point out, the C_2 and higher hydrocarbon abundances are surprisingly insensitive to changes in the assumed methane mixing ratio because the hydrocarbon photochemistry is limited by the number of available photons rather than by the number of available methane molecules. A decrease in the methane mixing ratio of a factor of 800 causes a decrease in the ethane concentration of only a factor of 4 at 0.1 mbar.

The differences in C_2 and higher hydrocarbon abundances among the different cases reflect the differences in the locations of the methane dissociation peaks and in the relative efficiencies of methane recycling. Although the magnitudes of the peak methane photolysis rates in the upper atmosphere are similar for all three cases, the high methane case (2% stratospheric methane) has the primary upper atmospheric methane dissociation peak at a lower pressure level (i.e., a higher altitude) than the 2×10^{-4} methane case, which, in turn, has a dissociation peak located above that of the 2.49×10^{-5} methane case. However, the methane production peak (from reaction R82) in the thermosphere does not vary much with altitude. For the high methane case, reaction R82 ($H + CH_3 + M \rightarrow CH_4 + M$) peaks at a few μbar while the methane photolysis region peaks near 0.1 μbar. This mismatch in location keeps methane from being as efficiently recycled in the upper atmosphere of the high methane case as it is in the low (2.49×10^{-5}) methane case; thus, the CH_4 dissociation products are free

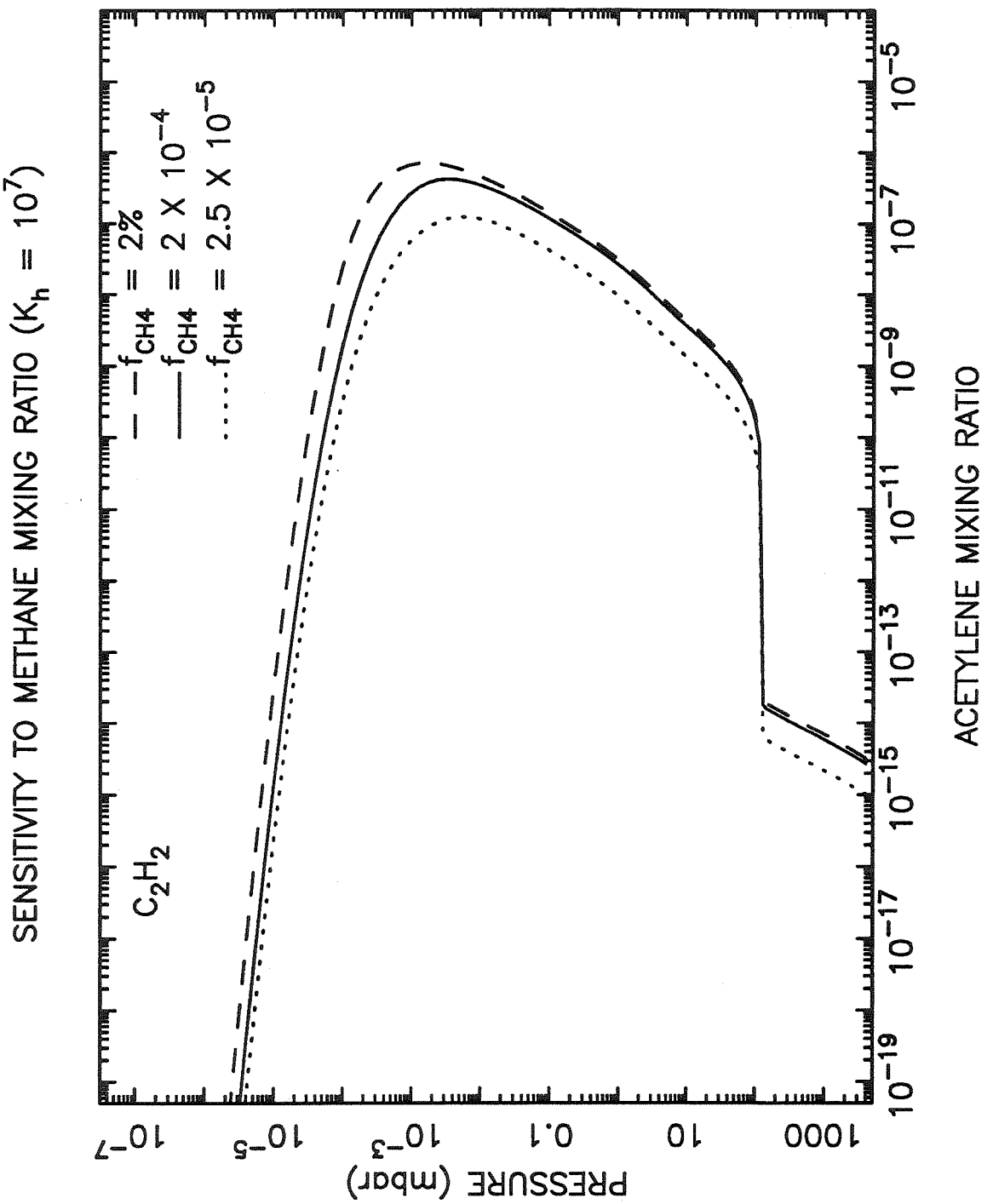

Figure 10a. Sensitivity of the acetylene mixing ratio to the stratospheric methane abundance.

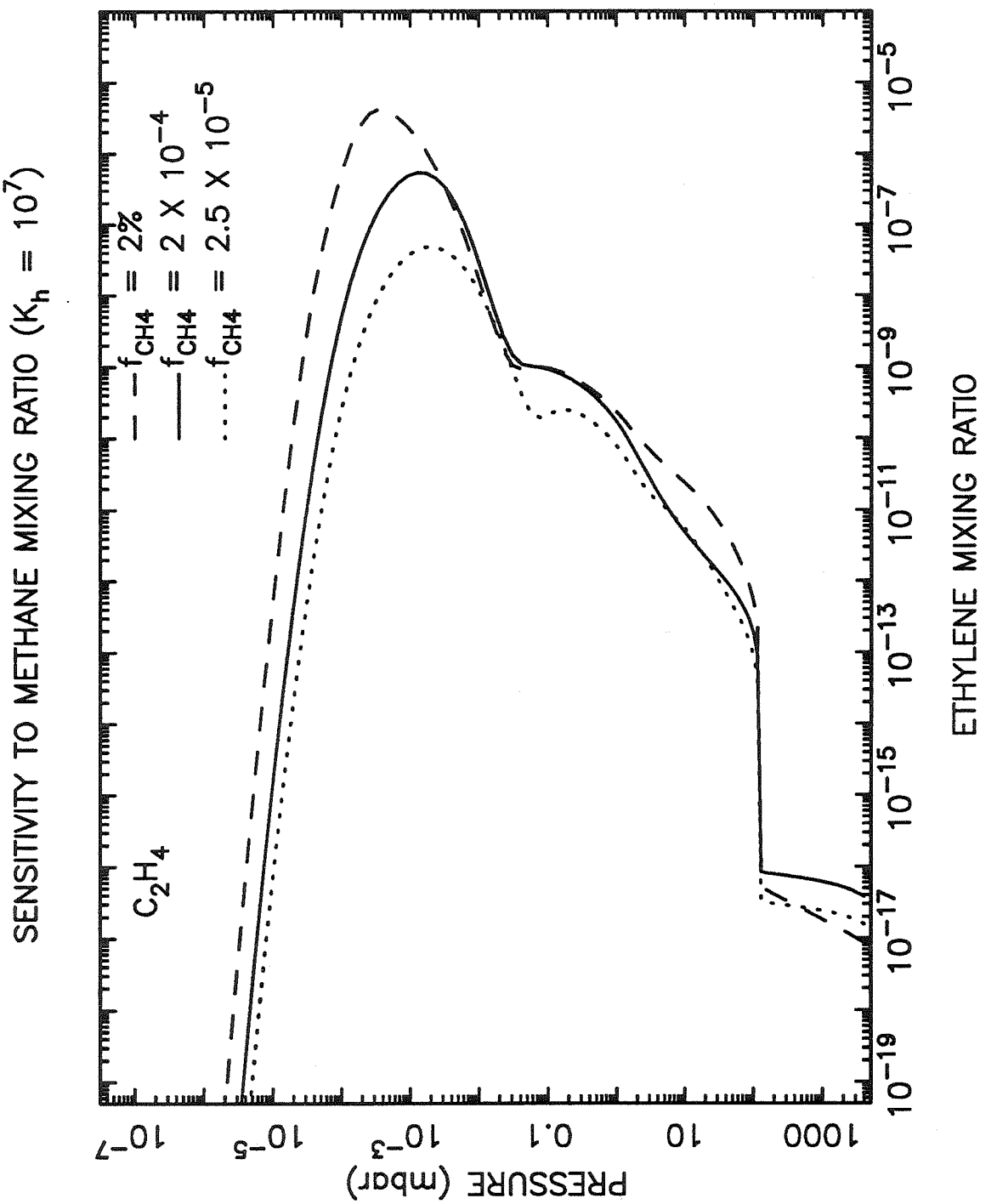

Figure 10b. Sensitivity of the ethylene mixing ratio to the stratospheric methane abundance.

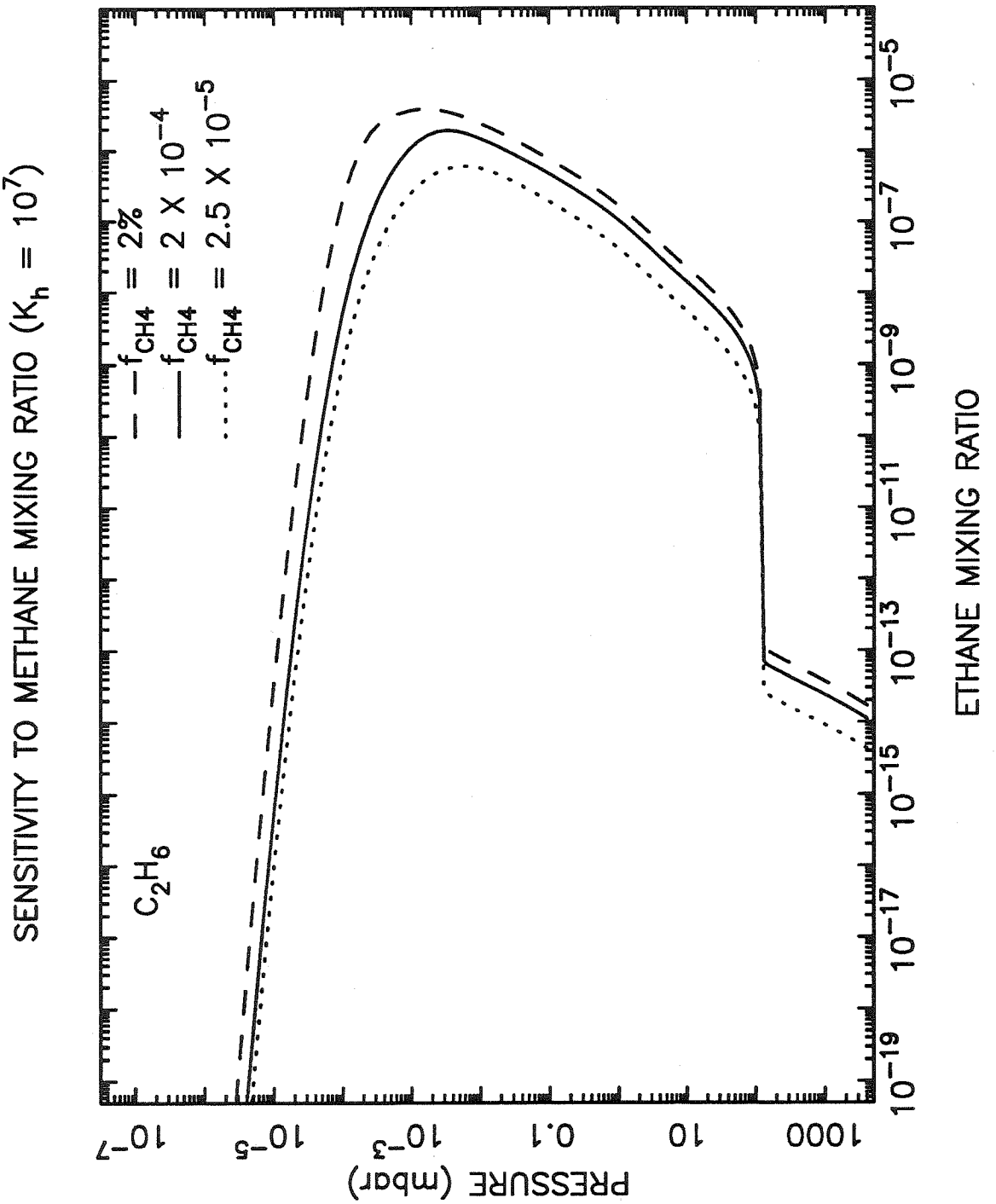

Figure 10c. Sensitivity of the ethane mixing ratio to the stratospheric methane abundance.

to form higher hydrocarbons. The net column production of C_2 species is 1.4 $\times$ 10^8 in the 2% methane case, 1.0 $\times$ 10^8 in the 2 $\times$ 10^{-4} methane case, and 4.0 $\times$ 10^7 in the 2.49 $\times$ 10^{-5} methane case.

Sensitivity to eddy diffusion

The only constraints we have concerning the eddy diffusion coefficient in Neptune's atmosphere are estimates of K at the methane homopause. On the basis of UVS solar occultation light curves, Broadfoot *et al.* (1989) suggest a value of 10^7 to 10^8 cm^2 s^{-1} at the CH_4 homopause, and, on the basis of He 584 Å emission from Neptune, Parkinson *et al.* (1990) favor values that range from 6 $\times$ 10^6 to 1.6 $\times$ 10^8 cm^2 s^{-1}. We now examine the sensitivity of our photochemical model to variations in the adopted eddy diffusion profile in the atmosphere. We consider the effect of changing the tropospheric diffusion coefficient, the effect of changing the slope of the stratospheric diffusion coefficient, and the effect of changing the value of K at the methane homopause.

Fig. 11 shows influence of the tropospheric eddy diffusion coefficient on our photochemical model results. In this figure, we plot the ethane mixing ratio for three different models; the first model has tropospheric diffusion coefficients estimated from free–convection theory (see Section 2.1 and Fig. 2; $K \sim 10^8$), and the second and third models have constant tropospheric coefficients of 10^6 and 10^4. The abundances of the higher order hydrocarbons in the stratosphere are not very sensitive to the diffusion coefficients in the troposphere. The ethane abundance in the lower stratosphere is increased slightly by a decrease in the tropospheric diffusion coefficient from $\sim 10^8$ to 10^4; however, the effects do not propagate very far into the stratosphere. The most important effect of varying the tropospheric diffusion coefficient is to change the

level at which any condensates can re–evaporate in the troposphere. Similar results were found for all the hydrocarbon species.

The mixing ratio profiles of the potentially condensable hydrocarbon species as a function of the eddy diffusion coefficient at the homopause are shown in Figs. 12a–h. The eddy diffusion profiles used in these models are illustrated in Fig. 2 and discussed in Section 2.1. Increasing the diffusion coefficient at the homopause increases hydrocarbon production (and methane dissociation) at high altitudes. In addition, since the diffusion coefficients fall off with the inverse square root of the atmospheric density in all three models, a high diffusion coefficient at the homopause implies a relatively high diffusion coefficient in the lower stratosphere. In these cases, eddy transport acts to remove the long–lived species more effectively than in the cases with a stagnant lower atmosphere (i.e., lower diffusion coefficients). A comparison of these models with *Voyager* and ground–based observations will be presented later.

Also shown in Figs. 12a–h are the saturation vapor density curves for each species in the lower stratosphere and upper troposphere (see Appendix A for a discussion of the vapor pressure expressions used in these calculations). The regions in which the mixing ratio profiles exceed the saturation mixing ratio curves define the locations at which the hydrocarbon species have the potential to condense. The question of whether condensation will actually occur in these regions is deferred to Section 4; the ability of a substance to condense in these regions depends on how efficiently particles can form under ambient conditions. Note that ethylene never reaches saturation in the lower atmosphere. Even when we increase the stratospheric methane abundance to 2%, the ethylene mixing ratio profiles never cross the saturation curve. Thus, ethylene will not condense in Neptune's lower atmosphere.

The sensitivity of the ethane mixing ratio profile to changes in the slope of the eddy diffusion coefficient is shown in Fig. 13. In these models, the diffusion coefficient

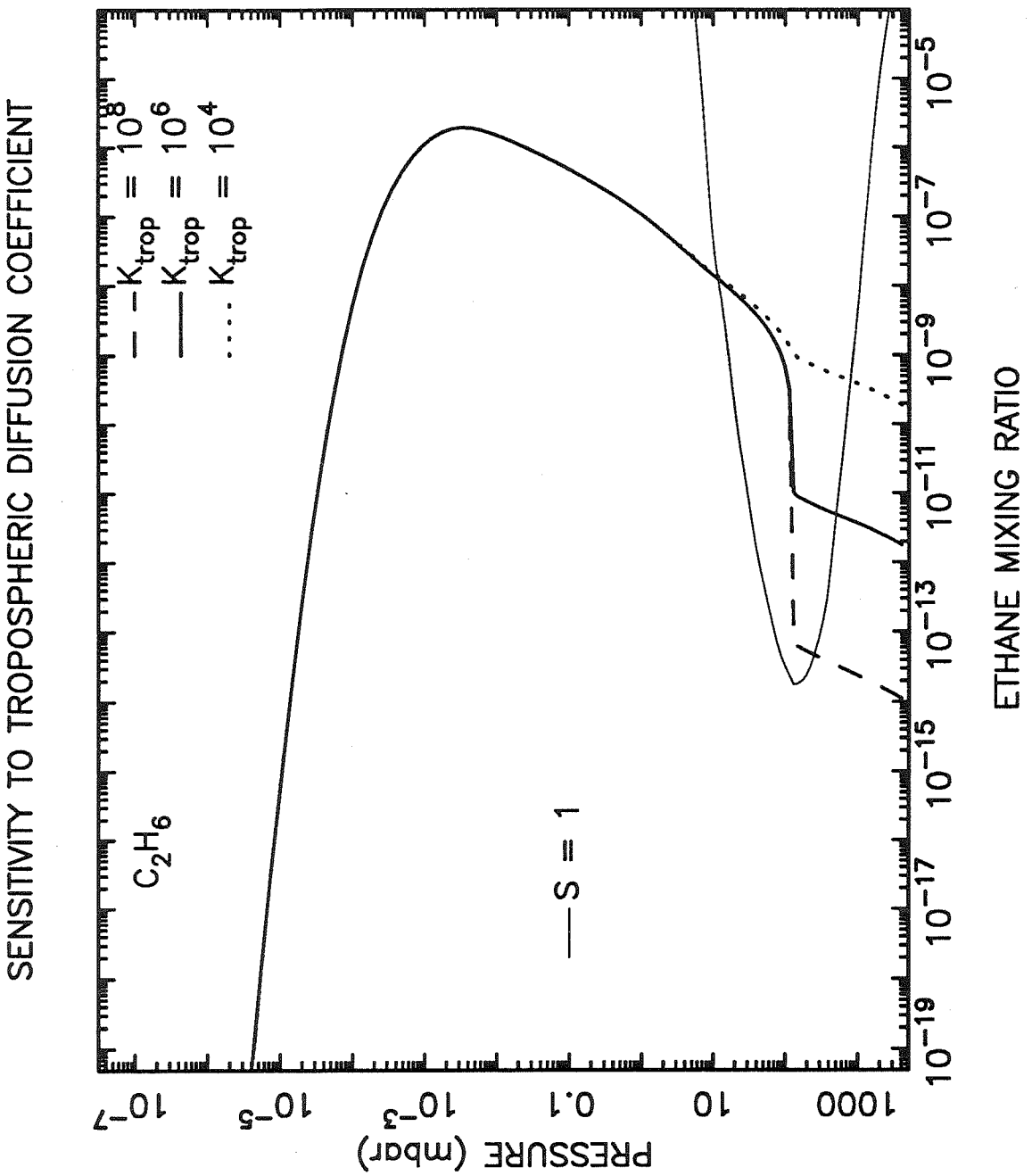

Figure 11. Sensitivity of the ethane mixing ratio to the tropospheric eddy diffusion coefficient (for a case of $K_h = 10^7$ and methane mixing ratio of 2.49×10^{-5}). The thin solid line shows the saturation vapor mixing ratio curve for ethane. Ethane can condense somewhere within this curve. Lowering the tropospheric diffusion coefficient will lower the level at which condensates can evaporate in the troposphere.

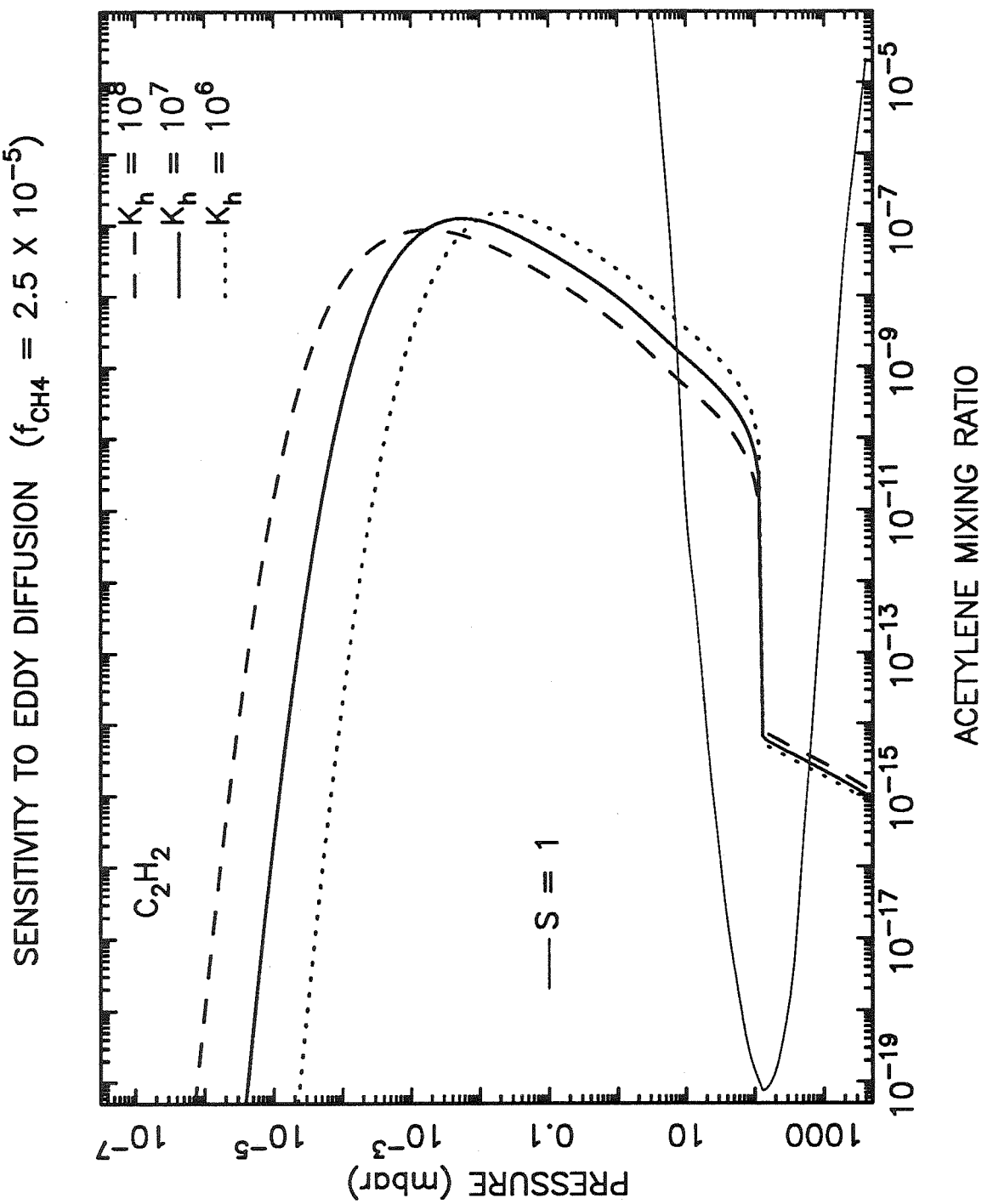

Figure 12a. Sensitivity of the acetylene mixing ratio to the eddy diffusion profile. The stratospheric methane mixing ratio in all three cases is 2.49 $\times$ 10^{-5}.

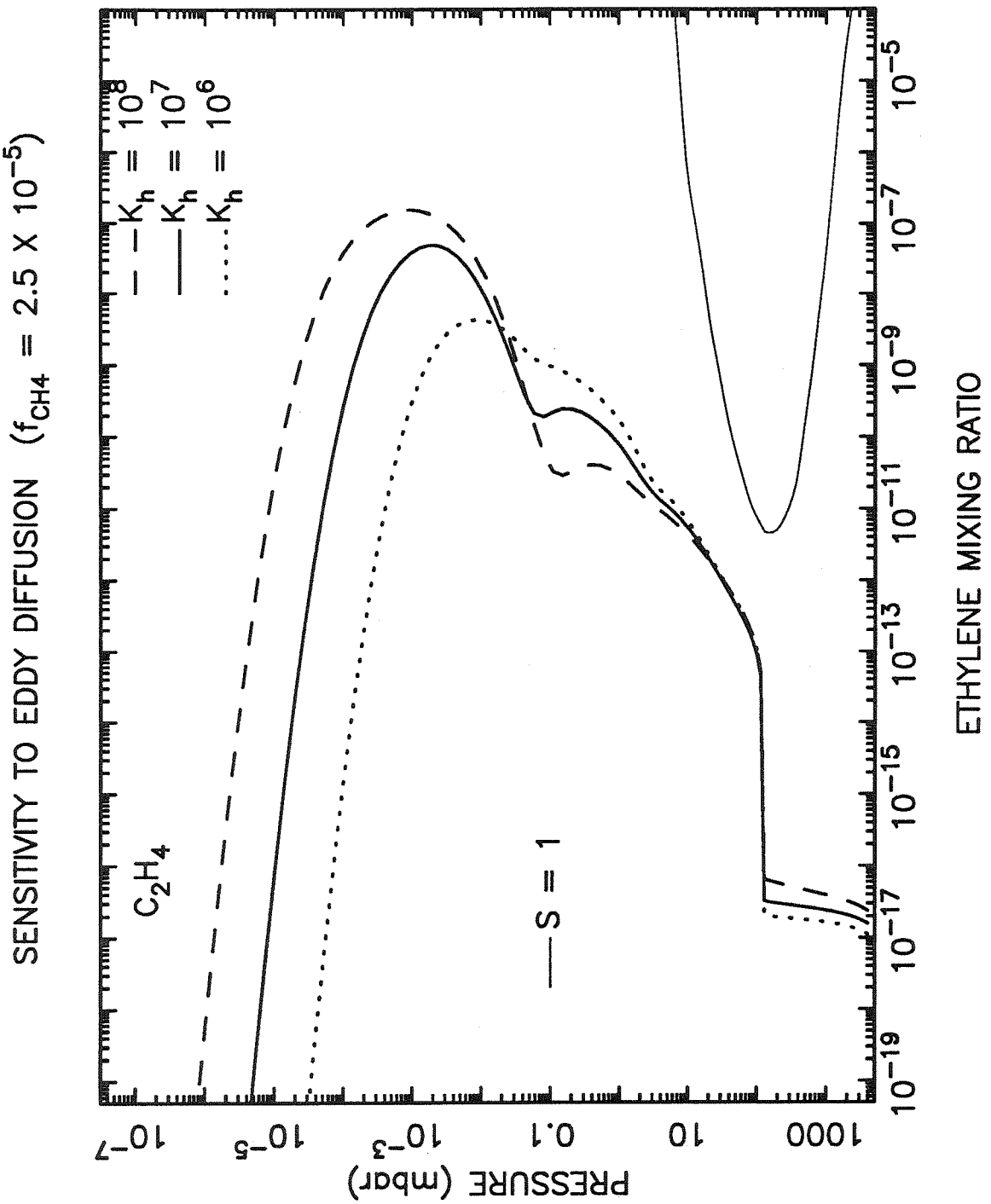

Figure 12b. Sensitivity of the ethylene mixing ratio to the eddy diffusion profile. The stratospheric methane mixing ratio in all three cases is 2.49 $\times$ 10^{-5}.

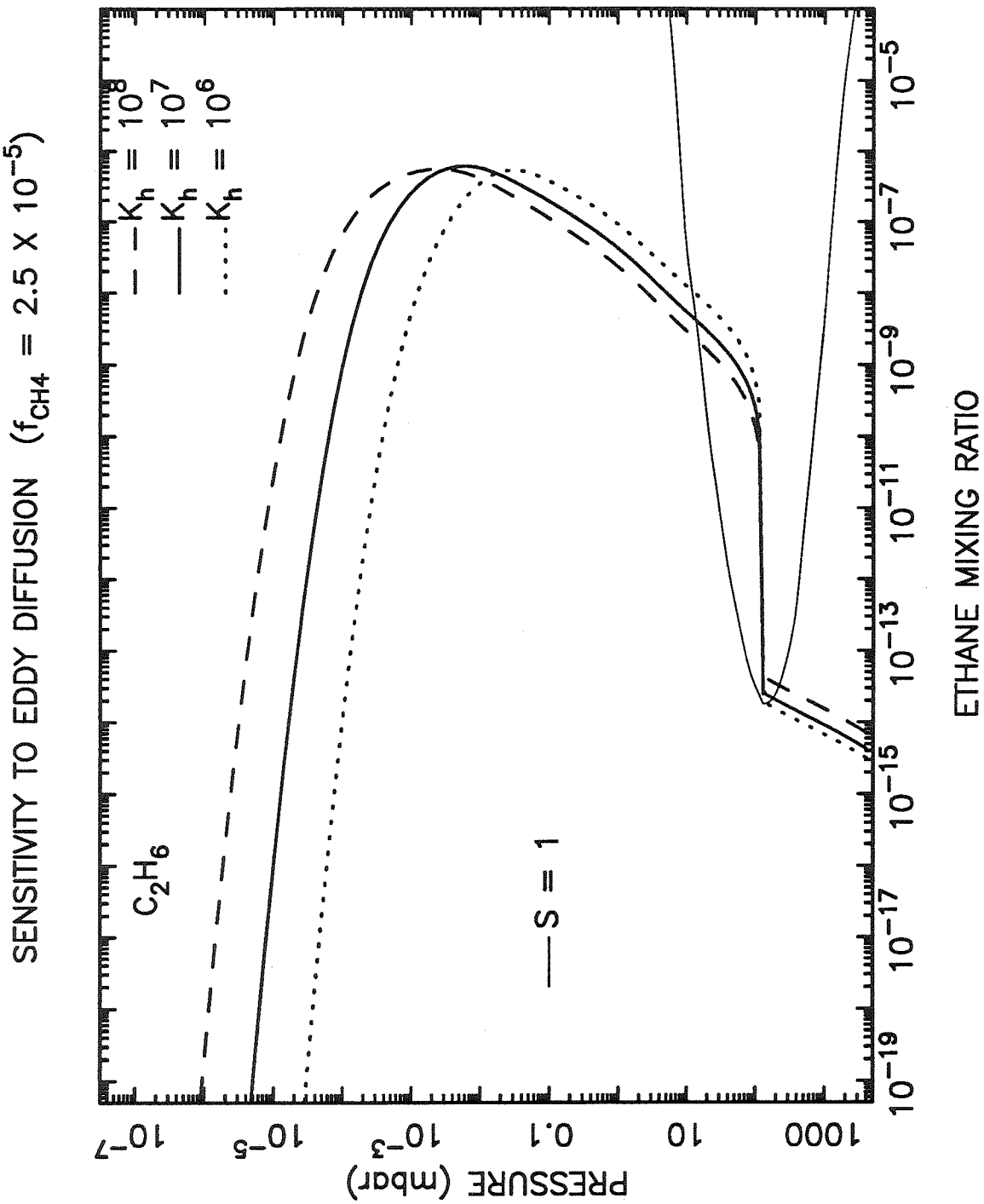

Figure 12c. Sensitivity of the ethane mixing ratio to the eddy diffusion profile. The stratospheric methane mixing ratio in all three cases is 2.49 $\times$ 10^{-5}.

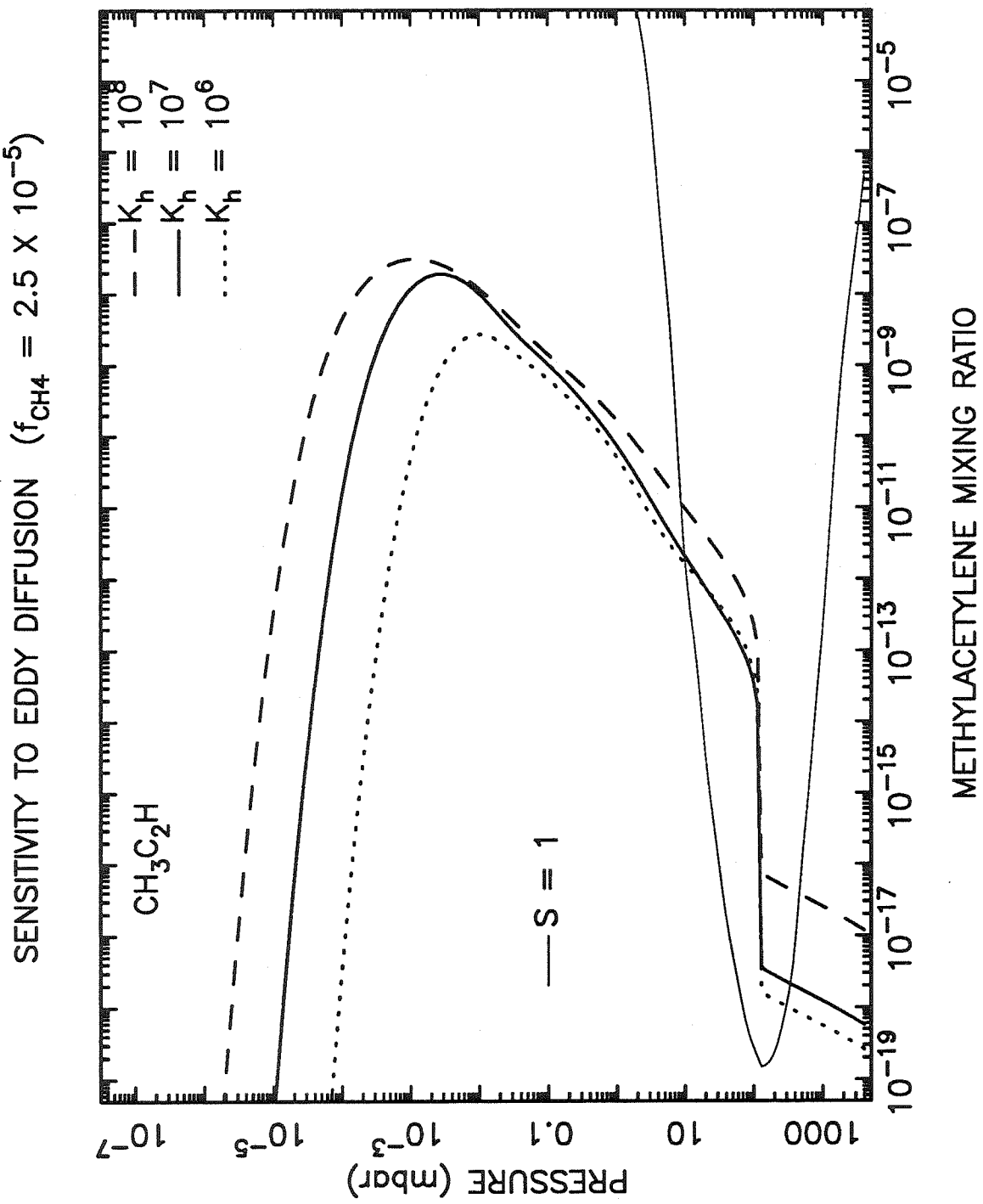

Figure 12d. Sensitivity of the methylacetylene mixing ratio to the eddy diffusion profile. The stratospheric methane mixing ratio in all three cases is 2.49 $\times$ 10^{-5}.

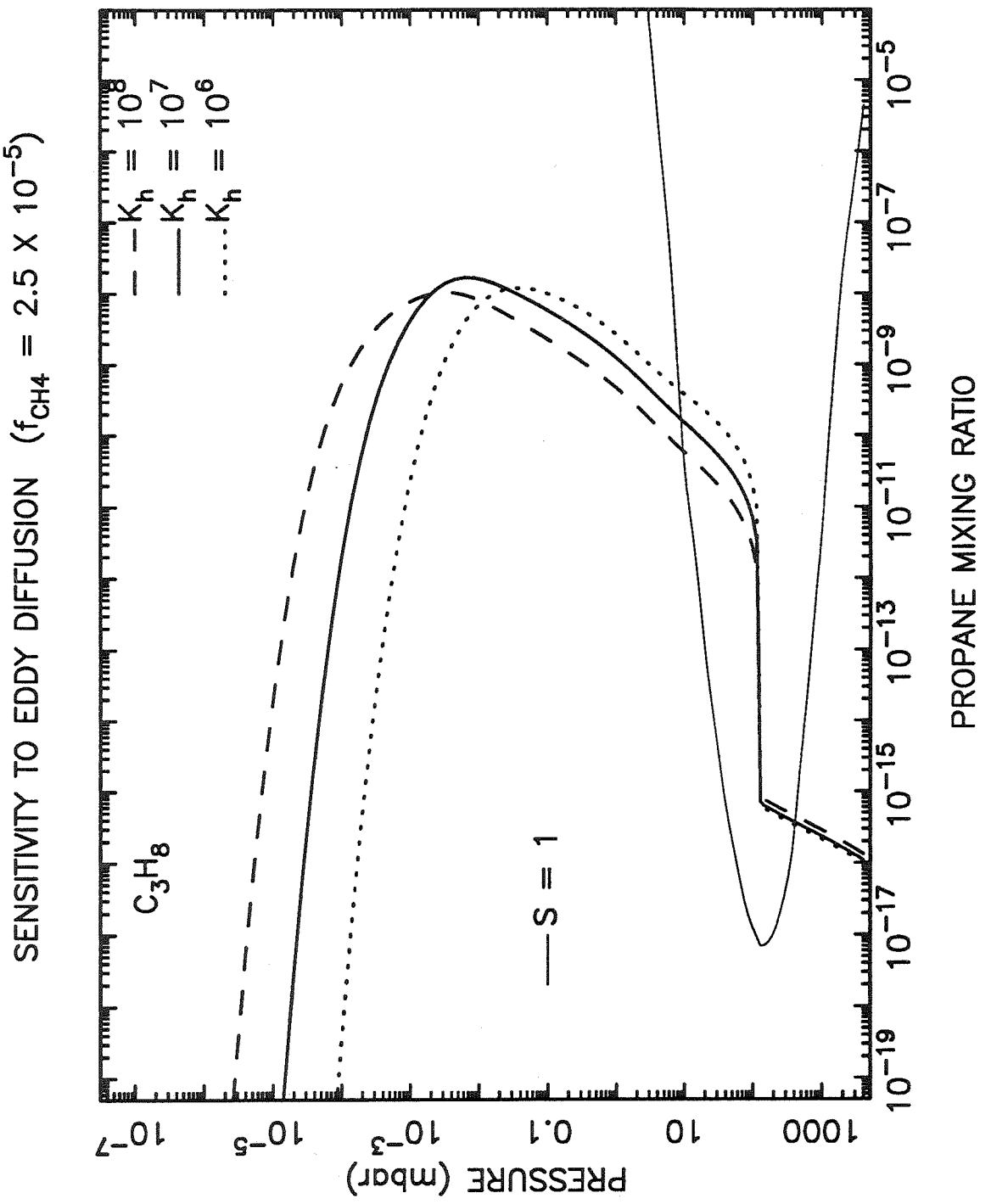

Figure 12e. Sensitivity of the propane mixing ratio to the eddy diffusion profile. The stratospheric methane mixing ratio in all three cases is 2.49 $\times$ 10^{-5}.

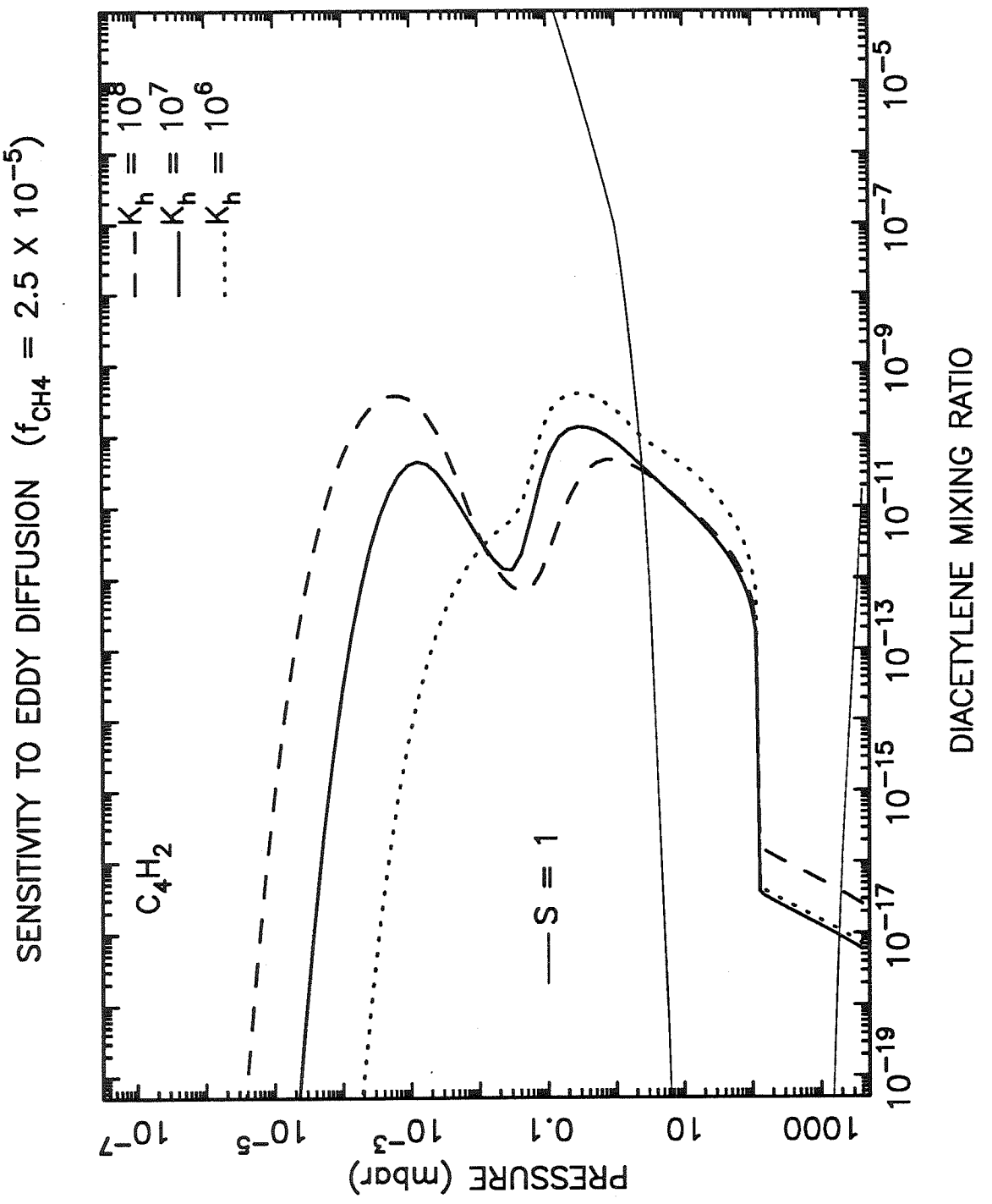

Figure 12f. Sensitivity of the diacetylene mixing ratio to the eddy diffusion profile. The stratospheric methane mixing ratio in all three cases is 2.49 $\times$ 10^{-5}.

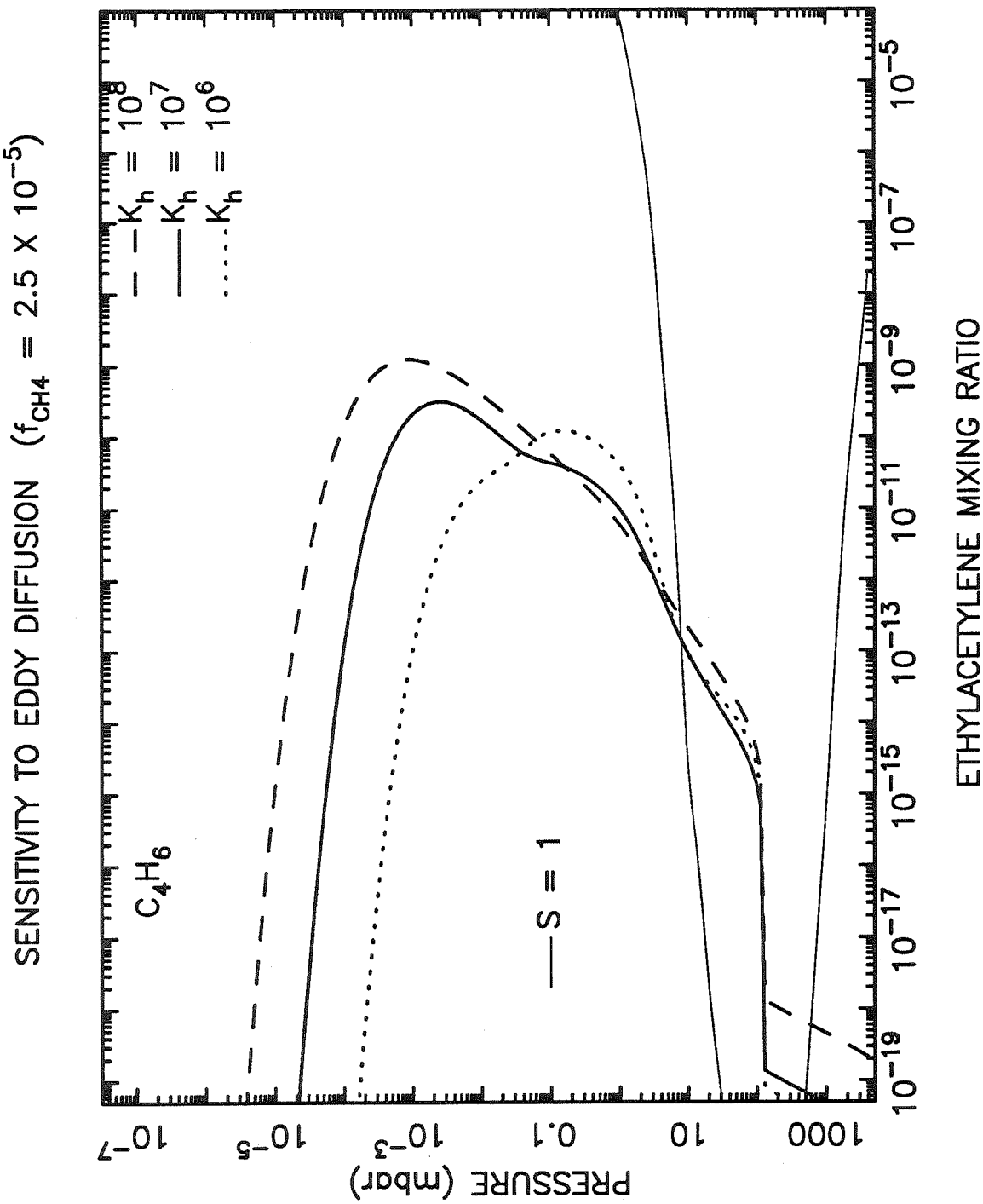

Figure 12g. Sensitivity of the ethylacetylene mixing ratio to the eddy diffusion profile. The stratospheric methane mixing ratio in all three cases is 2.49 $\times$ 10^{-5}.

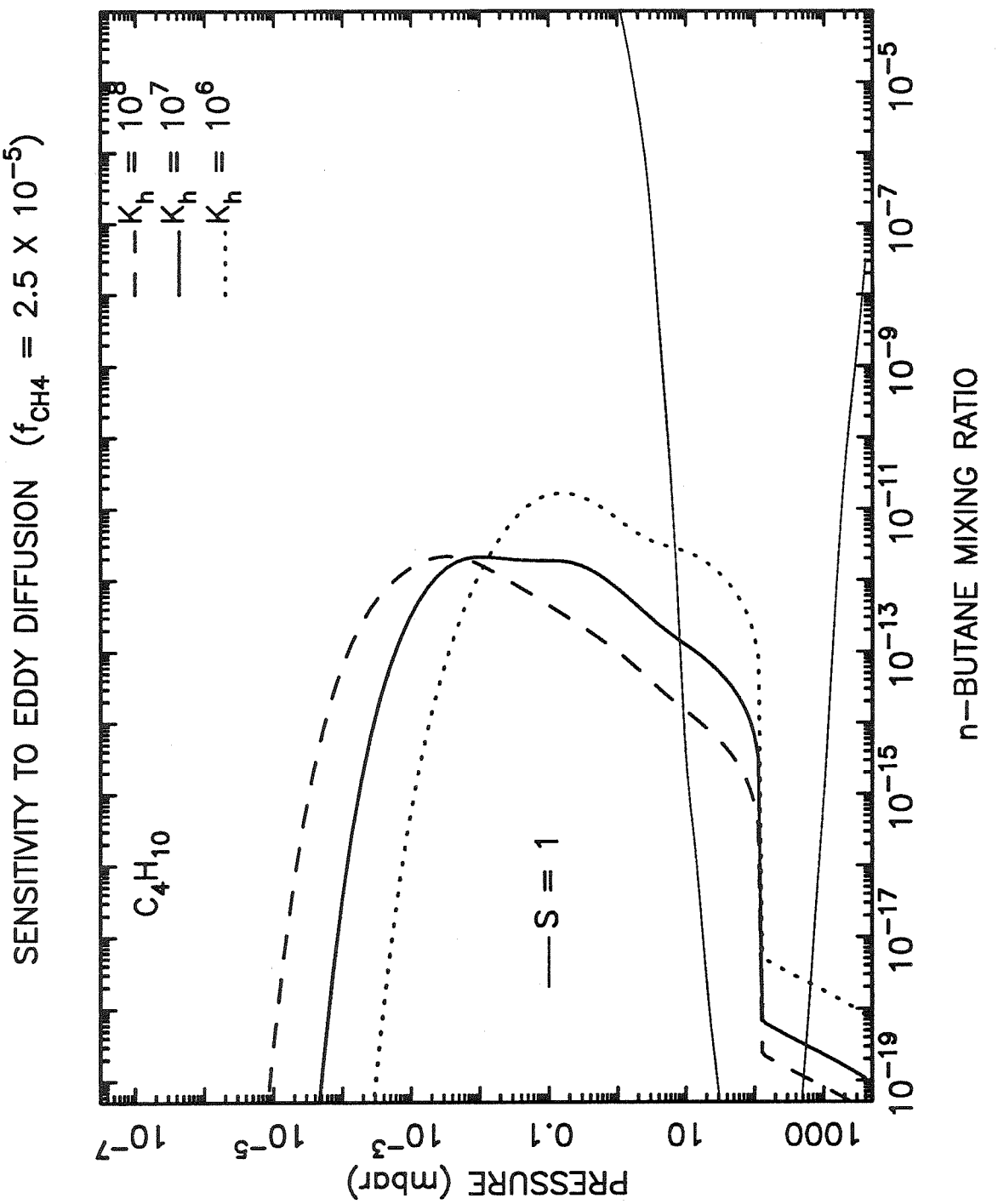

Figure 12h. Sensitivity of the butane mixing ratio to the eddy diffusion profile. The stratospheric methane mixing ratio in all three cases is 2.49 $\times$ 10^{-5}.

is determined by

$$K = K_h \left(\frac{n_h}{n}\right)^{\beta}$$

where K_h and n_h are, respectively, the eddy diffusion coefficient and the atmospheric number density at the methane homopause, and the slope β varies from 0.5 to 0.65. An increase in the value of β will increase the mixing ratios of the long–lived hydrocarbon species in the lower atmosphere because diffusive transport becomes less efficient at removing these species from the stratosphere.

Sensitivity to solar flux

The flux values we use in our standard model are representative of those observed near solar maximum; i.e., 1982 and 1988 values. Since the solar ultraviolet flux varies substantially with the 11–year solar cycle, we have also examined the sensitivity of our model to changes in the solar flux. The results are shown in Figs. 14a and 14b.

The solar minimum flux values we use are typical of those encountered in 1976 or 1985. From 50 to 1050 Å, the flux was taken from the 1976 solar minimum values of Torr and Torr (1985). We have estimated the flux in the 1050 to to 1175 Å range in the manner of Gladstone *et al.* (1991) and use Solar Mesospheric Explorer satellite observations to determine the flux in the 1175 to 3050 Å region. Between 3050 and 8000 Å, we use values compiled by the World Meteorological Organization (Frederick *et al.* 1985). The solar H Ly α flux (at 1 AU) used in our solar minimum model is 2.38×10^{11} photons cm^{-2} s^{-1}.

For solar maximum, we use flux values typical of those observed for the maximum of solar cycle 21. From 50 to 1050 Å, we have adopted the 1979 solar maximum values of Torr and Torr (1985). Between 1050 and 1200 Å, we estimate the flux as

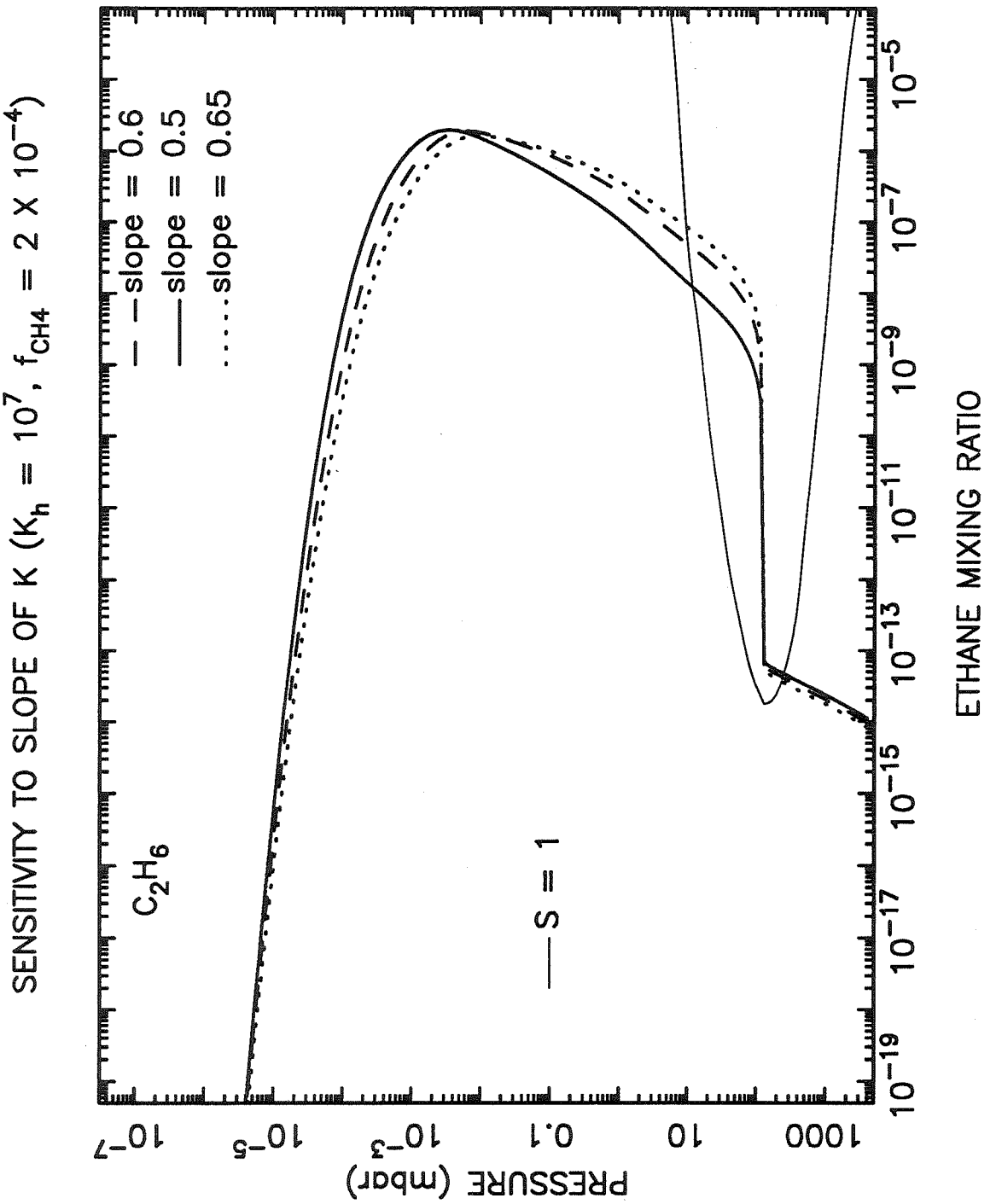

Figure 13. Sensitivity of the ethane mixing ratio to the slope of the eddy diffusion profile. The stratospheric methane mixing ratio in all three cases is 2.49 $\times$ 10^{-5}, and the eddy diffusion coefficient is $\sim$ 10^7 at the methane homopause.

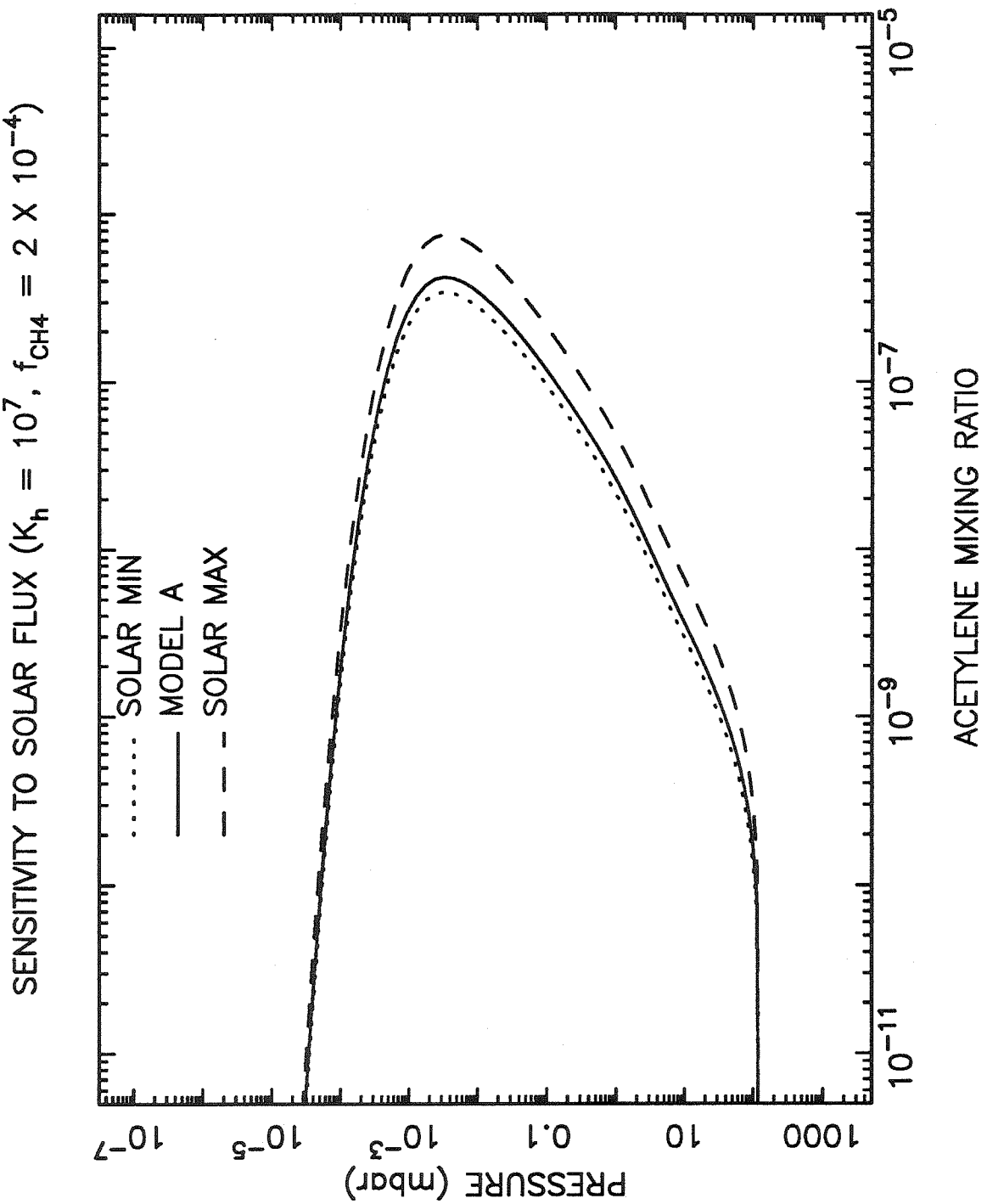

Figure 14a. Sensitivity of the acetylene mixing ratio to the solar flux.

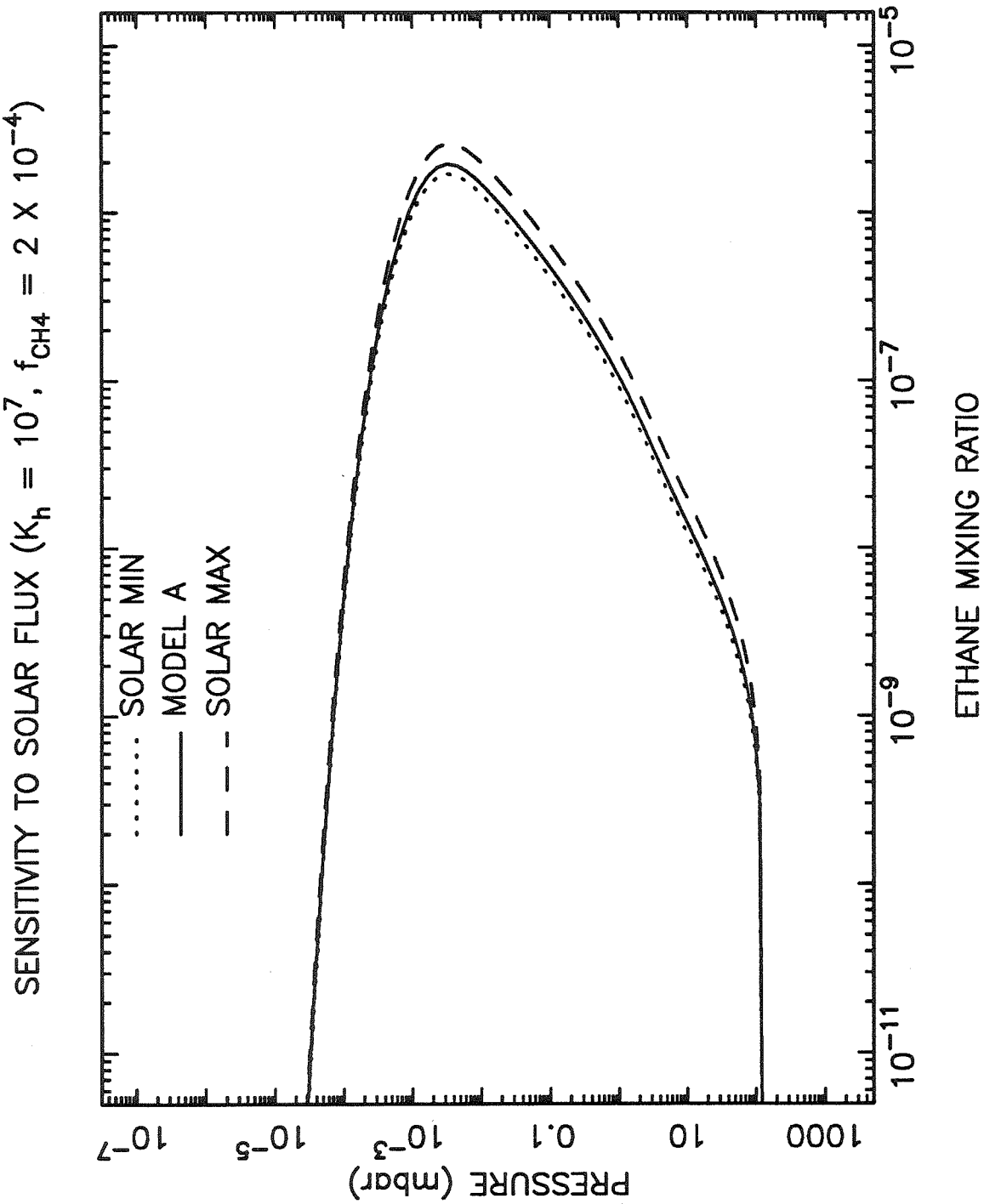

Figure 14b. Sensitivity of the ethane mixing ratio to the solar flux.

described in Gladstone *et al.* (1991), and from 1200 to 2800 Å, we use the July 1980 values of Mount and Rottman (1981). From 2800 to 3300 Å, we use the data of Mentall *et al.* (1981), and between 3300 and 8000 Å, we use values compiled by the World Meteorological Organization (Hudson *et al.* 1982). We use a very high solar H Ly α flux in our solar maximum model (5.1×10^{11} photons cm^{-2} s^{-1}) that is only achieved for short time periods during the solar cycle.

Figs. 14a and 14b show that the hydrocarbon abundances are somewhat sensitive to our choice of the solar flux. For instance, the acetylene abundance at the few μbar level doubles between solar minimum and maximum while the ethane abundance increases by about 50%. However, the Ly α value chosen in our solar maximum model is somewhat extreme. For most of the cycle, hydrocarbon abundances will vary between the values typified by the solar minimum model and model A. The solar flux does not have as large an effect as one might expect since interstellar H Ly α contributes strongly at both solar maximum and solar minimum. In addition, the chemical loss time constants of C_2H_2 and C_2H_6 are long in the middle and lower stratosphere, causing the solar effects to be "averaged."

Sensitivity to season

Since Neptune's rotational axis is tilted with respect to its orbital axis by 28.8°, seasonal effects can play a role in the hydrocarbon photochemistry. More solar energy is deposited in the summer hemisphere than in the winter hemisphere because the solar zenith angle is smaller and the day is longer during this season. Since methane photolysis drives the hydrocarbon photochemistry, more C_2 and higher hydrocarbons are produced at summer latitudes than at winter latitudes. Figs. 15a and 15b illustrate this effect for acetylene and ethane. The calculations were performed for

conditions relevant to the UVS solar occultations of the *Voyager* Neptune encounter. At this time, Neptune's southern hemisphere was approaching summer solstice; the atmosphere at 49° S latitude experienced more solar illumination than the 61° N case. In fact, 61° N latitude is almost in perpetual darkness at this time.

However, the hydrocarbon abundances are not as sensitive to latitude as one might expect if the photochemistry was driven by solar radiation alone. The large isotropic H Ly α source from the interplanetary medium ensures that C_2, C_3, and C_4 species are produced all year round. Ethane is particularly insensitive to latitude; the production of C_2H_6 by reaction R135 increases by only 30% in this model between 61° N and 49° S because Ly α is primarily responsible for the production of CH_3 and Ly α from the interstellar medium operates isotropically. Acetylene is more sensitive to seasonal effects because it is produced from the dissociation products of C_2H_6 and C_2H_4, both of which can be photolyzed at longer wavelengths than Ly α.

Comparison with other models

Our photochemical models differ somewhat from those of previous investigations. Most, if not all, of the differences emanate from different assumptions concerning the appropriate boundary conditions and inputs to the photochemical model. Romani and Atreya (1988) find ethane and acetylene mixing ratio profiles that are constant in altitude below $\sim 10^{-2}$ mbar. These constant profiles result from the use of the tropopause as the lower boundary and from the assumption of fixed concentrations at this location. When we use the same stratospheric methane mixing ratio and eddy diffusion profiles as Romani and Atreya (1988), we find very different results. Our hydrocarbon mixing ratios decrease with decreasing altitude due to our assumption that eddy diffusion coefficient increases again in the troposphere and to

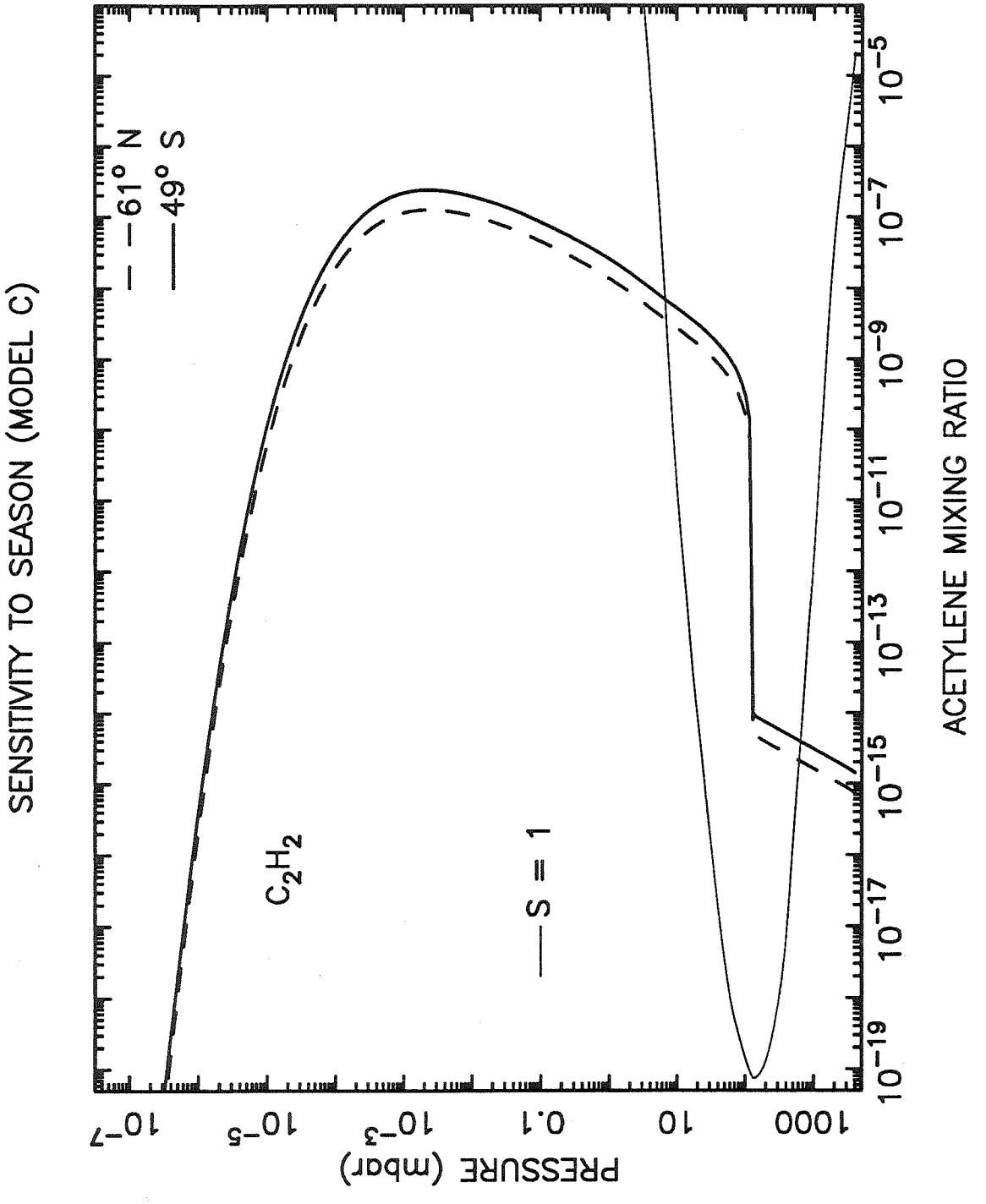

Figure 15a. Sensitivity of the acetylene mixing ratio to the planetary latitude (season). The model calculations were performed at 49° S and 61° N latitude for $L_s = 243°$. The stratospheric methane mixing ratio is 2×10^{-4} and the diffusion coefficient at the homopause is 1.1×10^8.

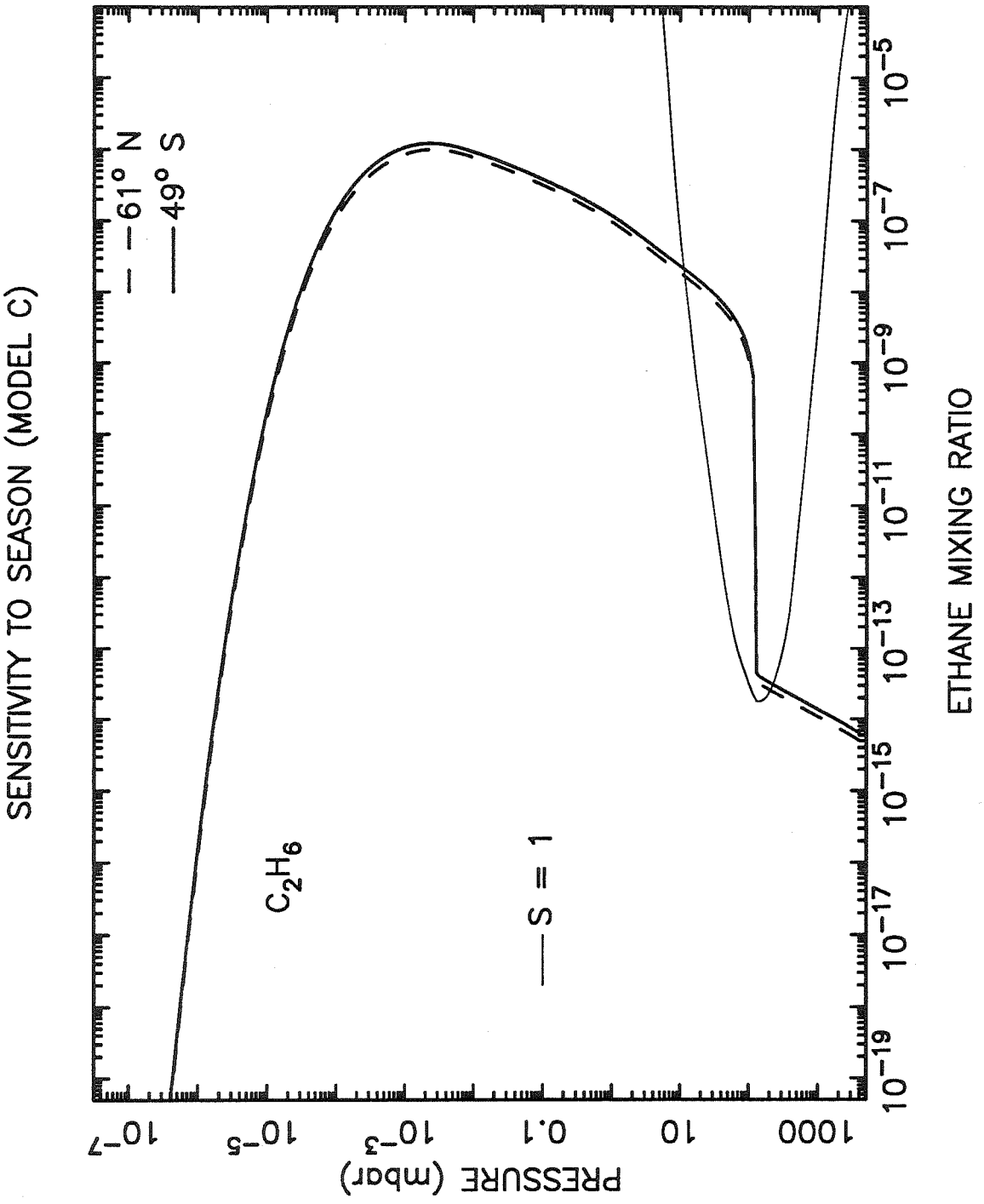

Figure 15b. Sensitivity of the ethane mixing ratio to the planetary latitude (season). The conditions were identical to those of Fig. 15a.

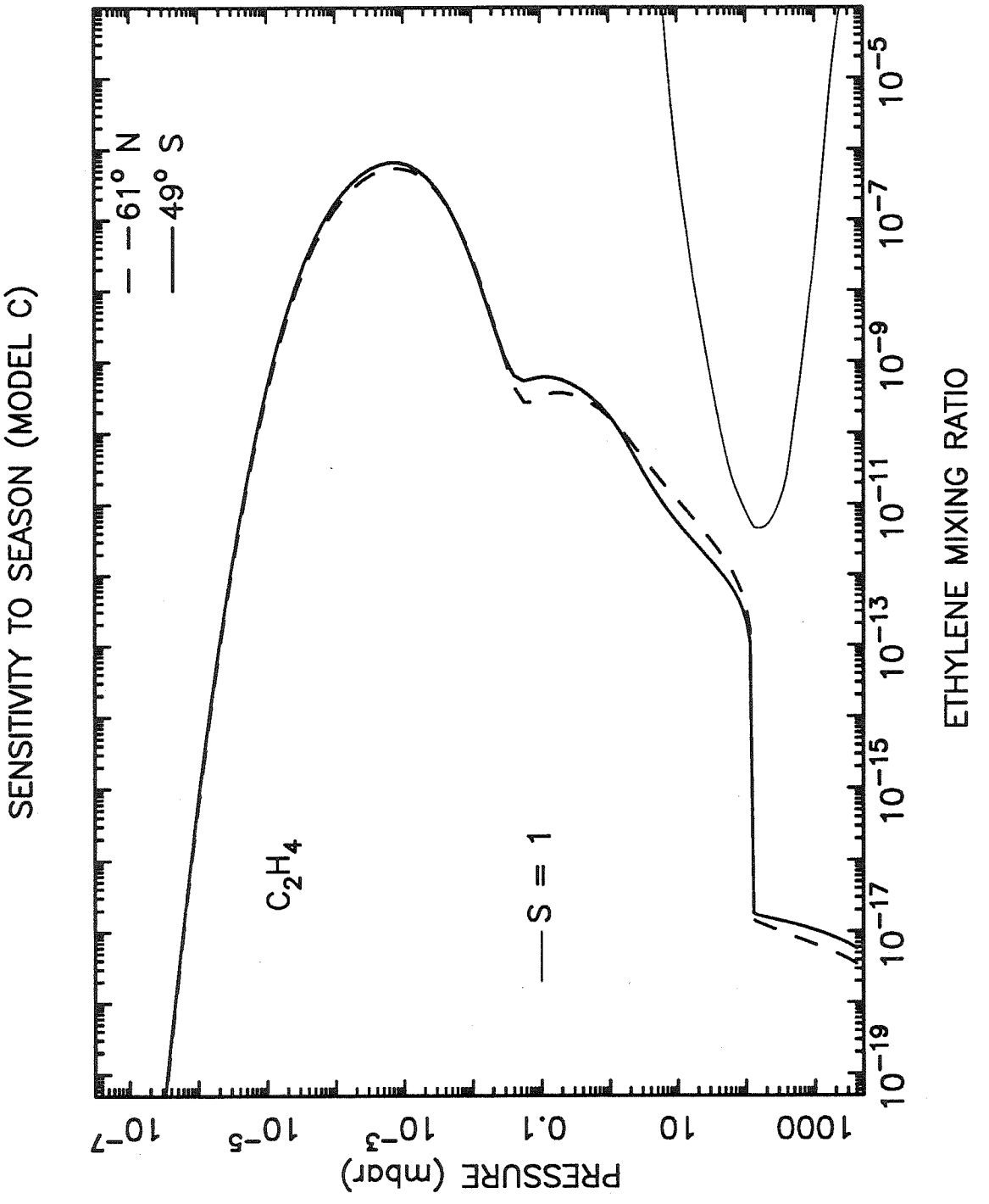

Figure 15c. Sensitivity of the ethylene mixing ratio to the planetary latitude (season). The conditions were identical to those of Fig. 15a.

our assumption that hydrocarbons are transported efficiently to lower atmospheric levels. We know that transport of non–equilibrium hydrocarbons such as C_2H_6 and C_2H_2 to deep tropospheric levels (where CH_4 can be recycled) must be occurring on Neptune or methane would be depleted from the atmosphere over time. Boundary conditions that do not allow for concentration gradients and transport effects into the lower atmosphere are probably unrealistic.

In addition, Romani and Atreya (1988) find that the diacetylene mixing ratio actually increases drastically in the lower atmosphere — a result quite different from ours. It is not clear whether the differences in the diacetylene profiles of our two models are due to different assumptions at the lower boundary or to different photochemistry. Note that Romani and Atreya (1988) do not directly couple their diacetylene chemistry in with the rest of the hydrocarbon chemistry.

Romani and Atreya (1989) updated their photochemical model on the eve of the *Voyager* Neptune encounter. They coupled C_4H_2 in with the rest of the chemistry and considered the effect of hydrocarbon condensation (growth only, not nucleation) on the mixing ratio profiles in the lower atmosphere. They now find mixing ratios that decrease with decreasing altitude as are expected from theoretical considerations as well as are indicated by observations (see below). However, the gradients in mixing ratios of their models are due to condensation loss rather than to vapor transport to the lower atmosphere. Our photochemical results (for C_2H_6 and C_2H_2 for the same assumed diffusion profile and methane abundance) are similar to those of Romani and Atreya (1989) to within a factor of two or so in the middle and lower stratosphere above $\sim$ 10 mbar. However, our diacetylene abundances are much higher than theirs.

To the best of our knowledge, Ashihara (1983) is the only other investigator who has considered the photochemistry C_3 and higher order hydrocarbons in photochemical models of outer planetary atmospheres. Ashihara's results for the C_2 species

on Jupiter, Uranus, and Neptune differ quite a bit from Gladstone (1983), Romani and Atreya (1988, 1989), Summers and Strobel (1989), Gladstone *et al.* (1991), and most photochemical models of outer planetary atmospheres. Some of the differences were suggested to be due to the inclusion of the higher hydrocarbons. However, Ashihara's C_3 and C_4 hydrocarbon abundances are both qualitatively and quantitatively different from ours. These differences are probably due to large differences in the transport assumptions and in the background model atmospheres. In particular, methane photolysis in the Ashihara models occurs at higher pressures and lower temperatures than our models. Thus, three–body reaction rates are more efficient and larger concentrations of complex species are produced. Ashihara (1983) finds that butane is actually more abundant than ethane or acetylene in his model Neptune atmosphere. Given our current knowledge of the temperature and density profiles of Neptune's atmosphere, these calculations are unlikely to be correct.

Bishop *et al.* (1991) use *Voyager* UVS observations to help constrain some of the input parameters to the photochemical models (e.g., the eddy diffusion profile and the stratospheric methane mixing ratio). Bishop *et al.*'s photochemical models are similar to ours in the sense that we use similar temperature profiles, we include the effect of radiation from the local interstellar medium, and, in one case, we test similar eddy diffusion profiles. Although we do not perform calculations at exactly the same conditions as the models of Bishop *et al.* (1991), the magnitudes and overall shape of our ethane and acetylene mixing ratios are similar to the corresponding models of Bishop *et al.* (1991). Specifically, our models correspond to the Bishop *et al.* models that have diffusion profiles that vary linearly with log pressure. Bishop *et al.* (1991) also examine the effect of substantially different eddy diffusion profiles. They conclude that the diffusion coefficient at the methane homopause must be large ($\sim 10^7$ cm^2 s^{-1}) and the diffusion coefficient in the lower stratosphere must

be low ($\lesssim$ a few $\times 10^4$ cm^2 s^{-1} at 1 mbar) to be consistent with the UVS observations. This conclusion is supported by our sensitivity tests and by comparisons of our photochemical models with ground–based and spacecraft observations.

Comparison with observations

Our primary purpose in developing the photochemical models discussed in the previous sections is to derive accurate hydrocarbon vapor abundances for Neptune's lower atmosphere. We can then identify the species that we believe will condense in Neptune's stratosphere and can provide more realistic estimates of the locations of the condensation regions. To determine whether our models accurately predict the hydrocarbon abundances, we now compare our model results with available observations.

Although data on hydrocarbon abundances are limited, the multiwavelength nature of the dataset allows determinations of abundances at varying levels throughout the atmosphere. Thus, altitude variations in the mixing ratios of the species can be directly compared to our photochemical models.

Ground–based and Earth–orbiting telescopes have identified CH_4, C_2H_2, C_2H_6, and C_2H_4 in Neptune's stratosphere. Methane has long been known to be a major constituent on Neptune (e.g., Macy and Sinton 1977, Fink and Larson 1979, Lellouch *et al.* 1986, Orton *et al.* 1987, 1990a). The most recent published analyses of infrared spectra of Neptune (e.g., Orton *et al.* 1990a) advocate a large stratospheric methane mixing ratio of 2%. Large implied abundances are also typically reported in the ground–based analyses of other hydrocarbon species; for example, Orton *et al.* (1990a) find that their emission spectra are consistent with implied maximum stratospheric mixing ratios of 3×10^{-7} for acetylene, 6×10^{-6} for ethane, and 3×10^{-9}

for ethylene. For comparison, the infrared heterodyne spectroscopic measurements of Kostiuk *et al.* (1990) suggest ethane values of 3×10^{-6} while the IUE observations of Caldwell *et al.* (1988) are consistent with lower acetylene mixing ratios of 4×10^{-9} at lower altitudes (in the 1 to 15 mbar range). All of the above observations are representative of global abundances (whole–disk observations), but were taken at different stages of the solar cycle (1981 to 1989). Variations in mixing ratios of a factor of two or less might be explained by variations in the solar flux, but larger variations are probably due to differences in the sampling altitudes or in the assumptions used in the analyses.

The ground–based infrared observations promote hydrocarbon abundances that are consistently higher than predictions from our photochemical models. However, caution should be exercised when considering the reports from the infrared data. The published mixing ratios are quite sensitive to the assumed atmospheric temperature structure. Unfortunately, little information is available at this time concerning the temperature profile in Neptune's middle atmosphere. Recent analyses of *Voyager* data indicate that middle stratospheric temperatures at equatorial regions on Neptune may be much higher than previously supposed (G. S. Orton, personal communication, 1991). Ground–based stellar occultations (French *et al.* 1985) also support this conclusion. Therefore, any observations that sample equatorial latitudes need to be reanalyzed to include possible high temperature components. Orton *et al.* (1990b) find that increasing the stratospheric temperature from the assumed ~150 K from the Orton *et al.* (1990a) analysis to 176 K causes a decrease in the implied stratospheric methane mixing ratio from 2% to $\sim 2 \times 10^{-4}$, a decrease in the C_2H_2 mixing ratio from 3×10^{-7} to $\sim 4 \times 10^{-8}$, and a decrease in the C_2H_6 mixing ratio from 3×10^{-6} to $\sim 9 \times 10^{-7}$. These lower values agree better with our models. Since updated values from ground–based infrared analyses are not yet available, we

do not directly compare these observations with our models.

Measurements of hydrocarbon abundances were also provided by the UVS and IRIS instruments aboard *Voyager*. From the absorption signatures of C_2H_2 and C_2H_6 in the UVS spectra, Broadfoot *et al.* (1989) estimate that acetylene has a mixing ratio of 2×10^{-7} and ethane has a mixing ratio of 3×10^{-5} in the 0.1 to 0.3 μbar range and, from solar occultation light curves, estimate that the acetylene mixing ratio is 2×10^{-8} in the 10 mbar region and the methane mixing ratio is 3×10^{-5} in the 0.1 to 0.01 μbar region of Neptune (at 61° N latitude). In the recent paper of Bishop *et al.* (1991), further analyses of UVS light curves are provided that help determine the methane density in the upper atmosphere and the acetylene mixing ratio in the middle atmosphere.

An analysis of an acetylene emission feature in the *Voyager* IRIS spectrum (Conrath *et al.* 1989) places the C_2H_2 abundance at 3×10^{-7} in the lower stratosphere; however, the analysis requires a knowledge of the temperature structure between 0.01 and 5 mbar. Conrath *et al.* use the temperature profile of Orton *et al.* (1987). As already mentioned, this profile may be too cold — especially at equatorial regions. Since the IRIS spectrum represents an average of individual spectra at latitudes between 10° S and 50° S, it is possible that the quoted abundance is a substantial overestimate. Further analyses are needed.

A comparison of these observations with the results of our photochemical models is presented in Figs. 16a–d. Model A refers to our standard model discussed in Section 2.3. Models B and C are described below and in Table IV. All three models are performed with stratospheric methane mixing ratios of 2×10^{-4}. Models B and C were developed to match the conditions at the time of the *Voyager* Neptune encounter. The latitudes 49° S and 61° N were chosen to correspond to the latitudes sampled during the UVS solar occultation; the 61° N model is presented in Figs. 16a–

TABLE IV

Description of Models A, B, and C

	Lat.	L_s	P_h (mbar)	K_h ($cm^2 s^{-1}$)	eddy slope
Model A	30°N	0°	5.1×10^{-5}	9.2×10^{6}	0.5
Model B	61°N	243°	2.0×10^{-6}	7.5×10^{8}	0.65
	49°S	243°	3.8×10^{-6}	4.7×10^{8}	0.65
Model C	61°N	243°	1.0×10^{-5}	1.1×10^{8}	0.65
	49°S	243°	9.8×10^{-6}	1.1×10^{8}	0.65

c and the 49° S model is presented in Fig. 16d. The UVS observations depicted in Figs. 16a–c (Broadfoot *et al.* 1989, Bishop *et al.* 1991) are from 61° N, but the IRIS observations (Conrath *et al.* 1989) are from 10 to 50° S, and the rest (Caldwell *et al.* 1988, Kostiuk *et al.* 1990) are from whole–disk observations. In Fig. 16d, the 49° S observations of Bishop *et al.* (1990) are presented.

The background atmosphere for the models in Figs. 16a–d is computed from the equation of hydrostatic equilibrium with the "warm" temperature profile of Fig. 1. Models B and C contain 19% helium by volume while Model A contains 14.7%. Since the temperature structure of Neptune's atmosphere is not well known, our altitude–pressure profile may be inaccurate. In addition, we approximate the gravitational acceleration by

$$g = \frac{GM}{r^2}\left[1 + \frac{3}{2}J_2\left(\frac{R_o}{r}\right)^2\left(1 - 3\sin^2\phi\right)\right] - \omega^2 r\cos^2\phi \qquad [2]$$

where r is the radial distance from the center of the planet, G is the universal gravitational constant, M is Neptune's mass, R_o is the equatorial radius, J_2 is the second zonal harmonic coefficient, ϕ is the latitude, and w is the angular velocity (the planet's

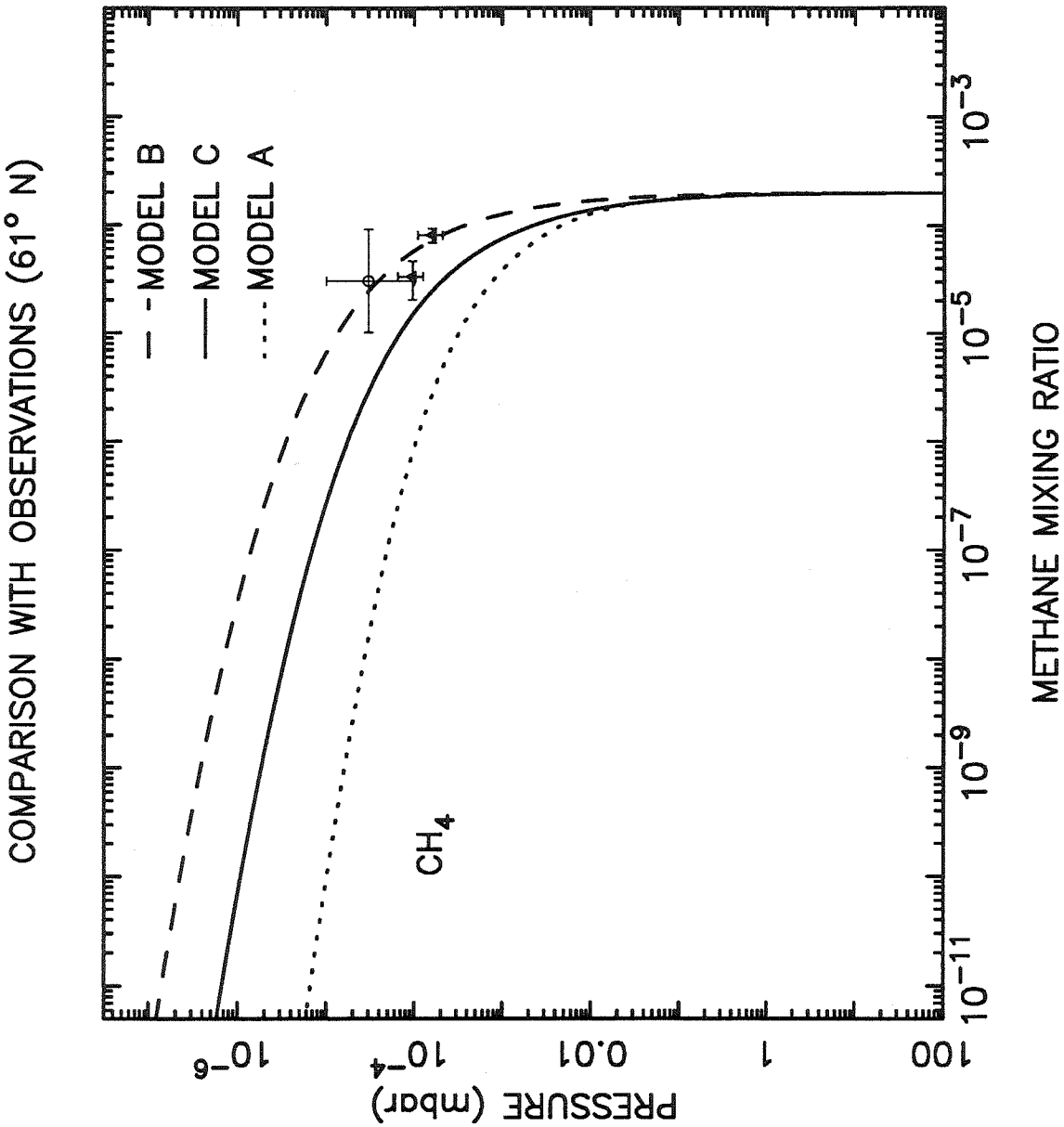

Figure 16a. A comparison of the methane mixing ratio profiles of three of our photochemical models with some Earth–based and *Voyager* observations. The models are described in the text and in Table IV. In Figs. 16a–c, the open circles refer to the observations of Broadfoot *et al.* (1989), the triangles to the observations of Bishop *et al.* (1991), the star to a measurement of Conrath *et al.* (1989), the solid circle to observations of Kostiuk *et al.* (1990), and the square to observations of Caldwell *et al.* (1988).

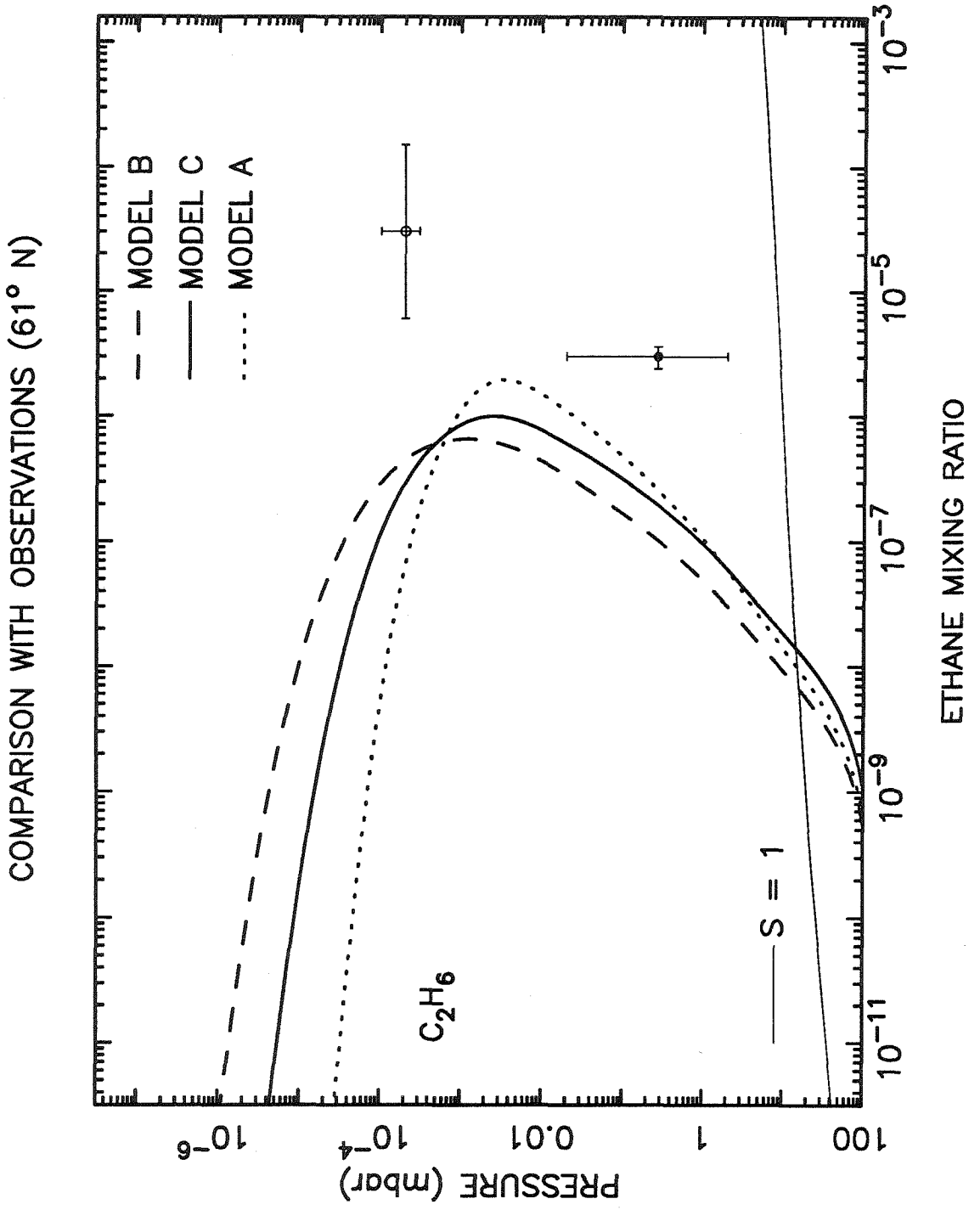

Figure 16b. A comparison of the ethane mixing ratio profiles of three of our photochemical models with various Earth–based and *Voyager* observations. See Fig. 16a for an explanation of the data points.

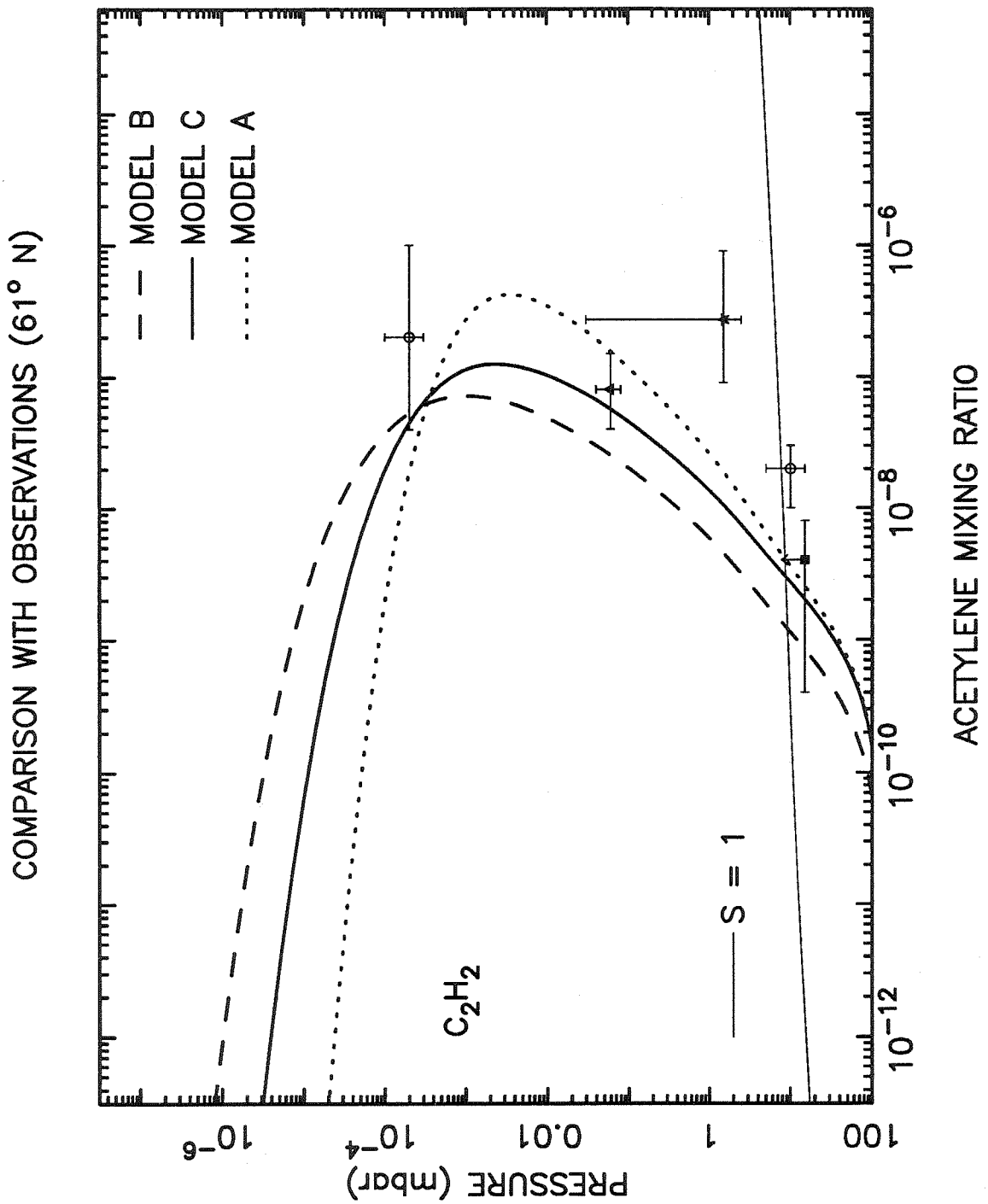

Figure 16c. A comparison of the acetylene mixing ratio profiles of three of our photochemical models with various Earth–based and *Voyager* observations. See Fig. 16a for an explanation of the data points.

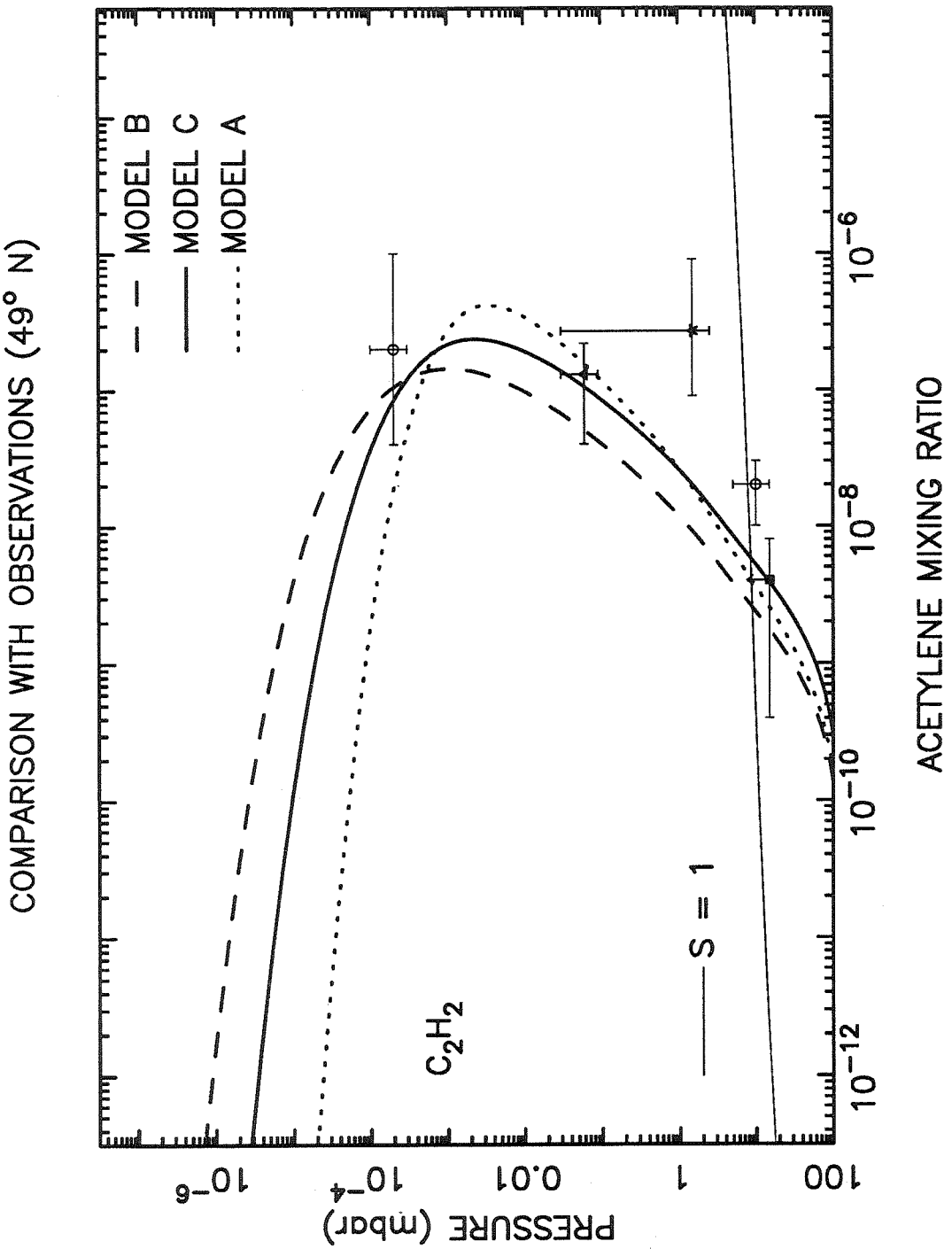

Figure 16d. A comparison of the acetylene mixing ratio profiles of three of our photochemical models with various Earth–based and *Voyager* observations (see Fig. 16a). Both the model and the observations of Bishop *et al.* (1991) refer to 49° S latitude.

rotation plus winds). Most of the parameters that go into equation [2] are determined by the *Voyager* RSS team (e.g., Lindal *et al.* 1990): $GM = 6.835 \times 10^{21}$ cm^3 s^{-2}, $J_2 = 3.411 \times 10^{-3}$, $R_o = 24764$ km at 1 bar, and the angular velocity equals

$$\omega = \left[\frac{2GM}{R_o^3}\left(f - \frac{3}{2}J_2\right)\right]^{1/2}$$

where f is the flattening $(R_o - R_{pole})/R_o$ observed by Lindal *et al.* (1990). By using this equation, we neglect the latitudinal component of the gravitational acceleration as well as J_4 and higher harmonic terms. As a result, our angular velocity is not quite consistent with *Voyager* observations and our hydrostatic atmosphere does not quite match that of Lindal *et al.* (1990) or Bishop *et al.* (1991).

In particular, our latitudinal variation of the 1 bar reference radius does not exactly follow that presented by Lindal *et al.* (1990). Although our polar and equatorial radii match those of Lindal *et al.*, we find a radius of 24523 km rather than 24535 km at 49° latitude and a radius of 24440 km rather than 24446 km at 61° latitude. In addition, our background atmosphere is slightly less dense than that of Bishop *et al.* (1991) at middle altitudes and might be quite a bit less dense at high altitudes.

Thus, our hydrostatic atmosphere may depart from those used in the presentations of the observations, and caution should be exercised when directly comparing our models to the observations. Discrepancies are minor at middle and lower altitudes (as is evident from comparing our background atmosphere with that of Bishop *et al.* 1991) but may become larger at high altitudes (e.g., in the regions of the methane measurements). Bishop *et al.* (1991) present their methane observations as density measurements at certain altitude levels. Because our upper atmosphere is less dense than that of Bishop *et al.*, our resulting mixing ratios are larger.

The modeled acetylene mixing ratios compare reasonably well with the ultraviolet observations but are much smaller than the IRIS determination. However,

as already mentioned, updated analyses using warmer temperature profiles may reduce the estimated IRIS C_2H_2 abundance. Except for the IRIS data point, the C_2H_2 abundance seems to be falling off with decreasing altitude in the stratosphere in approximately the manner predicted by the photochemical models.

Although the data are insufficient to distinguish between several different models, certain trends can be discovered from an examination of the methane and acetylene profiles in Figs. 16a and 16c and in previous figures: (1) the eddy diffusion coefficient at the methane homopause is unlikely to be less than 10^7 or the models would be unable to fit either the upper or lower atmospheric data; (2) either the stratospheric methane mixing ratio is high (e.g., greater than a few $\times 10^{-4}$) or the eddy diffusion coefficient is high in the upper atmosphere ($\gtrsim 10^8$ at the methane homopause) in order to fit the upper atmospheric observations; and (3) if $K_h \gtrsim 10^8$ at the CH_4 homopause then the diffusion coefficient must fall off in the stratosphere with a slope greater than 0.5; that is, the diffusion coefficient must be small in the lower stratosphere. The last conclusion was also discussed by Bishop *et al.* (1991).

Most of the observations can be fit by models with $10^7 < K_h < 10^8$, a 2% methane mixing ratio, and an eddy slope of 0.5, or with models that have a lower methane abundance ($\lesssim 2 \times 10^{-4}$), a high eddy diffusion coefficient in the upper atmosphere ($10^8 \lesssim K_h \lesssim 8 \times 10^8$), and a larger eddy slope ($0.6 \lesssim K_h \lesssim 0.75$). These conclusions may change slightly with the use of a different hydrostatic atmosphere.

The model ethane mixing ratios do not compare well with the ground-based or spacecraft observations. Since the stratospheric ethane observation is based on a thermal emission feature, independent knowledge of the temperature structure is necessary; without this knowledge, the observational results remain very uncertain. The UVS C_2H_6 observation (from absorption spectra) of 3×10^{-5} at 0.01 to 0.1 μbar (Broadfoot *et al.* 1989) is nearly impossible to reconcile with the 3×10^{-5}

CH_4 observation at slightly higher altitudes (reported in the same paper, Broadfoot *et al.*). Methane simply cannot be converted that efficiently to higher hydrocarbons in Neptune's atmosphere. At this time, we will not speculate further on the ethane abundance, but will await further data analyses. Allen *et al.* (1991) examined several factors that affect the ethane to acetylene ratio on Jupiter. None of the suggested adjustments of Allen *et al.* increases the ethane to acetylene ratio of our Neptune photochemical model to the very high values currently indicated by observations. Uncertainties in the photochemical rate constants could lead to mixing ratio uncertainties of at most a factor of five, not factors of several orders of magnitude.

In any case, our photochemical models can fit the observations of the acetylene mixing ratio in Neptune's stratosphere with reasonable accuracy. We will proceed with the assumption that those models that fit the acetylene abundances also provide reasonably good estimates of the abundances of ethane and the other hydrocarbon species.

2.4 Summary of Photochemistry Results

We have developed photochemical models of Neptune's atmosphere for use in a study of nucleation and particle formation in Neptune's atmosphere. We consider the photochemistry of hydrocarbon species that contain three and four carbon atoms as well as the traditional C_1 and C_2 species. Our models are based on the Jovian photochemistry models of Gladstone *et al.* (1991), but we use input parameters and boundary conditions relevant to Neptune. *Voyager* observations are used to constrain the temperature profile and composition of the bulk atmosphere; additional information concerning the eddy diffusion coefficient in Neptune's upper atmosphere is considered, but the profile of eddy diffusion with altitude essentially remains a free parameter.

Photolysis of methane by both local interstellar and solar ultraviolet radiation initiates the production of acetylene, ethylene, ethane, and higher hydrocarbon species. Both photolysis and reactions of C_2H_2, C_2H_4, and C_2H_6 with CH and CH_3 radicals lead to the formation of C_3 and C_4 species. About 50% of the C_2 species that are produced in our standard model get recycled back to C_1 species or are converted to C_3 and C_4 hydrocarbons. Most of the C_3 and C_4 compounds produced are converted back to C_2 and C_1 species. Ethane, acetylene, and propane are chemically stable in Neptune's lower stratosphere and are responsible for much of the flux of carbon back into the troposphere.

Several species are abundant enough and have low enough vapor pressures to potentially condense in Neptune's lower stratosphere. Ethane, acetylene, methylacetylene, propane, diacetylene, ethylacetylene, and butane are seven of the most important of these species.

The calculated abundances of the aforementioned species near their condensation regions turn out to be sensitive to the assumed stratospheric methane abundance, the assumed stratospheric and upper atmospheric eddy diffusion profile, the eleven-year variation in the solar ultraviolet flux, and the planetary latitude or season. The eddy diffusion profile is the single most important unknown parameter.

Very few constraints can be placed on the eddy diffusion profile in Neptune's atmosphere by comparing model results with ground-based and spacecraft observations. Some positive indications from our results are as follows: (1) The eddy diffusion coefficient is probably quite high ($> 10^7$ cm^2 s^{-1}) in the upper atmosphere, (2) the stratospheric methane abundance is not well constrained by comparisons of our models with observations, and (3) the diffusion coefficient in the $\sim$ 10 mbar region of the stratosphere is probably less than 10^4 cm^2 s^{-1}.

In order to get accurate vapor mixing ratios in the condensation regions of the

atmosphere, we must couple our photochemical model with a model that considers nucleation and condensation of the hydrocarbon aerosol particles. We do not present such coupled models in this paper. Instead, we examine the nucleation process in detail and predict the levels at which we expect significant particle formation to occur. The hydrocarbon vapor abundances at altitudes below the predicted condensation levels are therefore not well determined by our models.

3. Nucleation Theory

We now present a brief discussion of the thermodynamic and kinetic aspects of nucleation theory; in particular, we determine the rate of formation of condensed particles in a supersaturated vapor. Our discussion relies heavily on the nucleation rate derivations of McDonald (1962, 1963), Twomey (1977), and Seinfeld (1986). We focus on two broad types of nucleation phenomena — *homogeneous nucleation*, or the formation of new particles ("embryos" of a condensed phase) from the gas phase, and *heterogeneous nucleation*, or nucleation of vapor onto foreign material or surfaces such as ions, pre–existing aerosol particles, or container walls. We distinguish between heterogeneous nucleation about ions, which we will call ion–induced nucleation, and heterogeneous nucleation about spherical insoluble particles, for which we use the general term heterogeneous nucleation.

3.1 Homogeneous Nucleation

As is discussed by Twomey (1977), homogeneous nucleation occurs when vapor molecules develop associations or clusters of more than one molecule; for example, dimers, trimers, etc. These associations evolve during the frequent random encounters between individual molecules in a gas, and the clusters formed in this manner can exist for a finite period of time before being broken up by further collisions. At any one time, the probability that a grouping of g molecules can be found in a local region is finite, but generally very small, and depends on the change in energy of the system that is experienced upon the formation of the particle. If the molecular clusters grow to some arbitrary size (containing tens or hundreds of molecules), then they can be considered as embryos of a completely new phase rather than as vapor molecules.

The classical theory of homogeneous nucleation (often called the spherical or liquid drop model) is based on work by W. Thomson (later, the Lord Kelvin, 1870)

who used the fact that the vapor pressure of a spherical drop of finite radius in equilibrium with vapor is greater than that of a flat–surfaced liquid at the same temperature. In this theory, the formation of a spherical drop (either liquid or solid) of radius r from a system of pure vapor involves a change in free energy of the system of an amount

$$\Delta G(r) = \frac{4}{3}\pi r^3 \Delta G_{vol} + 4\pi r^2 \sigma \qquad [3]$$

where $\Delta G_{vol} = -(\rho/m_1)kT \ln S$ is the bulk free energy per unit volume of the transformation to the condensed phase, ρ is the mass density of the droplet, m_1 is the mass of one molecule of the condensable species, k is the Boltzmann constant, T is the temperature of the system, S is the saturation ratio of the vapor (the actual partial pressure of the condensable vapor divided by its saturation vapor pressure), and σ is the surface free energy of the condensed droplet (e.g., surface tension in the case of liquids). The first term on the right–hand side of equation [3] is proportional to the droplet volume and represents a decrease in the free energy of a system of supersaturated vapor resulting from the decrease in the volume energy occurring during the phase transformation. The second term on the right–hand side of equation [3] is proportional to the surface area of the droplet and represents the free energy increase caused by the creation of an interface between the condensed and vapor phases. For saturation ratios greater than one, the change in free energy of the system can be either positive or negative. Although the surface energy term dominates the behavior of $\Delta G(r)$ for small clusters such that the free energy change is positive, the volume energy term becomes progressively more important as the particle radius is increased. If the vapor is supersaturated, ΔG will eventually becomes negative for large particle radii (see Fig. 17), and there will be a maximum in ΔG at some critical radius $r = r_*$ for $S > 1$. Particle growth beyond the critical size is thermodynamically favored. The critical cluster radius r_* can be easily found by taking the derivative of ΔG with

respect to radius and setting the result equal to zero:

$$r_* = \frac{-2\sigma}{\Delta G_{vol}} = \frac{2m_1\sigma}{\rho kT \ln S}.$$

For a fixed temperature and droplet parameters, the value of r_* depends only on the saturation ratio. The more supersaturated the vapor is, the smaller the critical radius r_* and the more likely the formation of stable critical–sized clusters. The free energy of a critical–sized cluster is

$$\Delta G^* = \frac{4}{3}\pi\sigma\left(\frac{2\sigma m_1}{\rho kT \ln S}\right)^2.$$

ΔG^* acts as a barrier to the formation of stable clusters. For fixed particle properties and temperature, ΔG^* is sensitive only to the saturation ratio.

A major assumption in the above expression for ΔG (equation [3]) is that a macroscopic description can be used in formulating the free energy change. This assumption is most certainly invalid for small clusters of say less than ten molecules. For the case of small clusters, macroscopic parameters such as surface tension and particle density have very little meaning. Intricacies of the structure of a small droplet are ignored as well as are the rotation and translation of the droplet. Although corrections to the classical model have been presented, the classical theory reproduces experimental data with reasonable accuracy and will be used throughout this study.

For a dilute mixture of condensable vapor in an atmosphere, the concentration of molecular clusters can be described by a Boltzmann distribution

$$n_g = n_1 \exp\left(\frac{-\Delta G}{kT}\right)$$

where n_1 is the total number of molecules of condensable vapor in the system. Because of our use of the approximate expression for ΔG, this distribution function actually departs from reality for very small and very large particles. For instance, for particle radii much larger than r_*, we would expect ΔG to become negative and $n_g/n_1 > 1$.

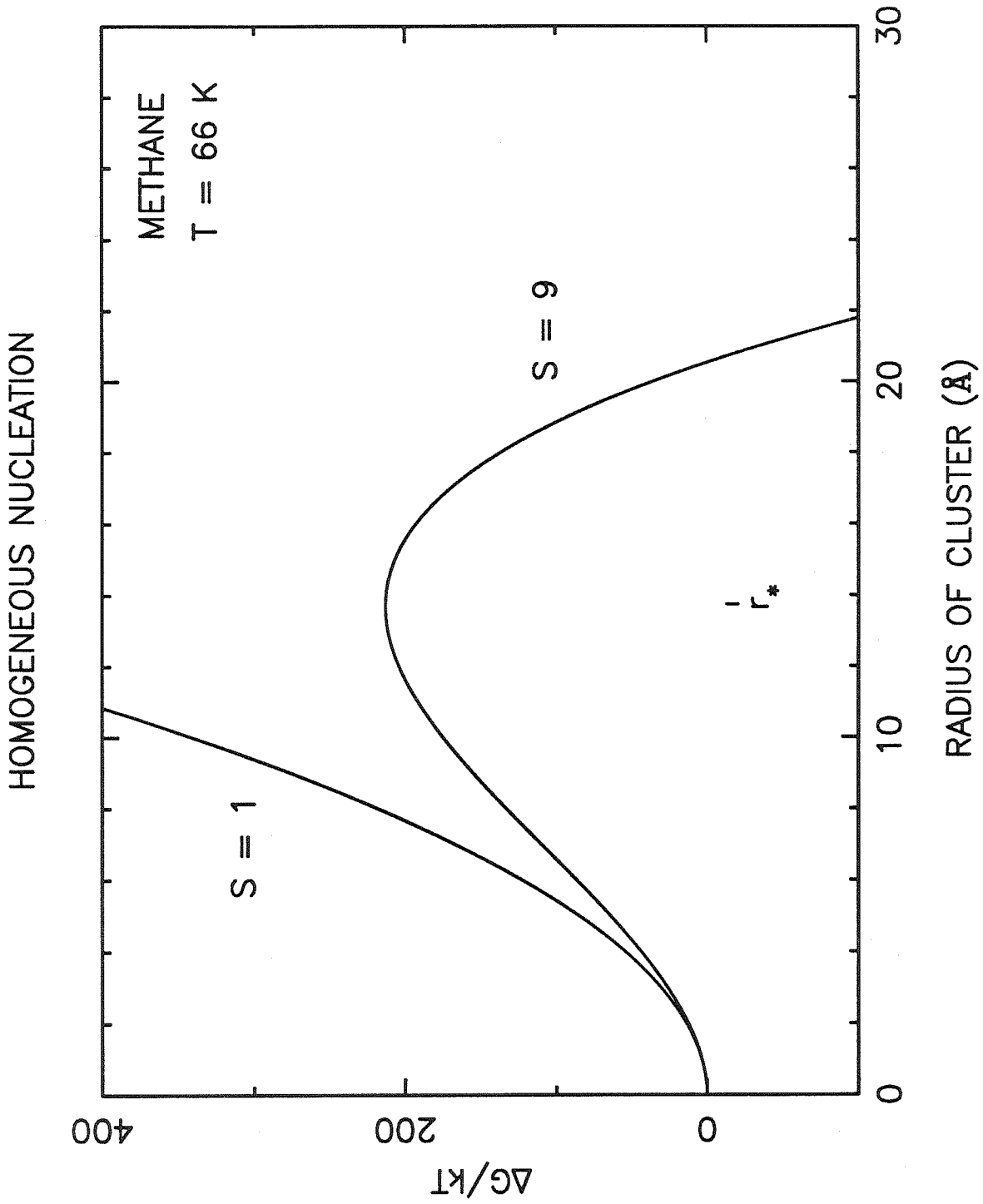

Figure 17. The free energy change as a function of droplet radius for a system of vapor with saturation ratio S.

Physically, this result has no meaning, and the distribution function is no longer valid when gn_g begins to approach n_1. Fortunately, however, the expression *is* appropriate in the region in which we are interested, near $r = r_*$.

Let us now consider the rate at which molecular clusters grow. A complete derivation of homogeneous nucleation rates can be found in Seinfeld (1986). When a dilute system of condensable vapor first becomes supersaturated, the Boltzmann–type distribution is not appropriate because only the smallest embryos have had time to develop. The population of small, subcritical–sized embryos will be built up quickly by collisional processes and by statistical microscopic density and temperature fluctuations with the system (Farley 1952). The system is unbalanced in the sense that an unequal number of monomers attach to and evaporate from the embryo surface at this time; condensation exceeds evaporation, and embryos of *all sizes* experience a net growth. After a short period of time, an unbalanced steady–state situation is achieved such that the concentration of clusters of size g does not change, but monomers of the condensable vapor flow through the system in such a manner as to balance evaporation and condensation and keep the nucleation rate at a constant, nonzero value. A description of the unbalanced steady–state situation provides the basis of nucleation theory; the steady–state assumption will be valid until the nucleation process begins to deplete the system of condensable vapor and thus force the saturation ratio back to $S = 1$.

The number of stable clusters that can form per second in this unbalanced steady–state situation is described by the following expression for the homogeneous nucleation rate (see Seinfeld 1986):

$$J = \beta\, a(g_*)\, n_1 \exp\left(\frac{-\Delta G^*}{kT}\right)\left(\frac{\gamma}{2\pi}\right)^{1/2} \qquad [4]$$

where β is the flux of monomers onto a unit surface area, $a(g_*)$ is the surface area of a critical–sized cluster, $n_1 \exp(-\Delta G^*/kT)$ is the equilibrium concentration of em-

bryos of critical radius r_*, $(\gamma/2\pi)^{1/2}$ is the Zeldovich factor Z which accounts for the nonequilibrium nature of the cluster distribution, and

$$\gamma = -\frac{1}{kT}\left[\frac{\partial^2 \Delta G}{\partial g^2}\right]$$

with the second derivative evaluated at $g = g_*$.

The number of molecules striking a unit area per unit time in a gas is $n\langle c\rangle/4$ where the mean molecular speed of the vapor molecules $\langle c\rangle = (8kT/\pi m)^{1/2}$. Since the partial pressure of monomers of the condensable species can be described by the ideal gas law, $p_1 = n_1 kT$, the flux, β, of monomers onto a unit surface area in the above expression for the nucleation rate can be written as

$$\beta = \frac{1}{4}\left(\frac{8kT}{\pi m_1}\right)^{1/2}\frac{p_1}{kT} = \frac{p_1}{(2\pi m_1 kT)^{1/2}}.$$

If we assume that the growing cluster is spherical, then the cluster surface area is $a(g_*) = 4\pi r_*^2$. Although β and n_1 are sensitive functions of temperature and saturation ratio (through the expression for vapor pressure), the exponential term generally dominates the nucleation rate. For a given saturation ratio, lower temperatures lead to slower nucleation rates because the exponential term varies with the inverse cube of the temperature. However, S generally increases drastically with decreasing temperature so if S is not fixed, then nucleation is more likely at cold temperatures. Descriptions of the behavior of the nucleation rate as a function of temperature and saturation ratio will be presented when we directly apply these equations to the conditions in Neptune's atmosphere (Section 4).

In summary, homogeneous nucleation can occur when large supersaturations are maintained for a long enough time that a net flow of single vapor molecules to larger clusters of molecules develops. Because a free energy barrier to the formation of large clusters exists, the equilibrium distribution of cluster sizes strongly favors small clusters; however, under the right conditions, cluster growth can be initiated.

Once the particles grow to a size where the free energy barrier is a maximum (at critical cluster radius r_*), any further growth is thermodynamically favored. Because of the exponential term in equation [4], the nucleation rate J is extremely sensitive to the saturation ratio S — a small increase in S results in a large increase in the rate of formation of stable particles.

3.2 Ion–Induced Nucleation

Ion–induced nucleation is a type of heterogeneous nucleation in which the condensable vapor species clusters about a gaseous ion. Because of an ion's electrostatic potential, molecules can cluster more efficiently about ions than about other vapor molecules. Wilson's cloud chamber experiments first demonstrated this effect (Wilson 1897). Clustering about ions can be so efficient that small clusters of vapor molecules about ions are stable in an atmosphere and may be thermodynamically preferred over the case of unclustered ions (see Castleman and Tang 1972, Castleman and Keesee 1988).

J. J. Thomson (1888) was the first to theorize that ions could promote the nucleation process. He expanded the classical homogeneous nucleation theory to include nucleation about an electrically–charged spherical droplet. In this theory (later called the classical theory of ion–induced nucleation), the growth of a spherical droplet of radius r consisting of g molecules of the condensable vapor surrounding a metastable ion cluster of radius r_a and charge q is regulated by the free energy change ΔG between the condensed phase and the pure vapor state (Volmer and Flood 1934, Tohmfor and Volmer 1938, Frenkel 1946, Russell 1969):

$$\Delta G_{ion}(r) = -\frac{4\pi\rho}{3m_1} kT \ln S \left(r^3 - r_a^3\right) + 4\pi\sigma\left(r^2 - r_a^2\right) - \frac{q^2}{2}\left(1 - \frac{1}{\epsilon}\right)\left(\frac{1}{r_a} - \frac{1}{r}\right) \quad [5]$$

where ϵ is the dielectric constant of the droplet, and the other parameters are the

same as in homogeneous nucleation. The first two terms on the right–hand side of equation [5] are equivalent to the homogeneous nucleation case, and the third term is the classical electrostatic energy term describing the interaction between the centrally located ion cluster and the surrounding molecules. Since this description of free energy is based on approximate macroscopic thermodynamics, the same uncertainties apply as in the homogeneous nucleation case.

Fig. 18 illustrates the behavior of ΔG_{ion} as a function of particle radius. Note that ΔG_{ion} exhibits both a maximum and a minimum for a certain range of saturation ratios. The thermodynamically–preferred stable cluster size r_a (i.e., at the minimum of ΔG_{ion}) and the critical cluster size r_{i*} (i.e., at the maximum of ΔG_{ion}) can be determined by evaluating the roots of the derivative of the free energy equation (equation [5]) with respect to r:

$$-\frac{4\pi\rho}{m_1}kT\ln S\,r^2 + 8\pi\sigma r - \frac{q^2}{2}\left(1-\frac{1}{\epsilon}\right)\left(\frac{1}{r^2}\right) = 0.$$

The difference in free energy between a cluster of size r_a and a cluster of size r_{i*} will act as an energy barrier and restrict the rate of formation of large clusters — only particles with radii greater than r_{i*} can grow spontaneously; smaller–radii clusters are unstable relative to evaporation. The larger the saturation ratio, the smaller the effective barrier. Fig. 19 shows the effect of variations in the saturation ratio on the free energy curve. Note that the critical cluster size increases and the critical free energy barrier ΔG^*_{ion} decreases with decreasing S. At large enough supersaturations, the free energy barrier can disappear entirely.

The derivation of the ion–induced nucleation rate J_{ion} parallels that of homogeneous nucleation. The free energy now has an additional electrostatic term and has a maximum at $g = g_{i*}$ (or $r = r_{i*}$) rather than at the homogeneous $g = g_*$ (or $r = r_*$). The critical radius r_{i*} is somewhat smaller than the corresponding case for homogeneous nucleation (r_*). The population of ion clusters is described by a

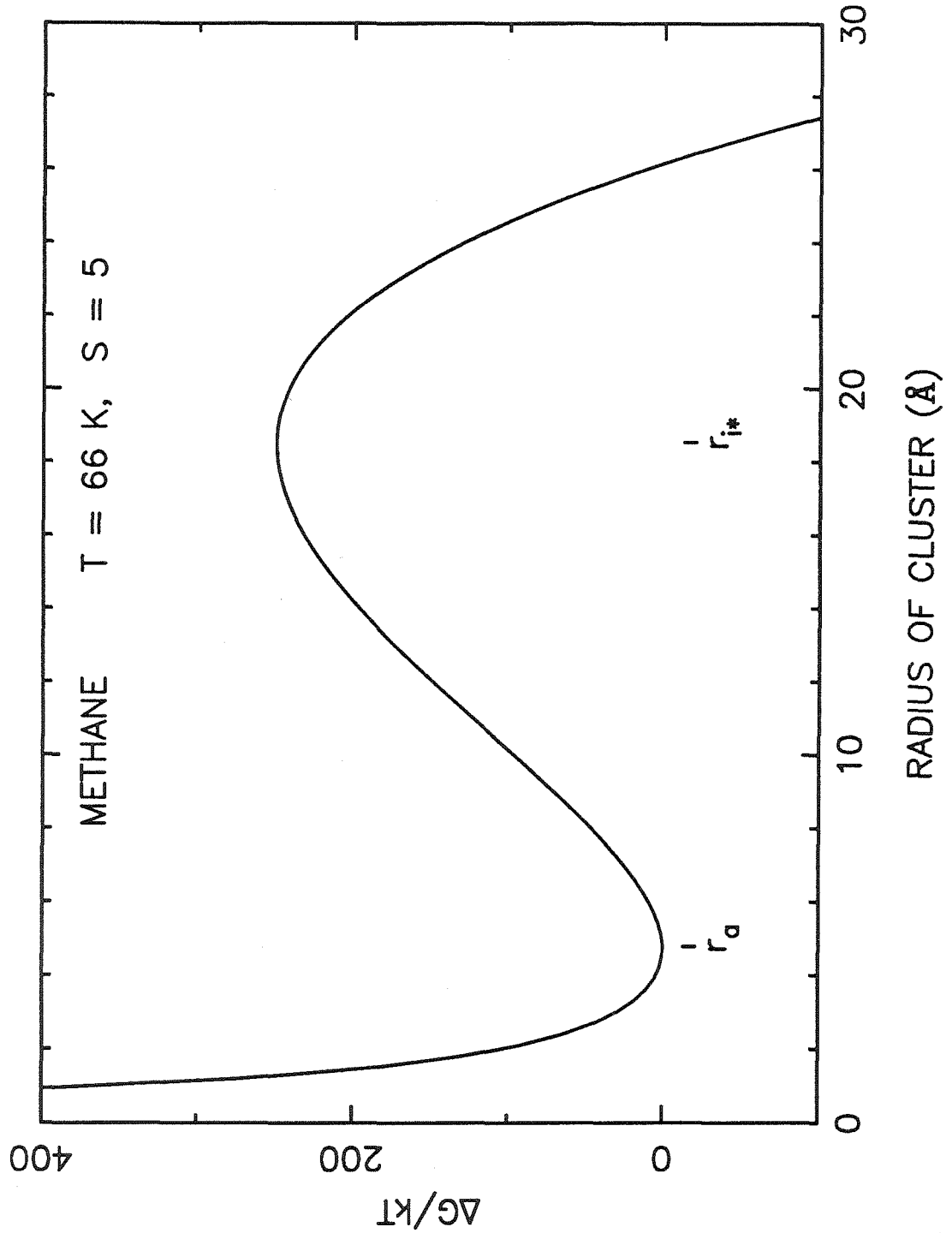

Figure 18. The shape of the free energy for ion–induced nucleation as a function of particle radius. In this paper, we define ΔG_{ion} relative to the free energy of a small metastable ion cluster of radius r_a.

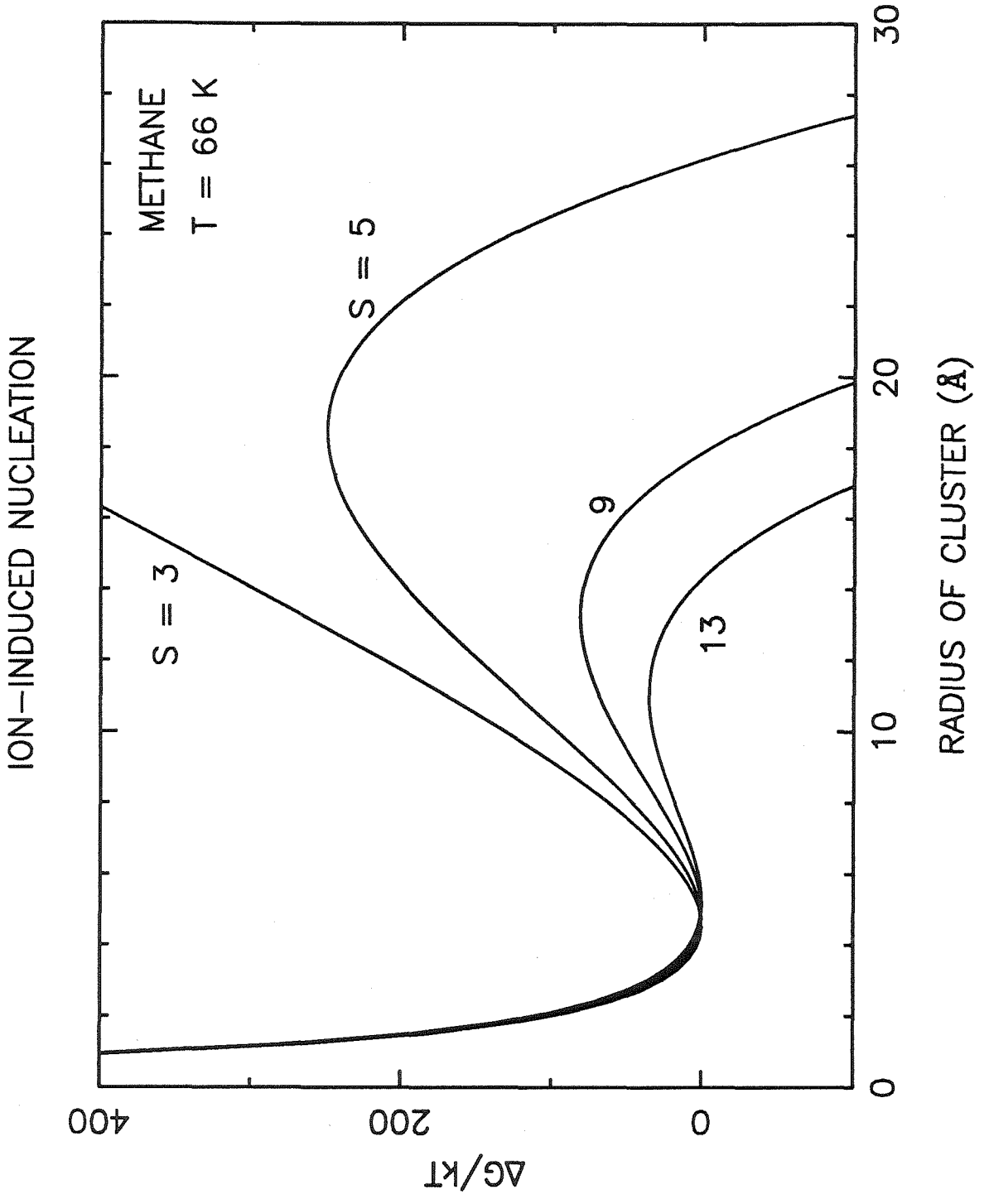

Figure 19. The sensitivity of the free energy curve for ion–induced nucleation to the saturation ratio S. Note that increasing S causes both a decrease in the critical cluster size and a decrease in the magnitude of the free energy barrier.

Boltzmann distribution defined in terms of the number of small stable ion clusters; that is,

$$n_g = n_a \exp\left(\frac{-\Delta G_{ion}}{kT}\right)$$

where n_a is the number density of stable ion clusters of radius r_a. In a dilute system, most of the ions are found in small clusters, so n_a is often approximated by n_{ion}, the total ion number density (Castleman and Tang 1972). The resulting ion–induced nucleation rate is

$$J_{ion} = \beta\, a(g_{i*})\, n_{ion} \exp\left(\frac{-\Delta G^*_{ion}}{kT}\right) Z \qquad [6]$$

where ΔG^*_{ion} is the free energy at $g = g_{i*}$, $a(g_{i*})$ is the surface area of the critical cluster ($4\pi r^2_{i*}$), β is the same as in homogeneous nucleation, and Z is the Zeldovich factor again, $(\gamma/2\pi)^{1/2}$, where

$$\gamma = -\frac{1}{kT}\left[\frac{\partial^2 \Delta G}{\partial g^2}\right]_{g=g_{i*}}$$

or

$$Z = \left(\frac{4\pi r^2_{i*} + \frac{q^2}{r_{i*}}\left(1 - \frac{1}{\epsilon}\right)}{9\pi g_{i*} kT}\right)^{1/2}.$$

For both homogeneous and ion–induced nucleation, the Zeldovich factor ranges from $\sim 10^{-4}$ to 10^{-1} for a wide variety of conditions and is usually $\gtrsim 10^{-2}$. Since the exponential terms can vary by hundreds of orders of magnitude with changes in conditions, variations in Z are not important, and the nucleation rates are really controlled by the size of the energy barriers ΔG^* and ΔG^*_{ion}.

For any given saturation ratio and particle radius, nucleation about charged particles is more efficient than homogeneous nucleation. In fact, as S becomes large, the energy barrier to ion–induced nucleation can disappear completely. At this point, the formation of stable clusters is not thermodynamically inhibited; however, cluster formation is still limited by the kinetics of gas motion and the probability of encounters between vapor molecules and the growing clusters.

As with homogeneous nucleation, the formula for the free energy change in classical ion–induced nucleation is inaccurate because of the adoption of some of the same approximations as in the homogeneous liquid drop model (e.g., macroscopic thermodynamic properties, no rotational or translational effects, etc.). In addition, classical ion theory ignores any perturbation effects that the ion may produce in the droplet itself. Numerous corrections to the classical ion model have been presented (e.g., Castleman 1979, Chan and Mohnen 1980, and Suck *et al.* 1982) but are often semi–empirical in nature and were designed to match experimental data on H_2O condensation about ions; thus, these formulations are probably not relevant to our hydrocarbon condensation problem. Also, many of the thermodynamic parameters required for evaluation of these theories are not known for the hydrocarbon species we are considering. Because of the lack of data on hydrocarbon nucleation and because the classical theories (both ion–induced and homogeneous nucleation) have had reasonable success in matching H_2O experimental data, we have decided to use the classical models in this paper. Large errors in the calculated nucleation rates will lead to only slight errors in the estimated critical saturation ratios for homogeneous or ion–induced nucleation because of the strongly exponential behavior of the nucleation rates; thus, any errors in our calculated nucleation rates resulting from our use of the classical theories would slightly raise or lower our estimates of the hydrocarbon mixing ratios in the condensation regions but would not affect the conclusions of this paper.

3.3 Heterogeneous Nucleation

Both homogeneous and ion–induced nucleation of water under terrestrial conditions require saturation ratios greatly in excess of those observed in the Earth's troposphere and stratosphere. Thus, some other process must be dominating. The presence of dust and other foreign particles in the terrestrial atmosphere allows par-

ticle formation to proceed by heterogeneous nucleation; specifically, nucleation can occur on particles that are either soluble or insoluble in the condensed species. Heterogeneous nucleation about soluble particles is the most effective nucleation process. According to Raoult's Law, the vapor pressure of a solution is lower than that of the pure solvent by an amount equal to the mole fraction of solute present. In the terrestrial atmosphere, nucleation of H_2O on soluble particles can proceed at saturation ratios near unity, or sometimes even at $S < 1$. Heterogeneous nucleation on insoluble particles is not as effective as on soluble particles but is still an important mechanism for particle formation. Because the surface area per given volume of liquid exhibited with condensation about a pre–existing particle is reduced as compared with the surface area which the same volume would exhibit as a homogeneous sphere, heterogeneous nucleation on insoluble particles is more efficient than homogeneous nucleation.

In the terrestrial mesosphere, however, temperatures are so cold that liquids are not involved, and nucleation cannot proceed about soluble particles. Ice nucleation about insoluble particles is very inefficient at cold temperatures ; Keesee (1989) and others estimate that noctilucent cloud formation in the Earth's polar mesosphere requires saturation ratios $\sim$ 100. Since conditions in the Earth's mesosphere are similar to those of Neptune's lower stratosphere and upper troposphere, we now examine the theory of heterogeneous nucleation on an insoluble, partially–wettable spherical substrate. Much of this discussion can be found in Pruppacher and Klett (1978) or Sigsbee (1969).

If an insoluble substrate is immersed in a supersaturated vapor, individual molecules of the condensable vapor can impinge on, adsorb to, and desorb from the substrate surface. Eventually, a steady state of adsorbing and desorbing monomers will be obtained such that the temperature and chemical potential of a molecule

adsorbed on the substrate are the same as a molecule in the vapor phase. Once adsorbed monomers are present on the substrate, embryos of the condensed phase can form on the substrate surface by impingement of one monomer at a time, either directly from the vapor or by surface diffusion of adsorbed monomers across the substrate.

For a spherical insoluble substrate, we assume that a nucleating embryo acquires a cap shape as illustrated in Fig. 20. We can then determine the embryo free energy from the geometry of this figure.

The free energy of formation of a cap–shaped embryo on a spherical substrate is

$$\Delta G_{het}(r) = V(r)\Delta G_{vol} + \sigma A(r)$$

where $\Delta G_{vol} = -\rho/m_1 kT \ln S$, $V(r)$ is the volume of the embryo of radius r, and $A(r)$ is its surface area. Both $V(r)$ and $A(r)$ can be found from the geometry of Fig. 20. First, we note that the contact angle θ that the embryo makes with the substrate is related to the surface tensions of the interfaces of the embryo by Young's relation,

$$\cos\theta = \frac{\sigma_{vN} - \sigma_{cN}}{\sigma_{cv}},$$

where the subscripts v, c, and N refer respectively to the vapor, condensate, and substrate. Following Pruppacher and Klett (1978) and Fig. 20, if we let $\overline{AD} = r(1 - \cos\psi)$ and $\overline{AC} = r_N(1 - \cos\zeta)$ then the volume of the embryo is $V(r) = \pi(\overline{AD})^2\,(3r - \overline{AD})/3 - \pi(\overline{AC})^2(3r_N - \overline{AC})/3$, and the interface surface areas of the embryo are $A_{Nc} = 2\pi r_N \overline{AC}$ and $A_{cv} = 2\pi r \overline{AD}$. Therefore, the volume and total surface energy terms can be written

$$V(r) = \frac{\pi r^3}{3}(2 - 3\cos\psi + \cos^3\psi) - \frac{\pi r_N^3}{3}(2 - 3\cos\zeta + \cos^3\zeta)$$

and

$$\begin{aligned}\sigma A(r) &= \sigma_{cv}(A_{cv} - A_{Nc}\cos\theta) \\ &= 2\pi\sigma_{cv}\left[r^2(1 - \cos\psi) - r_N^2\cos\theta(1 - \cos\zeta)\right]\end{aligned}$$

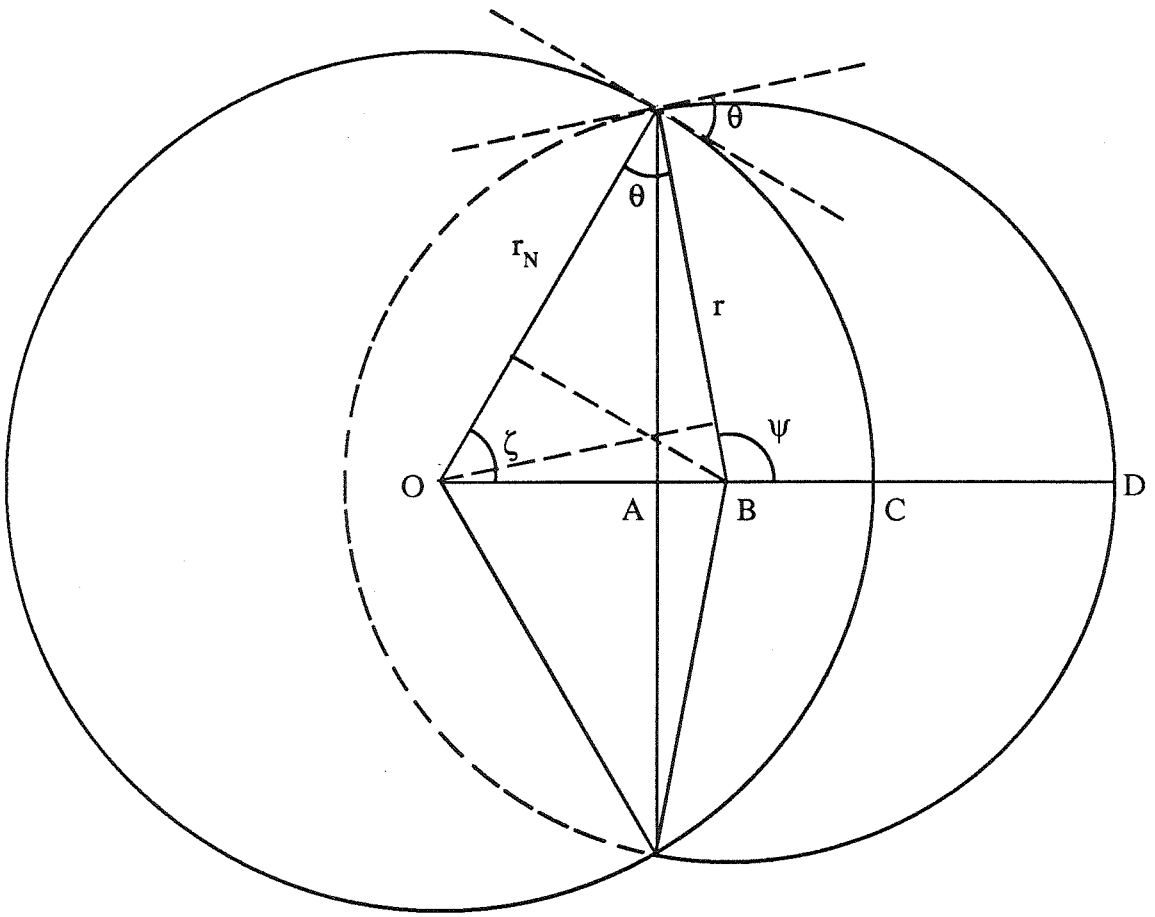

Figure 20. Illustration describing the nucleation of a spherical cap–shaped embryo about a spherical, insoluble, partially wettable substrate of radius r_N.

where

$$\cos\zeta = (r_N - r\cos\theta)/d$$

$$\cos\psi = -(r - r_N\cos\theta)/d$$

$$d = (r_N^2 + r^2 - 2rr_N\cos\theta)^{1/2}.$$

To simplify the equations somewhat, we let $x = r_N/r$, $m = \cos\theta$, and $\phi = (1 - 2mx + x^2)^{1/2}$. Thus,

$$\Delta G_{het} = \Delta G_{vol}\frac{\pi r^3}{3}\left[2 + \frac{3(1-mx)}{\phi} - \frac{(1-mx)^3}{\phi^3} - x^3\left(2 - \frac{3(x-m)}{\phi} + \frac{(x-m)^3}{\phi^3}\right)\right] + 2\pi\sigma_{cv}r^2\left[1 + \frac{1-mx}{\phi} - mx^2\left(1 - \frac{x-m}{\phi}\right)\right]. \quad [7]$$

This expression is similar to the free energy change found in homogeneous nucleation in the sense that both a volume and a surface energy term are present and will compete for $S > 1$.

If we take the derivative of ΔG_{het} with respect to r, we find that ΔG_{het} is a maximum at $r = r_* = -2\sigma/\Delta G_{vol}$, the same result as for homogeneous nucleation (see Fig. 21). However, the free energy barrier at r_* is smaller, in general, than that of homogeneous nucleation. The critical free energy of embryo formation is

$$\Delta G^*_{het} = \frac{16\pi m_1^2\sigma^3}{3(kT\rho\ln S)^2}f(m,x)$$

where

$$2f(m,x) = 1 + \left(\frac{1-mx}{\phi}\right)^3 + x^3\left[2 - 3\left(\frac{x-m}{\phi}\right) + \left(\frac{x-m}{\phi}\right)^3\right] + 3mx^2\left(\frac{x-m}{\phi} - 1\right)$$

with x, m, ϕ as in the previous equation (equation [7]) for $\Delta G_{het}(r)$.

The shape of ΔG_{het} versus embryo radius is illustrated in Fig. 21 for various values of θ. In this figure, we also compare the free energy barriers for ion–induced nucleation and homogeneous nucleation with those of heterogeneous nucleation. Note

that heterogeneous nucleation has a much smaller barrier than that of homogeneous nucleation, but the relative magnitude of the ion–induced nucleation barrier relative to that of heterogeneous nucleation depends on the value of the contact angle. Although r_N was held fixed in these cases, the magnitude of the energy barrier is also quite sensitive to the insoluble particle radius r_N. Note that the critical cluster radius for ion–induced nucleation (r_{i*}) in this case is not much different from that of homogeneous or heterogeneous nucleation (r_*); differences show up more readily in plots of ΔG versus the number of molecules in a critical–sized cluster.

Having derived an expression for ΔG^*_{het}, we can now determine the heterogeneous nucleation rate on spherical insoluble particles. This derivation is based on work by Fletcher (1958), Sigsbee (1969), and Pruppacher and Klett (1978). A spherical substrate of radius r_N in a supersaturated vapor will frequently encounter individual molecules of vapor. We have already assumed that a steady–state situation develops and the chemical potential of the adsorbed molecules is identical to that of the vapor molecules. Different–sized embryos of the condensed phase will form on the substrate surface as monomers collect together. As in homogeneous nucleation, the equilibrium distribution of embryos (this time on the substrate surface) follows a Boltzmann distribution; that is, an embryo consisting of g molecules will have the form

$$c_g = c_1 \exp\left[\frac{-\Delta G_{het}}{kT}\right]$$

where ΔG_{het} is the energy of formation of an embryo of g molecules, and c_1 is the surface concentration of adsorbed monomers (molecules cm^{-2}). In analogy with homogeneous nucleation, the rate at which stable, critical–sized embryos form on the substrate surface per unit time and unit surface area can be written

$$J^s_{het} = \beta\, a(g_*)\, c_1 \exp\left[\frac{-\Delta G^*_{het}}{kT}\right] Z$$

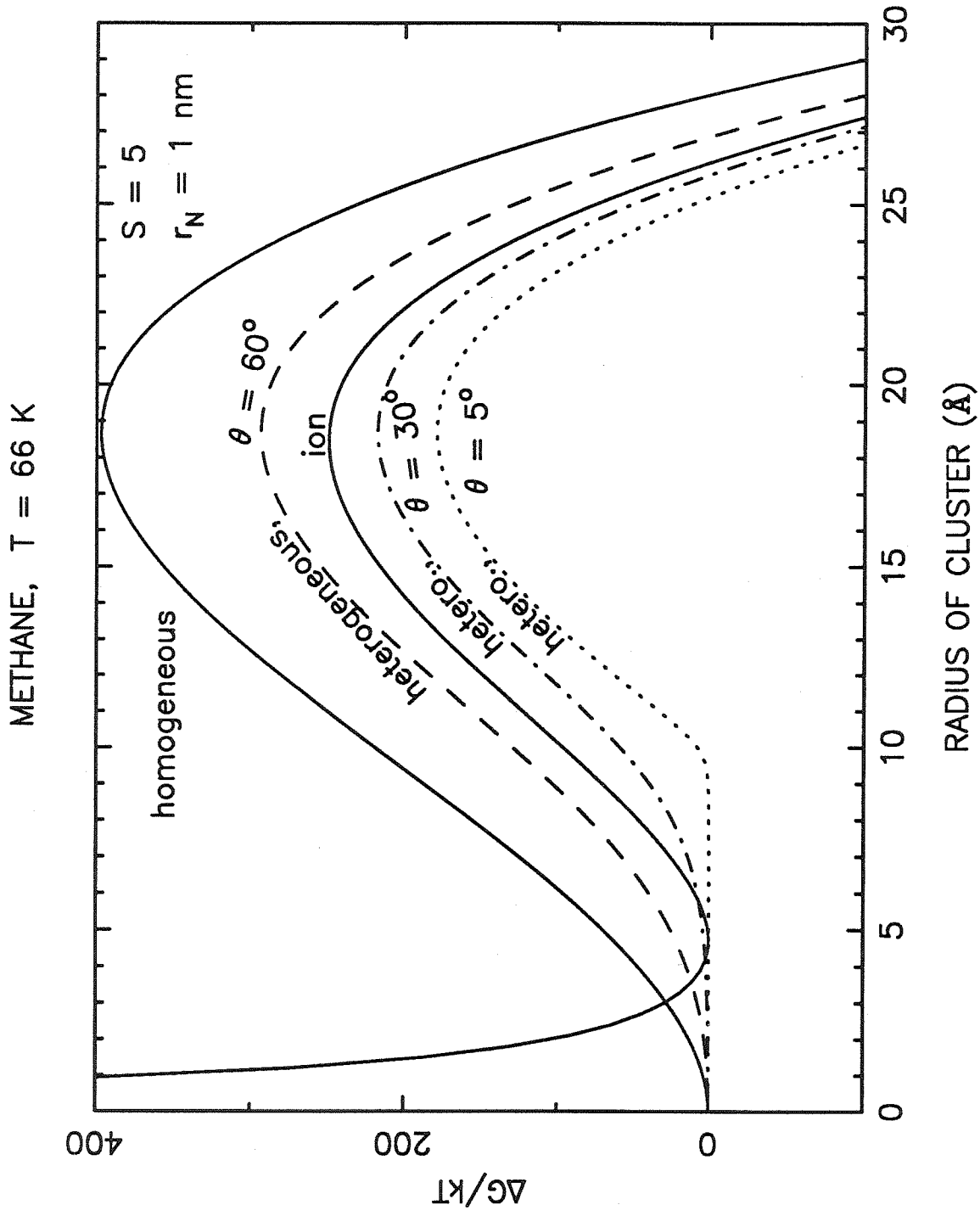

Figure 21. The shape of the free energy curve for heterogeneous nucleation on a spherical insoluble substrate as a function of contact angle and embryo radius. Also shown for comparison are the free energy curves for homogeneous and ion–induced nucleation under the same atmospheric conditions.

where the Zeldovich factor is now

$$Z = \left(- \frac{1}{2\pi kT} \left[\frac{\partial^2 \Delta G_{het}}{\partial g^2} \right]_{g=g*} \right)^{1/2} .$$

The second derivative of ΔG_{het} with respect to g is very messy. We have included the equation for $\partial^2 \Delta G_{het}/\partial r^2$ in Table V below, and one can simply use the derivative chain rule (noting that $g = 4\pi\rho r^3/3m_1$) to find $\partial^2 \Delta G_{het}/\partial g^2$. Since the nucleation rate is relatively insensitive to Z, many workers simply approximate Z by $[\Delta G^*_{het}/(3\pi kT g_*^2)]^{1/2}$, the solution for nucleation on a smooth flat surface. This approximation is valid for both small and large particles as long as r_N does not approach r_*. Even then, the approximate form for Z only differs from the actual expression by a factor of 10 or so — a minor deviation in view of the dominance of the exponential term.

There are two mechanisms by which embryos on a substrate can grow: (1) by direct deposition from the vapor and (2) by surface diffusion of monomer to the embryo. For the direct–deposition case, the mechanism is similar to that of homogeneous nucleation, and

$$\beta a(g_*) = \frac{p_1 \pi r_*^2}{(2\pi m_1 kT)^{1/2}}$$

if we approximate the cap surface area as πr_*^2 (Pruppacher and Klett 1978). For the surface diffusion case, on the other hand, we must take into account the number of monomers adsorbed on the substrate and the rate at which an adsorbed monomer will attach to the embryo. In the surface–diffusion case,

$$\beta a(g_*) = 2\pi r_* \delta \sin\theta \, c_1 \, \nu_s \exp\left[-\Delta G_{sd}/kT\right]$$

where $2\pi r_* \sin\theta$ is the circumference of the cap–shaped embryo, δ is the average distance a monomer will move during a diffusion step, c_1 is the monomer concentration on the substrate surface, ΔG_{sd} is the activation energy for surface diffusion, and

TABLE V

The second derivative of ΔG_{het} with respect to r.

$$
\begin{aligned}
\frac{\partial^2 \Delta G}{\partial r^2} = \frac{\pi \Delta G_{vol}}{3} \Bigg[& - m r_N^2 \left(\frac{-3\,(r_N - mr)\,(r - mr_N)^2}{(r^2 - 2mrr_N + r_N^2)^{\frac{5}{2}}} + \frac{r_N - mr}{(r^2 - 2mrr_N + r_N^2)^{\frac{3}{2}}} \right. \\
& \left. - \frac{2m\,(r - mr_N)}{(r^2 - 2mrr_N + r_N^2)^{\frac{3}{2}}} \right) + r^2 \left(\frac{3(r - mr_N)^3}{(r^2 - 2mrr_N + r_N^2)^{\frac{5}{2}}} - \frac{3\,(r - mr_N)}{(r^2 - 2mrr_N + r_N^2)^{\frac{3}{2}}} \right) \\
& + 4r \left(\frac{-(r - mr_N)^2}{(r^2 - 2mrr_N + r_N^2)^{\frac{3}{2}}} + \frac{1}{\sqrt{r^2 - 2mrr_N + r_N^2}} \right) + 2 \left(1 + \frac{r - mr_N}{\sqrt{r^2 - 2mrr_N + r_N^2}} \right) \Bigg] \\
& + 2\pi\sigma_{vc} \Bigg[- r_N^3 \left(\frac{15(r_N - mr)^3 (r - mr_N)^2}{(r^2 - 2mrr_N + r_N^2)^{\frac{7}{2}}} - \frac{3(r_N - mr)^3}{(r^2 - 2mrr_N + r_N^2)^{\frac{5}{2}}} \right. \\
& + \frac{18m(r_N - mr)^2\,(r - mr_N)}{(r^2 - 2mrr_N + r_N^2)^{\frac{5}{2}}} - \frac{9\,(r_N - mr)\,(r - mr_N)^2}{(r^2 - 2mrr_N + r_N^2)^{\frac{5}{2}}} + \frac{3\,(r_N - mr)}{(r^2 - 2mrr_N + r_N^2)^{\frac{3}{2}}} \\
& \left. + \frac{6m^2\,(r_N - mr)}{(r^2 - 2mrr_N + r_N^2)^{\frac{3}{2}}} - \frac{6m\,(r - mr_N)}{(r^2 - 2mrr_N + r_N^2)^{\frac{3}{2}}} \right) + r^3 \left(\frac{-15(r - mr_N)^5}{(r^2 - 2mrr_N + r_N^2)^{\frac{7}{2}}} \right. \\
& + \frac{30(r - mr_N)^3}{(r^2 - 2mrr_N + r_N^2)^{\frac{5}{2}}} - \frac{15\,(r - mr_N)}{(r^2 - 2mrr_N + r_N^2)^{\frac{3}{2}}} \Bigg) + 6r^2 \left(\frac{3(r - mr_N)^4}{(r^2 - 2mrr_N + r_N^2)^{\frac{5}{2}}} \right. \\
& - \frac{6(r - mr_N)^2}{(r^2 - 2mrr_N + r_N^2)^{\frac{3}{2}}} + \frac{3}{\sqrt{r^2 - 2mrr_N + r_N^2}} \Bigg) + 6r \left(2 - \frac{(r - mr_N)^3}{(r^2 - 2mrr_N + r_N^2)^{\frac{3}{2}}} \right. \\
& \left. \left. + \frac{3\,(r - mr_N)}{\sqrt{r^2 - 2mrr_N + r_N^2}} \right) \right] .
\end{aligned}
$$

ν_s is the frequency of vibration ($\approx 10^{13}\,\mathrm{s}^{-1}$) of an adsorbed monomer against the substrate (Pruppacher and Klett 1978).

The adsorbed monomer concentration c_1 is generally not known but can be estimated by equating the flux of monomers to the surface (β) with the desorption

flux from the surface; or,

$$\frac{p_1}{(2\pi m_1 kT)^{1/2}} = c_1 \nu_s \exp\left[-\frac{\Delta G_{des}}{kT}\right]$$

where ΔG_{des} is the desorption energy of a monomer from the substrate. Thus,

$$c_1 = \frac{p_1 \exp[\Delta G_{des}/kT]}{\nu_s (2\pi m_1 kT)^{1/2}}.$$

If we substitute this result into the equation for heterogeneous nucleation, we find that the rate of nucleation onto a spherical insoluble surface for the case of embryo growth by direct deposition is

$$\begin{aligned} J^s_{het} &= Z \frac{p_1 \pi r_*^2}{(2\pi m_1 kT)^{1/2}} c_1 \exp\left[-\frac{\Delta G^*_{het}}{kT}\right] \\ &= Z \frac{p_1^2 r_*^2}{2 m_1 kT \nu_s} \exp\left[\frac{\Delta G_{des} - \Delta G^*_{het}}{kT}\right]. \end{aligned}$$

The surface nucleation rate for the case of embryo growth by surface diffusion is

$$J^s_{het} = Z \frac{p_1^2 r_* \delta \sin\theta}{\nu_s m_1 kT} \exp\left[\frac{2\Delta G_{des} - \Delta G_{sd} - \Delta G^*_{het}}{kT}\right].$$

The determination of the energy terms ΔG_{des} and ΔG_{sd} is difficult, but experiments indicate that, in general, $\Delta G_{des} > \Delta G_{sd}$ (Pruppacher and Klett 1978). Seki and Hasegawa (1983) report that the desorption energy of water from silicate surfaces is approximately 0.18 eV and estimate that ΔG_{sd} is about one tenth of this ΔG_{des} value.

Since we have little or no information concerning ΔG_{des} and ΔG_{sd} for our hydrocarbon species, we will use the direct–deposition case and will assume $\Delta G_{des} \sim$ 0.18 eV. To a first approximation, the nucleation rate per insoluble particle is $J_{het} = 4\pi r_N^2 J^s_{het}$, or

$$J_{het} = Z \frac{4\pi^2 r_N^2 r_*^2 p_1}{(2\pi m_1 kT)^{1/2}} c_1 \exp\left[-\frac{\Delta G_{het}}{kT}\right]. \qquad [8]$$

As already mentioned, both heterogeneous and ion–induced nucleation are much more efficient than homogeneous nucleation. The relative effectiveness of heterogeneous

versus ion–induced nucleation depends on the size of the insoluble particle and on the "wettability" of its surface. For instance, large r_N's and small θ's promote nucleation while small r_N's and large θ's inhibit it. Although θ has little meaning when we are dealing with solid crystals forming on a solid substrate, $m = \cos\theta$ still is useful in defining a compatibility parameter when discussing the effectiveness of heterogeneous ice nucleation (Pruppacher and Klett 1978).

This formulation for heterogeneous nucleation is clearly oversimplified but agrees fairly well with laboratory work. Its use is warranted by our lack of experimental data on the physical properties and nucleation behavior of hydrocarbons at low temperatures. More detailed descriptions of the variation of the nucleation rate with saturation ratio, substrate size, and contact angle will be given in the next section when we consider nucleation under conditions directly relevant to Neptune. At that time, we will also discuss in more detail the relative efficiencies of homogeneous, ion–induced, and heterogeneous nucleation and will give specific examples of hydrocarbon nucleation rates on Neptune.

4. Application to Neptune

We now apply classical nucleation theory to the formation of hydrocarbon aerosols on Neptune. This work was originally motivated by a study of nucleation and particle formation in the Earth's mesosphere by Keesee (1989); the structural organization of our paper is heavily influenced by Keesee's work. Keesee (1989) and others who have studied nucleation in the terrestrial mesosphere (e.g., Arnold 1980, Gadsen 1981) find that nucleation rates at the Earth's mesopause are negligible until substantial supersaturations of water vapor are established. Although similar situations might be encountered on the outer planets, most studies of cloud and aerosol formation on these planets assume that cloud and haze layers form at saturation ratios of unity.

The cold temperatures found in Neptune's lower stratosphere and upper troposphere severely limit the effectiveness of homogeneous nucleation. Thus, ion–induced or heterogeneous nucleation (or both) must be responsible for particle formation in these regions of Neptune's atmosphere. Before we can discuss these heterogeneous processes in detail, we must first consider the possible sources of ions and condensation nuclei on Neptune and determine whether a sufficient source of ions or foreign nuclei with the appropriate physical properties exists to facilitate nucleation in Neptune's atmosphere.

4.1 Source of Ionization

High energy galactic cosmic rays (GCR's) can provide a source of ionization in Neptune's lower stratosphere. On Earth, galactic and solar cosmic rays are responsible for ion pair production at low levels in the terrestrial ionosphere (e.g., the D layer). The possible importance of cosmic ray ionization in inducing nucleation and forming aerosols in the terrestrial atmosphere has been discussed in the literature

(e.g., Dickinson 1975, Arnold 1980, 1982, Turco *et al.* 1982, Hofmann and Rosen 1983). To determine the importance of ion–induced nucleation as a source of aerosol particle formation in Neptune's atmosphere, we need to determine whether GCR's can produce enough ions to make ion–induced nucleation a viable option. Moses *et al.* (1989) first considered this option for Neptune and our derivation of GCR–induced ionization is similar to theirs.

Very few models of outer planetary ionospheres include the effects of ionization by galactic cosmic rays in spite of the fact that GCR ionization becomes increasingly important relative to solar ultraviolet radiation for planets that are far from the sun. Complete, detailed models of cosmic ray ionization in the atmospheres of Saturn, Uranus, and Neptune presented by Capone *et al.* (1977) show that ionization by GCR's in the stratospheres of the outer planets is considerable. Unfortunately, the models of Capone and his colleagues were based on pre–*Voyager* views of the composition and temperature profiles of the outer planets and are no longer sufficiently accurate for use in examining the importance of ion–induced nucleation in the hydrocarbon condensation regions on Neptune. We have therefore constructed our own model ionosphere of Neptune based on some of the same physical principles as the ionosphere models of Capone *et al.* (1976, 1977, 1979) but have included in our model updated estimates of the temperature structure and composition of Neptune.

According to various models of the 11–year solar–cycle modulation of galactic cosmic rays (GCR's), convection in the outward–spiralling solar wind (Parker 1965, and Gleeson and Axford 1968) and drifts in the large–scale interplanetary magnetic field (Jokipii and Kopriva 1979) cause cosmic rays to diffuse into the heliosphere less efficiently at solar maximum than at solar minimum. Therefore, the GCR flux will be reduced at solar maximum and fewer cosmic rays will enter the atmosphere of Neptune at that time. Since recent spacecraft results from *Pioneer 10* and *11* and

Voyager 1 and *2* (Van Allen and Randall 1985, McKibben *et al.* 1985, and Webber and Lockwood 1987) indicate that a substantial difference in the cosmic ray flux at sunspot maximum and sunspot minimum exists even at 30 AU, we examine the ionization rate at both solar maximum and minimum.

For our ion model, we assume a uniform neutral atmospheric composition with volume mixing ratios $f_{H_2} = 0.83$, $f_{He} = 0.15$, and $f_{CH_4} = 0.02$ at all altitudes. The total absorption cross section σ for the incident cosmic rays is taken to be

$$\sigma = 2f_{H_2}\sigma_H + f_{He}\sigma_{He} + f_{CH_4}(\sigma_C + 4\sigma_H)$$

where σ_H, σ_{He}, and σ_C are the elementary nucleon–nucleus cross sections of H, He, and C and the f's represent the volume mixing ratios listed above. We use the empirical values of $\sigma_H = 3.5 \times 10^{-26}$ cm^2, $\sigma_{He} = 1.15 \times 10^{-25}$ cm^2, and $\sigma_C = 2.6 \times 10^{-25}$ cm^2 that are also used in the models of Capone *et al.* (1976, 1977, 1979) and were obtained from Schopper (1973) and Belletini *et al.* (1966). As in the models of Capone *et al.*, we assume the cross sections to be independent of energy for the range of energies important for the incident cosmic ray particles. The above expression yields a mean cross section for cosmic ray absorption in the atmosphere of $\sigma = 8.3 \times 10^{-26}$ cm^2, implying that an average cosmic–ray particle entering the atmosphere at normal incidence will be stopped by a column of $\sim 10^{25}$ molecules cm^{-2} (or will penetrate to about 50 mbar in our model).

Our ion model is much cruder than the models of Capone *et al.* (1976, 1977, 1979, and 1983) in one important aspect. We consider only the absorption of primary cosmic ray particles and neglect the secondary particle cascade that will result from interactions between primary rays and atmospheric nuclei. For instance, Capone *et al.*'s models take into account the production of secondary protons, neutrons, and pions from high–energy primary particles; the production of gamma radiation from the decay of neutral pions; the production of muons from the decay of charged pions;

and the production of energetic electrons from the absorption and decay of muons. To first order, the secondary particle cascade can be ignored since we are mainly interested in the total deposition of energy with altitude; however, our neglect of secondary particles will cause some errors in our estimates of the magnitudes of the ion production rate profiles in our model. To get a first–order estimate of the errors introduced by neglecting the secondary particle cascade, see Figure 1 of Capone *et al.* (1979), which shows the effect of neglecting the muon flux component of the particle cascade. The muon component only becomes important at large optical depths where the primary cosmic ray flux is severely attenuated (i.e., the troposphere), so our neglect of this component will cause us to underestimate the ion–production rate at tropospheric levels in our model.

The general formula for the number of ion pairs produced (cm^{-3} s^{-1}) at altitude z in a planet's atmosphere by corpuscular radiation can be written (Dubach and Barker 1971, Velinov 1968)

$$q(z) = \frac{1}{W} \int_{E_o}^{\infty} \int_{\Omega} \frac{dE}{dz} j(E, z, \Omega)\, dE d\Omega$$

where W is the mean energy required to form an ion pair in an H_2 atmosphere (36.5 eV, Condon and Odishaw 1972), dE/dz $(= \sigma(E)\, n(z)\, E_k)$ represents the energy lost during the inelastic collision that produced the ionization, E_k is the kinetic energy of the ionizing particle, $j(E, z, \Omega)$ represents the differential energy spectrum (particles cm^{-2} s^{-1} sr^{-1} MeV^{-1}) of incoming ionizing particles, and Ω is the solid angle. For cosmic rays entering the atmosphere at a zenith angle θ, the differential spectrum can be written

$$j(E, z, \theta) = j_o(E) \exp\left(- \frac{\sigma(E)}{\cos\theta} \int_z^{\infty} n(z) dz \right)$$

where $j_o(E)$ is the differential spectrum just outside the atmosphere. If we assume that σ is independent of energy and that the cosmic rays are entering isotropically

into the atmosphere, the ion production rate can be simplified to

$$q(z) = \frac{2\sigma n(z)}{W}\phi_o \int_0^{\pi/2} \exp\left(-\frac{\sigma}{\cos\theta}\int_0^{\infty} n(z)\,dz\right)\sin\theta\,d\theta$$

where ϕ_o is the energy flux (GeV cm^{-2} s^{-1}) of cosmic rays greater than E_o:

$$\phi_o = \pi \int_{E_o}^{\infty} E_k\, j_o(E_k)\, dE_k.$$

The energy flux ϕ_o provides a useful measure of the cosmic–ray spectrum; another convenient measure that we occasionally use is the energy density (eV cm^{-3}),

$$\epsilon = 4\pi \int_{E_o}^{\infty} \frac{j(E_k)\,E_k}{v}\,dE_k \quad ,$$

where v is the velocity of the cosmic–ray particle. In our model, E_o = 20 MeV; the energy flux below this somewhat arbitrary cutoff is negligible. The lowest energy cosmic rays from 20 MeV to 10 GeV are modulated substantially in the interplanetary medium so that the integrated spectral measures ϕ_o and ϵ are smaller at solar maximum than at solar minimum.

The differential cosmic ray spectrum used in our model is similar to that presented by Webber (1987). However, we have noticed that Webber's proton spectrum seems to provide an integrated energy density that is somewhat larger at solar minimum, 1 AU, than provided by the spectra of Ip and Axford (1985) and Simpson (1983). This discrepancy seems to be due to the fact that Webber's proton spectrum falls off less rapidly in the 10^3 – 10^5 MeV energy region than the data presented by Simpson (1983). In any case, we have used Webber's proton spectrum in order to be consistent with his sunspot minimum versus maximum calculations and to be consistent with the extrapolations to 30 AU of Webber and Lockwood (1987), but the reader should keep in mind that the energy densities derived from Webber's spectra are almost 0.3 – 0.4 eV cm^{-3} larger than some previously–quoted values. Consistent with all three references, we have assumed that the spectra at energies greater than

10^5 MeV fall off as $E^{-2.75}$. The 30 AU solar maximum and minimum spectra that we use in our model are shown in Fig. 22 along with an inferred unmodulated interstellar spectrum (Webber 1987). The two 30 AU spectra were estimated from the cosmic ray gradients measured by *Pioneer 10* and *11* and *Voyager 1* and *2* (Webber and Lockwood 1987). Webber and Lockwood's gradient measurements indicate that the total integrated rate of cosmic rays greater than 60 MeV measured at Neptune's orbit should be 2.2 times (for solar minimum, 30 AU) and 0.8 times (for solar maximum, 30 AU) the rate measured at 1 AU at solar minimum.

The penetration of charged particles is inhibited by a planetary magnetic field. In particular, a dipole magnetic field will restrict the penetration of all but the most energetic particles to high magnetic latitudes, so GCR ionization effects will be observed only at polar magnetic latitudes on a planet with a strong dipole field. As a first order approximation, charged particles with magnetic rigidity $P = pc/Ze$ (p = momentum, c = velocity of light, Z = charge number, e = electron charge) less than a certain threshold rigidity,

$$P_o = \frac{M_d}{4R^2} \cos^4 \lambda$$

(M_d = magnetic dipole moment, R = planetary radius, λ = magnetic latitude), will be unable to enter the atmosphere below magnetic latitude λ. Thus, the energy flux and density of cosmic rays entering the atmosphere will be integrated from a new E_o associated with the threshold rigidity at the desired planetary latitude. Table VI summarizes the cutoff rigidities and integral limit E_o for various magnetic latitudes on Neptune for an assumed dipole field of 0.13 G (Ness *et al.* 1989). The energy flux corresponding to the cutoff rigidity at 60 degrees latitude on Neptune is 5.56 GeV cm^{-2} s^{-1} at solar maximum and 7.56 GeV cm^{-2} s^{-1} at solar minimum. Neptune's magnetic field is weak enough that a noticeable difference in the GCR–induced ionization rate between solar maximum and solar minimum will be observed at mid and

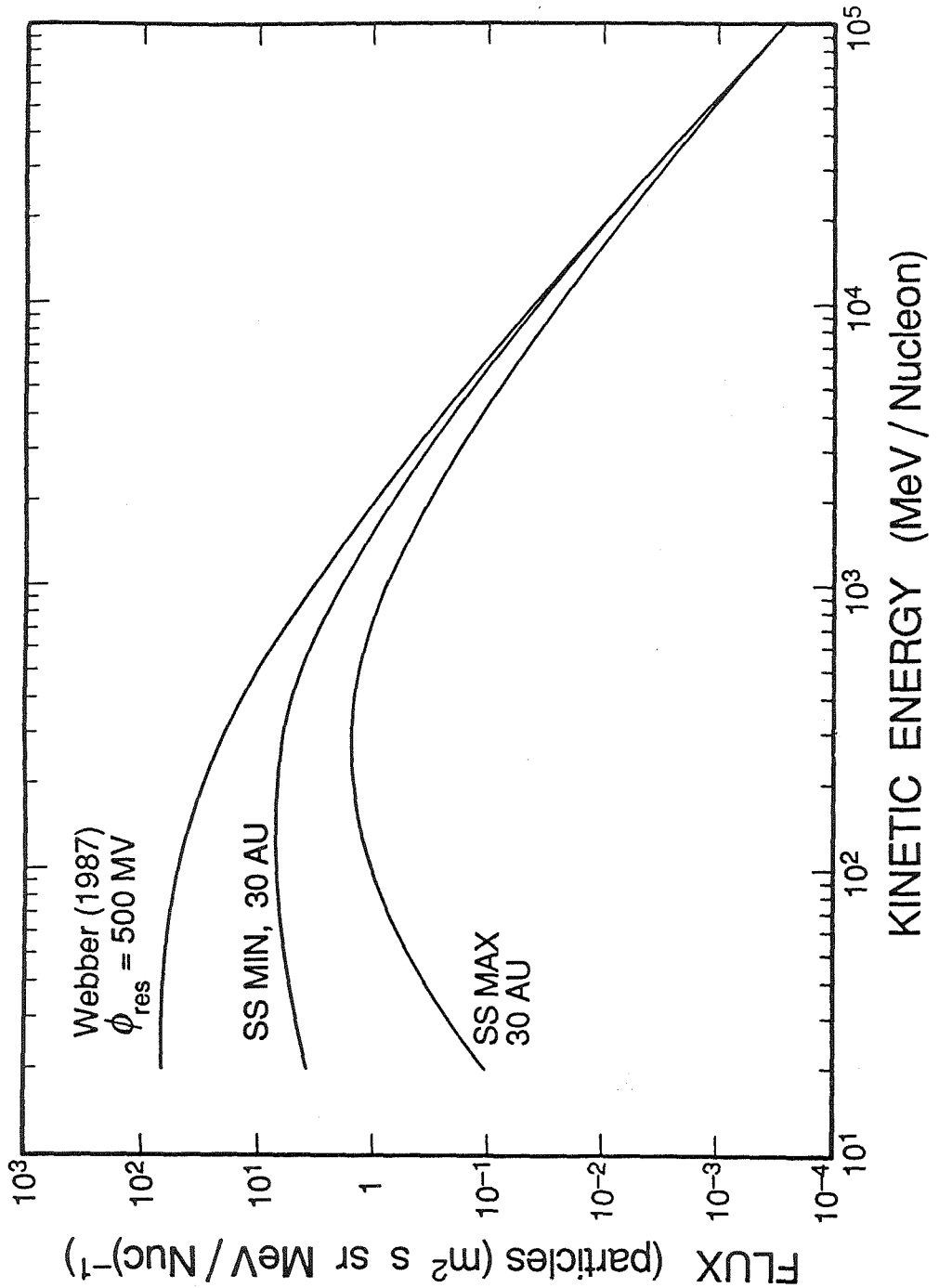

Figure 22. Differential energy spectra of galactic cosmic ray particles at 30 AU for solar maximum and minimum (from Moses *et al.* 1989). The upper curve is an inferred interstellar cosmic ray spectrum for a residual modulation of 500 MV (see Webber 1987) and is included for scale.

TABLE VI

P_o (cutoff rigidity) and E_o for various magnetic latitudes on Neptune
(assuming a dipole moment of 0.13 Gauss)

Magnetic Latitude	P_o (GV)	E_o (for protons)
40°	8.3	7.4 GeV
50°	4.1	3.3 GeV
60°	1.5	830 MeV
70°	0.33	56 MeV
80°	0.022	0.26 MeV

high magnetic latitudes.

The ion chemistry used in our model is a greatly simplified version of that of Capone *et al.* (1977), with cosmic rays as the only source of ionization. The important ions produced initially by GCR ionization of H_2, He, and CH_4 are H_2^+, He^+, CH_4^+, CH_3^+, and CH_2^+. At the altitudes that we are considering, these ions react rapidly with H_2 and CH_4 (see Capone *et al.* 1979 for a more thorough discussion of the ion chemistry) to form a CH_5^+ ion about which neutral hydrocarbon molecules can efficiently cluster. Therefore, the ion chemistry can be simplified to the following sequence:

$$\text{Cosmic Ray} + (H_2, \text{He}, CH_4) \rightarrow CH_5^+ + e^- \quad ,$$

$$CH_5^+ + CH_4 + M \rightarrow CH_5^+ \cdot CH_4 + M$$

$$CH_5^+ \cdot (CH_4)_n + CH_4 + M \rightarrow CH_5^+ \cdot (CH_4)_{n+1} + M \quad (n = 1, 2, \cdots)$$

$$CH_5^+ \cdot (CH_4)_n + e^- \rightarrow \text{neutrals}$$

in the troposphere, or the same in the stratosphere except the CH_4 molecules are replaced by other hydrocarbon molecules. To be consistent with Capone's work, we

have estimated that the last step proceeds (for n = 0, 1, 2 ...) with a recombination rate of 4×10^{-6} $cm^3 s^{-1}$. Fig. 23 shows the GCR–produced electron density profiles for Neptune's lower atmosphere computed using the one–dimensional kinetics and diffusion model described previously (Section 2.1). Our electron density profile reproduces the essential features of Capone *et al.* (1977); however, we use an updated model atmosphere that results in "stretching" the ionization profile. Consequently, our computed peak ion production rate is less than that reported by Capone *et al.* by a factor of six, but the integrated column production rate appears to be close. The results shown in Fig. 23 also illustrate the differences between the ion profile at solar maximum versus solar minimum. The production rate at 60 degrees magnetic latitude at any altitude is ~40% higher at solar minimum than at solar maximum.

In summary, a source of ions from galactic cosmic rays exists in the lower stratosphere of Neptune. Ion–induced nucleation is therefore possible in the hydrocarbon condensation regions. More ions are produced at solar minimum and at high magnetic latitudes than at solar maximum and low magnetic latitudes. Therefore, ion–induced nucleation and particle formation might vary with the 11–year solar cycle (see Moses *et al.* 1989) and with location on the planet.

4.2 Source of Condensation Nuclei

For heterogeneous nucleation to operate on Neptune, a source of condensation nuclei, or particles that act as sites for growth of the condensed phase, must be present. On Earth, such particles are abundant — soil and clay particles, organic debris, sea salt, soot, resin, volcanic aerosols, and pollutants all act as condensation nuclei (CN). Most terrestrial CN are derived from sources at the Earth's surface as is evident from the decrease in CN with altitude above the surface (Pruppacher and Klett 1978). On Neptune, no "surface" as such exists, and a large source of CN from lower

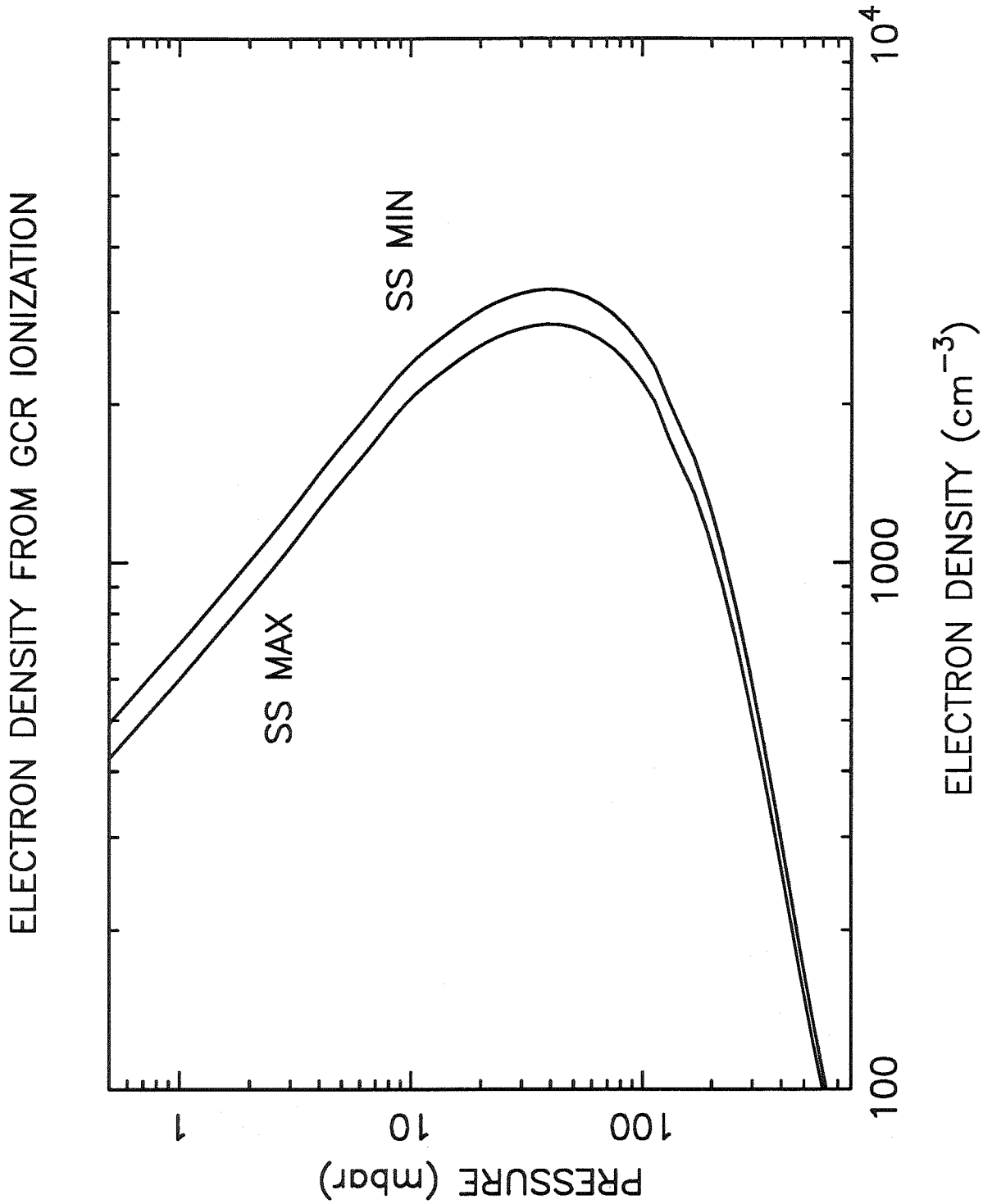

Figure 23. The number density of electrons produced from ionization by galactic cosmic rays at lower stratospheric levels on Neptune.

atmospheric levels is unlikely to be important (especially for stratospheric aerosol formation). Some mixing of cloud and aerosol particles or non–equilibrium species of low volatility from deeper regions to upper tropospheric or lower stratospheric levels may occur, but the major source of CN on Neptune will probably be from chemical products raining down from above or from extraplanetary sources.

As already mentioned, heterogeneous nucleation will be more difficult on Neptune than on the Earth because the low temperatures encountered in Neptune's atmosphere imply nucleation of the ice phase rather than the liquid phase. Nucleation of supercooled liquids (followed possibly by the freezing of the droplet) might occur if the difference between the surface energy of the liquid phase compared to the solid phase were to outweigh the decrease in vapor pressure of the ice phase relative to the liquid phase. Although we do not have enough information about the hydrocarbon species at low temperatures to evaluate the extent of any supercooling under Neptune conditions, we do know that stratospheric temperatures are far below the triple point temperatures of most of the hydrocarbon species except possibly methane, ethane, and propane (see Appendix A). Thus, we would not expect supercooled liquids to form at most levels in Neptune's lower stratosphere. However, methane, ethane, and propane have triple point temperatures approximately ten degrees or so above their predicted condensation region temperatures on Neptune (see Section 4.5). These species may condense as liquids (at least initially) and could therefore nucleate more efficiently than the other hydrocarbon species.

Very few particles make good ice–forming nuclei (i.e., condensation nuclei for the ice phase). The characteristics of good ice–forming nuclei are described by Pruppacher and Klett (1978). First of all, the particles should be insoluble in the condensate. The presence of dissolved material lowers the freezing temperature, and soluble particles tend to disintegrate during nucleation and do not have the struc-

tural integrity needed for crystal formation. Secondly, good ice–forming nuclei tend to have sizes larger than the critical radius for cluster formation. Small particles ($\lesssim 0.01$ μm) are less efficient at supporting growing ice embryos. Thirdly, the particles should have similar chemical characteristics as the ice embryos (such as similar bond strength, polarity, and rotational symmetry). Fourthly, since the growth of the ice phase usually exhibits preferred orientation, the ice–forming nuclei should have similar crystallographic arrangements as the ice phase to augment atomic matching across the interface between the ice crystal and the particle. Finally, the ice–forming nuclei should have surface sites capable of adsorbing the condensable molecules. On Earth, some metal oxides, silicate particles, and organic debris exhibit enough of the above characteristics to act as good water ice–forming nuclei.

A large percentage of aerosol material in the stratosphere and upper atmosphere of Neptune could originate from its passage of meteors through the planet's atmosphere. Most meteoric material would evaporate during the passage through the atmosphere; however, metals and refractory vapor could recondense in the tail of the meteor to form small smoke–like dust particles (see Hunten *et al.* 1980 for a terrestrial analogy). In addition, some micrometeoroid particles are small enough to survive the ablation process either relatively untouched or as residual meteorites that do not fully evaporate. Thus, an extraplanetary source of condensation nuclei may be present in the hydrocarbon condensation regions in the lower stratosphere of Neptune.

Meteoroid ablation and recondensation have only been studied in the context of the Earth's atmosphere (e.g., Rosinski and Snow 1961, Hunten *et al.* 1980), and direct comparisons of terrestrial meteoroid studies with the situation on Neptune are problematical. A detailed analysis of the process of meteoric dust ablation and recondensation in Neptune's atmosphere is beyond the scope of this work. We will

assume that the terrestrial analysis of Hunten *et al.* (1980) is qualitatively similar to the situation on Neptune and will point out possible differences as they arise.

Although Southworth and Sekanina (1973) predict smaller populations of micrometeoroids with increasing distance from the sun, actual meteoroid experiments aboard *Pioneer 10* and *11* (e.g., Humes 1980) indicate that the spatial density of micrometeoroids is approximately constant in interplanetary space from 1 to 18 AU. However, the micrometeoroids in the outer solar system may be composed of more volatile material than the meteoroids that typically encounter the Earth. Many ices are stable in the outer solar system. Humes (1980) finds better agreement with his interplanetary data if he assumes the micrometeoroids are in randomly inclined orbits of high eccentricity (i.e., comet–like orbits) rather than the regular circular orbits that are observed near the Earth. If the interplanetary spatial density and velocity distribution of meteoroids were constant, then one might expect a slightly higher density of meteoroids near Neptune than near the Earth because of gravitational focusing and Neptune's larger escape velocity (see Humes 1980). However, there is no indication that the velocity distribution of meteoroids near Earth and near other planets (i.e., Saturn and Jupiter) are similar (Humes 1980).

Because the meteoroids near Neptune are probably more volatile, more of the particles may evaporate during their passage through the upper atmosphere. Some of the volatile vapor may interact chemically with atmospheric constituents and lead to condensable products that could also act as ice–forming nuclei.

The recondensed refractory material such as silicates or metals should have the structural integrity required for good ice–forming nuclei and should be insoluble in the condensed hydrocarbon species, but might not have sizes large enough to promote heterogeneous nucleation. Hunten *et al.* (1980) predict that the bulk of dust particles that result from meteoroid ablation and recondensation in the Earth's

atmosphere have radii less than a few nanometers. The question of whether these small particles could act as good ice–forming nuclei is addressed in Section 4.3.

A second possible source of condensation nuclei on Neptune is from photochemical products that condense in the upper stratosphere and fall to the lower altitude haze and cloud condensation regions. For instance, C_6H_2, C_8H_2, other polyacetylenes, or complex hydrocarbons with low vapor pressures might be abundant enough to condense and form small amounts of condensation nuclei at high altitudes. These particles will settle through the atmosphere and eventually encounter regions that are supersaturated with respect to some of the vapor species we are considering (e.g., diacetylene and butane). Each of the lower vapor pressure hydrocarbon species that condenses can act as a source of CN for the higher vapor pressure species below it. For instance, diacetylene can be a source of CN for ethylacetylene, which can be a source for acetylene, which can be a source for ethane, and so on. All these species can be sources of CN for methane in the upper troposphere provided the particles do not evaporate before they reach the methane condensation region.

The ability of the photochemical condensates to act as good ice–forming nuclei depends on some of the properties discussed previously. For example, the particles should have high surface energies with respect to the vapor and low surface energies with respect to the condensable species in order to have a low contact angle and a high degree of "wettability". Fig. A2 in Appendix A illustrates that the surface tensions of liquid hydrocarbons tend to increase with increasing molecular weight of the species; therefore, the fulfillment of the above criterion looks promising. However, the particle should also be insoluble in the condensate to act as a good ice–forming nucleus. Some of the hydrocarbon species we consider have reasonably high mutual solubilities and might fail to satisfy this criterion. Large particles tend to be better ice–forming nuclei. It is impossible to estimate the sizes of particles that are derived from photochemical

sources. The sizes will be limited by the amount of vapor originally available and by the mechanics of bringing vapor molecules or small clusters together (i.e., nucleation, condensation, and coagulation).

Products from interactions of magnetospheric and other high–energy charged particles with atmospheric constituents may be a third source of CN on Neptune. This source is similar to the photochemical source in the sense that the material is probably hydrocarbon in nature and is formed at higher altitudes in the atmosphere. Laboratory experiments of plasma discharges in simulated Uranus and Neptune atmospheres find that some condensed material is produced from the irradiation of mixtures of methane, helium, and hydrogen vapor (e.g., Khare *et al.* 1987). Tholin, soot, or other hydrocarbon condensates produced by charged–particle impact might be present in quantities significant enough to provide a source of CN on Neptune. In addition, charged–particle impact might be a source of C_5 and higher hydrocarbon vapor that might condense in Neptune's middle stratosphere.

In summary, several possible sources of condensation nuclei exist for heterogeneous nucleation in Neptune's atmosphere. The presence of dust particles formed from meteoric debris and relatively involatile products from photochemistry and from charged–particle impact may allow hydrocarbon particle formation in Neptune's lower stratosphere and upper troposphere to proceed by heterogeneous nucleation. It is uncertain whether the CN produced by the sources mentioned above would have the necessary physical properties to act as good sites for ice condensation. Therefore, when examining heterogeneous nucleation in the next section, we consider a wide variety of physical properties of condensation nuclei.

4.3 Efficiency of Nucleation

We now have enough information to determine the efficiency of nucleation

and particle formation in the hydrocarbon condensation regions of Neptune. Our nucleation equations can be applied to a study of aerosol formation in Neptune's atmosphere provided we know the atmospheric temperatures and physical properties of the hydrocarbon species of interest in our model. The atmospheric temperature structure is assumed to be that used in our photochemical models (see Fig. 1). The surface tensions, dielectric constants, bulk densities, and vapor pressures of the important hydrocarbons are discussed in Appendix A. No data are available for the physical properties of diacetylene (except the vapor pressure). We assume that C_4H_2 has the same density, surface tension, and dielectric constant as C_2H_2 and discuss the sensitivity of the diacetylene nucleation rates to the adopted physical properties. Since many of the hydrocarbon physical properties are poorly known at low temperatures, our quoted nucleation rates are uncertain. Surface energy is the single most sensitive poorly known quantity.

Homogeneous nucleation

Homogeneous nucleation will be very inefficient on Neptune. In other words, homogeneous nucleation will only proceed at temperatures far below those encountered when the condensable vapors reach saturation. Very large saturation ratios are required to obtain observable homogeneous particle formation rates. For instance, a saturation ratio of 10^4 for ethane at 60 K leads to a homogeneous nucleation rate of only 6×10^{-21} new particles cm^{-3} s^{-1}; that is, one new ethane particle would be formed per cubic centimeter of atmosphere every 5×10^{12} years. Particle formation rates this small will clearly not contribute to observable hazes. Since ethane is the most abundant condensable molecule in Neptune's lower stratosphere and since condensed ethane will probably be the dominant stratospheric aerosol mass compo-

nent, we examine the efficiency of homogeneous nucleation of ethane in more detail (Fig. 24). In this figure, we plot the homogeneous nucleation rate versus saturation ratio for ethane at several temperatures below its saturation temperature on Neptune (see also Fig. 12). Note the very large vertical scale of Fig. 24.

The exponential term in the expression for the homogeneous nucleation rate (equation [4]) dominates the overall shape of Fig. 24. Although the pre–exponential term is proportional to S^2 and contributes somewhat to the behavior of J, the nucleation barrier ΔG^* and exponential term will dominate and will control the nucleation rate provided that the saturation ratio is not so large that $\Delta G^* \rightarrow 0$. For any particular saturation ratio, the nucleation rate decreases rapidly with decreasing temperature due to the inverse cube dependence of $\Delta G^*/kT$ with temperature. In our photochemical Model C discussed in Section 2, ethane becomes saturated at $\sim$ 65 K (11 mbar). Homogeneous nucleation of ethane will be minimal unless very large saturation ratios are built up. Because the temperature continues to decrease with decreasing altitude, the rapidly decreasing vapor pressure of ethane may permit such large saturation ratios to be achieved in theory; however, heterogeneous nucleation (both on ions and on insoluble particles) should begin to operate long before such large supersaturations can develop.

Ion–induced nucleation

The previous discussion of ion–induced nucleation in Section 3.2 does not completely describe the situation that would be encountered on Neptune. The classical description of ion–induced nucleation inherently assumes that the ions have infinite lifetimes. In real atmospheres, the ions may recombine with free electrons and be neutralized before the ion cluster has had a chance to reach a thermodynamically stable

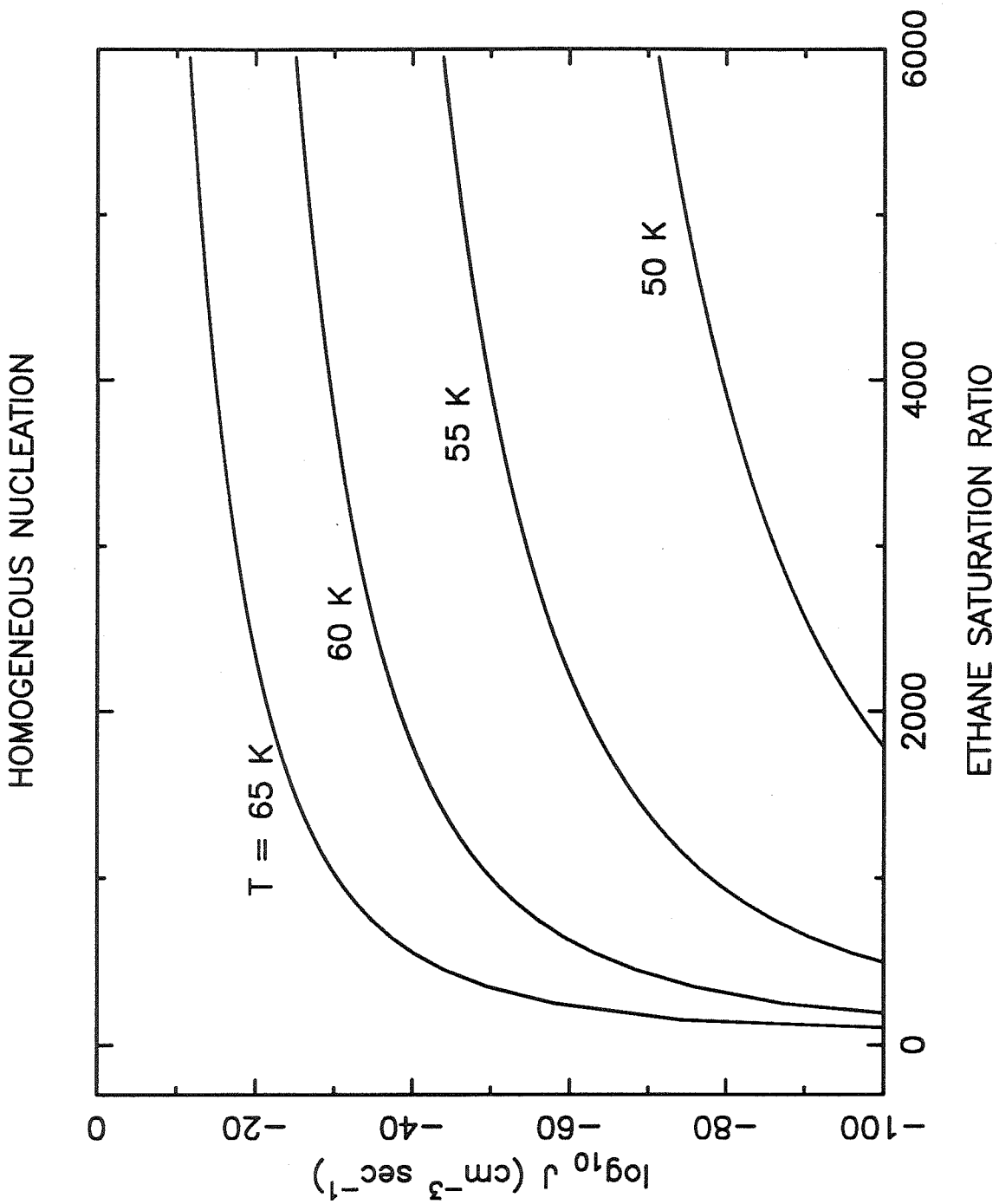

Figure 24. The homogeneous nucleation rate of ethane (new particles formed per cm^3 per second) as a function of saturation ratio and temperature. The ordinate is scaled logarithmically. Homogeneous nucleation is minimal unless large supersaturations develop.

size. To account for this possibility, we add a correction factor to the nucleation rate that describes the probability of forming a critical–sized cluster before recombination occurs.

We assume that the time constant for an ion cluster to recombine with a species of opposite charge (e.g., an electron) is independent of the size of the cluster and can be estimated as in Bauer (1973):

$$\tau_r = \frac{1}{\alpha\, n_{ion}}$$

where q is the ion production rate ($\mathrm{cm^{-3}\ s^{-1}}$), α is the recombination rate of the hydrocarbon ion clusters described in Section 4.1 ($\alpha \sim 4 \times 10^{-6}\ \mathrm{cm^3\ s^{-1}}$), and n_{ion} is the electron number density (assumed to be equal to the ion number density). The time required for a critical number g_{i*} of condensable hydrocarbon molecules to impinge on the cluster is approximately

$$\tau_{imp} = \frac{g_{i*}}{4\pi r_{i*}^2\, \beta}$$

where β is again the flux of condensable molecules encountering a surface area $4\pi r_{i*}^2$. We can estimate the probability that an ion survives long enough to acquire a critical number of hydrocarbon molecules in a manner similar to Hamill *et al.* (1982):

$$P \approx \exp\left[-\frac{\tau_{imp}}{\tau_r}\right] = \exp\left[-\left(\frac{\alpha\, n_{ion}\, \rho\, r_{i*}}{S\, n_v}\right)\left(\frac{2\pi}{9 m_1 kT}\right)^{1/2}\right]$$

where S is the saturation ratio, n_v is the saturation vapor density, ρ is the bulk density of the condensed phase, and m_1 is the mass of a single molecule of the condensed phase. We then get a rough determination of the ion–induced nucleation rate by multiplying the classical nucleation rate (equation [6]) by this probability factor.

The electron density in Neptune's lower stratosphere never exceeds a few thousand per cubic centimeter (see Fig. 23). Thus, recombination times are fairly long, typically $\gtrsim 100$ sec. For most supersaturated conditions in the stratosphere and upper

troposphere, $\tau_{imp} \ll \tau_r$, and the probability factor is near unity. Nevertheless, conditions do exist where the probability for critical cluster formation is negligibly small. These conditions are distinguished by nucleation rates that are limited kinetically; that is, conditions where the encounter probability between condensable monomers and a growing cluster is quite small. Low temperatures and low vapor abundances distinguish these situations.

Methane cluster formation never falls in the category of nucleation that is kinetically limited. Under tropospheric conditions, the clusters grow rapidly compared to the lifetime of an ion. However, a relatively involatile species such as diacetylene reaches the kinetically limited regime much faster and can be much more affected by the correction factor. If the saturation ratio is fixed at 200, then at 105 K, the probability of growing a stable diacetylene cluster in the time allotted is 0.88, but the probability falls to 0.09 at 100 K and 3×10^{-27} at 95 K. Therefore, the region in which C_4H_2 can nucleate is limited and must be characterized by high temperatures and/or large saturation ratios.

The efficiency of ion–induced nucleation of ethane at various temperatures is illustrated in Fig. 25. Note that this figure has the same scale as Fig. 24. In Fig. 25, we plot the nucleation rate per ion, and one must multiply the plotted values by the ion number density ($\sim 2000\,cm^{-3}$ in the ethane condensation region) to truly compare these nucleation rates with those in Fig. 24. However, even with the factor of $\sim$ 2000 deficit, ion–induced nucleation is clearly much more effective than homogeneous nucleation for the same conditions. Observable nucleation rates ($> 10^{-3}\,cm^{-3}$) are found at saturation ratios less than 1000 for 65 and 60 K and less than 10^4 for 50 K.

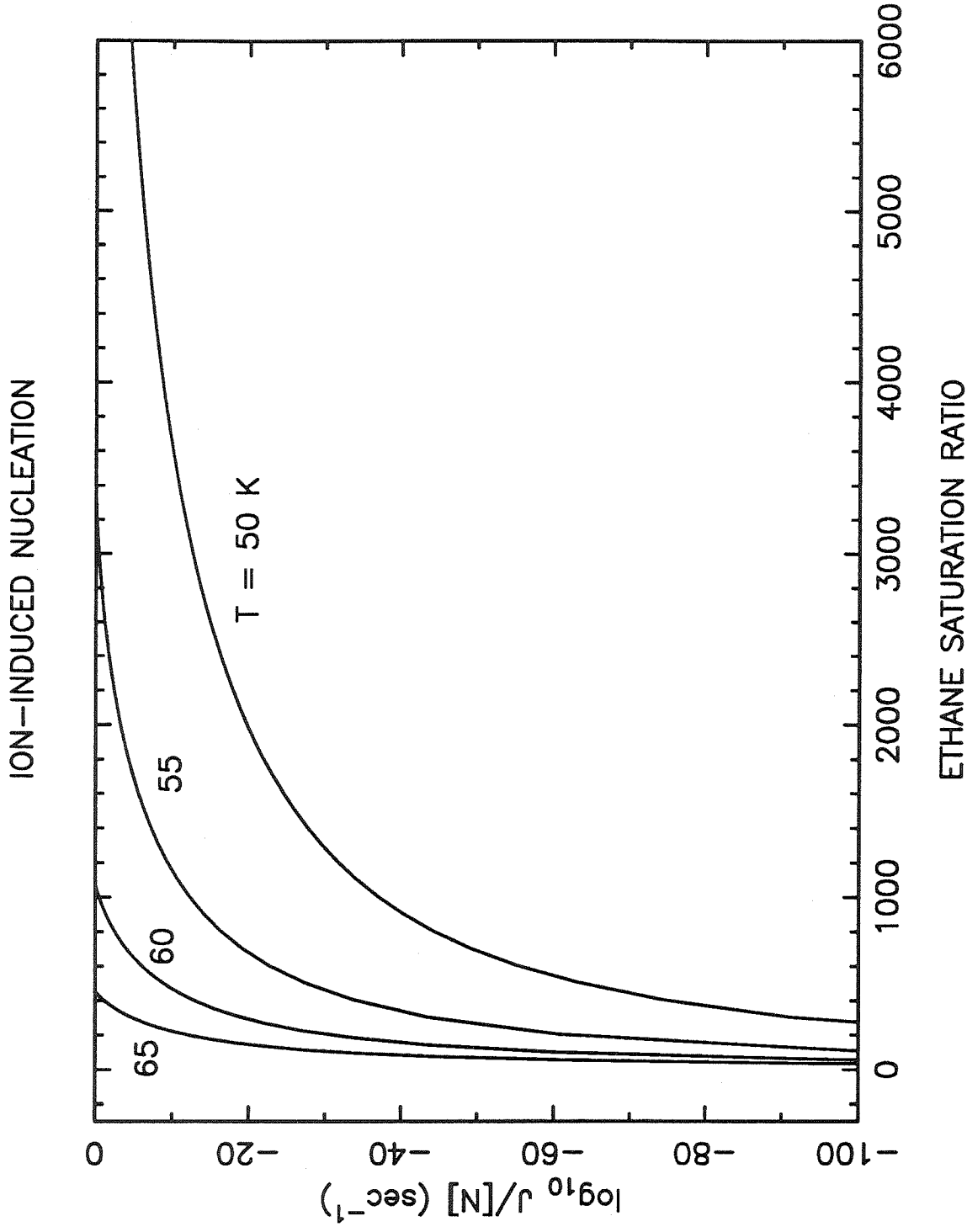

Figure 25. The ion–induced nucleation rate of ethane (particles formed per ion per second) as a function of saturation ratio and temperature. The scale is the same as in Fig. 24.

Heterogeneous nucleation

The efficiency of heterogeneous nucleation depends strongly on the properties of the insoluble particle upon which the vapors condense. In particular, the heterogeneous nucleation rate depends on the size of the particle and its "compatibility" with the condensed phase (which is described by the contact angle between the condensed phase and the substrate). For meteoroid ablation in the Earth's mesosphere and stratosphere, Hunten *et al.* (1980) predict that recondensation of ablated meteor vapor will create particles in the 0.2 – 10 nm range (most probable radius $\sim$ 2 nm) with very few particles larger than 20 nm. Residual micrometeoroids could be larger but are much less abundant than the theoretical predictions for recondensed meteoric material. Although meteoric ablation calculations for Neptune may be different from those of the Earth, we use the values of Hunten *et al.* (1980) in our nucleation calculations; that is, we test the sensitivity of the nucleation rate to changes in particle size for particles with radii between 1 – 10 nm (0.001 – 0.01 μm). Condensation nuclei composed of involatile chemical species produced from either charged–particle impact or photochemistry may also be precipitating down into the nucleation regions. The size range 1 – 10 nm is probably a decent estimate for most of these aerosol particles but might be an underestimate if the original vapor source is abundant.

Contact angles are even more difficult to estimate than particle radii and, unfortunately, are very sensitive indicators of nucleation rate. Contact angles for liquid water on most metals, silicates, and natural terrestrial condensation nuclei are usually greater than 45°. In order to get efficient heterogeneous nucleation, smaller contact angles and more "wettable" nuclei are preferred. Low contact angles arise from substrates with high surface energies with respect to the vapor and low surface energies with respect to the condensate in order that monomers diffuse easily across the sub-

strate surface. We have no data on contact angles for our important hydrocarbon compounds on appropriate substrates, so we examine a wide range of contact angles in our nucleation calculations.

Calculations of the heterogeneous nucleation rate versus saturation ratio for three different hydrocarbon species are shown in Figs. 26a–c. The three figures should not be compared directly with each other; the calculations were performed for different temperatures — a convention necessitated by the different vapor pressures of the different species. To give a realistic picture of heterogeneous nucleation on Neptune, each temperature is chosen to be a lower temperature than that encountered when the vapor becomes supersaturated in Neptune's atmosphere. The ion–induced nucleation rate is shown in each figure for comparison.

Fig. 26a shows that methane particle formation proceeds relatively efficiently at a tropospheric temperature of 75 K for both ion–induced and heterogeneous nucleation. Small saturation ratios permit significant embryo formation rates. Although the nucleation rate is very sensitive to the assumed contact angle, all reasonable assumed values for θ give relatively efficient nucleation rates at saturation ratios less than ~ 10. If we knew the contact angle and insoluble particle radius, we could predict with good accuracy the saturation ratio at which observable numbers of particles would form (i.e., the critical saturation ratio, a term that will be discussed in more detail later). The accuracy of such estimates arises because of the extreme sensitivity of J to S for the conditions shown in Fig. 26a. Unfortunately, we have little knowledge of r_N and θ, and our estimates of the critical saturation ratios will be uncertain.

The ethane nucleation rate at a stratospheric temperature of 60 K is shown in Fig. 26b. Depending on the properties of the insoluble particle, large saturation ratios might be required to initiate observable nucleation at this temperature. The calculated nucleation rate is very sensitive to the assumed contact angle: small contact

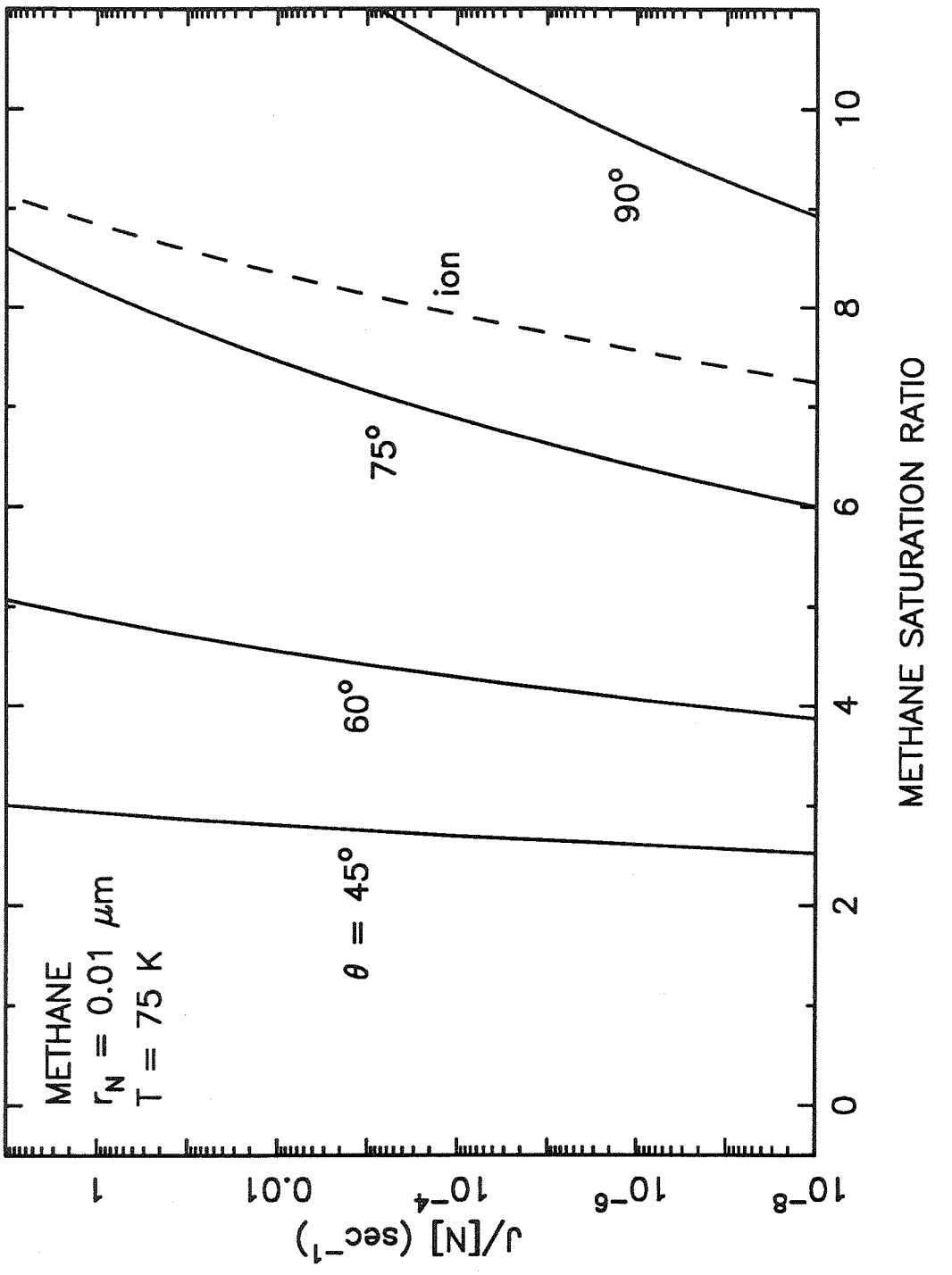

Figure 26a. Heterogeneous nucleation of methane on 10 nm particles as a function of saturation ratio and contact angle. The nucleation rate is plotted in terms of the number of stable embryos condensing on the insoluble particle (per particle per second). The ion–induced nucleation rate is shown for comparison.

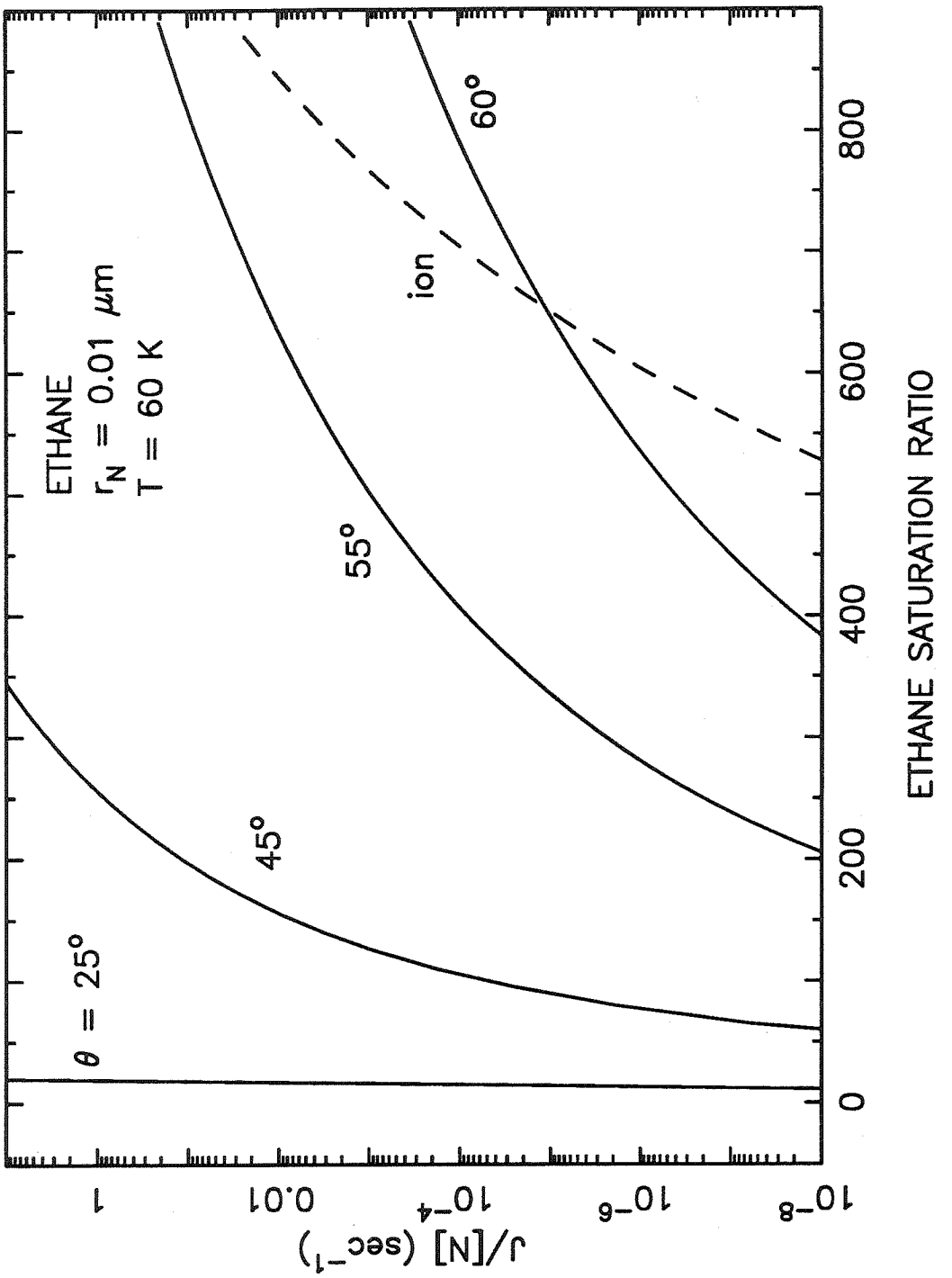

Figure 26b. Heterogeneous nucleation of ethane on 10 nm particles as a function of saturation ratio and contact angle. The ion–induced nucleation rate is shown for comparison.

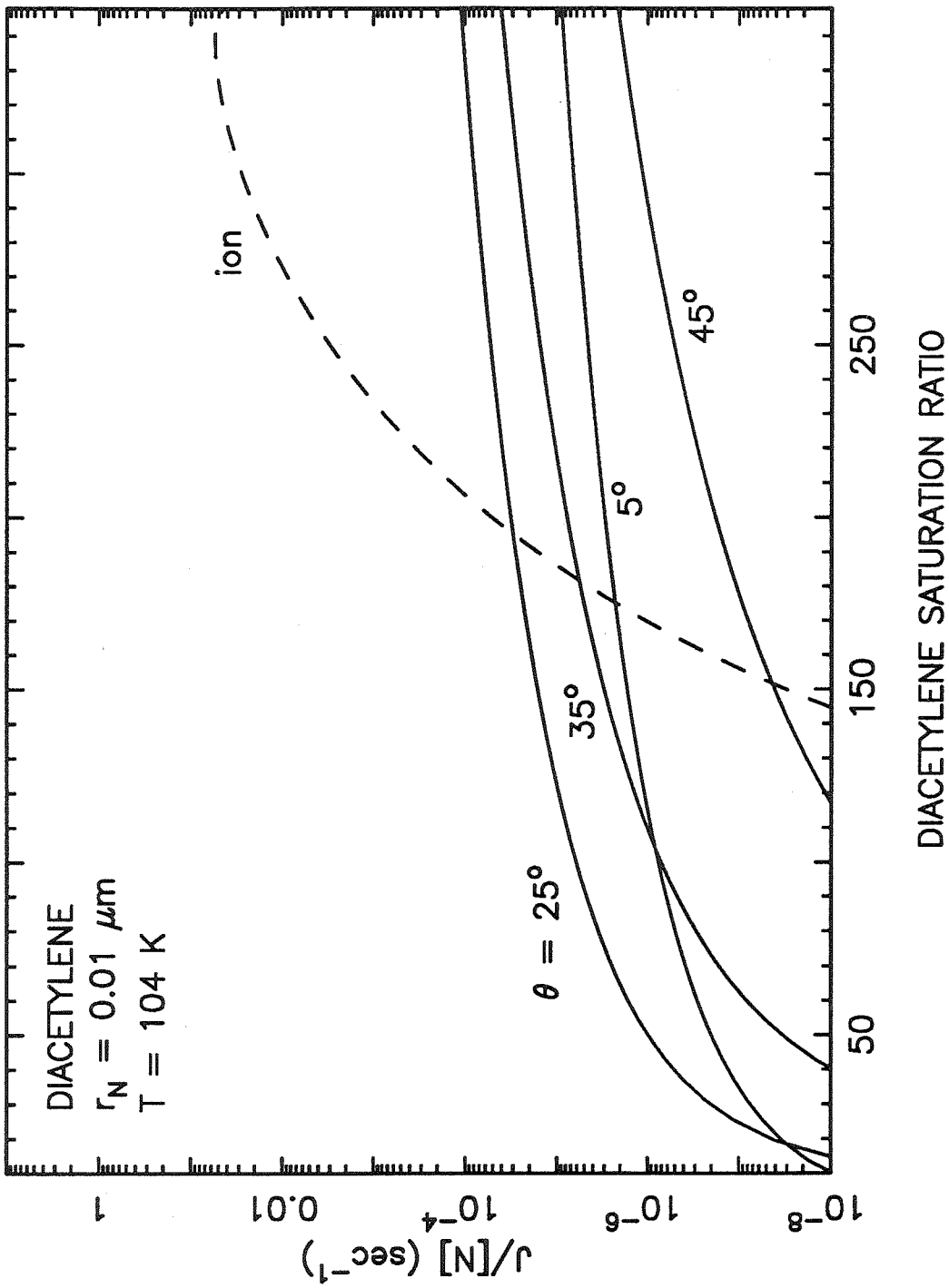

Figure 26c. Heterogeneous nucleation of diacetylene on 10 nm particles as a function of saturation ratio and contact angle. The ion–induced nucleation rate is shown for comparison.

angles ($< 30°$) imply efficient nucleation at low supersaturations whereas large contact angles ($> 50°$) require much larger saturation ratios. Under the conditions illustrated in Fig. 26b, heterogeneous nucleation operates much more efficiently than ion–induced nucleation unless the contact angle for ethane condensing on the substrate is greater than $\sim 60°$ (i.e., an incompatible substrate).

Fig. 26c shows the case for diacetylene nucleating at a stratospheric temperature of 104 K. Diacetylene just becomes supersaturated at this temperature in Neptune's stratosphere (in our photochemical Model C), so large supersaturations will not have developed. Thus, no particle formation will proceed until lower temperatures and higher supersaturations are achieved. However, we have chosen to present the calculations at this high temperature to keep the figures in Fig. 26a–c on the same vertical scale. If we were to plot the nucleation rate at a more reasonable temperature for diacetylene nucleation on Neptune, say 90 K, nothing would be visible on this scale — the nucleation rates for all the diacetylene cases would be less than 10^{-8} s^{-1} unless extremely large saturation ratios were achieved. Diacetylene nucleation is extremely inefficient on Neptune.

Diacetylene nucleation is the exception to the rule that states that nucleation rates are controlled only by the exponential term in the nucleation rate equations [4], [6], and [8]. The overall shape of the nucleation rate still depends on the exponent, but nucleation rates never become significant even when the nucleation barrier $\Delta G_{het} \rightarrow 0$ for large S. The pre–exponential term, which depends on the square of the vapor pressure, remains low because diacetylene is so involatile (see Appendix A). Observable nucleation rates are not achieved until the vapor becomes *extremely* supersaturated.

Because large errors in the calculated diacetylene nucleation rates lead to large errors in the saturation ratios required for observable particle formation (as opposed

to the usual case of J being very sensitive to S), we can no longer be sure of our estimates of the critical saturation ratio for diacetylene. Of course, our knowledge of the physical properties of condensed C_4H_2 is so minimal that our results would have been mainly qualitative anyway. The only positive statement we can make about diacetylene nucleation on Neptune is that C_4H_2 is abundant enough to nucleate somewhere in the stratosphere (i.e., huge saturation ratios are achieved at lower stratospheric temperatures), but it is not certain diacetylene nucleation will produce significant numbers of particles anywhere near its initial saturation level (near 2 mbar). Ion–induced nucleation may operate more efficiently at these high altitudes but only at marginally observable rates. More laboratory experiments on the physical properties of diacetylene must be conducted before we can make any definitive statements about diacetylene nucleation on Neptune.

One interesting feature of nucleation of involatile species like diacetylene is evident in Fig. 26c: in some instances, nucleation on low–contact–angle substrates actually becomes less efficient than on high–contact–angle substrates. This effect commences as the nucleation barrier ΔG^*_{het} becomes negligible. When the exponential term loses dominance (at high saturation ratios), nucleation on substrates with low contact angles is less efficient because the Zeldovich factor Z is smaller. The effect is relatively minor and only becomes noticeable for species whose pre–exponential factors are small due to low vapor pressures.

Since we have no information concerning the physical properties of condensed diacetylene, we have examined the sensitivity of our calculated nucleation rates to changes in the assumed values of the surface tension, dielectric constant, and density. The results indicate that the nucleation rate is a sensitive function of the assumed physical properties as long as the nucleation rate resides in the regime of rapid change in J with increasing saturation ratio. However, for diacetylene, nucleation does not

become significant until supersaturations are large and the nucleation barrier is small. Since ΔG^*_{het} is approaching zero in this regime, small changes in σ or ρ do not have much effect on the heterogeneous nucleation rate. For instance, we replaced our assumed value of the surface tension of diacetylene from that of acetylene to that of ethylacetylene (see Appendix A). Ethylacetylene (1–C_4H_6) has a higher surface tension than acetylene (C_2H_2) in the temperature regions of interest and may be more representative of diacetylene. This change in the surface tension (for $T = 100$ K, $r_N = 10$ nm, $\theta = 5°$, $S = 400$) leads to a 20 order of magnitude reduction in the homogeneous nucleation rate of C_4H_2, and a 10 order of magnitude reduction in the ion–induced nucleation rate, but results in practically no change in the heterogeneous nucleation rate. The calculations are even less sensitive to changes in the bulk density. Thus, our heterogeneous nucleation rates are not as sensitive to assumptions concerning the physical properties of C_4H_2 as one might expect. The ion–induced nucleation rate, however, is more sensitive to such changes in physical properties.

Although we have kept r_N fixed in the previous examples, the heterogeneous nucleation rate is also sensitive to the size of the insoluble nucleus. Fig. 27 illustrates this sensitivity. The nucleation rate of ethane at 60 K is plotted again, this time as a function of insoluble particle radius. As $r_N \rightarrow r_*$ (the critical embryo size), nucleation becomes less and less efficient. Relatively large particles (greater than a few nm) are required for significant ethane nucleation; however, the nucleation rate is still most sensitive to the contact angle.

Because heterogeneous nucleation requires the presence of foreign particles, the nucleation rate is ultimately limited by the influx of new condensation nuclei. If the residence time for particles in the supersaturated region is long, new embryos may not form, but the existing particles will continue to grow until the vapor becomes depleted. The growth of newly formed embryos is not a topic of discussion in this

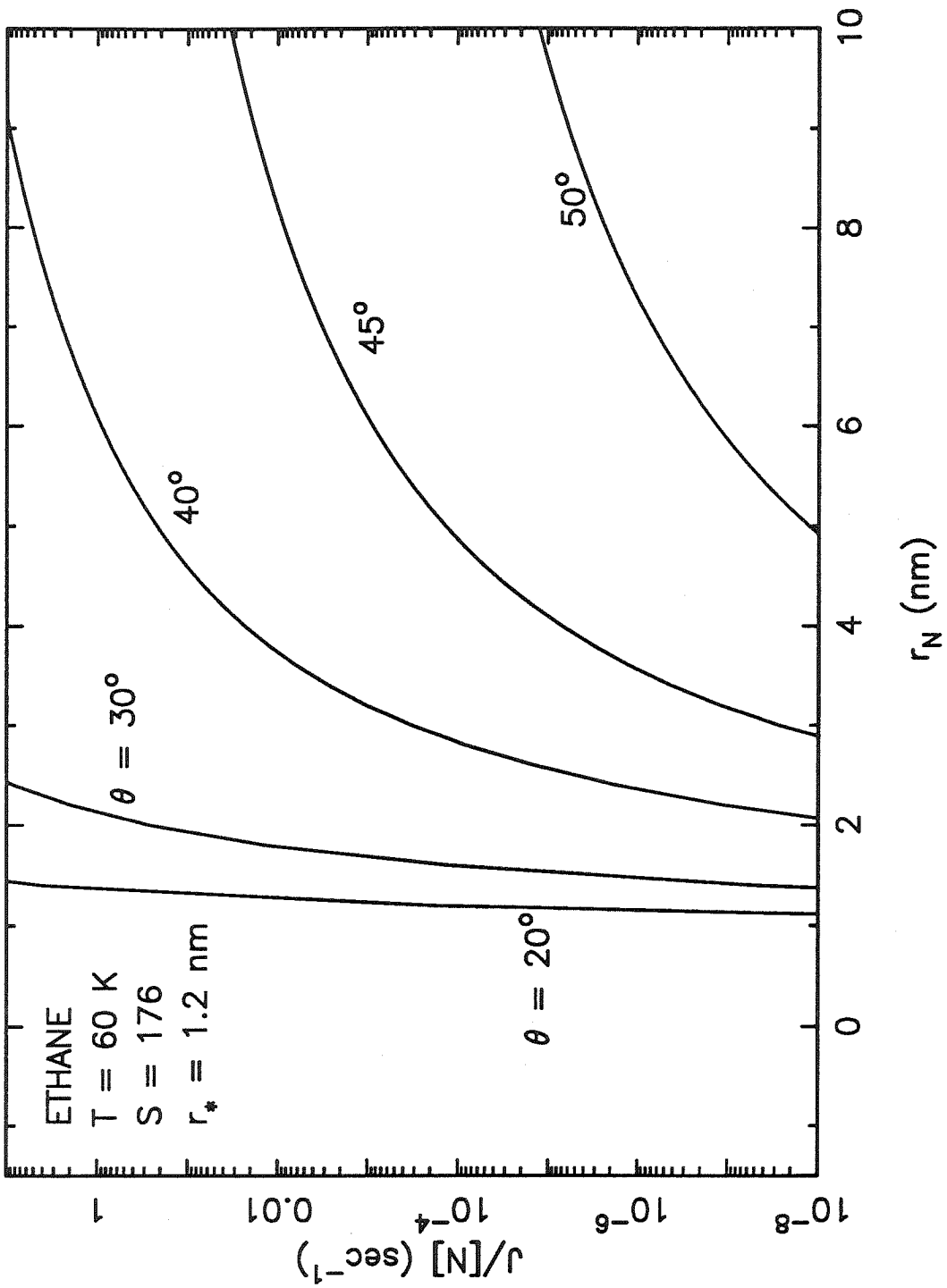

Figure 27. Heterogeneous nucleation of ethane as a function insoluble particle radius and contact angle. The saturation ratio is fixed at 176.

paper but is important for a full description of the properties of the hydrocarbon haze layers on Neptune. The properties of the haze layers cannot be predicted accurately without solving the full aerosol dynamics equations that consider particle growth (by condensation, Brownian coagulation, gravitational coalescence), and loss (by evaporation, gravitational settling, and turbulent mixing). The nucleation rate just gives us an idea of the initial number of new particles that are formed and provides an estimate of the location of particle formation.

Critical saturation ratios

Although we have already mentioned the term *critical saturation ratio*, we have never clearly defined it. We use the term to describe the saturation ratio at which observable nucleation rates are obtained. Our choice of an "observable nucleation rate" is somewhat arbitrary; nucleation rates 10^{-3} particles per cubic centimeter per second are generally observable in the laboratory or in the terrestrial atmosphere. We have chosen the critical saturation ratio for heterogeneous (or ion–induced) nucleation to be where J_{het} (or J_{ion}/n_{ion}) equals 10^{-3} s^{-1} per particle (or per ion). Since these values must be multiplied by the number density of insoluble particles (or ions), this choice will lead to "observable" nucleation rates provided that the concentration of condensation nuclei (or ions) is at least 1 cm^{-3}. Similarly, we define the critical saturation ratio for homogeneous nucleation to be where $J = 10^{-3}$ particles cm^{-3} s^{-1}.

The concept of a critical saturation ratio is a useful one for comparing nucleation theory with laboratory experiments or with real atmospheres. In an atmosphere, small clusters of molecules will form throughout the atmosphere at finite, but usually negligible, rates. The critical saturation ratio (S_{crit}) provides a good indication

of where particle formation will actually become important. If the abundance of a condensable vapor species exceeds S_{crit}, then nucleation and particle formation are likely to occur. A large S_{crit} implies an efficient nucleation process while a small S_{crit} implies an inefficient one.

Like the nucleation rate itself, S_{crit} is sensitive to the atmospheric temperature and to other properties such as the total charge on the ion or the size and compatibility of the insoluble condensation nucleus. For species that nucleate efficiently (i.e., methane), S_{crit} is well constrained provided we have good estimates of θ, r_N, and the physical properties of the condensates. However, for species that nucleate inefficiently, any errors in J can lead to large errors in the estimated S_{crit}.

The critical saturation ratios for heterogeneous and ion–induced nucleation of ethane at different temperatures and different conditions are shown in Figs. 28a and 28b. In a real atmosphere, if the saturation ratio lies above the curve, then particle formation will proceed at a rapid rate. Particle formation is minimal at saturation ratios below the curve. The nucleation rate is larger and S_{crit} is smaller for higher temperatures, larger insoluble particles, and smaller contact angles. The relative efficiency of ion–induced and heterogeneous nucleation depends on the properties of the insoluble nuclei.

The general behavior of the critical saturation curves as they vary with temperature and with particle properties is similar for the other hydrocarbon species besides ethane; however, the magnitudes of S_{crit} may be different. Table VII shows the critical saturation ratios for all the important condensable hydrocarbon species at temperatures relevant to their saturation regions. Remember that the critical saturation ratios are defined to be where the nucleation rate J equals 10^{-3} s^{-1} per particle or per ion for heterogeneous and ion–induced nucleation and 10^{-3} particles cm^{-3} s^{-1} for homogeneous nucleation. Again, one should not compare the species

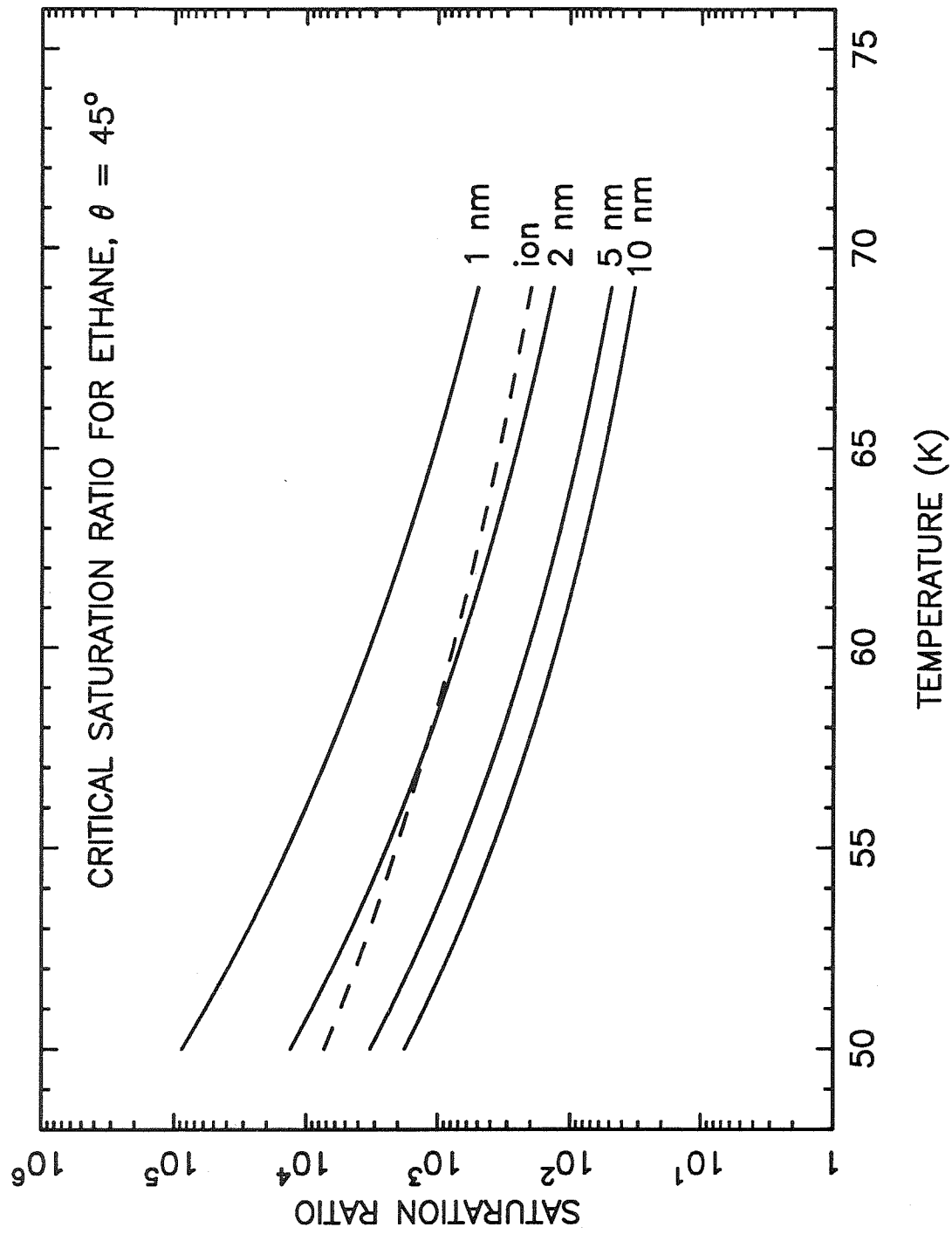

Figure 28a. Critical saturation ratios for ethane as a function of temperature for various assumed insoluble particle radii.

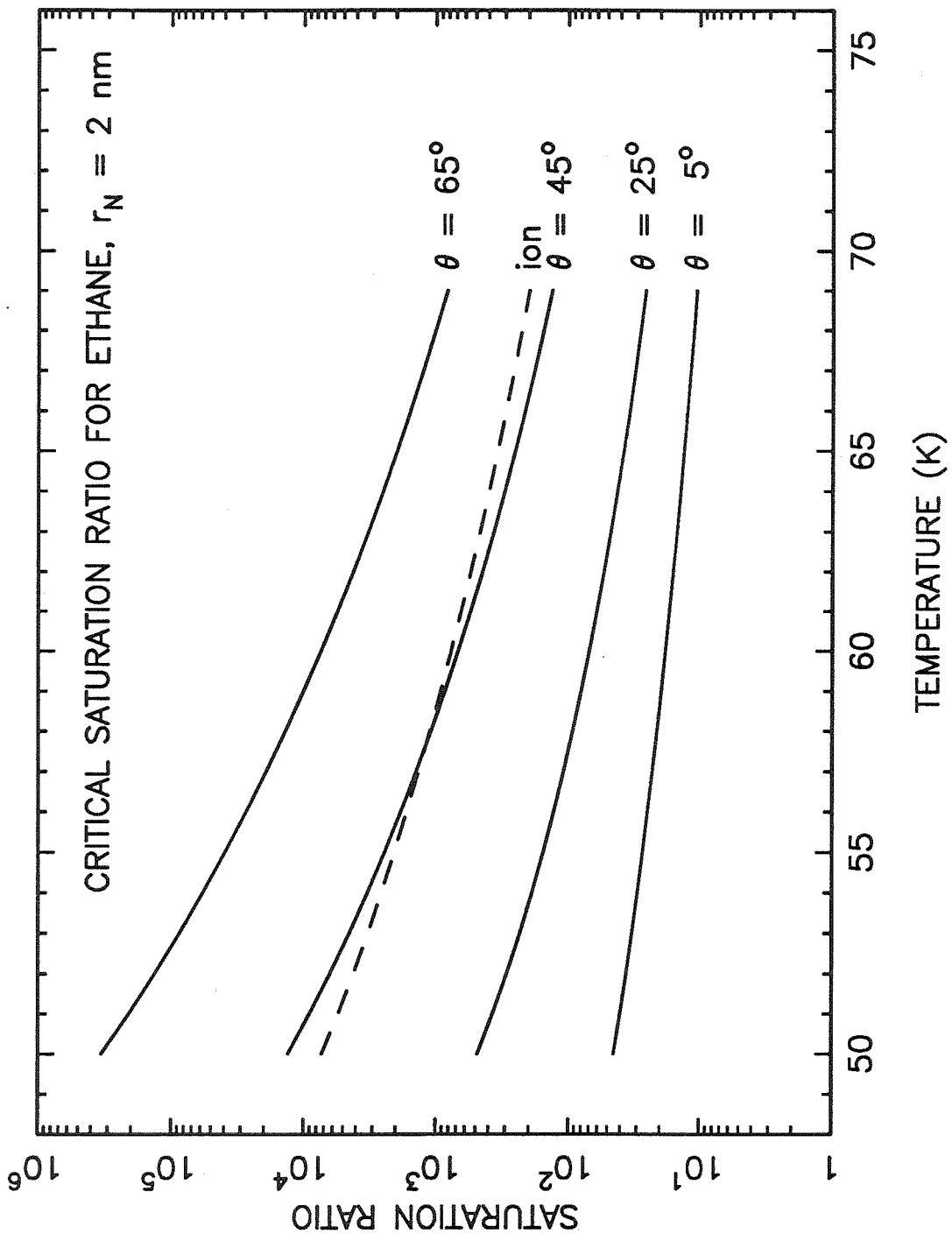

Figure 28b. Critical saturation ratios for ethane as a function of temperature for various assumed contact angles.

TABLE VII

Critical Saturation Ratios

Species	S_{homo}	S_{ion}	$S_{het}(A)$	$S_{het}(B)$
CH_4 (70 K)	28	11	1.3	12
C_2H_2 (70 K)	2.4×10^4	180	1.8	1600
C_2H_6 (55 K)	2.1×10^6	2100	2.2	1.4×10^4
CH_3C_2H (60 K)	2.8×10^8	*6700	1100	1.0×10^6
C_3H_8 (55 K)	1.1×10^{10}	2.0×10^5	400	7.3×10^6
C_4H_2 (100 K)	3.1×10^4	390	2.4×10^4	1.1×10^5
C_4H_{10} (65 K)	6.0×10^9	*2.2×10^5	6.3×10^4	3.3×10^7

with each other unless the calculations were performed for the same temperature. $S_{het}(A)$ defines a case of heterogeneous nucleation on a spherical insoluble particle of radius $r_N = 10$ nm and $\theta = 5°$ (*i.e.*, an efficient case). $S_{het}(B)$ is for the case of $r_N = 1$ nm and $\theta = 45°$ (*i.e.*, an inefficient case). The asterisks (*) indicate situations in which the ion–induced nucleation rate does not reach 10^{-3} sec^{-1} at the listed temperature; in these cases, the saturation ratios quoted are those at which no barrier to ion–induced nucleation exists. Note that homogeneous nucleation is much less efficient than either ion–induced or heterogeneous nucleation. The relative efficiency of ion–induced versus heterogeneous nucleation depends on the size and "compatibility" of the pre–existing insoluble nucleus.

4.4 Critical Nucleation Levels

If we calculate the critical saturation ratios of each hydrocarbon species as a function of temperature, we can compare these numbers with the actual densities and saturation ratios from our Neptune photochemical model; hence, we can predict

the altitude levels at which we expect significant particle formation to occur. We call these altitudes the *critical nucleation levels.*

As discussed in Section 4.3, the critical saturation ratios for heterogeneous nucleation are sensitive to unknown properties of the insoluble nucleus. For our calculations of the critical levels, we assume $r_N = 2$ nm and $\theta = 25°$. We chose $r_N = 2$ nm on the basis of the terrestrial meteor ablation and recondensation study of Hunten *et al.* (1980). Our choice of θ is somewhat arbitrary but represents an intermediate case between two "extreme" cases listed for heterogeneous nucleation in Table VII.

Fig. 29 illustrates how the critical nucleation ratios are calculated. The density of ethane from our photochemical Model C in Section 2 is divided by the saturation vapor density of the species at the temperature at each altitude level. This result gives us the value of the saturation ratio S in the atmosphere if no particle formation were occurring. We then compare this saturation ratio with the critical saturation ratio required for observable particle formation (in this case for heterogeneous nucleation on particles with $r_N = 2$ nm and $\theta = 25°$). In regions where S exceeds S_{crit}, haze particle formation is likely to take place. Also shown in Fig. 29 is the $S = 1$ line. Previous modelers have assumed that aerosol formation is initiated as soon as S crosses the $S = 1$ line.

The actual region in which significant particle formation can take place is narrower than that estimated by assuming particles form at $S = 1$ because nucleation is an inefficient process. Haze particles may be found below the region bracketed by S_{crit}; that is, particles will not begin to evaporate until the saturation ratio falls below $S = 1$. However, particle formation is unlikely to be effective *above* the intersection of the S and S_{crit} curves. Note that ethane condensates may begin to evaporate before they fall to the level of the methane clouds ($\sim$ 1 bar). Most of the other hydrocarbon

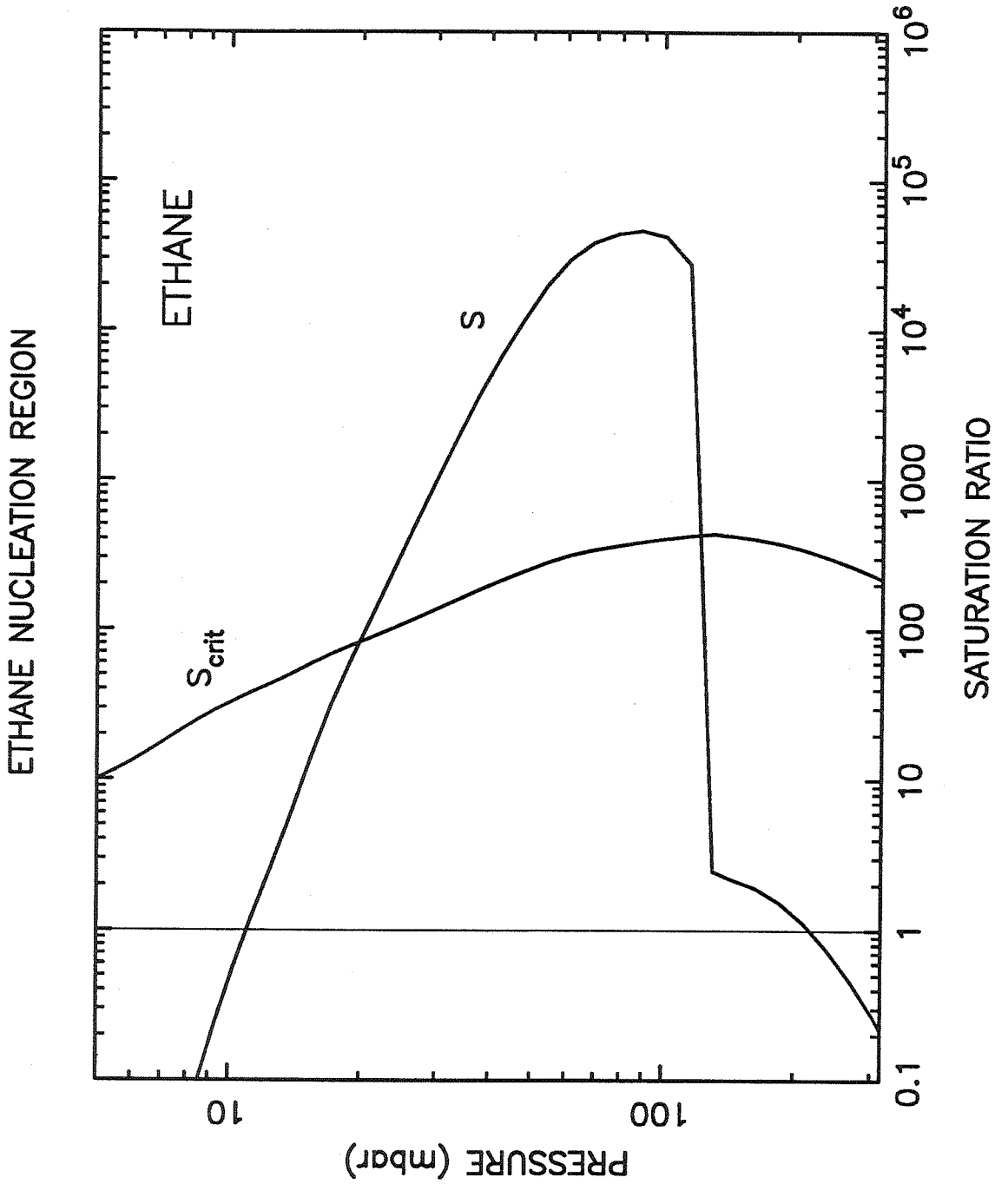

Figure 29. The nucleation region for ethane on Neptune (for heterogeneous nucleation, $r_N = 2$ nm, $\theta = 25°$). Ethane will nucleate at a substantial rate where the atmospheric abundance of ethane (the curve labeled S) exceeds the critical saturation ratio S_{crit}. The particles can evaporate where S falls below a saturation ratio of 1.

species can evaporate above this methane cloud region as well.

The assumption of $r_N = 2$ nm and $\theta = 25°$ for heterogeneous nucleation on Neptune results in critical levels that are 6 to 50 km below (for the stratosphere) the $S = 1$ levels. The critical nucleation levels for all the hydrocarbon species are listed in Table VIII. Both ion–induced and heterogeneous nucleation are considered, but in all cases except the formation of diacetylene condensates, heterogeneous nucleation on $r_N = 2$ nm, $\theta = 25°$ particles dominates. Ethylacetylene (1–C_4H_6) is not listed in Table VII or Table VIII because it never reaches critical saturation in our model Neptune atmosphere. If the condensation nuclei on Neptune are larger or more "wettable" than we assume, then 1–C_4H_6 condensates could be produced as well.

Fig. 30 demonstrates the effect of finite nucleation rates on aerosol formation in Neptune's stratosphere and upper troposphere. The figure on the left shows the $S = 1$ levels on Neptune. The vapor species first become saturated here, and if nucleation were not inefficient, haze particles could form at these levels. The figure on the right shows our calculated critical nucleation levels. By assuming that particle formation is not instantaneous as the vapor becomes supersaturated, we find that the stratospheric haze layers may form a lot lower in the atmosphere than has previously been supposed. The effect is more pronounced for heavier and for less abundant species.

Methane nucleates very efficiently. Observable numbers of methane cloud particles should begin to form just a few kilometers above the $S = 1$ level; thus, a methane "cold trap" should operate efficiently on Neptune unless very strong vertical winds can carry condensates to stratospheric levels where they might evaporate.

Both ethane and acetylene nucleate fairly efficiently. Because acetylene is less abundant and has a higher surface tension, ethane will nucleate more efficiently

TABLE VIII

Critical Levels Defining the Onset of Nucleation

Species	Case	P (mbar)	T (K)	Δz (km) from $S = 1$	S_{crit}
	$S = 1$	1400	82	0	
CH_4	heterogeneous	1100	73	6	3.6
	ion-induced	820	67	12	14
	$S = 1$	11	65	0	
C_2H_6	heterogeneous	21	58	12	88
	ion-induced	37	54	22	2500
	$S = 1$	6.5	76	0	
C_2H_2	heterogeneous	8.5	69	6	24
	ion-induced	9.3	68	8	250
	$S = 1$	8.5	69	0	
CH_3C_2H	heterogeneous	54	52	34	2×10^5
	ion-induced	none			
	$S = 1$	8.5	69	0	
C_3H_8	heterogeneous	24	57	20	5000
	ion-induced	48	53	32	4×10^5
	$S = 1$	2.0	107	0	
C_4H_2	heterogeneous	12	64	48	10^{17}
	ion-induced	*3.3	*96	*16	*760
	$S = 1$	6.5	76	0	
C_4H_{10}	heterogeneous	78	51	46	10^9
	ion-induced	none			

These levels describe the location at which the nucleation rate reaches $J = 10^{-3}$ sec^{-1} per particle or per ion cluster. The heterogeneous nucleation case is for an insoluble particle radius $r_N = 2$ nm and a contact angle of $\theta = 25°$. The ion–induced nucleation case is for a singly–charged ion cluster. The level marked with an asterisk (*) is a level at which the nucleation rate does not reach 10^{-3} sec^{-1}; instead, we define the critical level to be where there is no barrier to ion–induced nucleation.

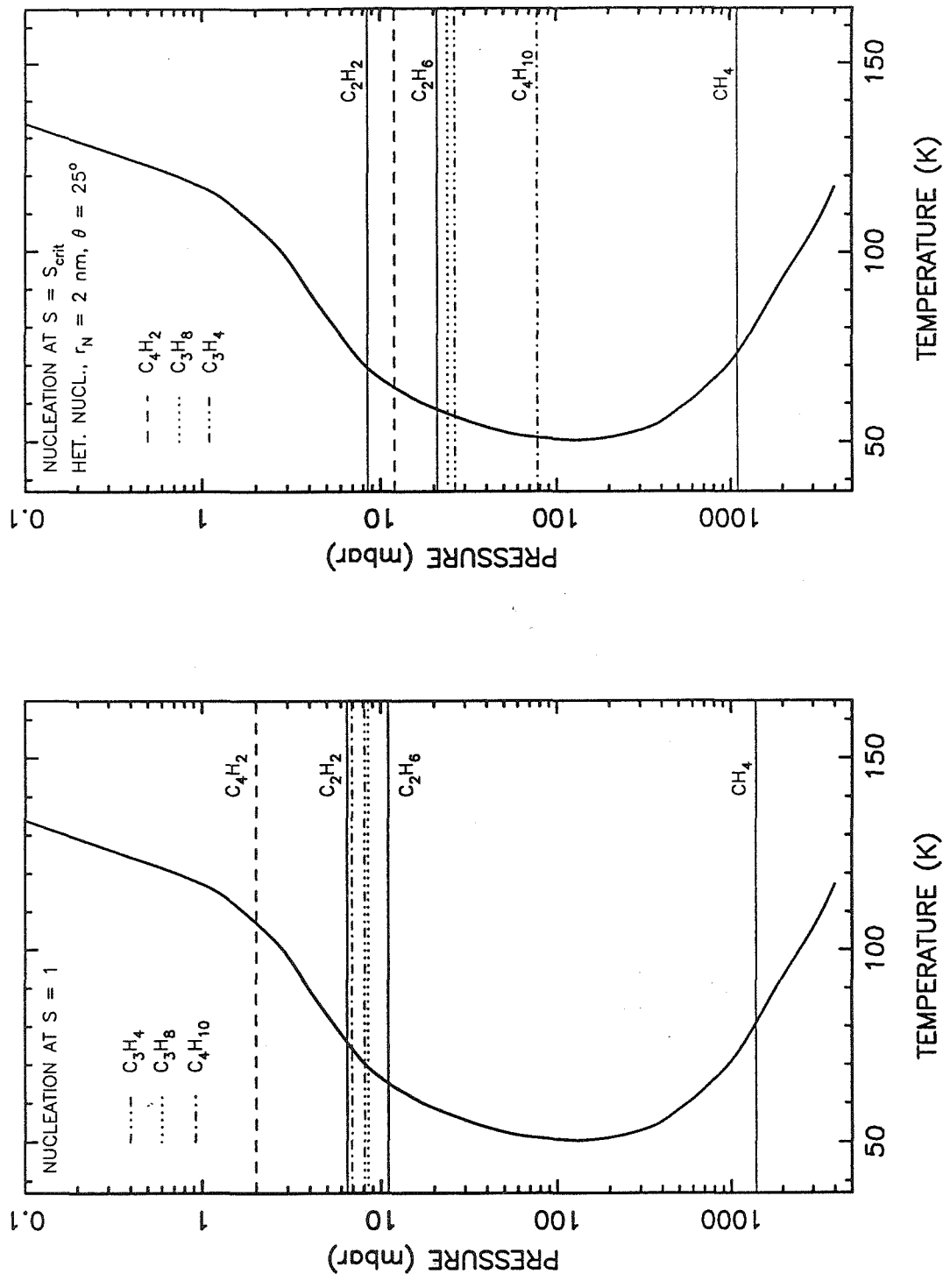

Figure 30. Nucleation levels on Neptune. The figure on the left illustrates the $S = 1$ levels for the different hydrocarbon species. The figure on the right illustrates the critical nucleation levels for homogeneous nucleation about a spherical insoluble particle of raduis $r_N = 2$ nm and contact angle $\theta = 25°$.

than acetylene at any given temperature. However, because C_2H_2 is less volatile, it becomes supersaturated at higher temperatures and nucleates more efficiently due to the $1/T^3$ dependence of the exponent in the nucleation rate equation.

On the other hand, diacetylene's extremely low vapor pressure and low mean molecular mass inhibit nucleation. Although C_4H_2 becomes supersaturated at relatively high temperatures, its high mean molecular mass limits nucleation because of the m_1^2 dependence of the exponent in the nucleation rate equation. Higher supersaturations are required to achieve significant nucleation, implying that nucleation can only occur at lower temperatures where large supersaturations develop. The vapor pressure of diacetylene is extremely low at low stratospheric temperatures, and although the high saturation ratios allow the nucleation barrier to fall to negligible values, the vapor molecules are not abundant enough to form clusters at an appreciable rate. Butane has a similar problem. Propane and methylacetylene lie somewhere between the relatively efficient nucleation case of C_2H_2 and C_2H_6 and relatively inefficient nucleation case of C_4H_2 and C_4H_{10}.

Because particle formation can occur over a relatively wide altitude range in the stratosphere (e.g., Fig. 29), the different hydrocarbon species are often nucleating in the same regions. Ethane and acetylene, being the most abundant species and the most efficient at forming particles, will dominate the particle formation in any region of overlap. In the example presented in Fig. 30 (heterogeneous nucleation, $r_N = 2$ nm, $\theta = 25°$), acetylene haze particles will form at the highest altitudes, followed by diacetylene, ethane, and the other hydrocarbon species. However, if nucleation is for some reason more efficient than we have assumed (e.g., if condensation nuclei are large or allow low contact angles) then diacetylene might nucleate at the highest altitudes.

In summary, the fact that nucleation is not instantaneous under Neptunian

conditions implies that particle formation will not occur until large supersaturations develop. None of the hydrocarbon species including methane nucleate efficiently by homogeneous nucleation. Thus, particle formation on Neptune requires the presence of foreign condensation nuclei or ions. Sources of both foreign particles and ions do exist for stratospheric and upper tropospheric regions of Neptune; however, unless the condensation nuclei have extremely favorable properties, the formation of hydrocarbon condensates will still be slow at low supersaturations. Thus, we expect aerosol and cloud particles to form at levels somewhat different from those predicted on the basis of 100% saturation.

5. Summary and Conclusions

The carbon cycle in Neptune's atmosphere describes the sequence through which carbon–bearing molecules are transported between Neptune's upper and lower atmosphere. In this paper, we have examined the details of an important stage in the carbon cycle on Neptune; specifically, we have studied the photochemistry of methane in Neptune's upper atmosphere and have identified the processes that could lead to the formation of hydrocarbon condensates in Neptune's lower stratosphere and upper troposphere. This work will hopefully inspire further investigations into the details of the carbon cycle on Neptune. The major conclusions from our photochemistry and nucleation studies are now presented, and implications for further research are discussed.

5.1 Photochemistry Conclusions

We have developed theoretical models of hydrocarbon photochemistry in Neptune's atmosphere. In our models, we consider the photochemistry of hydrocarbon species that contain three and four carbon atoms as well as the traditional C_1 and C_2 species. Our models are based on the Jovian photochemical models of Gladstone *et al.* (1991), but we use input parameters and boundary conditions relevant to Neptune. *Voyager* observations are used to constrain the temperature profile and composition of the bulk atmosphere; additional information concerning the eddy diffusion coefficient in Neptune's upper atmosphere is considered, but the profile of eddy diffusion with altitude essentially remains a free parameter.

Photolysis of methane by both local interstellar and solar ultraviolet radiation initiates the production of acetylene, ethylene, ethane, and higher hydrocarbon species. The major hydrocarbon species that result from methane photolysis are ethane, acetylene, propane, methylacetylene, diacetylene, ethylene, hexatriyne, ethy-

lacetylene, propylene, and butane. Several of these species have number densities in our models that exceed their saturation vapor densities in Neptune's lower stratosphere. Thus, these species may condense and form haze layers in the stratosphere. Ethane, acetylene, propane, methylacetylene, diacetylene, and butane are probably the six most important potential condensates.

The calculated abundances of the aforementioned species near their condensation regions turn out to be sensitive to the assumed stratospheric methane abundance, the assumed stratospheric and upper atmospheric eddy diffusion profile, the eleven-year variation in the solar ultraviolet flux, and the planetary latitude or season. The eddy diffusion profile is the single most important unknown parameter.

Very few constraints can be placed on the eddy diffusion profile in Neptune's atmosphere by comparing model results with ground-based and spacecraft observations. Some positive indications from our results are as follows: (1) The eddy diffusion coefficient is probably quite high ($> 10^7$ cm^2 s^{-1}) in the upper atmosphere, (2) the diffusion coefficient in the $\sim$ 10 mbar region of the stratosphere is probably less than 10^4 cm^2 s^{-1}. The observations are consistent with models that assume widely different stratospheric methane mixing ratios (e.g., 2.5×10^{-5} to 2×10^{-2}), so the methane abundance is not constrained by our photochemical models.

Our photochemical results are not accurate in the regions of hydrocarbon condensation. In order to get accurate vapor mixing ratios in these regions, we would need to couple our photochemical model with models that consider nucleation and condensation of the hydrocarbon aerosol particles. We do not present such coupled models in this paper. However, we do examine the possible mechanisms that can lead to particle formation and determine the mechanisms that are viable on Neptune.

5.2 Nucleation Conclusions

We have examined the roles of homogeneous, ion–induced, and heterogeneous nucleation in forming particles under stratospheric and upper tropospheric conditions on Neptune. Because of the lack of laboratory data on hydrocarbon nucleation, we have decided to use the classical theories of nucleation in this study. We find that nucleation is very inefficient at the low temperatures encountered in Neptune's atmosphere. Particle formation will not occur until large supersaturations are achieved. None of the condensable hydrocarbon species that we have examined will nucleate efficiently by homogeneous nucleation. Thus, particle formation in Neptune's lower stratosphere and upper troposphere requires the presence of foreign condensation nuclei or ions.

Several sources of ions and condensation nuclei may exist in Neptune's atmosphere. Ions are produced at low altitude levels on Neptune from interactions of galactic cosmic rays with neutral atmospheric molecules. In a simple model of cosmic–ray ionization, we find the peak ion production rate to be at $\sim$ 40 mbar, a pressure level well within the stratospheric condensation regions. The peak electron density at this location is $\sim$ 3000 cm^{-3} and varies slightly with the eleven–year solar cycle. Thus, ions are abundant enough to allow ion–induced nucleation to operate, provided that other conditions are favorable.

The major sources of condensation nuclei at stratospheric and upper tropospheric levels on Neptune are recondensed meteoric material, residual meteoroids, chemical species of low volatility produced by charged–particle impact or photochemical reactions at higher levels in the atmosphere, or the mixing of solid particles from deeper tropospheric regions to higher altitude levels. These sources should provide abundant potential condensation nuclei (CN), but it is uncertain whether the CN from these sources will have the necessary properties to initiate nucleation at low

vapor supersaturations.

By examining the efficiency of heterogeneous nucleation on substrates with widely varying physical properties, we can at least bracket the conditions under which we expect particle formation by heterogeneous nucleation to be important. Table VII demonstrates the range of critical saturation ratios expected for each of the potentially condensable hydrocarbon species — Case A refers to an efficient while Case B refers to an inefficient one. The critical saturation ratios required for efficient ion–induced nucleation (also shown in Table VII) usually fall within the range bracketed by the heterogeneous nucleation results. Thus, the relative importance of ion–induced versus heterogeneous nucleation on Neptune depends on the properties of the condensation nuclei.

By comparing the critical saturation ratios of the different nucleation mechanisms with the results from our photochemical models, we can determine the levels at which we expect significant hydrocarbon particle formation to occur. For all the nucleation mechanisms considered, we find that particles will not form in significant numbers at the saturation levels; large supersaturations are required. Thus, particles will form at levels significantly different from their saturation levels. In our model, methane cloud particles will form a few kilometers above the $S = 1$ level for methane in the troposphere while the other hydrocarbon haze particles will form at levels 5 to 50 km below their saturation levels in the stratosphere. Methane, ethane, and acetylene nucleate relatively efficiently; diacetylene and butane nucleate inefficiently; and propane and methylacetylene are intermediate between these two cases (see Table VIII and Fig. 30). Thus, workers who model the radiative transfer properties of the aerosol layers should be aware that haze particles might form at much different altitudes than are indicated by their saturation vapor densities.

Although we have tried, both through photochemical models and nucleation

calculations, to isolate the important factors that contribute to the formation of cloud and haze particles in Neptune's visible atmosphere, the real situation on Neptune is unlikely to be as simple as we have imagined. The hydrocarbon species will be condensing about each other throughout the stratosphere; chemical interactions between the species may become important. Condensation, coagulation, and coalescence will be operating to increase the size of the particles as they fall, so nucleation may be more efficient at lower altitudes. Galactic and solar cosmic rays may disrupt the condensates, may produce multiply charged particles, or may otherwise complicate the situation. Energetic charged particles (or photons if the particles are small enough to have long residence times in the stratosphere) may initiate chemical changes in the solid phase that make the material less volatile (see Allen *et al.* 1980, Khare *et al.* 1987); thus, the particles would be less likely to evaporate until they reached lower tropospheric levels.

Much of our work depends on laboratory results that are only known at high temperatures and/or high pressures. We need more data on the physical properties of the hydrocarbons at low temperatures and on the important reaction pathways, rate constants, and absorption cross sections at low temperatures and pressures before we have confidence in our conclusions. Therefore, our conclusions are tentative and suggest many avenues for future research.

5.3 Implications for Future Research

The photochemical models could be improved in several ways. Some key rate constants have yet to be measured at low temperatures. For instance, the only reaction the produces ethane in appreciable quantities is the methyl recombination reaction R135; yet the reaction rate for R135 has only been measured in the laboratory at temperatures above 296 K. The sensitivity of the photochemical model

to higher stratospheric temperatures and to different assumed hydrogen fluxes at the upper boundary should also be studied in future models. A better background hydrostatic atmosphere should be developed that more closely matches the *Voyager* Radio Science data.

The nucleation model would be vastly improved by new laboratory measurements of the physical properties of the hydrocarbon species at low temperatures. The surface energy, bulk density, and dielectric constant are especially essential to the nucleation calculations. Further laboratory determinations of the vapor pressures of diacetylene, methylacetylene, propane, ethylacetylene, and butane at low temperatures would be useful, as would estimates of ΔG_{des} for the hydrocarbons on different substrates. Direct nucleation experiments of the hydrocarbons at low temperatures would most assuredly provide insight into the problem of particle formation on Neptune.

A more realistic model of cosmic ray ionization is called for and would be interesting in its own right. More realistic estimates of the properties of any stratospheric condensation nuclei would vastly improve the quality of our conclusions.

The photochemical models developed here suggest several directions for further observations of Neptune. Advances in high spectral resolution ground–based detectors may allow infrared emission features of CH_3C_2H, C_3H_8, or other important stratospheric molecules to be detected. A determination of the relative abundances of the heavier hydrocarbon species relative to C_2H_2 and C_2H_6 would provide an important check on the soundness of the photochemical model and might help distinguish between the relative importance of photochemical and charged–particle–impact processes in controlling the chemistry of Neptune's stratosphere. Continued observations of C_2H_2 and C_2H_6 absorption and emission features at different wavelengths would provide vertical profiles of the ethane and acetylene mixing ratios that would

help further constrain the eddy–diffusion profile in the stratosphere. Ground–based and spacecraft infrared data should be reanalyzed to consider the possibility of high stratospheric temperatures.

The photochemistry and nucleation models developed in this paper represent the first stage in the forward modeling of complex coupled gas–phase and aerosol processes. The next step in the modeling would be to couple nucleation and condensation directly in with the photochemistry. This upgrade to the photochemical model would involve the addition of two terms to the continuity equation as well as the inclusion of an additional equation that derives particle masses. More accurate determinations of stratospheric vapor abundances would be obtained from this coupled model. The third step in such modeling would be to include aerosol dynamics (cloud microphysics) to follow the evolution of the aerosol particles as they grow by condensation, Brownian coagulation, and gravitational coalescence and are lost by gravitational settling and turbulent mixing. Such aerosol dynamics models would provide information concerning the steady–state properties of the clouds and hazes, the rates at which hydrocarbons are lost from the stratosphere by precipitation and diffusion, and the time scales for certain recycling processes. Finally, the scattering properties of the predicted haze and cloud layers could be examined with radiative transfer models.

Direct comparisons of the predictions of the forward models discussed above with inversions of observational data from *Voyager* (e.g., the Uranus study of Pollack *et al.* 1987) or from Earth–based telescopes (e.g., Baines and Smith 1990, Hammel *et al.* 1989) would provide further constraints on the properties of the haze layers. The current aerosol models of Neptune (e.g., Baines and Smith 1990 and Hammel *et al.* 1989) assume high stratospheric methane abundances. Reanalyses of the Baines and Smith (1990) and Hammel *et al.* (1989) datasets — analyses that consider possibly

lower methane abundances and possibly lower haze altitude levels — would be quite interesting.

Although we have limited our discussion to the planet Neptune, the photochemical and nucleation models have direct applicability to the other outer planets. A complete photochemical and aerosol model might provide insights into the temporal variability of Neptune over the past two decades (e.g., Lockwood and Thompson 1986, 1991). In summary, our study of photochemistry and aerosol formation on Neptune opens many avenues for future research.

Acknowledgments

We have benefitted from discussions with G. S. Orton. The first author gratefully acknowledges support from the NASA Graduate Student Researchers Program.

Appendix A: Physical Properties of the Important Hydrocarbons

To evaluate the details of hydrocarbon nucleation and aerosol formation on Neptune, we must have information concerning some of the physical properties of the condensable hydrocarbons. In particular, we need to know the vapor pressure, liquid and/or solid density, surface energy, and dielectric constant of the condensable hydrocarbons at low temperatures ($65 < T < 110$ K). Data reported for the low temperatures typical in Neptune's lower stratosphere and upper troposphere are rare; therefore, we must often extrapolate the available data to much lower temperatures. We will clearly indicate the occasions when our chosen values are in doubt. Values pertaining to the solid phase are used whenever possible, but liquid data are generally more available. Plots of the temperature dependence of the vapor pressure and the surface tension of the hydrocarbon species are given in Figs. A1 and A2.

Methane

For the vapor pressure of methane over methane ice, we use the expression of Romani and Atreya (1988):

$$\log_{10} P_v(\text{atm}) = 4.425070 - \frac{453.92414}{T} - \frac{4055.6016}{T^2} + \frac{115352.19}{T^3} - \frac{1165560.7}{T^4}$$

$$\text{for } 67 < T < 90.65 \text{ K}.$$

The above expression was originally reported by Kirk and Ziegler (1965). Note that the triple point of methane is at 90.65 K.

The surface tension of liquid methane (erg cm^{-2}) was taken from Fuks and Bellemans (1966):

$$\sigma = 38.618 - 0.1873T - 3.56 \times 10^{-4}T^2$$

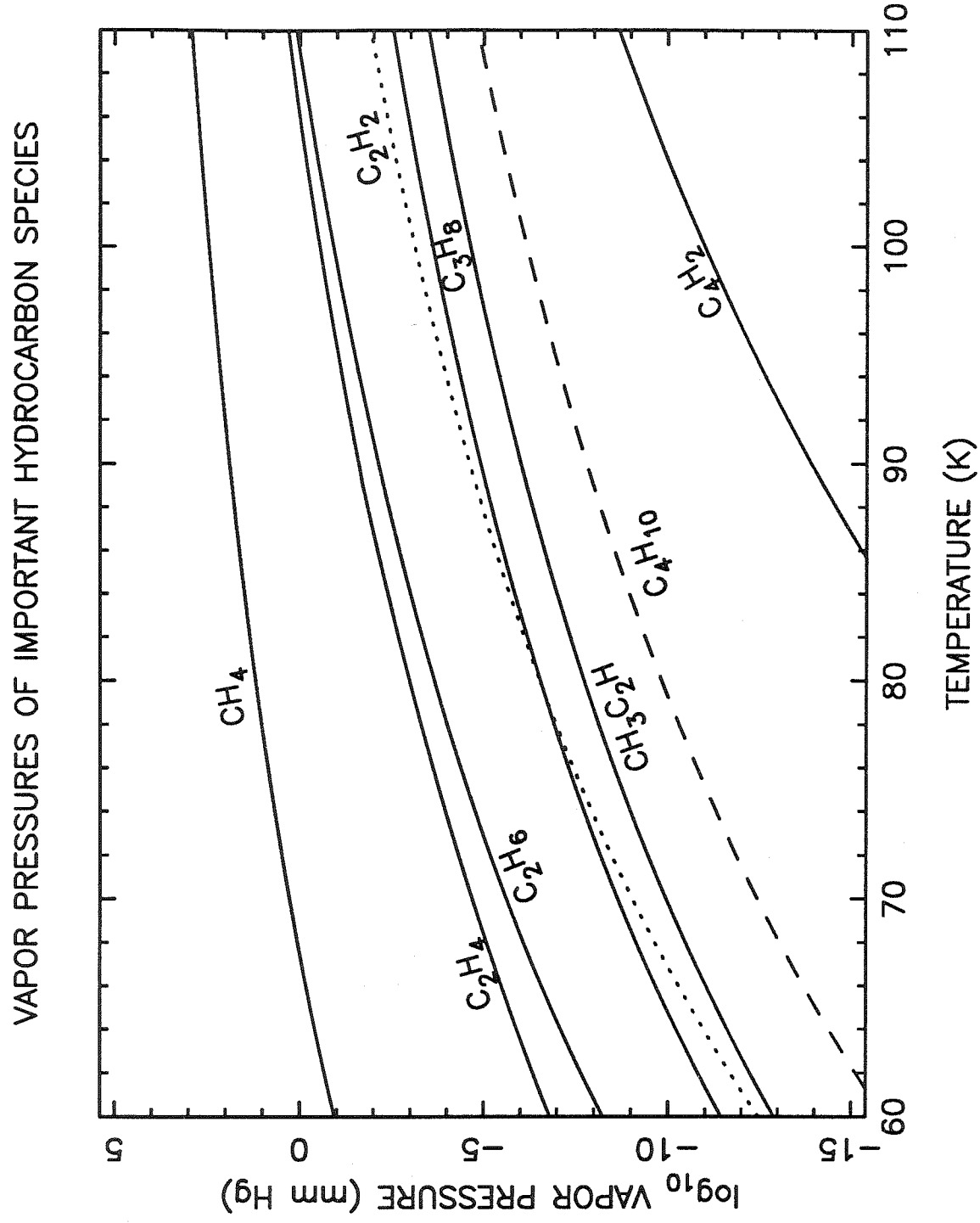

Figure A1. The vapor pressures of the important condensable hydrocarbon species on Neptune. The vapor pressures of many of these species are uncertain at low temperatures due to lack of data (see text).

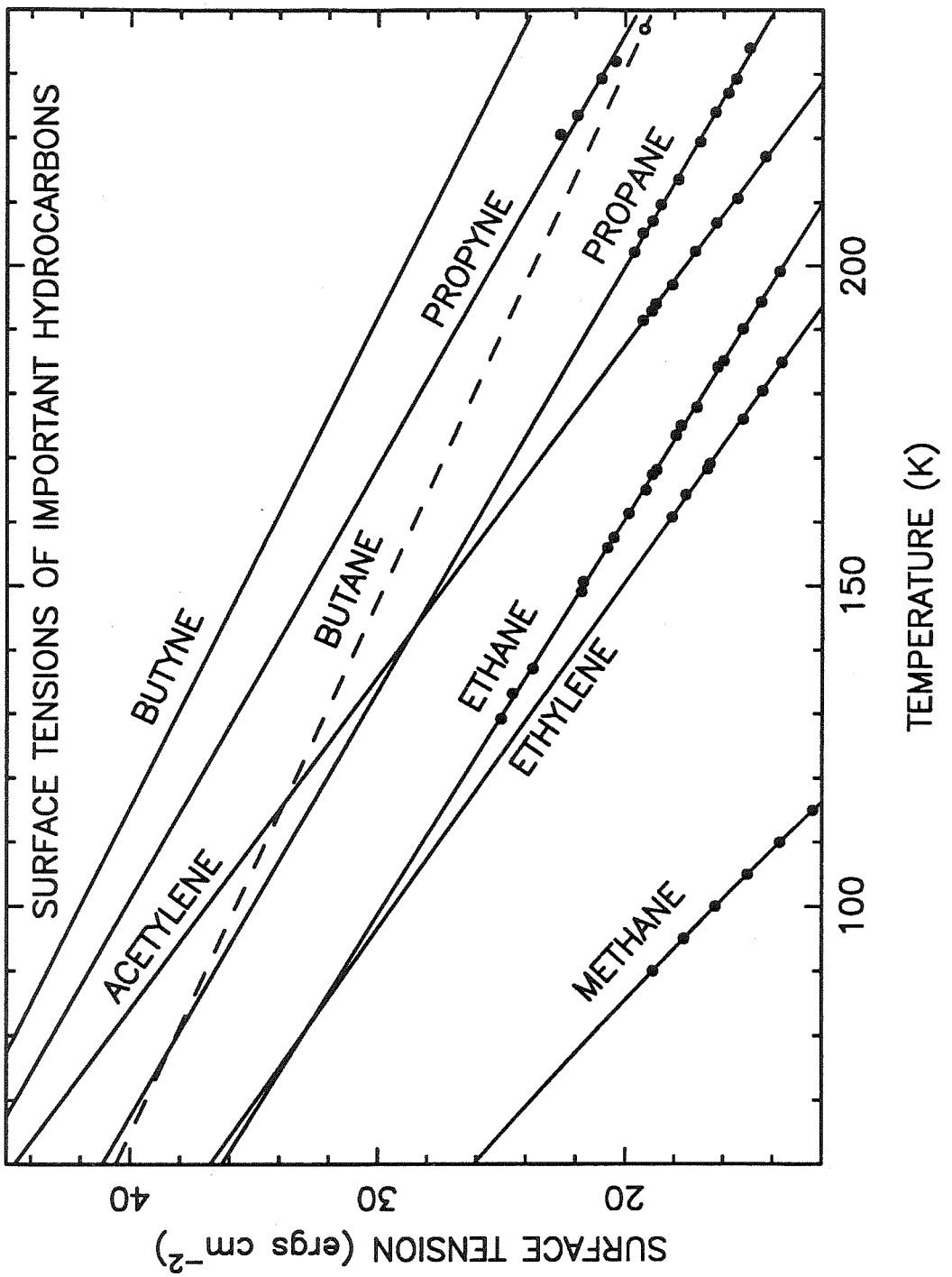

Figure A2. The surface tensions of the important condensable hydrocarbon species on Neptune. Individual data points are included to emphasize that the low temperature values represent considerable extrapolations from the available data.

$$\text{for } 90 < T < 115 \text{ K}.$$

No data on the surface energy of the solid were found. We have used the above expression to extrapolate to lower temperatures.

McClune (1976) found that the density of liquid methane (in kg m^{-3}) could be described by the expression

$$\rho = 511.712 + 0.180922T - 1.158657 \times 10^{-2}T^2 + 2.5157 \times 10^{-5}T^3$$

$$\text{for } 93 < T < 123 \text{ K}.$$

This expression also fits (to within 1%) the experimental determination of the density of solid methane at 20 K (Johnson 1961).

The expression for the dielectric constant of liquid methane was derived from data presented by Johnson (1961) and Younglove and Ely (1987):

$$\epsilon = 1.8166 - 8.4349 \times 10^{-4}T - 7.6963 \times 10^{-6}T^2$$

$$\text{for } 91 < T < 140 \text{ K}.$$

Ethane

The expression for the vapor pressure of ethane over ethane ice was also taken from Romani and Atreya (1988) and is presumably a fit to the calculated values of Ziegler *et al.* (1964):

$$\log_{10} P_v(\text{mm Hg}) = 10.01 - \frac{1085.0}{T - 0.561}$$

$$\text{for } 30 < T < 90 \text{ K}.$$

The ethane triple point is at 90 K.

The surface tension of liquid ethane was found from a fit to data of Leadbetter *et al.* (1964) and Maass and Wright (1921):

$$\sigma(\text{erg cm}^{-2}) = 46.1385 - 0.164076T + 7.01635 \times 10^{-6}T^2$$

$$\text{for } 129 < T < 200 \text{ K}.$$

We use this expression to extrapolate to lower temperatures.

The density of solid ethane is 0.713 g cm^{-3} at 77 K (Stewart and LaRock 1958).

We find the dielectric constant of liquid ethane to be

$$\epsilon = 2.10142 - 1.60401 \times 10^{-3}T - 1.5955 \times 10^{-6}T^2$$

$$\text{for } 90 < T < 140 \text{ K}$$

based on the data of Younglove and Ely (1987) and Weber (1976).

Acetylene

The vapor pressure of acetylene is derived from a fit to the data of J. E. Allen, Jr. (personal communication, 1990) and Tickner and Lossing (1951); each data point is weighted by the authors' estimate of the error of the measurement:

$$\log_{10} P_v(\text{mm Hg}) = 6.09748 - \frac{1644.1}{T} + 7.2333 \log_{10}\left(\frac{1000}{T}\right)$$

$$\text{for } 80 < T < 145 \text{ K}.$$

The triple point of acetylene is at 192 K. Allen's low temperature data (< 91 K) were obtained from a thin film infrared (TFIR) spectroscopic technique (see Khanna *et al.* 1990) that may underestimate the actual vapor pressure. However, our fit to the data

falls above the low temperature (TFIR) data points; e.g., the expression leads to a vapor pressure estimate almost a factor of 2 higher than the data at 80 K. Since the expression does not accurately fit all the available data we would like to emphasize that the above expression is uncertain below ~100 K.

An expression for surface tension of liquid acetylene was obtained from Jasper (1972):

$$\sigma(\text{erg cm}^{-2}) = 3.42 - 0.1935(T - 273.15)$$

$$\text{for } 191 < T < 218 \text{ K.}$$

The original data were from Maass and Wright (1921). We need to extrapolate to temperatures far below the actual measurements to find the surface energy at temperatures typical on Neptune.

The density of solid acetylene is 0.81 g cm^{-3} at 77 K and 0.79 g cm^{-3} at 90 K (Amamchyan and Moroz 1965).

We assume that the dielectric constant of acetylene has the following form:

$$\epsilon = 2.484 - 10^{-3}(T - 195) - 5 \times 10^{-6}[T^2 - (195)^2]$$

based on the value at 195 K given by Gee *et al.* (1986) and on our estimate of the temperature dependence. Any errors in our adoption of this expression for ϵ should have little effect on our calculated ion–induced nucleation rates.

Ethylene

We use the expression given by Atreya (1986) for the vapor pressure of ethylene (where P_v is given in mm Hg):

$$\log_{10} P_v = 6.74756 - \frac{585.00}{T - 18.16}$$

$$\text{for } 120 < T < 155 \text{ K},$$

$$\log_{10} P_v = 50.79 - \frac{1703}{T} - 17.141 \log_{10} T$$

$$\text{for } 104 < T < 120 \text{ K},$$

$$\log_{10} P_v = 8.724 - \frac{901.6}{T - 2.555}$$

$$\text{for } 89 < T < 104 \text{ K},$$

$$\log_{10}(P_v \times 10^3) = 1.5477 - 1038.1\left(\frac{1}{T} - 0.011\right) + 16537\left(\frac{1}{T} - 0.011\right)^2$$

$$\text{for } T < 89 \text{ K}.$$

The ethylene triple point is at 104 K.

The surface tension of liquid ethylene (erg cm^{-2}) is found from the expression of Jasper (1972):

$$\sigma = -2.37 - 0.1854(T - 273.15)$$

$$\text{for } 113 < T < 163 \text{ K}.$$

The data were originally from Maass and Wright (1921).

Solid ethylene has a density of 0.732 g cm^{-3} at 77 K (Stewart and LaRock 1958). The liquid data as reported by Younglove (1982) obey the following expression:

$$\rho(\text{g cm}^{-3}) = 0.775011 - 1.056087 \times 10^{-3} T - 9.565318 \times 10^{-7} T^2$$

$$\text{for } 104 < T < 140 \text{ K}.$$

We could not find information concerning the dielectric constant of ethylene. We have estimated ϵ to be 2.5 at low temperatures.

Methylacetylene

The expression for the vapor pressure of methylacetylene was fit from values given in Stull (1947). The data originally came from Maass and Wright (1921), Morehouse and Maass (1931), and Heisig and Hurd (1933):

$$\log_{10} P_v(\text{mm Hg}) = 7.7759 - \frac{1240.32}{T}$$

$$\text{for } 162 < T < 250 \text{ K.}$$

Note that a substantial extrapolation is required to get values at the temperatures typical on Neptune; thus, our expression is very uncertain at low temperatures.

The expression for the surface tension of liquid methylacetylene is again from Jasper (1972):

$$\sigma = 14.51 - 0.1482(T - 273.15)$$

$$\text{for } 183 < T < 233 \text{ K.}$$

The data were originally from Maass and Wright (1921). Note the necessity of extrapolation to much lower temperatures.

According to Gee *et al.* (1986), the density and dielectric constant of liquid methylacetylene have the following forms:

$$\rho(\text{kgm}^{-3}) = 971.9 - 1.205T$$

$$\epsilon = 6.087 - 11.72 \times 10^{-3}T$$

$$\text{for } 185 < T < 246 \text{ K.}$$

Propane

Based on data from Tickner and Lossing (1951), Ziegler (1959) suggests that the vapor pressure of propane has the following expression:

$$\log_{10} P_v(\text{mm Hg}) = 8.16173 - \frac{1176}{T}$$

for $105 < T < 165$ K.

The triple point of propane is at 85 K.

The surface tension of liquid propane is found from the data of Maass and Wright (1921):

$$\sigma(\text{erg cm}^{-2}) = 50.1965 - 0.15115T$$

for $202 < T < 234$ K.

A large extrapolation to low temperatures is required.

The expression for the density of liquid propane was taken from McClune (1976):

$$\rho(\text{kg m}^{-3}) = 830.239 - 1.260146T + 1.89701 \times 10^{-3}T^2 - 4.779 \times 10^{-6}T^3$$

for $93 < T < 173$ K.

This expression fits (to within 3%) the experimental determination of the density of solid propane at 77 K (0.763 g cm^{-3}, Stewart and LaRock 1958).

The dielectric constant of propane is taken from the values of Younglove *et al.* (1987):

$$\rho(\text{g cm}^{-3}) = 2.305606 - 2.782719 \times 10^{-3}T + 3.15638 \times 10^{-6}T^2$$

for $85 < T < 130$ K.

Diacetylene

Very little data exist for diacetylene. The following expression for the vapor pressure of diacetylene (in mm Hg) is from a generalized least squares fit to the data

of Tanneberger (1933) and Khanna *et al.* (1990) (again, each point is weighted by its estimated error):

$$\log_{10} = 5.3817 - \frac{3300.5}{T} + 16.63415 \log_{10}\left(\frac{1000}{T}\right)$$

$$\text{for } 127 < T < 249 \text{ K}.$$

The expression is considerably higher than the TFIR low temperature data of Khanna *et al.* (1990) and so is very uncertain at low temperatures. We could find no data for the surface tension, dielectric constant, and density of liquid or solid diacetylene.

Ethylacetylene (1–Butyne)

The expression for the vapor pressure of ethylacetylene is from Schlessinger (1970):

$$\log_{10} P_v(\text{mm Hg}) = 8.032581 - \frac{1441.42}{T}$$

$$\text{for } 181 < T < 282 \text{ K}.$$

Note the large extrapolation in temperature that is required to get values at temperatures relevant to the condensation regions on Neptune. Since the vapor pressure of ethylacetylene is almost identical to that of butane at low temperatures, we do not show the vapor pressure curve for both butane and ethylacetylene in Fig. A1.

The surface tension of ethylacetylene is found from the data of Morehouse and Maass (1931):

$$\sigma(\text{erg cm}^{-2}) = 55.1122 - 0.130837T$$

$$\text{for } 242 < T < 282 \text{ K}$$

and is very uncertain at the temperatures we are considering.

From the data of Morehouse and Maass (1931), we also find the density of liquid ethylacetylene:

$$\rho(\text{g cm}^{-3}) = 0.979147 - 1.10278 \times 10^{-3}T$$

$$\text{for } 242 < T < 282 \text{ K.}$$

We could not find information concerning the dielectric constant of ethylacetylene and estimate it to be ~3.

Butane

The expression for the vapor pressure of n-butane was taken from Ziegler (1959):

$$\log_{10} P_v(\text{mm Hg}) = 8.446 - \frac{1461.2}{T}$$

$$\text{for } 128 < T < 196 \text{ K}$$

from data originally presented by Tickner and Lossing (1951). The triple point of n-butane is 135 K.

The expression for the surface tension of liquid butane was taken from Jasper (1972):

$$\sigma(\text{erg cm}^{-2}) = 14.87 - 0.1206(T - 273.15)$$

$$\text{for } 203 < T < 293 \text{ K.}$$

A large extrapolation to lower temperatures is required.

The expression for the liquid and solid density of n-butane was taken from McClune (1976):

$$\rho(\text{kg m}^{-3}) = 853.249 - 0.86941T + 6.505 \times 10^{-5}T^2 - 9.57 \times 10^{-7}T^3$$

for $93 < T < 173$ K

while the expression for the dielectric constant was derived from a fit to values given by Younglove *et al.* (1987):

$$\epsilon = 2.25857 - 1.62946 \times 10^{-3}T$$

for $135 < T < 150$ K

References

Allen, M., J. P. Pinto, and Y. L. Yung 1980. Titan: Aerosol photochemistry and variations related to the sunspot cycle. *Astrophys. J. Lett.* **242**, L125 – L128.

Allen, M., Y. L. Yung, and G. R. Gladstone 1991. The relative abundance of ethane to acetylene in the jovian stratosphere. Submitted to *Astrophys. J. Lett.*

Allen, M., Y. L. Yung, and J. W. Waters 1981. Vertical transport and photochemistry in the terrestrial mesosphere and lower thermosphere (50 – 120 km). *J. Geophys. Res.* **86**, 3617 – 3627.

Amamchyan, R. G., and A. I. Moroz 1965. Density of solid acetylene at low temperatures. *Tr., Vses. Nauchn.-Issled. Inst. Kislorodn. Mashinostr.* **10**, 150 – 162.

Appleby, J. F. 1986. Radiative–convective equilibrium models of Uranus and Neptune. *Icarus* **65**, 383 – 405.

Arnold, F. 1980. Ion-induced nucleation of atmospheric water vapor at the mesopause. *Planet. Space Sci.* **28**, 1003 – 1009.

Arnold, F. 1982. Ion nucleation — a potential source for stratospheric aerosols. *Nature* **299**, 134 – 137.

Ashihara, O. 1983. *Methane photochemistry in the outer planets*, 154 pp., Inst. Space Astronaut. Sci., Tokyo Report No. 602.

Atreya, S. K. 1986. *Atmospheres and Ionospheres of the Outer Planets and Their Satellites*, 224 pp., Springer–Verlag, Berlin.

Baines, K. H., and W. H. Smith 1990. The atmospheric structure and dynamical properties of Neptune derived from ground–based and IUE spectrophotometry. *Icarus* **85**, 65 – 108.

Bauer, S. J. 1973. *Physics of Planetary Ionospheres*, 230 pp., Springer–Verlag, Berlin.

Belletini, G., G. Cocconi, A. N. Diddens, E. Lillethun, G. Matthide, J. P. Scanlon, and A. M. Wetherell 1966. Proton–nuclei cross sections at 20 GeV. *Nucl. Phys.* **29**, 609 – 624.

Bergstralh, J. T., and K. H. Baines 1984. Properties of the upper tropospheres of Uranus and Neptune derived from observations at "visible" and near–infrared wavelengths. In *Uranus and Neptune* (J. T. Bergstralh, Ed.), pp. 179 – 206. NASA CP–2330.

Bishop, J., S. K. Atreya, P. N. Romani, F. Herbert, and B. R. Sandel 1991. Voyager 2 UVS occultations at Neptune: Constraints on stratospheric hydrocarbon abundances and comparison with photochemical models. Submitted to *J. Geophys. Res.*

Broadfoot, A. L., S. K. Atreya, J. L. Bertaux, J. E. Blamont, A. J. Dessler, T. M. Donahue, W. T. Forrester, D. T. Hall, F. Herbert, J. B. Holberg, D. M. Hunten, V. A. Krasnopolsky, S. Linick, J. I. Lunine, J. C. McConnell, H. W. Moos, B. R. Sandel, N. M. Schneider, D. E. Shemansky, G. R. Smith, D. F. Strobel, and R. V. Yelle 1989. Ultraviolet spectrometer observations of Neptune and Triton. *Science* **246**, 1459 – 1466.

Cadle, R. D. 1962. The photochemistry of the upper atmosphere of Jupiter. *J. Atmos. Sci.* **19**, 281 – 285.

Caldwell, J., R. Wagener, and K.–H. Fricke 1988. Observations of Neptune and Uranus below 2000 Å with the IUE. *Icarus* **74**, 133 – 140.

Caldwell, J., R. Wagener, T. Owen, M. Combes, and T. Encrenaz 1984. Ultraviolet Observations of Uranus and Neptune below 3000 Å. In *Uranus and Neptune* (J. T. Bergstralh, Ed.), pp. 157 – 178. NASA CP–2330.

Capone, L. A., J. Dubach, S. S. Prasad, and R. C. Whitten 1983. Galactic cosmic rays and N_2 dissociation on Titan. *Icarus* **55**, 73 – 82.

Capone, L. A., J. Dubach, R. C. Whitten, and S. S. Prasad 1979. Cosmic ray ionization of the jovian atmosphere. *Icarus* **39**, 433 – 449.

Capone, L. A., R. C. Whitten, J. Dubach, S. S. Prasad, and W. T. Huntress, Jr. 1976. The lower ionosphere of Titan. *Icarus* **28**, 367 – 378.

Capone, L.A., R.C. Whitten, S.S. Prasad, and J. Dubach 1977. The ionospheres of Saturn, Uranus, and Neptune. *Astrophys. J.* **215**, 977 – 983.

Castleman, A. W., Jr. 1979. Nucleation and molecular clustering about ions. *Adv. in Colloid. and Interface Sci.* **10**, 73 – 128.

Castleman, A. W., Jr., and R. G. Keesee 1986. Ionic clusters. *Chem. Rev.* **86**, 589 – 618.

Castleman, A. W., Jr., and I. N. Tang 1972. Role of small clusters in nucleation about ions. *J. Chem. Phys.* **57**, 3629 – 3638.

Chan, L. Y., and V. A. Mohnen 1980. Ion nucleation theory. *J. Atmos. Sci.* **37**, 2323 – 2331.

Condon, E. Q., and H. Odishaw, Eds. 1972. *Handbook of Physics*, 3rd. ed. American Institute of Physics, New York.

Conrath, B., F. M. Flasar, R. Hanel, V. Kunde, W. Maguire, J. Pearl, J. Pirraglia, R. Samuelson, P. Gierasch, A. Weir, B. Bezard, D. Gautier, D. Cruikshank, L. Horn, R. Springer, W. Shaffer 1989. Infrared observations of the Neptunian system. *Science* **246**, 1454 – 1459.

Dickinson, R. E. 1975. Solar variability and the lower atmosphere. *Bull. Am. Meteorol. Soc.* **56**, 1240 – 1248.

Dubach, J., and W. A. Barker 1971. Charged particle induced ionization rates in planetary atmospheres. *J. Atmos. Terr. Phys.* **33**, 1287 – 1288.

Farley, F. J. M. 1952. The theory of condensation of supersaturated ion–free vapour. *Proc. R. Soc. (London)* A*212*, 530 – 542.

Fink, U., and H. P. Larson 1979. The infrared spectra of Uranus, Neptune, and Titan from 0.8 to 2.5 microns. *Astrophys. J.* **233**, 1021 – 1040.

Fletcher, N. H. 1958. Size effect in heterogeneous nucleation. *J. Chem. Phys.* **29**, 572 – 576. (see also erratum, *J. Chem. Phys.* **31**, 1136, 1959).

Frederick, J. E., C. Leovy, D. E. Anderson, Jr., G. P. Anderson, R. E. Dickinson, S. R. Drayson, S. Fels, L. A. Hall, J. Kiehl, J. E. Mentall, G. H. Mount, M. Nicolet, C. D. Rodgers, G. Rottman, and P. C. Simon 1985. Radiative processes: Solar and terrestrial. In *Atmospheric Ozone 1985*, pp. 349 – 392. NASA, WMO Global Ozone Research and Monitoring Project Report No. 16, Washington, DC.

French, R. G., J. H. Elias, D. J. Mink, and J. L. Elliot 1983. The structure of Neptune's upper atmosphere: The stellar occultation of 24 May 1981. *Icarus* **55**, 332 – 336.

French, R. G., P. A. Melroy, R. L. Baron, E. W. Dunham, K. J. Meech, J. L. Elliot, D. A. Allen, M. C. B. Ashley, K. C. Freeman, E. F. Erickson, J. Goguen, and H. B. Hammel 1985. The 1983 June 15 occultation by Neptune. II. The oblateness of Neptune. *Astron. J.* **90**, 2624 – 2638.

Frenkel, J. 1946. *Kinetic Theory of Liquids*, 488 pp., Dover, New York.

Fuks, S., and A. Bellemans 1966. The surface tension of krypton, methane, and their mixtures. *Physica* **32**, 594 – 602.

Gadsen, M. 1981. The silver–blue cloudlets again: Nucleation and growth of ice in the mesosphere. *Planet. Space Sci.* **29**, 1079 – 1087.

Gee, N., K. Shinsaka, J.-P. Dodelet, and G. R. Freeman 1986. Dielectric constant against temperature for 43 liquids. *J. Chem. Thermodyn.* 18, 221 – 234.

Gladstone, G. R. 1983. *Radiative transfer and photochemistry in the upper atmosphere of Jupiter.* Ph.D. thesis, California Institute of Technology, Pasadena.

Gladstone, G. R., M. Allen, and Y. L. Yung 1991. To be submitted to *Icarus.*

Gleeson, L. J. and W. I. Axford 1968. Solar modulation of galactic cosmic rays. *Astrophys. J.* **154**, 1011 – 1026.

Hamill, P., R. P. Turco, C. S. Kiang, O. B. Toon, and R. C. Whitten 1982. An analysis of various nucleation mechanisms for sulfate particles in the stratosphere. *J. Aerosol. Sci.* **13**, 561 – 585.

Hammel, H. B., K. H. Baines, and J. T. Bergstrahl 1989. Vertical aerosol structure of Neptune: Constraints from center–to–limb profiles. *Icarus* **80**, 416 – 438.

Heisig, G. B., and C. D. Hurd 1933. Vapor pressure and boiling point of pure methylacetylene. *J. Am. Chem. Soc.* **55**, 3485 – 3487.

Hofmann, D. J., and J. M. Rosen 1983. Condensation nuclei events at 30 km and possible influences of solar cosmic rays. *Nature* **302**, 511 – 514.

Hubbard, W. B., H. P. Avey, B. Carter, J. Frecker, H. H. Fu, J.-A. Gehrels, T. Gehrels, D. M. Hunten, H. D. Kennedy, L. A. Lebovsky, K. Mottram, T. Murphy, A. Nielson, A. A. Page, H. J. Reitsema, B. A. Smith, D. J. Tholen, B. Varnes, F. Vilas, M. D. Waterworth, H. H. Wu, and B. Zellner 1985. Results from observations of the 15 June 1983 occultation of the Neptune system. *Astron. J.* 90, 655 – 667.

Hubbard, W. B., P. D. Nicholson, E. Lellouch, B. Sicardy, A. Brahic, F. Vilas, P. Bouchet, R. A. McLaren, R. L. Millis, L. H. Wasserman, J. H. Elias, K. Matthews, and J. D. McGill 1987. Oblateness, radius, and mean stratospheric

temperature of Neptune from the 1985 August 20 occultation. *Icarus* **72**, 635 – 646.

Hudson, R. D., E. I. Reed, and R. D. Bojkov, Eds. 1982. *The Stratosphere 1981, Theory and Measurements.* WMO Global Ozone Research and Monitoring Project No. 11, Washington, DC.

Humes, D. H. 1980. Results of Pioneer 10 and 11 Meteoroid Experiments: Interplanetary and Near–Saturn. *J. Geophys. Res.* **85**, 5841 – 5852.

Hunten, D. M. 1974. Introduction and summary. In *The Atmosphere of Uranus* (D. M. Hunten, Ed.) Proceedings of a NASA workshop held at ARC, pp. 1 – 7.

Hunten, D. M. 1975. Vertical transport in atmospheres. In *Atmospheres of Earth and the Planets* (B. M. McCormac, Ed.), pp. 59 – 72. Reidel, Dordrecht.

Hunten, D. M., R. P. Turco, and O. B. Toon 1980. Smoke and dust particles of meteoritic origin in the mesosphere and stratosphere. *J. Atmos. Sci.* **37**, 1342 – 1357.

Ip, W.–H., and W. I. Axford 1985. Estimates of galactic cosmic ray spectra at low energies. *Astron. Astrophys.* **149**, 7 – 10.

Jasper, J. J. 1972. The surface tension of pure liquid compounds. *J. Phys. Chem. Ref. Data* **1**, 841 – 1009.

Johnson, V. J., Ed. 1961. *Properties of Materials at Low Temperature (Phase 1): A Compendium*, Peragammon Press, New York.

Jokipii, J. R., and D. A. Kopriva 1979. Effects of particle drift on the transport of cosmic rays. III. Numerical models of galactic cosmic–ray modulation. *Astrophys. J.* **234**, 384 – 392.

Keesee, R. G. 1989. Nucleation and particle formation in the upper atmosphere. *J. Geophys. Res.* **94**, 14683 – 14692.

Khanna, R. K., J. E. Allen, Jr., C. M. Masterson, and G. Zhao 1990. Thin–film infrared spectroscopic method for low–temperature vapor pressure measurements. *J. Phys. Chem.* **94**, 440 – 442.

Khare, B. N., C. Sagan, W. R. Thompson, E. T. Arakawa, and P. Votaw 1987. Solid hydrocarbon aerosols produced in simulated Uranian and Neptunian stratospheres. *J. Geophys. Res.* **92**, 15067 – 15082.

Kirk, B. S., and W. T. Ziegler 1965. A phase–equilibrium apparatus for gas–liquid systems and the gas phase of gas–solid systems: Application to methane–hydrogen from 66.88 to 116.53 K and up to 125 atmospheres. In *Advances in Cryogenic Engineering* (K.D. Timmerhaus, Ed.), Vol. 10, Part 2, pp. 160 – 170. Plenum, New York.

Kostiuk, T., F. Espenak, P. Romani, D. Zipoy, and J. Goldstein 1990. Ethane abundance on Neptune. *Icarus* **88**, 87 – 96.

Landry, B., M. Allen, and Y. L. Yung 1991. Troposphere–stratosphere interactions in a one–dimensional model of jovian photochemistry. *Icarus* **89**, 377 – 383.

Lane, A. L., R. A. West, C. W. Hord, R. M. Nelson, K. E. Simmons, W. R. Pryor, L. W. Esposito, L. J. Horn, B. D. Wallis, B. J. Buratti, T. G. Brophy, P. Yanamandra–Fisher, J. E. Colwell, D. A. Bliss, M. J. Mayo, and W. D. Smythe 1989. Photometry from Voyager 2: Initial results from the Neptunian atmosphere, satellites, and rings. *Science* **246**, 1450 – 1454.

Leadbetter, A. J., D. J. Taylor, and B. Vincent 1964. The densities and surface tensions of liquid ethane and nitrous oxide. *Can. J. Chem.* **42**, 2930 – 2932.

Lellouch, E., W. B. Hubbard, B. Sicardy, F. Vilas, and P. Bouchet 1986. Occultation determination of Neptune's oblateness and stratospheric methane mixing ratio. *Nature* **324**, 227 – 231.

Lindal, G. F., J. R. Lyons, D. N. Sweetnam, V. R. Eshleman, D. P. Hinson, and G. L. Tyler 1990. The atmosphere of Neptune: Results of radio occultation measurements with the Voyager 2 spacecraft. *Geophys. Res. Lett.* **17**, 1733 – 1736.

Lindzen, R. S. 1971. Tides and gravity waves in the upper atmosphere. In *Mesospheric Models and Related Experiments* (G. Fiocco, Ed.), pp. 122 – 130. Reidel, Dordrecht.

Lockwood, G. W., and D. T. Thompson 1986. Long–term brightness variations of Neptune and the solar cycle modulation of its albedo. *Science* **234**, 1543 – 1545.

Lockwood, G. W., and D. T. Thompson 1991. Solar cycle relationship clouded by Neptune's sustained brightness maximum. *Nature* **349**, 593 – 594.

Lunine, J. I., and D. M. Hunten 1989. Abundance of condensable species at planetary cold traps: The role of moist convection. *Planet. Space. Sci.* **37**, 151 – 166.

Maass, O., and C. H. Wright 1921. Some physical properties of hydrocarbons containing two and three carbon atoms. *J. Am. Chem. Sic.* **43**, 1098 – 1111.

Macpherson, M. T., M. J. Pilling, and M. J. C. Smith 1985. Determination of the absorption cross section for CH_3 at 216.36 nm and the absolute rate constant for methyl radical recombination over the temperature range 296 – 577 K. *J. Phys. Chem.* **89**, 2268 – 2274.

Macy, W., Jr., and W. Sinton 1977. Detection of methane and ethane emission on Neptune but not on Uranus. *Astrophys. J.* **218**, L79 – L81.

Macy, W., Jr., and L. Trafton 1975. Neptune's atmosphere: The source of thermal inversion. *Icarus* **26**, 428 – 436.

Mathis, J. S., P. G. Mezger, and N. Panagia 1983. Interstellar radiation field and dust temperatures in the diffuse interstellar matter and in giant molecular clouds.

Astron. Astrophys. **128**, 212 – 229.

McClune, C. R. 1976. Measurements of the densities of liquified hydrocarbons from 93 to 173 K. *Cryogenics* **16**, 289 – 295.

McDonald, J. E. 1962. Homogeneous nucleation of vapor condensation I. Thermodynamic aspects. *Amer. J. Phys.* **30**, 870 – 877.

McDonald, J. E. 1963. Homogeneous nucleation of vapor condensation II. Kinetic aspects. *Amer. J. Phys.* **31**, 31 – 41.

McKibben, R. B., K. R. Pyle, and J. A. Simpson 1985. Changes in radial gradients of low–energy cosmic rays between solar minimum and maximum: Observations from 1 to 31 AU. *Astrophys. J.* **289**, L35 – L39.

Mentall, J. E., J. E. Frederick, and J. R. Herman 1981. The solar irradiance from 200 to 330 nm. *J. Geophys. Res.* **86**, 9881 – 9884.

Morehouse, F. R., and O. Maass 1931. The preparation and physical properties of ethyl and methyl acetylene. *Can. J. Research* **5**, 306 – 312.

Moses, J. I., M. Allen, and Y. L. Yung 1989. Neptune's visual albedo variations over a solar cycle: A pre–Voyager look at ion–induced nucleation and cloud formation in Neptune's troposphere. *Geophys. Res. Lett.* **16**, 1489 – 1492.

Mount, G. H., and G. J. Rottman 1981. The solar spectral irradiance 1200 – 3184 Å near solar maximum: 15 July 1980. *J. Geophys. Res.* **86**, 9193 – 9198.

Mount, G. H., and G. J. Rottman 1983. The solar absolute spectral irradiance 1150 – 3173 Å: May 17, 1982. *J. Geophys. Res.* **88**, 5403 – 5410.

Neff, J. S., D. C. Humm, J. T. Bergstrahl, A. L. Cochran, W. D. Cochran, E. S. Barker, and R. G. Tull 1984. Absolute spectrophotometry of Titan, Uranus, and Neptune: 3500 – 10,500 Å. *Icarus* **60**, 221 – 235.

Ness, N. F., M. H. Acuña, L. F. Burlaga, J. E. P. Connerney, R. P. Lepping, F. M. Neubauer 1989. Magnetic fields at Neptune. *Science* **246**, 1473 – 1478.

Orton, G., D. K. Aitken, C. Smith, P. F. Rouche, J. Caldwell, and R. Snyder 1987. The spectra of Uranus and Neptune at 8 – 14 and 17 – 23 μm. *Icarus* **70**, 1 – 12.

Orton, G. S., and J. F. Appleby 1984. Temperature structures and infrared–derived properties of the atmospheres of Uranus and Neptune. In *Uranus and Neptune* (J. T. Bergstralh, Ed.), pp. 89 – 156. NASA CP–2330.

Orton, G., K. H. Baines, J. Caldwell, P. Romani, A. T. Tokunaga, and R. A. West 1990a. Calibration of the 7– to 14–μm brightness spectra of Uranus and Neptune. *Icarus* **85**, 257 – 265.

Orton, G., J. Lacy, J. Achterman, and P. Parmar 1990b. Isotopic ratios in Neptune and Titan. *Bull. Am. Astron. Soc.* **22**, 1093.

Orton, G., A. T. Tokunaga, and J. Caldwell 1983. Observational constraints on the atmospheres of Uranus and Neptune from measurements near 10 μm. *Icarus* **56**, 147 – 164.

Parker, E. N. 1965. The passage of energetic charged particles through interplanetary space. *Planet. Space Sci.* **13**, 9 – 49.

Parkinson, C. D., J. C. McConnell, B. R. Sandel, R. V. Yelle, and A. L. Broadfoot 1990. He 584 Å dayglow at Neptune. *Geophys. Res. Lett.* **17**, 1709 – 1712.

Pollack, J. B., K. Rages, K. H. Baines, J. T. Bergstralh, D. Wenkert, and G. E. Danielson 1986. Estimates of the bolometric albedos and radiation balance of Uranus and Neptune. *Icarus* **65**, 442 – 446.

Pollack, J. B., K. Rages, S. K Pope, M. G. Tomasko, P. N. Romani, and S. K. Atreya 1987. Nature of the stratospheric haze on Uranus: Evidence for condensed

hydrocarbons. *J. Geophys. Res.* **92**, 15037 – 15065.

Pruppacher, H. R., and J. D. Klett 1978. *Microphysics of Clouds and Precipitation*, 741 pp., Reidel, Hingham, Mass.

Romani, P. N., and S. K. Atreya 1988. Methane photochemistry and haze production on Neptune. *Icarus* **74**, 424 – 445.

Romani, P. N., and S. K. Atreya 1989. Stratospheric aerosols from CH_4 photochemistry on Neptune. *Geophys. Res. Lett.* **16**, 941 – 944.

Rosinski, J., and R. H. Snow 1961. Secondary particulate matter from meteor vapors. *J. Meteor.* **18**, 736 – 745.

Russell, K. C. 1969. Nucleation on gaseous ions. *J. Chem. Phys.* **50**, 1809 – 1816.

Sandel, B. R., D. E. Shemansky, and A. L. Broadfoot 1978. Hydrogen Lβ and Lα emission lines observed from the interplanetary medium by the Voyager UV spectrometer. *Nature* **274**, 666 – 667.

Schlessinger, G. G. 1970. Vapor pressures, critical temperatures and critical pressures of organic compounds. In *Handbook of Chemistry and Physics.* Chemical Rubber Co., Cleveland.

Schopper, H. 1973. In *Landolt–Bornstein Numerical Data and Functional Relationships in Science and Technology* **7**. Springer–Verlag, New York.

Seinfeld, J. H. 1986. *Atmospheric Physics and Chemistry of Air Pollution*, 738 pp., Wiley, New York.

Seki, J., and H. Hasegawa 1983. The heterogeneous condensation of interstellar ice grains. *Astrophys. Space Sci.* **94**, 177 – 189.

Sigsbee, R. A. 1969. Vapor to condensed–phase heterogeneous nucleation. In *Nucleation* (A.C. Zettlemoyer, Ed.), pp. 151 – 224. Marcel Dekker, New York.

Simpson, J. A. 1983. In *Composition and Origin of Cosmic Rays* (M.M. Shapiro, Ed.), pp. 1 – 24. Reidel, Dordrecht.

Slagle, I. R., D. Gutman, J. W. Davies, and M. J. Pilling 1988. Study of the recombination reaction $CH_3 + CH_3 \rightarrow C_2H_6$. 1. Experiment. *J. Phys. Chem.* **92**, 2455 – 2462.

Smith, B. A., L. A. Soderblom, D. Banfield, C. Barnet, A. T. Basilevsky, R. F. Beebe, K. Bollinger, J. M. Boyce, A. Brahic, G. A. Briggs, R. H. Brown, C. Chyba, S. A. Collins, T. Colvin, A. F. Cook II, D. Crisp, S. K. Croft, D. Cruikshank, J. N. Cuzzi, G. E. Danielson, M. E. Davies, E. De Jong, L. Dones, D. Godfrey, J. Goguen, I. Grenier, V. R. Haemmerle, H. Hammel, C. J. Hansen, C. P. Helfenstein, C. Howell, G. E. Hunt, A. P. Ingersoll, T. V. Johnson, J. Kargel, R. Kirk, D. I. Kuehn, S. Limaye, H. Masursky, A. McEwen, D. Morrison, T. Owen, W. Owen, J. B. Pollack, C. C. Porco, K. Rages, P. Rogers, D. Rudy, C. Sagan, J. Schwartz, E. M. Shoemaker, M. Showalter, B. Sicardy, D. Simonelli, J. Spencer, L. A. Stromovsky, C. Stoker, R. G. Strom, V. E. Suomi, S. P. Synott, R. J. Terrile, P. Thomas, W. R. Thompson, A. Verbiscer, and J. Veverka 1989. Voyager 2 at Neptune: Imaging science results. *Science* **246**, 1422 – 1449.

Southworth, R. B., and Z. Sekanina 1973. *Physical and dynamical studies of meteors*, 106 pp., NASA Contractor Rep. CR–2316.

Stewart, J. W., and R. I. LaRock 1958. Compression and densities of four solidified hydrocarbons and carbon tetrafluoride at 77 K. *J. Chem. Phys.* **28**, 425 – 427.

Stoker, C. R., and O. B. Toon 1989. Moist convection on Neptune. *Geophys. Res. Lett.* **16**, 929 – 932.

Stone, P. H. 1976. The meteorology of the Jovian atmosphere. In *Jupiter* (T. Gehrels, Ed.), pp. 586 – 618. University of Arizona Press, Tucson.

Strobel, D. F. 1969. The photochemistry of methane in the Jovian atmosphere. *J. Atmos. Sci.* **26**, 906 – 911.

Strobel, D. F. 1973. The photochemistry of hydrocarbons in the Jovian atmosphere. *J. Atmos. Sci.* **30**, 489 – 498.

Strobel, D. F. 1985. The photochemistry of the atmospheres of the outer planets and their satellites. In *The Photochemistry of Atmospheres* (J. S. Levine, Ed.), pp. 393 – 434. Academic, Orlando.

Strobel, D. F., M. E. Summers, F. Herbert, and B. R. Sandel 1990. The photochemistry of methane in the atmosphere of Triton. *Geophys. Res. Lett.* **17**, 1729 – 1732.

Stull, D. R. 1947. Vapor pressure of pure substances. Organic compounds. *Ind. Eng. Chem.* **39**, 517 – 540.

Suck, S. H., T. S. Chen, R. W. Emmons, D. E. Hagen, and J. L. Kassner, Jr. 1982. Role of ions in heteromolecular nucleation: Free energy change of hydrated ion clusters. In *Heterogeneous Atmospheric Chemistry* (D.R. Schryer, Ed.), Geophysical Monograph 26, pp. 28 – 32. American Geophysical Union, Washington, D.C.

Summers, M. E., and D. F. Strobel 1989. Photochemistry of the atmosphere of Uranus. *Astrophys. J.* **346**, 495 – 508.

Tanneberger, H. 1933. Einige Bemerkungen über die Dampf–druck–Kurve des Diacetylens (Butadiins). *Berichte D. Chem. Ges.* **66**, 484 – 486.

Thompson, W. R., T. Henry, B. N. Khare, L. Flynn, J. Schwartz, and C. Sagan 1987. Light hydrocarbons from plasma discharge in H_2–He–CH_4: First results and Uranian auroral chemistry. *J. Geophys. Res.* **92**, 15083 – 15092.

Thomson, J. J. 1888. *Application of Dynamics to Physics and Chemistry*, 1st ed., p.

165, Cambridge Univ. Press, London.

Thomson, W. (Lord Kelvin) 1870. On the equilibrium of vapour at a curved surface of liquid. *Proc. Roy. Soc. Edinburgh* **7**, 63 – 68.

Tickner, A. W., and F. P. Lossing 1951. The measurement of low vapor pressures by means of a mass spectrometer. *J. Phys. Colloid Chem.* **55**, 733 – 740.

Tohmfor, G., and M. Volmer 1938. Die Keimbildung unter dem Einfluss elektrischer Landungen. *Annln. Phys. (Leipzig),* Ser. 5, **33**, 109 – 131.

Toon, O. B., C. P. McKay, R. Courtin, and T. P. Ackerman 1988. Methane rain on Titan. *Icarus* **75**, 255 – 284.

Torr, M. R., and D. G. Torr 1985. Ionization frequencies for solar cycle 21: Revised. *J. Geophys. Res.* **90**, 6675 – 6678.

Trafton, L. 1981. The atmospheres of the outer planets and satellites. *Rev. Geophys. Space Phys.* **19**, 43 – 89.

Turco, R. P., O. B. Toon, R. C. Whitten, R. G. Keesee, and D. Hollenbach 1982. Noctilucent clouds: Simulation studies of their genesis, properties and global influences. *Planet. Space Sci.* **30**, 1147 – 1181.

Twomey, S. 1977. *Atmospheric Aerosols*, 302 pp. Amsterdam: Elsevier Scientific Pub. Co.

Van Allen, J. A., and B. A. Randall 1985. Interplanetary cosmic ray intensity: 1972 – 1984 and out to 32 AU. *J. Geophys. Res.* **90**, 1399 – 1412.

Velinov, P. 1968. On ionization in the ionospheric D–region by galactic and solar cosmic rays. *J. Atmos. Terr. Phys.* **30**, 1891 – 1905.

Volmer, M., and H. Flood 1934. Tropfchenbildung in Dampfen. *Z. Phys. Chem.* A*170*, 273 – 285.

Wagener, R., J. Caldwell, and K.–H. Fricke 1986. The geometric albedos of Uranus and Neptune between 2100 and 3350 Å. *Icarus* **67**, 281 – 288.

Webber, W. R. 1987. The interstellar cosmic ray spectrum and energy density. Interplanetary cosmic ray gradients and a new estimate of the boundary of the heliosphere. *Astron. Astrophys.* **179**, 277 – 284.

Webber, W. R., and J. A. Lockwood 1987. Interplanetary radial cosmic–ray gradients and their implication for a possible large modulation effect at the heliosphere boundary. *Astrophys. J.* **317**, 534 – 542.

Weber, L. A. 1976. Dielectric constant data and the derived Clausius–Mossotti function for compressed gaseous and liquid ethane. *J. Chem. Phys.* **65**, 446 – 449.

Wilson, C. T. R. 1897. Condensation of water vapor in the presence of dust–free air and other gases. *Phil. Trans. R. Soc.* **A189**, 265 – 274.

Woods, T. N., and G. J. Rottman 1990. Solar EUV irradiance derived from a sounding rocket experiment on November 10, 1988. *J. Geophys. Res.* **95**, 6227 – 6236.

Younglove, B. A. 1982. *Thermophysical Properties of Fluids. I. Argon, Ethylene, Parahydrogen, Nitrogen, Nitrogen Trifluoride, and Oxygen.* National Bureau of Standards Technical Note 1048.

Younglove, B. A., and J. F. Ely 1987. Thermophysical properties of fluids. II. Methane, ethane, propane, isobutane, and normal butane. *J. Phys. Chem. Ref. Data* **16**, 577 – 798.

Yung, Y. L., M. Allen, and J. P. Pinto 1984. Photochemistry of the atmosphere of Titan: Comparison between model and observations. *Astrophys. J. Suppl. Ser.* **55**, 465 – 506.

Ziegler, W. T. 1959. *The Vapor Pressures of Some Hydrocarbons in the Liquid and Solid State at Low Temperatures*, 18 pp., National Bureau of Standards Technical

Note 4.

Ziegler, W. T., B. S. Kirk, J. C. Mullins, and A. R. Berquist 1964. *Calculation of the vapor pressure and heats of vaporization and sublimation of liquids and solids below one atmosphere pressure. VII. Ethane*, 57 pp, Technical Report No. 2, Eng. Expt. Station, Georgia Institute of Technology.